Study of hydro-mechanical instabilities in geomaterials

Siddhartha Harsha Ommi

CENTRALE NANTES

THÈSE DE DOCTORAT DE

L'ÉCOLE CENTRALE DE NANTES

ÉCOLE DOCTORALE N° 602
Sciences pour l'Ingénieur
Spécialité : *Génie Civil*

Par
Siddhartha Harsha. OMMI

Study of hydro-mechanical instabilities in geomaterials

Thèse présentée et soutenue à l'École Centrale de Nantes le 14 avril 2022
Unité de recherche : UMR 6183, Institut de Recherche en Génie Civil et Mécanique (GeM)

Rapporteurs avant soutenance :

Pierre SEPPECHER	Professeur des universités, Université de Toulon
Sergey GAVRILYUK	Professeur des universités, Université d'Aix-Marseille

Composition du Jury :

Président :	Pierre SEPPECHER	Professeur des universités, Université de Toulon
Examinateurs :	Laura De LORENZIS	Professeure, ETH Zürich
	Laurent STAINIER	Professeur des universités, École Centrale de Nantes
Dir. de thèse :	Giulio SCIARRA	Professeur des universités, École Centrale de Nantes
Co-dir. de thèse :	Panagiotis KOTRONIS	Professeur des universités, École Centrale de Nantes

Doctoral Thesis

École Centrale de Nantes
Université Bretagne Loire
École docotrale N° 602 : Sciences pour l'Ingénieur
Spécialité: Génie Civil

Study of hydro-mechanical instabilities in geo-materials

by Siddhartha Harsha. OMMI

Thesis presented and defended at École Centrale de Nantes on 14 april 2022
Research unit: UMR 6183, Institut de Recherche en Génie Civil et Mécanique (GeM)

RAPPORTEURS BEFORE THE DEFENSE:

	Pierre SEPPECHER	Professeur des universités, Université de Toulon
	Sergey GAVRILYUK	Professeur des universités, Université d'Aix-Marseille

COMPOSITION OF THE JURY:

President :	Pierre SEPPECHER	Professeur des universités, Université de Toulon
Examinators :	Laura De LORENZIS	Professor, ETH Zürich
	Laurent STAINIER	Professeur des universités, École Centrale de Nantes
Dir. of thesis :	Giulio SCIARRA	Professeur des universités, École Centrale de Nantes
Co-dir. of thesis :	Panagiotis KOTRONIS	Professeur des universités, École Centrale de Nantes

ACKNOWLEDGMENTS

The experience of pursuing a PhD could have been expressed using several words. In view of being concise, here I choose one: fulfilling. There are several individuals that have accompanied me in this journey of over three years. While a single typeset page would not do justice to their contributions, I owe them all a sincere acknowledgment.

Foremost, I would not have been able to complete this thesis without the unwavering guidance of my advisers: Giulio Sciarra and Panagiotis Kotronis. I express my deepest gratitude to both of you for your continued support and excellent direction during my first steps. Giulio, thank you for introducing me to this strangely complex world of porous media and guiding me onto the right path whenever I tend to meander. I especially admire and envy your unrelenting patience that has been constructive in shaping my thoughts and work. Panos, I am indebted to you for your enthusiasm and your meticulous comments on my work. Many a time, your encouragement has pushed me to pursue aspects that I originally deemed arduous. I am grateful for the jury members and deeply honored by their kind acceptance of the invitation. I thank M. Sergey Gavrilyuk and M. Pierre Seppecher for accepting to spend their invaluable time in reading my thesis. I thank also the committee that has followed-up my work for this thesis: M. Corrado Maurini and M. Pierre Bésuelle, whose guidance has been indispensable.

I have been fortunate to be part of the GeM laboratory especially because of the environment it has created to nourish younger researchers at the beginning of their career. I thank M. Thomas Heuzé and M. Laurent Stainier for giving me the opportunity to teach along side them which has been a rewarding experience. I thank all my colleagues for being no less than kind towards me and for providing plentiful positive energy. I am grateful to Sara and Quentin who have shared the office with me all these years. Sara, I thank you deeply for the friendship and warmth that you have shared throughout. Quentin, I thank you for sharing your enthusiasm and, mostly french, anecdotes. I thank, Katia for her energetic presence and support, Eric for sharing his know-how and for keeping the Titan cluster running through the heaviest of loads. The colleagues in the ANR-STOWENG project deserve a special mention: Rana for her meticulous experimentation, Mohammed for sharing the other side of modeling and colleagues of the 3SR laboratory at Université Grenoble Alpes for sharing their experimental observations. Special thanks goes to people who gathered around the table for lunch everyday sharing their laughs: Alex, Georges, Praveen, Mickäel, Filippo, Diego, Jinane, Imane/s, Youmna, Ahmad, Abdallah, Guillemette, Aliénor, … the list is long but is incomplete without mentioning Julietta for bringing much joy. I thank my dear friend Vasu for always being an example and bearing with my peculiar humor throughout our long journey together. A heartfelt thanks goes to Serge Lefrant, Annie Simon and to Cataldo, Clara for being kind enough to open their doors to me and to Claude… for being Claude! I am indebted to the numerous individuals who have spent their hours in supporting various open-source and community-driven softwares/libraries that have been invaluable for my thesis: special mention goes to the Linux-Mint team, FEniCS, PETSc/TAO and SLEPc.

I finally thank my large family, the list of which would fill another page. My mother and grand mother, for all their sacrifices and patience throughout my endeavors. My grandfather, for encouraging me to explore

the world and whose presence I dearly miss. Both my uncles and my aunts who have been the pillars of my growth and my siblings who give me a sense of togetherness. This page would be incomplete without thanking my most beloved one, Graziana, for being an unrelenting support and source of energy for me all these years. Your essential presence has been THE most exceptional influence through this journey.

All these individuals and many others, known and unknown, have had their supportive hand in my journey up until now and hopefully in the future.

ABSTRACT

Hydraulic and mechanical instabilities in geomaterials refer to a variety of non-linear phenomena that can be triggered by heterogeneities inherent to such materials. Hydraulic instabilities in partially saturated conditions can manifest themselves as heterogeneous fluid invasion causing 'fingering' phenomenon. Mechanical instabilities on the other hand can present themselves as strain localizations and/or fractures. These instabilities and their associated coupling pose a major obstacle for a myriad of applications involving geomaterials like Carbon dioxide (CO_2) sequestration, rain water infiltration and also for reliable predictions such as for contaminant flow in ground waters. Existing classical models do not resolve this behavior due to their lack of pattern-forming ingredients in their formulation and thus being stable against perturbations. The essence of current thesis work is to propose and investigate modeling techniques that allow to describe these instabilities in a simple and natural manner. The constitutive approach adopted in this thesis is that of micro-structured continua, in particular that of enhanced continua with a constitutive law depending on the gradient of so-called phase field variables.

The first part of the work deals with description of a fluid-fluid front that has been modeled as a diffused interface. This has been done by interpreting the presence of two fluids within the pore space as a single non-uniform fluid and the degree of saturation of one of the fluids as the corresponding phase field. While classical one-to-one relation between capillary pressure and saturation degree is expected to describe the retention properties of the porous network due to its texture, an enhanced relation is obtained by prescribing a chemical potential in the spirit of Cahn-Hilliard type modeling of multi-phase fluids. This enhanced relation together with a non-local energy contribution provides the ingredients required to describe fluid-fingering and non-local phenomena such as pinching and coalescence of fluids due to variations in capillary forces. Using asymptotic matching techniques it has been shown analytically, in a one-dimensional setting, that the particular choice of energy contributions employed in the above framework allows to replicate 'overshoot' type non-monotonic saturation profiles during constant-rate infiltration into relatively dry medium. This has been found to match qualitatively with experimental observation. Further, a slight non-convexity introduced into the flux function has been shown numerically to allow the modeling of drainage fronts, besides imbibition, without employing any additional complexities into the model. A careful linear stability analysis (LSA) of the homogeneous solutions against arbitrary perturbations has been done. The growth in time of the amplitude of imposed transverse perturbations is understood as the fingering phenomenon. The predictions of the LSA have been followed-up by two-dimensional simulations portraying the ability of the proposed model to describe fluid fingering and segregation.

In the second part the triggering of a fracture within a drying porous medium has been studied. A prevailing modeling perspective, in the spirit of gradient damage modeling, has been first tested for its ability to replicate periodic fracture formation as observed in representative experiments. Further an investigation is done, starting from the gradient damage modeling framework, but interpreting the presence of a fracture within a drying porous material as a loss of its capillary properties, thus allowing the passage of non-wetting fluid under vanishing capillary pressure. This paradigm is

of particular interest in modeling cohesion-less and unconsolidated fine-grained soils, where the resistance against tensile loading is negligible and thus fracturing induced due to development of tensile stresses is not the prevailing phenomenon. Starting from the principles of variational approach used to construct the model, it has been shown that for sufficiently strong desiccation, damage initiates homogeneously on the drying face while progressing into the body with time. The possible occurrence of bifurcations of this base solution has been analyzed, again in the framework of LSA.

This works sets the stage for various possibilities, the most natural one being the study of coupling between the above mentioned instabilities. Apart from that, two-dimensional simulations of fluid-fingering have shown that the model predicts additional features of unstable flow, such as pinching and coalescence of the wetting phase, which need to be investigated using carefully designed experiments. Initiation of damage induced due to evolving drainage finger is also of particular interest in the context of earlier mentioned applications. Lastly, advanced numerical techniques can be sought after for resolution of the above problems with an intent to provide accurate solutions more efficiently.

CONTENTS

I Introduction 1

1 Preamble 2

2 Phenomenology 5
2.1 Unstable bi-phasic flow in porous media 5
2.2 Fracturing in fine-grained soils 10
2.3 Synopsis 13

3 Partially saturated poromechanics & a non-uniform fluid 14
3.1 Classical approach to partial saturation 15
3.2 A phase field approach to partial saturation 25
3.3 Synopsis 36

II Hydraulic instabilities 37

4 One-dimensional analysis: Imbibition & Drainage 38
4.1 Summary of the model - Governing equations 38
4.2 Dimensional analysis & scaling 39
4.3 Limit of vanishing diffusion & the flux function 40
4.4 PDE simulations 42
4.5 Traveling wave analysis 49
4.6 Synopsis 57

5 Linear stability analysis 58
5.1 Stability against transverse perturbations 58
5.2 Stability against longitudinal perturbations 65
5.3 Synopsis 67

6 Two-dimensional simulations 68
6.1 Imbibition fronts 68
6.2 Drainage fronts 71
6.3 Synopsis 74

III Mechanical instabilities 75

7 Gradient damage modeling of tensile fracture 76
7.1 Mathematical model 77
7.2 Numerical approximation & Algorithm 85
7.3 Two-dimensional desiccation problem 86
7.4 Synopsis 90

8 Gradient damage modeling of 'capillary' fracture 91
8.1 Mathematical model 92
8.2 Numerical approximation & Algorithm 99
8.3 Two-dimensional desiccation problem 100
8.4 Synopsis 111

9 Conclusion & perspectives **112**

Bibliography **113**

IV Appendices **121**

PART I
INTRODUCTION

1 PREAMBLE

Context It comes as a no surprise that since the industrial revolution human activity is affecting, at a grand scale, the natural cycles that preserve the habitability of our planet. For instance, anthropogenic contribution of carbon dioxide (CO_2), especially due to the use of fossil fuels, to the carbon cycle is a major cause of its accumulation in the Earth's atmosphere, dropping pH of the oceans and increasing global temperatures. Each of these in turn have an array of devastating affects on the delicate balance that is needed . Our accumulated knowledge is sufficient to know that even though there exist sinks within this cycle that can potentially reduce the harmful impact, there is no existing natural savior that can act as a silver bullet (Falkowski et al., 2000). However, various techniques have been proposed, a combination of which could do this job. *Carbon Capture & Storage* (CCS) being one of them, has proven (Loria and Bright, 2021) over the past 50 years to be a promising solution especially because it ensures a smooth transition to renewable resources instead of a sharp shift in the energy supply. It is especially attractive because it can be employed to directly target CO_2 generated at coal or gas fired power plants and cement production plants, which account for over 40% of the worldwide emissions. This is because these plants act as stationary and predictable sources of CO_2. Apart from CCS, a solution that focuses on the convergence towards a low carbon economy and balancing of supply and demand is the large-scale underground storage of energy. This has shown (Pasten and Carlos Santamarina, 2011; Matos et al., 2019) the potential to integrate renewable energy sources while efficiently managing the grid, thus increasing energy security.

While the operational aspects of the above mentioned solutions are similar, for the purpose of being concise we contextualize CCS. This involves capturing at a large scale the atmospheric CO_2 and then sequestering it at its super-critical conditions. At these conditions the gas retains its low viscosity but attains an increased density, reducing substantially the required storage volume. At depths of around 1km and higher within the Earth's crust the conditions are just right for this purpose, thus providing a relatively vast storage volume. The injection of compressed CO_2 in high permeable rock formations at suitable geological sites involves displacement of the resident wetting fluid, usually brine water (in saline aquifers) or residual oil

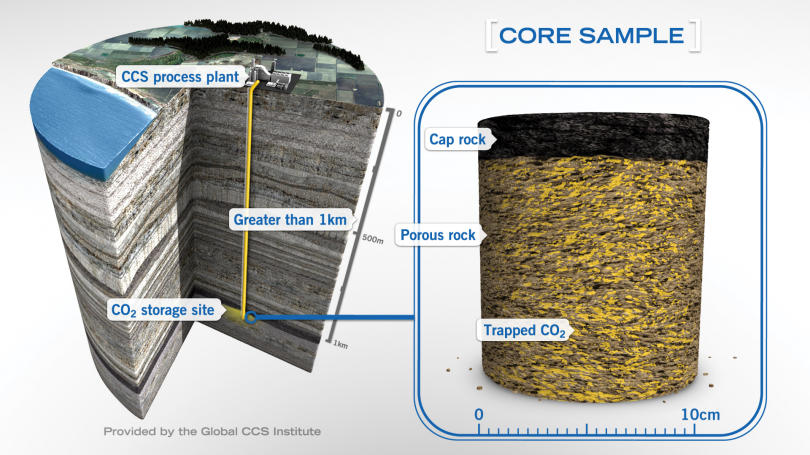

Figure 1.1: Schematic of geological storage of CO_2. Inset: Schematic of core sample showing trapped CO_2 in yellow and the sealing cap-rock. Image provided by Global Carbon Capture and Storage Institute Ltd.

(in depleted oil fields). A low permeable cap-rock usually acts as a natural barrier to trap the injected CO_2, Fig.(1.1). As any other operation involving geomaterials, the above process comes with a myriad of complexities and risks. One of the major concerns is the proper containment of CO_2 during the injection and ensuing migration of the gas plume. Geomaterials are known to be inherently inhomogeneous with existing fractures and new ones on the cusp of being triggered. It is known and well-studied (Wiprut and Zoback, 2000; Chiaramonte et al., 2008; Espinoza and Santamarina, 2017) that the previously dormant faults within cap-rocks can be triggered due to pressure changes within the vicinity. Another concern is the predictability of the flow itself. Any instability relative to an advancing fluid front could lead to reduced efficiency of the operation (Yamabe et al., 2015; Zacharoudiou et al., 2018). It can even pose an environmental risk if preferential paths for the fluid flow are triggered within the cap-rock due to fault planes, thus providing an escape route to the rising or migrating CO_2 plumes (Macminn et al., 2010; Gilfillan et al., 2011; Song and Zhang, 2013).

The motion of two immiscible fluids, in the above case CO_2 and brine, one displacing the other through an inhomogeneous material which itself could fail is a coupled problem. While such coupled phenomena are contextualized above for CCS operations, there are numerous other applications within soil hydrology that fall victim to inhomogeneous fluid flow and coupled failure mechanisms. Transport of solutes and contaminants to the ground waters, Fig.(1.2), is a phenomenon that has far-reaching consequences (Glass et al., 1988; Jarvis, 2007; Clothier et al., 2008). While natural rain and irrigation waters replenish the ground waters, they also tend to carry the surface pollutants such as fertilizers and toxic wastes. However, the soil layers act as natural filters of these pollutants before they could reach the water table. The efficiency of this process and the ability to make predictions of ground water contamination are known to be negatively impacted by the formation of preferential pathways due to unstable infiltration.

Another context where immiscible fluid flow can trigger pore network failure is in the hydrate stability zone (HSZ) found under ocean sediments along continental margins (Sloan, 2003). In HSZs it has been observed that methane hydrates, methane gas and brine can co-exist (Gorman et al., 2002). While methane hydrates are widely believed to be a potential source of energy supply, the prevailing risk is the release of trapped methane gas through existing or newly formed faults within the sediments. It has been hypothesized that continued gas accumulation below the HSZ can result in activation of fractures (Zuhlsdorff and Spie, 2004; Liu and Flemings, 2006) which could also be the reason for underwater oceanic land slides (Paull et al., 2002) in addition to the release of the highly potent green-house gas.

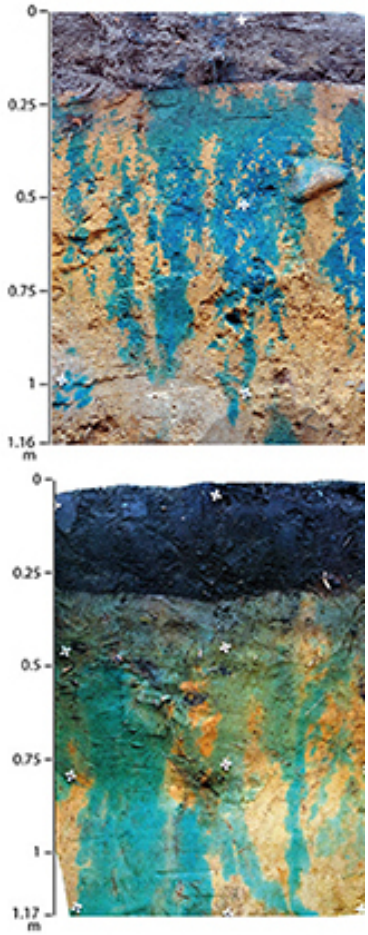

Figure 1.2: Dye tracer experiments (Schneider et al., 2018) exhibiting solute movement along preferential flow paths in relicit charcoal hearth soils.

Motivation While the prediction and control capabilities in real-world applications of the immiscible fluid-fluid displacement coupled to the porous matrix could be ridden with uncertainties, efficient modeling of the phenomena involved gives a head-start. Models provide new insights into individual phenomena involved within the coupling and their associated failure mechanisms. This has been the rationale for an ever-growing body of research within which the current thesis is a small part.

Objectives Failure in the current context is the formation of preferential pathways for the fluids to flow. For immiscible fluid-fluid displacements this could be viewed as an instability of the moving front also called fluid fingering. On the other hand, mechanical failure of the porous matrix that creates a pathway could be viewed as a localized re-structuring of the soil grains which could lead to an opening mode fracture or at least a localized modification of the material properties such that one fluid can displace the other with ease. While classical theories that have been used over

the years to model bi-phasic flow in deformable porous media are able to model ideal/stable processes, they have been known to be lacking the ability to model unstable phenomena and coupling involved. However, various modeling extensions have been proposed to remedy this lacking, each building upon the existing classical models. It is the purpose of the current thesis to propose such extended models and investigate their ability to describe both hydraulic and mechanical instabilities.

Plan The current thesis is organized as follows. Chp.(2) is dedicated to the phenomenology, recounting the existing experimental investigations of the unstable phenomena. Particular observations are done of the evolution structure especially of the spatial fluid distribution, that seem to trigger the said instabilities. Chp.(3) sets the stage for modeling with a concise recall of the classical model of partial saturation and a phase field approach. Part II is dedicated to the modeling of hydraulic instabilities starting from the governing equations of the phase field approach in the context of non-deformable porous network. An in-depth analysis of the one-dimensional solution structure is presented followed by a linear stability analysis under imposed perturbations and two-dimensional simulations. Part III concerns the mechanical instabilities within a deformable porous network. First an application of an existing technique to model fracture initiation is extended to the context of classical partial saturation. Following this, an investigation of an alternative triggering phenomenon of opening mode fractures, that is motivated by experimental observations, is investigated by revisiting the driving force employed in the modeling.

Actors The current thesis study was conducted under the framework of a doctoral contract supported by the French ministry: Ministère de l'Enseignement Supérieur, de la Recherche et de l'Innovation through the doctoral school: École doctorale Bretagne Loire - Science pour l'ingenieur. Also the reaserch work falls under the broad framework of the ANR-STOWENG project (ANR-18-CE05-0033) (ANR-STOWENG, 2018). The work in its entirety was conducted at the Institut de Recherche en Génie Civil et Mécanique (GeM), UMR 6183 CNRS, École Centrale de Nantes.

PHENOMENOLOGY

2

CONTENTS

2.1 Unstable bi-phasic flow in porous media 5
2.1.1 Effect of gravity 6
2.2 Fracturing in fine-grained soils 10
2.2.1 Drainage induced fracturing 11
2.3 Synopsis 13

ABSTRACT

Unstable fluid flow and fracturing are two distinct phenomena that characterize failure of porous media. In this chapter we present evidence of these phenomena from the existing literature. The various regimes of flow morphology and the analogous nature of bi-phasic porous media flow to that of Hele-Shaw flow are highlighted. The role that gravity plays in infiltration and drainage scenarios is as well discussed with a focus on saturation profiles and their link to destabilization of the flow. The phenomenon of fracturing is presented with a prevailing treatment for opening mode fractures during drainage scenarios such as desiccation. An alternate phenomenological treatment is recounted, supported by experimental evidence. Overall, this exposition sets the stage for phenomenological motivations and qualitative evaluations of the modeling results.

2.1 UNSTABLE BI-PHASIC FLOW IN POROUS MEDIA

Stability of a moving interface between two immiscible fluids of contrasting viscosities and densities is a classical problem in fluid mechanics. Further when a solid substrate is involved the problem becomes more complex with the addition of wettability of the solid surface with respect to the fluid combination. This is almost always the case when two fluids are involved such as in the Hele-Shaw flow and in multi-phase flow in porous media such as soils.

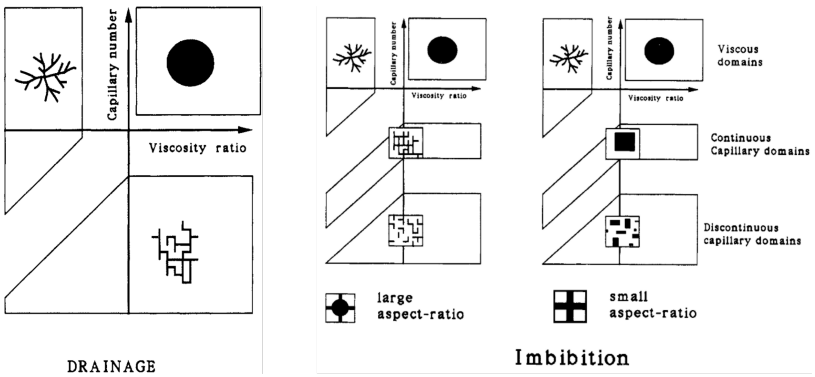

Figure 2.1: Phase diagrams from Lenormand (1990) depicting qualitatively the zones of stable and unstable porous media flow. Irrespective of the wetting properties of the invading and defending fluids these extremes of flow morphology were demonstrated experimentally to exist at similar extremes both for imbibition and drainage.

When the resident/ defending fluid preferentially wets the solid substrate the displacement of it by a non-wetting fluid is termed as drainage. The contrary is termed imbibition, when the invading fluid is wetting. In both these scenarios, numerous experimental campaigns have been carried out by various researchers with an intent to characterize the unstable displacement and the ensuing pattern formation. One can refer to the seminal works of Lenormand and his colleagues in the 1980s (Lenormand, 1985; Lenormand et al., 1988; Lenormand, 1990) and the other researchers who followed this path. See Chen et al. (2017); Guo and Aryana (2019), to name a few. Their work has laid the foundations for a more systematic way to identify various regimes of such flow by employing the so-called 'Phase diagram' (Lenormand, 1985; Lenormand et al., 1988). See Fig.(2.1). In essence, a stable and two morphologically different unstable regimes have been characterized by the dominant forces at play within the flow. These forces are either the capillary forces or the viscous forces. These forces were quantified by two non-dimensional numbers: capillary number, Ca, and viscosity ratio, M, defined as,

$$Ca = \frac{V_i \mu_i}{\gamma}, \qquad M = \frac{\mu_i}{\mu_d}, \tag{2.1}$$

where γ is the surface tension between the two fluids, μ and V are respectively the dynamic viscosity and mean velocity of the fluids. Subscripts i and d represent the invading and defending fluids respectively. The phase diagrams were plotted with the log-scale of these two numbers. In essence the capillary number quantifies the ratio of viscous forces within the invading fluid to that of the capillary forces acting at the various fluid menisci. The viscosity ratio on the other hand quantifies the ratio of viscous forces within the invading and defending fluids.

As summarized in Lenormand (1990) the stable regime is the one in which the viscous forces within the invading fluid dominate both the viscous forces within the defending fluid and the capillary forces. Viscous fingering regime is characterized by dominating viscous forces within the defending fluid compared to those within the invading fluid and the capillary forces. In this regime at initial times the front destabilizes into several fingers followed by some fingers growing faster than others and inhibition of shorter fingers. All the fingers tend to orient towards the exit forming a characteristic tree-like pattern (Lenormand et al., 1988). Capillary fingering regime has capillary forces dominating those due to viscous effects and is characterized by fingers that grow in all the directions and even forming loops that trap the displaced fluid. Wetting conditions have been known to impact how the invading fluid advances at the pore-scale and even for the same wetting condition, the pore-scale geometric features, such as the pore-to-throat size ratio in the case of imbibition and throat size distribution in the case of drainage, have consequential effects on the invasion morphology. Notwithstanding these differences, the phase diagrams revealed that these regimes of stable and unstable flow do exist at similar extremes in both imbibition and drainage.

2.1.1 Effect of gravity

It is to be noted that in the works of Lenormand and others cited above, the flow is within a slow regime (no inertial effects) and in the absence of gravity. Now in a practical setting, gravity almost always exists and plays a key role in either stabilizing or destabilizing the interface depending on the relative densities of the fluids involved. At a low flow rate the viscous forces within the fluids are negligible and the competition between gravity and capillary forces takes control of the displacement. This regime has been studied by (Birovljev et al., 1991; Auradou et al., 1999) where gravity

Figure 2.2: The celebrated "Saffmann-Taylor" fingering observed at the interface between air (top) and glycerine (bottom), showing the development of instabilities and the inhibiting effect that the fastest growing finger has on its neighbors (Saffman and Taylor, 1958). In the first image, the velocity of the interface was $V = 0.1\text{cm.s}^{-1}$ and the critical wave length is $\ell_{cr} = 1.2\text{cm}$. The average wave length of the disturbance observed at initiation was 2.2cm which is in the expected range. Note that this experiment was done with the motion of the interface along the direction of gravity.

was found to provide a stabilizing effect on the drainage front when a denser fluid is displaced by a lighter one from the top. On the other hand at a higher flow rate when capillary forces are negligible, the competition between gravity and viscous forces has been studied early on both theoretically and experimentally (in an analogous Hele-Shaw flow context) in the seminal work Saffman and Taylor (1958). As an extension to the work of Taylor (1950) concerning the condition for instability of a moving interface between two fluids of contrasting densities and negligible viscosities in a Hele-Shaw cell, Saffman and Taylor (1958) has derived analytically a similar condition applicable to viscous fluids in a porous medium:

> *"[...]. When two superposed fluids of different viscosities are forced through a porous medium in a direction perpendicular to their interface, this surface is stable or unstable to small deviations according as the direction of motion is directed from the more viscous to the less viscous fluid or vice versa, whatever the relative densities of the fluids, provided that the velocity is sufficiently large."*
>
> – Saffman and Taylor (1958)

For any generic disturbance applied to an interface moving vertically upwards, the above implication was done based on the following analytical condition,

$$\begin{aligned} \textit{stable if}: &\quad \left(\frac{\mu_i}{k_i} - \frac{\mu_d}{k_d}\right) V + (\rho_i - \rho_d)\, g > 0, \\ \textit{unstable if}: &\quad \left(\frac{\mu_i}{k_i} - \frac{\mu_d}{k_d}\right) V + (\rho_i - \rho_d)\, g < 0. \end{aligned} \tag{2.2}$$

V is the velocity of the interface, g the acceleration due to gravity and ρ is the density of the fluid under consideration. Note that in the above analysis the invading fluid is below the defending fluid, in other words the direction of motion of the interface is against that of gravity. Also, no direct consideration has been done as to the wetting properties of the fluids involved, to the solid surface and the effect of surface tension between the fluids. However, Saffman and Taylor (1958) did indicate, with suggestion from Dr.Chuoke R.L., that the effect of surface tension, T, is to limit the range of wavelengths of the disturbances to which the interface is unstable. Including surface tension, a linear stability analysis allowed to identify a critical wave length, ℓ_{cr}, given by,

$$\ell_{cr} = 2\pi\sqrt{T}b\left\{12v\,(\mu_d - \mu_i) + b^2 g\,(\rho_d - \rho_i)\right\}^{-\frac{1}{2}}, \tag{2.3}$$

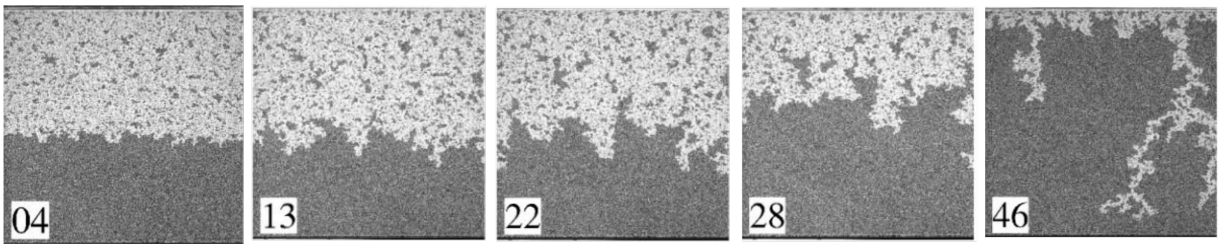

Figure 2.3: Drainage experiments by Méheust et al. (2002) where air (in white) displaced glycerol-water mixture (in gray) saturating a synthetic two-dimensional rigid porous medium. The drainage is simulated by constant rate with drawl from the bottom of the sample. The gravity component was tuned to study its stabilizing/destabilizing effect, by tilting the sample from an inclined position ≈ 56 deg with respect to the ground (left-most), to a completely horizontal position parallel to the ground (right-most).

disturbances of wavelengths larger than which destabilize the interface. b above is the gap between the plates of an analogous Hele-Shaw cell. The above analysis, complimented with experimental characterization (Fig.(2.2)) paved way to some pioneering works in the context of porous media flow. Chuoke et al. (1959) proposed the existence of a macroscopic surface tension, akin to T in Eq.(2.3), within porous media flow and thus having the same effect as in Hele-Shaw flow. Later Peters and Flock (1981) extended such result to three dimensions.

Remark: While Hele-Shaw flow is mathematically akin to two-dimensional flow in porous media, there exist striking differences especially in the transition region from one fluid to another and in the morphology of the fingering instabilities (Chen and Wilkinson, 1985; Stokes et al., 1986). In porous media, the transition region from the part of the domain fully saturated with one fluid, to the one which is fully saturated with the second fluid can be described as a mixing region where both fluids partially saturate the pores. On the other hand this transition is sharp in immiscible Hele-Shaw flow. This difference is primarily due to existence of several internal length scales in the case of porous media (Stokes et al., 1986; Homsy, 1987). Therefore, the viscous fingering instabilities observed in porous media flow have a fractal structure rather than smooth formations as in the case of Hele-Shaw flow.

As mentioned earlier, in the derivation of Eq.(2.2) gravity was considered acting opposite to the direction of motion of the fluid interface. The analysis of the converse case amounts only to changing the sign of acceleration due to gravity giving,

$$\begin{aligned} \textit{stable if}: &\quad \left(\frac{\mu_i}{k_i} - \frac{\mu_d}{k_d}\right) V + (\rho_d - \rho_i)\, g > 0, \\ \textit{unstable if}: &\quad \left(\frac{\mu_i}{k_i} - \frac{\mu_d}{k_d}\right) V + (\rho_d - \rho_i)\, g < 0. \end{aligned} \tag{2.4}$$

In fact, more recent works such as Méheust et al. (2002); Løvoll et al. (2005), have shown experimentally that gravity, when acting in the direction of motion of the fluid interface, helps to stabilize the invasion of a less dense non-wetting fluid ($\rho_i < \rho_d$) into a porous medium that is saturated with more viscous ($\mu_i < \mu_d$) and denser wetting fluid. See Fig.(2.3).

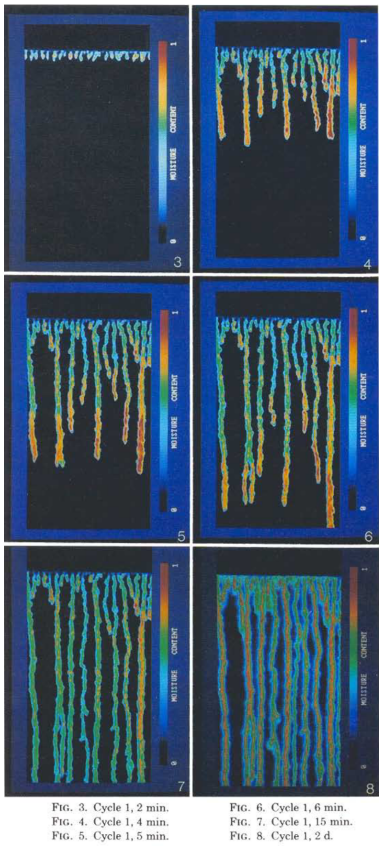

Fig. 3. Cycle 1, 2 min.
Fig. 4. Cycle 1, 4 min.
Fig. 5. Cycle 1, 5 min.
Fig. 6. Cycle 1, 6 min.
Fig. 7. Cycle 1, 15 min.
Fig. 8. Cycle 1, 2 d.

Figure 2.4: Evolution of moisture content during infiltration into dry 20/30 silica sand measured by the intensity of light transmitted (Glass et al., 1989a). The light transmission through sands increases with an increase in the moisture content. Higher moisture content areas are thus visualized in the range of yellow to red.

Gravity driven infiltration

On the contrary, when a denser ($\rho_i > \rho_d$) and more viscous ($\mu_i > \mu_d$) wetting fluid displaces a resident non-wetting fluid, the viscosity contrast is not in favor of destabilization, Eq.(2.4), and gravity is expected to assist in destabilizing the flow. This latter regime was the focus and a well-engaged topic of research in soil hydrology since the 1970s. One can look into DiCarlo (2013); Xiong (2014) among others for a historical review of gravity driven infiltration of water into soil.

Experimental evidence in this context suggested that fingering type instabilities that occur during infiltration have a non-monotonic profile

along their length, with their tips having higher water content compared to their tails. This was quite evident in the light transmission experiments by Glass et al. (1989a), Fig.(2.4), a technique novel to this field. The leading tips of the generated fingers were clearly of higher moisture content. This observation and related numerical studies (Nieber et al., 2000; Eliassi and Glass, 2001) have lead to the hypothesis that this non-monotonicity is the cause rather than the consequence of the ensuing instability (Eliassi and Glass, 2001). This 'overshoot' of water content has been further evidenced experimentally to be present during two-dimensional (Bauters et al., 2000; Shiozawa and Fujimaki, 2004) and quasi one-dimensional (DiCarlo, 2004; DiCarlo et al., 2010) experiments with transverse domain size smaller than the finger size expected.

Especially the quasi one-dimensional experiments, Fig.(2.5), due to their absence of macroscopic fingering, allowed to justify the presence of saturation overshoot during infiltration in the range of fluxes for which the two-dimensional experiments were found to exhibit fingering. This lead to an effort of evaluating the new models for their one-dimensional solution profiles in order to predict their ability to describe fingering in higher-dimensions DiCarlo (2013). On the other hand, this technique could also potentially be useful to determine if fingering could be expected for infiltration into certain types of sands that would otherwise have finger widths limited by the experimental chamber sizes. Only caveat being the edge effect (DiCarlo et al., 2010) that is inevitable due to the contrast between porosities of the bulk and at the edge. Also, it is worth to point out at this moment that, to our knowledge, such quasi one-dimensional experiments were not yet attempted in the case of drainage.

Apart from solution profiles along the direction of infiltration, a feature that is of practical importance is the finger width. This is because instabilities with thinner fingers tends to reduce the efficiency (say of filtration) by completely bypassing large areas of dry soil. Many numerical models intend to exhibit the experimentally observed finger width predictions and their relation with applied infiltration flux. While no comprehensive experimental work exists studying the finger width sensitivity to a large range of flux values, DiCarlo (2013) managed to consolidate results from independent two and three dimensional experimental campaigns with appropriate scaling. See Fig.(2.6). Two limits of stable flow were made apparent. At higher fluxes, as the flux increased, tending to the saturated conductivity, the finger width increased. In the two-dimensional slab experiments by Glass et al. (1989b), Fig.(2.7), this increase in the finger width tended to the transverse size chamber. On the other hand, at lower fluxes, as the flux reduced the finger width increased as well, tending to stabilized flow. In essence unstable flow is restricted to a certain range of intermediate fluxes. This particular feature of the infiltration into dry soil was not predicted by the analytical results according to DiCarlo (2013). However, the ability to predict this behavior,

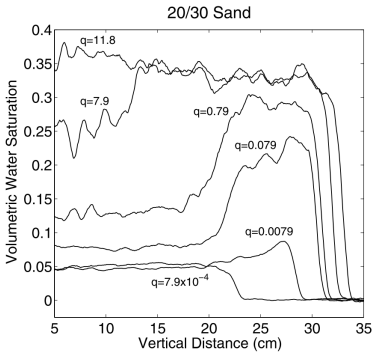

Figure 2.5: Results of saturation profile versus infiltration flux, q [cm.m^{-1}], in quasi one-dimensional experiments by (DiCarlo, 2004). The saturation profiles were obtained by light transmission through sands confined within tubes with diameter smaller than their typical finger sizes during infiltration.

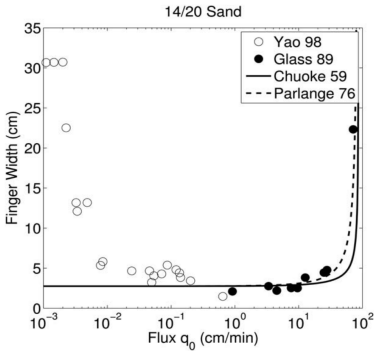

Figure 2.6: Consolidated figer width versus infiltration flux results by DiCarlo (2013) of low (Yao and Hendrickx, 1996) and high (Glass et al., 1989b) flux ranges with comparison of analytical finger width predictions by Chuoke et al. (1959); Parlange and Hill (1976).

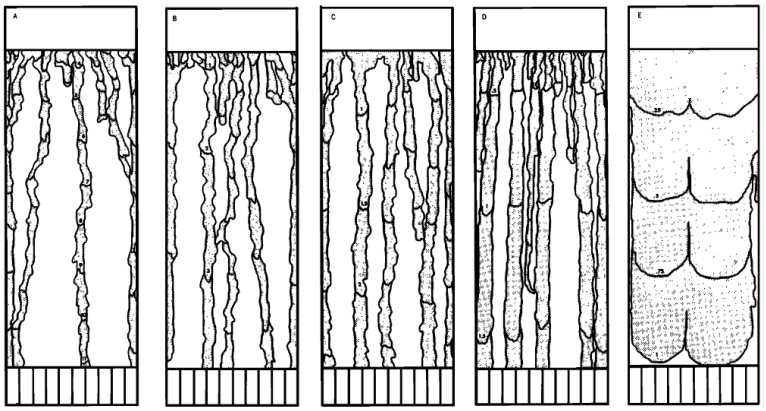

Figure 2.7: Two-dimensional infiltration experiments by Glass et al. (1989b) into initially dry 14/20 size fraction white silica sand. The experiments were conducted at increasing ratio, R_s, of flux to saturated conductivity flux rates. R_s = (0.012, 0.041, 0.088, 0.32, 0.82) to be read from left to right in the figure.

in tandem with the one-dimensional saturation overshoot feature, could be a useful measure to evaluate numerical models. This perspective gains strength due to the correlation between the absence of one-dimensional saturation overshoot at the same extremes of applied flux at which the finger widths tend to be larger, implying stabilization of the front.

2.2 FRACTURING IN FINE-GRAINED SOILS

Mode-I fracture openings are of primary concern in geomaterials when it comes to preferential pathways generated due to loss of mechanical integrity of the porous skeleton. Such fractures are prevalent in porous media either saturated or partially saturated. Typical scenarios involving soils are, desiccation cracks due to drying induced evaporation, pressure driven hydraulic fracturing of intact formations, emergence of complex sub-vertical hydrate veins in deep-water marine sediments among others. While the consequences are similar, each scenario has a different underlying mechanism that initiates/ propagates the fracture.

In metals owing to their obvious non-granular nature and in cemented materials owing to their cementation, mode-I fracture opening is classically treated as caused by the tensile nature of stresses in the bulk. Typical mode-I brittle fracture treated à la Griffith involves inherent defects on the material surface or the bulk at which fractures initiate and propagate, driven by the release of stored elastic energy which is of a tensile nature.

Unlike metals and cemented materials, soils are inherently granular and the resistance offered by them is due to their effective stress dependent cohesion-less frictional behavior. Such 'toughness' of soils has its origins in the confining stress, inter-granular adhesion due to fluid films in the case of partial saturation, inter-granular friction due to grain texture and packing configuration. Under such conditions, full saturation would mean that there are no fluid films either, that could have otherwise provided some adhesion. So, the sources of resistance against fracturing are the inter-granular friction and the confining stress, σ_c. Such is the case of saturated soft marine sediments, brine-saturated sub-surface formations and surface soil layers following rainfall/flooding among others.

When the invading fluid is the same as, or miscible with, the one already saturating the porous skeleton, the mechanism behind initiation of fractures at pre-existing defects is the same as that of classical hydraulic fracture. The fluid tends to leak-off into the bulk along the normal to the faces of the defect and in proportion to the intrinsic permeability of the porous skeleton. Seepage induced drag forces thus develop within the soil mass around the initial defect. See Fig.(2.8). For fracture to initiate and propagate these drag

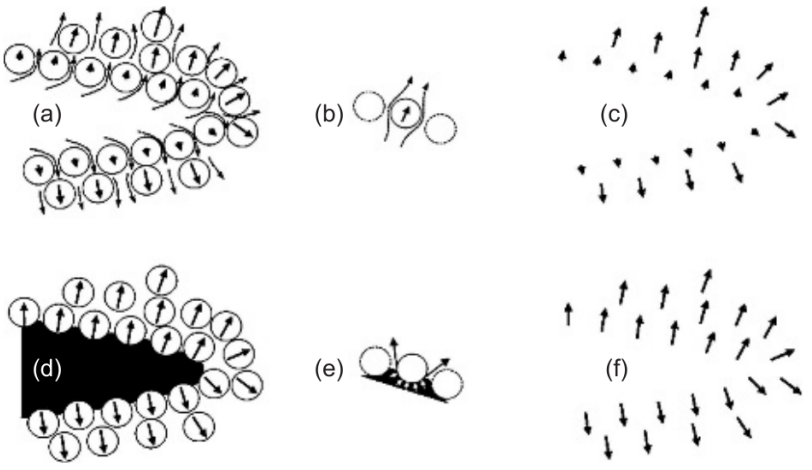

Figure 2.8: Schematic from Shin and Santamarina (2011b) of particle-level forces at play in the vicinity of a defect in the case of (a,b,c). miscible fluid invasion and (d,e,f). immiscible fluid invasion into an a priori saturated porous medium.

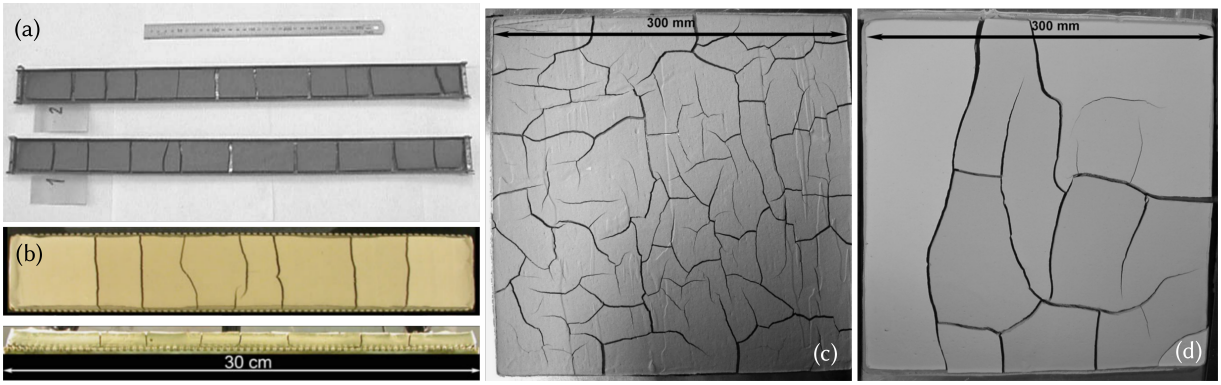

Figure 2.9: Examples of desiccation induced fractures in different soils. Evenly spaced fractures in relatively shallow samples that are longer than they are wide in experiments with (a) clay (Nahlawi and Kodikara, 2006) (b) silt (Peron et al., 2009). Polygonal fracture networks observed (Peron et al., 2009) at the end of the drying experiment with square shaped silt samples of different depths: (c) 4mm, (d) 8mm.

forces, that are proportional to the difference in fluid pressures within the fracture and the far-field, must exceed the effective compressive stresses in the far-field due to the confinement.

2.2.1 Drainage induced fracturing

If the invading fluid is non-wetting to the pore walls with respect to the saturating fluid, then the mechanism behind a mode-I fracture initiation under compressive effective stress conditions has been a topic of debate and investigations since the last decade. Indeed, this would be an entry into the realm of partial saturation and a fluid-fluid displacement that is drainage. A typical example of this scenario is that of desiccation cracks in drying soils. Desiccation is a process of evaporation induced at the surface of soil that is saturated typically with water. As the surface water evaporates, the water level reaches the soil surface and the air (or water-vapour) resists to invade the surface pores exposed to the exterior. However, air being non-wetting can invade the largest pores only once the capillary pressure difference between air and water exceeds the entry pressure/ critical capillary pressure. Until such a time the soil mass experiences shrinkage induced by the increasing suction. Once the capillary pressure attains the entry pressure, air starts to invade the pore spaces. This is when mode-I desiccation cracks seem to be initiated and eventually form networks as observed in various experimental campaigns, notably that of Nahlawi and Kodikara (2006); Peron et al. (2009); Stirling (2014); Cordero et al. (2021). See Fig.(2.9).

One prevailing point of view is that, these fractures are generated under the influence of tensile forces that are induced either due to boundary conditions that restrain the shrinkage of the whole soil mass (in shallow samples) or due to differential shrinkage along its depth (in thicker/deeper samples). Relatively recent modeling attempts (Cajuhi et al., 2018; Choo and Sun, 2018; Heider and Sun, 2020; Hu et al., 2020) based on a continuum description of fracture have incorporated such a perspective.

An alternative phenomenon has been championed in the works of Shin and Santamarina (2010, 2011a,b) and that of Jain and Juanes (2009), which is compatible with the earlier mentioned fundamental behavior of soils, that is to exhibit toughness only under compressive effective stresses. In this case fracturing is thought to be caused by the forced invasion of the porous network by either fluids: immiscible (for instance desiccation) or miscible (earlier explained hydraulic fracturing). In the experiments by Shin and Santamarina (2010), a water saturated slurry of clay in a cylindrical chamber has been subjected to pressure by a superposed fluid which is either immiscible oil or miscible water. See Fig.(2.10). The miscible case has been setup with an intentional defect that looks like hole. The soil mass is drained in both cases from the bottom. This is a scenario which unambiguously generates compressive effective stresses within the confined sample with

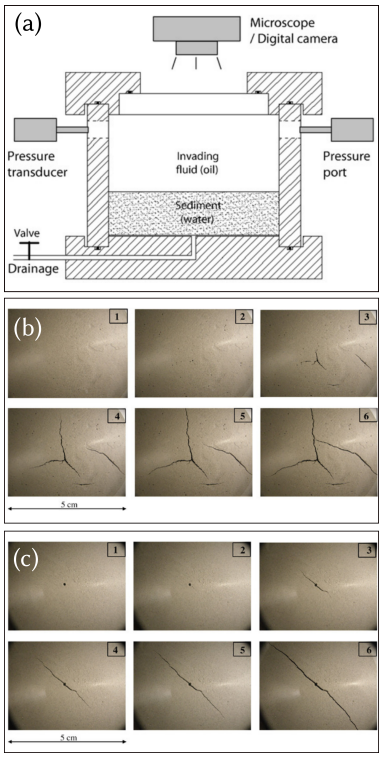

Figure 2.10: (a) Experimental setup in Shin and Santamarina (2010) for immiscible fluid invasion. (b) Fractures originating at sub-millimeter "craters" on the surface of the sediment (immiscible fluid invasion). (c) Fractures originating at the edges of an initial bore-shaped defect (miscible fluid invasion). In both cases the fractures propagate vertically into the sample and laterally outwards.

the ratio of horizontal to vertical effective stresses less than 1 that is typical to granular media. As the superposed fluid pressure is increased, mode-I fracture initiation has been observed in both cases, starting at surface defects and propagating vertically downward and laterally within a plane normal to the minor principal effective stress. This definitely cannot be explained through a tensile stress driven mechanism.

In Shin and Santamarina (2010, 2011a,b) this has been explained through a particle level phenomenology at a supposed surface defect, supported by representative numerical simulations. Numerical simulations for the immiscible case were conducted on a Gaussian defect in a two-dimensional domain using a Modified Cam Clay model assuming zero soil-cohesion and an increasing uniform internal suction, $u_c(t)$, applied on the whole domain. The simulations revealed that while consolidation takes place everywhere within the sample accompanied by a reduction in the void ratio, $e(x,t)$, the tip of the defect experiences a lower rate of reduction in void ratio. Thus as time progresses, in the far-field the path followed in the space of (u_c, e) is that of the normal consolidation line (NCL), whereas the tip deviates from this path thus obtaining a relatively higher void ratio. This higher void ratio corresponds to a lower air-entry suction and thus one comes to a conclusion that air invades first at the tip of the defect and propagates owing to the same mechanism. The effective stress, while being lower at the tip, was always found to be in compression throughout the computational domain.

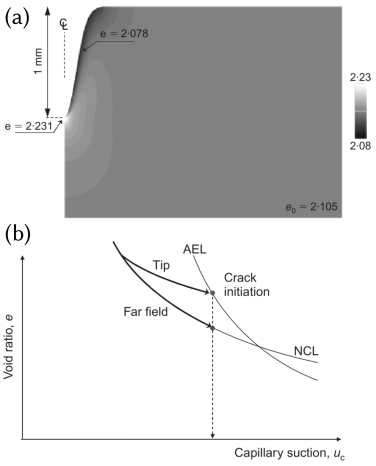

Figure 2.11: Two-dimensional plane strain finite element simulations by Shin and Santamarina (2011a) of a representative Gaussian-shaped defect of depth 1mm within a rectangular domain (6×6)mm with an initial homogeneous void ratio of $e(x, 0) = 3.92$. The boundaries at the bottom and right-hand side are setup as no friction surfaces and the loading was a uniform suction on the whole domain increasing with time. (a) Void ratio, $e(x, t)$, when $u_c(t) = 100$KPa. (b) Plots depicting trends of the normal consolidation (NCL) and the air-entry (AEL) lines. The tip of the defect in the simulations is shown to deviate from NCL path thus reaching the AEL first.

Dependency on grain size and confining stress

A similar explanation of the non-wetting fluid invasion has been arrived at by Jain and Juanes (2009) employing discrete element method (DEM) simulations to replicate buoyant methane gas invading marine sediments from below. Here the focus was on the effect of grain size on the invasion mechanism. Two types of gas invasion into initially saturated granular porous media have been classified: classical capillary invasion and invasion by creation of opening mode fracture/s. When the grain size is large, the invasion seem to follow the classical pore-by-pore invasion where the invading gas pressure exceeds the capillary pressure limit at the pore throats which could be sufficiently described by invasion percolation theory (Lenormand, 1985). However, when the grain size is reduced, the capillary pressure limit for gas entry at the pore throats is much higher and the increasing invasion gas pressure reaches a fracturing limit whereby the DEM network no longer behaves as a rigid medium. Fractures were found to initiate at the invading boundary and propagate vertically into the network along the direction normal to that of the minor principal effective stress similar to the experiments in Shin and Santamarina (2010). Accordingly a local condition for fracture opening has been identified in Jain and Juanes (2009), on the basis of classical fracture mechanics, requiring the gas pressure to exceed the

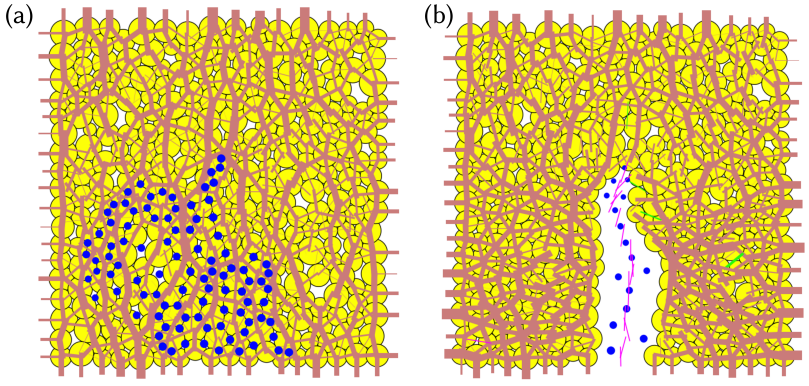

Figure 2.12: Pore-scale two-dimensional DEM simulations by Jain and Juanes (2009) with grain packs of 300 grains with size range $[r_{min}, 2r_{min}]$. The lateral boundaries were fixed and the grain pack is compacted vertically under constant pore-pressure until vertical effective stress of 3Mpa is reached. Then an incrementally increasing gas pressure is applied at the bottom central pore. Maroon lines depict the compression at the inter-granular contacts, the blue dots are the pores fully occupied by gas and the pink lines are where the inter-granular cohesive bonds are broken. (a) Classical capillary invasion for $r_{min} = 50\mu$m at capillary pressure of 6KPa. (b) Fracture opening for $r_{min} = 0.1\mu$m at capillary pressure of 2.55MPa.

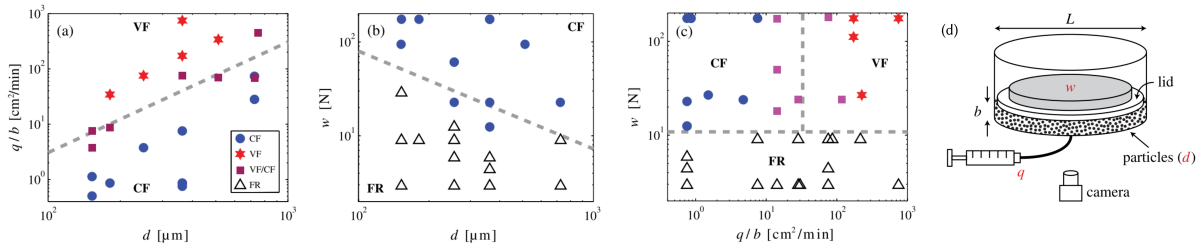

Figure 2.13: (a,b,c) Experimental results from Holtzman et al. (2012) of invasion morphologies for varying injection flux (q), glass bead diameter (d), and confining weight (w). The legend reads CF: capillary fingering, VF: viscous fingering, VF/CF: transition between the two former regimes and FR: fracturing. (d) Schematic of the experimental setup.

minimum compressive stress at the far-field and the inter-granular adhesion due to fluid films.

Holtzman et al. (2012) has carried out an experimental investigation by injecting air into a thin bed of water saturated glass bead pack confined within a shallow cylindrical chamber with variable weight on top. Effect of the weight that generates a confining stress, the diameter of the glass beads and the injection flux have been studied by varying them. Apart from the classical fingering transition from capillary to viscous regime with an increasing injection flux, a transition from fingering to fracturing has been observed with reducing confining stress and as well with reducing bead diameter. See Fig.(2.13). Notably, the latter transition did not seem to be affected by the varying injection flux.

2.3 SYNOPSIS

In the case of bi-phasic flow in rigid porous media, even though there is a clear fractal nature to the invasion morphology, at a macroscopic continuum scale destabilization of the invasion seem to be analogous to that of Hele-Shaw flow. This is further corroborated by the ability of the simplistic stability analysis by Saffman and Taylor (1958) being able to qualitatively explain the various regimes of destabilization in the presence of gravity. Moreover, the quasi one-dimensional gravity driven infiltration profiles potentially provide a basis for evaluating any modeling techniques, even before demonstrating their capability to describe fingering in higher dimensions.

The prevailing explanation for appearance of opening mode fractures in soils during drainage has been the build up of tensile stresses. The available evidence, both experimental and pore-scale simulations, unequivocally supports an alternate phenomenon, that is of local grain rearrangement caused by the invading capillary film. Unlike the prevailing explanation, this alternate rationale is inline with the fundamental behavior of granular media like soils, that is an effective stress dependent frictional strength. This and the state of current advances within continuum description of fractures, provide suitable grounds for a thorough investigation at a continuum scale by isolating capillarity as the driving mechanism for fracture initiation/propagation.

3

PARTIALLY SATURATED POROMECHANICS & A NON-UNIFORM FLUID

CONTENTS

3.1 Classical approach to partial saturation 15
3.1.1 Kinematics & preliminaries 15
3.1.2 Balance of Mass 17
3.1.3 Balance of Momentum 17
3.1.4 Hypothesis of small perturbations (HSP) 18
3.1.5 Classical constitutive relations 19
3.1.6 Summary of Governing equations under HSP 22
3.1.7 Boundary & initial conditions 23
3.1.8 Soil hydrology & Richards' equation 23
3.1.9 Criticism and extensions of Richards' equation . . . 24
3.2 A phase field approach to partial saturation 25
3.2.1 Kinematics & preliminaries 26
3.2.2 Balance of Mass 27
3.2.3 Power of external forces & balance of momentum . . 27
3.2.4 Thermodynamics 29
3.2.5 Poroelastic constitutive relations 33
3.2.6 Extended Richards' equation: Rigid porous skeleton 36
3.3 Synopsis 36

ABSTRACT

This chapter serves as a recall for two mathematical descriptions of partially saturated poromechanics. The first one is the classical approach in which starting from the principles of conservation and the classical constitutive laws, the governing equations are derived. A partial linearization of the governing equations is arrived at, under the hypothesis of small perturbations applicable to poroelasticity. In the special case of a non-deformable porous network, Richards' equation describing the evolution of fluids is derived. A phase field approach is then introduced assuming the presence of two fluids as equivalent to a single non-uniform fluid fully saturating the pore spaces. While the classical formulation of unsaturated poromechanics is only briefly summarized listing the main hypotheses of the model and the governing equations of the problem, a more detailed deduction of the phase field approach is discussed. Specifically the thermodynamic restrictions imposed by an extended form of the Clausius-Duhem inequality to derive admissible constitutive laws for generalized stresses and average fluid flux are detailed. Under such a framework the governing equations are derived and an extension to Richards' equation in the non-deformable case is arrived at.

3.1 CLASSICAL APPROACH TO PARTIAL SATURATION

The following deductions in this section are meant to be a recall to partial saturation as treated in Coussy (2004) using a classical approach. Accordingly a macroscopic treatment is adopted considering the porous medium as a homogenized continuum whose representative elementary volume (REV) is assumed to account for the phase-averaged quantities such as the porosity, saturation degrees, densities, etc.

We consider the pore space to be saturated by two fluid phases, one wetting (subscript 'w') and another non-wetting (subscript 'nw') to a deformable skeleton representing the solid phase (subscript 's'). The particular simplifications that could be obtained by choosing the wetting fluid to be water and the non-wetting fluid to be air that is typical to soil hydrology are detailed at a later moment in Sec.(3.1.8). Moreover the following terminology holds for the entirety of this work. A porous medium is the ensemble of the solid skeleton and the fluids. A porous solid is a so-called wetted solid skeleton, with a thin layer of immobile wetting fluid attached to its pore walls. Solid matrix is the fabric of the skeleton, which in the current case constitutes the grains of soil.

The primary characteristic of a porous skeleton is its porosity. The Eulerian porosity, n, is defined as the volume fraction of the pore space within an elementary unit volume of the porous medium, $d\Omega^t$ at the current time t. Accordingly, partial porosities, n_α, $\alpha \in \{w, nw\}$, distinguish the volume fraction of the pore space occupied by each fluid within $d\Omega^t$ such that $n = n_w + n_{nw}$. The Lagrangian counter parts ϕ_α, ϕ are defined such that $n_\alpha d\Omega^t = \phi_\alpha d\Omega_s^0$ and $\phi = \phi_w + \phi_{nw}$ with $d\Omega_s^0$ representing the unit volume of the porous medium in the reference configuration of the solid skeleton.

Similarly, another useful quantity to define is the volume fraction of each fluid within the available pore space of $d\Omega^t$. This quantity is the saturation degree denoted S_α such that $1 = S_w + S_{nw}$.

If ρ_c, $c \in \{s, w, nw\}$ denote the intrinsic mass densities of each phase, then their apparent Eulerian mass densities are given by $\rho_\alpha n_\alpha = \rho_\alpha n S_\alpha$ for the fluids and $\rho_s(1 - n)$ for the solid. The Lagrangian counterparts to the apparent mass densities are given by $m_\alpha = \rho_\alpha \phi_\alpha = \rho_\alpha \phi S_\alpha$ for the fluids and $m_s = \rho_s(1 - \phi)$ for the solid.

For most Eulerian quantities appropriate Lagrangian counterparts exist owing to the deformation of the porous skeleton. Eventually we introduce the hypothesis of small perturbations (HSP) that lets us work under infinitesimal deformations thus unifying both frameworks.

3.1.1 Kinematics & preliminaries

Let Ω_s^0 and Ω^t indicate respectively the reference and current configurations occupied by the porous medium at time $t = 0$ and $t > 0$. Since the porous medium is considered as a homogenized continuum, each spatial position $x \in \Omega^t$ at time t is simultaneously occupied by the solid and the fluid particles whose individual reference positions are given by X_c, $c \in \{s, w, nw\}$. The individual deformation maps are given by $x = x_c(X_c, t)$ and their inverse mappings, with an abuse of notation, by $X_c = X_c(x, t)$. It is to be noted that it is customary in poromechanics to transport the governing equations of the fluids and the solid from their common current configuration, Ω^t, to the reference configuration of the solid skeleton, Ω_s^0, so as to allow the usual continuum mechanics approach to constitutive characterization of the solid skeleton.

The time derivatives giving velocity fields of the solid and fluid particles

identified in their current configurations are,

$$v_c(x,t) = \left.\frac{\partial x_c(X_c,t)}{\partial t}\right|_{X_c=X_c(x,t)}, \quad c \in \{s,w,nw\}. \tag{3.1}$$

Consequently the relative velocity of the fluid particles, X_α, w.r.t a solid particle, X_s, at every current position $x = x_s(X_s,t)$ can be obtained as,

$$w_\alpha(x,t) = v_\alpha(x,t) - v_s(x,t), \quad \alpha \in \{w,nw\}. \tag{3.2}$$

The Lagrangian gradient w.r.t the solid reference configuration is denoted ∇_s whereas the Eulerian gradient in the current configuration is denoted ∇. Analogously, the divergence operators are denoted $\nabla_s\cdot$ and $\nabla\cdot$. With the above notations in place, the deformation gradients of the earlier defined maps are given by,

$$\begin{aligned} F_s(X_s,t) &= \nabla_s x_s(X_s,t), \\ F_\alpha(X_\alpha,t) &= \nabla_s x_\alpha(X_\alpha,t), \quad \alpha \in \{w,nw\}. \end{aligned} \tag{3.3}$$

The following transport formulas hold for elementary oriented surfaces,

$$\hat{n}da = J_s F_s^{-T} \hat{N}_s dA_s, \tag{3.4}$$

and for elementary volumes,

$$d\Omega^t = J_s d\Omega_s^0, \tag{3.5}$$

where $J_s = \det F_s$. $\hat{n}da$ and $d\Omega^t$ are the current elementary oriented surface and elementary volume corresponding to the reference counterparts $\hat{N}_s dA_s$ and $d\Omega_s^0$ respectively.

As usual in continuum mechanics, the displacement of the solid skeleton is measured as $u(X_s,t) = x_s(X_s,t) - X_s$. The changes in the lengths of material vectors of the solid skeleton and their included angles are measured by the Green-Lagrange strain tensor given by,

$$E = \frac{1}{2}\left(F_s^T \cdot F_s - I\right) = \frac{1}{2}(C - I) = \frac{1}{2}\left(\nabla_s u + \nabla_s^T u + \nabla_s^T u \cdot \nabla_s u\right), \tag{3.6}$$

where I represents the second-order identity tensor and C is the Cauchy-Green strain tensor.

Particle derivatives

Particle derivative of any differentiable Eulerian field $\mathcal{G}$ w.r.t the solid or the fluid particles is given by,

$$\frac{d^c\mathcal{G}}{dt} = \frac{\partial \mathcal{G}}{\partial t} + \nabla\mathcal{G}\cdot v_c, \quad c \in \{s,w,nw\}. \tag{3.7}$$

Similarly, the particle derivative applied to a volume integral of any differentiable field $\mathcal{G}$ is given by,

$$\begin{aligned} \frac{d^c}{dt}\int_{\Omega^t} \mathcal{G}d\Omega^t &= \int_{\Omega^t}\left(\frac{d^c\mathcal{G}}{dt} + \mathcal{G}\nabla\cdot v_c\right)d\Omega^t, \\ &= \int_{\Omega^t}\left(\frac{\partial\mathcal{G}}{\partial t} + \nabla\cdot(\mathcal{G}v_c)\right)d\Omega^t, \\ &= \int_{\Omega^t}\frac{\partial\mathcal{G}}{\partial t}d\Omega^t + \int_{\partial\Omega^t}\mathcal{G}v_c\cdot\hat{n}dS^t, \quad c \in \{s,w,nw\}, \end{aligned} \tag{3.8}$$

where for the last step the divergence theorem is employed. $\partial\Omega^t$ is the boundary of Ω^t where the outward unit normal is $\hat{n}$.

For any Lagrangian field, $\mathcal{G}(X_s,t)$, the particle derivative w.r.t the solid, $d^s\mathcal{G}/dt$, is further denoted by $d\mathcal{G}/dt$ for convenience.

3.1.2 Balance of Mass

Following Coussy (2004), in the absence of any sources/ sinks within the bulk and any surface supplies, the Eulerian mass balances applicable everywhere in Ω^t for each fluid phase $\alpha \in \{w, nw\}$, and the solid phase in their differential forms read,

$$\begin{aligned} \frac{\partial(\rho_\alpha n S_\alpha)}{\partial t} + \nabla \cdot (\rho_\alpha n S_\alpha v_\alpha) = 0, \\ \frac{\partial(\rho_s(1-n))}{\partial t} + \nabla \cdot (\rho_s(1-n) v_s) = 0. \end{aligned} \tag{3.9}$$

As a general practice in poromechanics the time derivative in fluid mass balance is rewritten w.r.t the solid reference configuration using Eq.(3.7) as follows,

$$\frac{d^s(\rho_\alpha n S_\alpha)}{dt} + \rho_\alpha n S_\alpha \, (\nabla \cdot v_s) + \nabla \cdot (\rho_\alpha n S_\alpha w_\alpha) = 0. \tag{3.10}$$

With the definition of the Eulerian relative fluid mass flow vector $w_\alpha(x,t) = \rho_\alpha n S_\alpha w_\alpha = \rho_\alpha n S_\alpha (v_\alpha - v_s)$ and the Lagrangian relative fluid mass flow vector, M_α, such that $w_\alpha \cdot nda = M_\alpha \cdot N_s dA_s$, one can obtain using the transport formulae, the pull-back of the balance of fluid masses into the solid reference configuration,

$$\frac{dm_\alpha}{dt} + \nabla_s \cdot M_\alpha = 0, \quad \text{with } M_\alpha = m_\alpha F_s^{-1} \cdot (v_\alpha - v_s). \tag{3.11}$$

On the other hand, solid mass balance can be rewritten from the integral form of Eq.(3.9(b)) and then integrating it,

$$\rho_s(1-n) d\Omega^t = \rho_s^0 (1-\phi_0) d\Omega_s^0, \tag{3.12}$$

where ρ_s^0 and ϕ_0 are the initial mass density and initial porosity of the solid skeleton. It is apparent that the current density of the solid skeleton is related to the current porosity through an algebraic relation knowing J_s,

$$\rho_s = \frac{\rho_s^0 (1-\phi_0)}{J_s (1-n)}. \tag{3.13}$$

3.1.3 Balance of Momentum

In a Galilean reference frame, the instantaneous momentum balance with respect to all the matter included in the porous domain, Ω^t dictates that the sum of variations in time of momenta of each constituent, $c \in \{s, w, nw\}$, should be equal to the sum of surface and internal supplies. This reads in an integral form as follows for linear momentum,

$$\frac{d^s}{dt} \int_{\Omega^t} \rho_s(1-n) v_s d\Omega^t + \frac{d^\alpha}{dt} \int_{\Omega^t} \rho_\alpha n S_\alpha v_\alpha d\Omega^t = \int_{\Omega^t} \rho f_b d\Omega^t + \int_{\partial\Omega^t} f_t dS^t, \tag{3.14}$$

with $\alpha \in \{w, nw\}$. f_t and f_b are respectively the surface traction acting on the boundary and the body force acting within the domain of the porous medium as a whole. $\rho = \rho_s(1-n) + \rho_w n_w + \rho_{nw} n_{nw}$, is the overall mass density of the porous medium. Under a quasi-static assumption, neglecting the dynamic terms in the equation above leads to,

$$0 = \int_{\Omega^t} \rho f_b d\Omega^t + \int_{\partial\Omega^t} f_t dS^t. \tag{3.15}$$

Classical Cauchy stress theorem (Coussy, 2004) linearly relates the surface traction to the outward unit normal at the boundary where it is applied through the identification of a Cauchy stress tensor, $\sigma(x,t)$, for the overall porous medium, such that $f_t = \sigma \cdot \hat{n}$. Using this in Eq.(3.15) results in,

$$0 = \int_{\Omega^t} (\rho f_b + \nabla \cdot \sigma)\, d\Omega^t. \tag{3.16}$$

Whereas, the balance of angular momentum as usual in continuum mechanics would amount to the symmetry of the tensor $\sigma(x,t)$.

3.1.4 Hypothesis of small perturbations (HSP)

The hypothesis of small perturbations in the context of poromechanics amounts to a set of assumptions that allow a partial linearization of the highly non-linear problem. These are listed below in no particular order:

- Hypothesis of infinitesimal transformations:

  $$\|\nabla u\| \ll 1. \tag{3.17}$$

  According to which the Lagrangian and Eulerian approaches coincide up to a first-order approximation. It also implies infinitesimal deformations giving $\|E\| \ll 1$. As a consequence the Green-Lagrange strain tensor, E, can be approximated by the linearized strain tensor, ε, given by,

  $$E(u) \approx \varepsilon(u) = \frac{1}{2}\left(\nabla u + \nabla^T u\right). \tag{3.18}$$

- Hypothesis of small displacements: This states that the displacements of the solid skeleton are much smaller than the characteristic length scale, L, of the structure as a whole,

  $$\|u/L\| \ll 1. \tag{3.19}$$

  This amounts to a merger of the reference and the current configurations $\Omega_s^0 \equiv \Omega^t = \Omega$ and their respective boundaries $\partial\Omega_s^0 \equiv \partial\Omega^t = \partial\Omega$. Such a merger is only as far as the spatial arguments of unknown fields are concerned, i.e., $x \approxeq X$ whenever they appear as arguments of unknown functions. As result of the above two hypotheses, the operator ∇ can be used directly without specific reference to the configuration, $\nabla \equiv \nabla_s$.

- Hypothesis of small variations of Lagrangian porosity: This amounts to,

  $$|(\phi - \phi_0)/\phi_0| \ll 1. \tag{3.20}$$

  It is to be noted that this is not equivalent to a non-deformable porous skeleton, $\phi = \phi_0$, which is treated at a later point.

- Hypothesis of small variations of fluid mass densities: This amounts to,

  $$|(\rho_\alpha - \rho_\alpha^0)/\rho_\alpha^0| \ll 1, \quad \alpha \in \{w, nw\}. \tag{3.21}$$

  Superseding this hypothesis, fluids in liquid state are assumed incompressible and uniform in the current work, such that $\rho_\alpha(x,t) = \rho_\alpha^0$.

3.1.5 Classical constitutive relations

With a choice of minimum primary unknowns, the balance laws are supplemented by constitutive relations that are derived employing the hypothesis of energy separation (see Sec.(6.4.1) in Coussy (2004)). According to this, the individual contributions of the free energy density of the porous skeleton, $\psi_s(\varepsilon, \phi)$, and the interfacial energy density, $U(S_w)$, are separated from within the free energy density of the porous solid, $\Psi_s(\varepsilon, \phi, S_w)$,

$$\Psi_s(\varepsilon, \phi, S_w) = \psi_s(\varepsilon, \phi) + \phi U(S_w). \tag{3.22}$$

In doing so, $U(S_w)$ is understood as encompassing both the solid-fluid and fluid-fluid interfacial contributions. Starting from $\psi_s(\varepsilon, \phi)$, after a Legendre transformation involving the conjugate pair (ϕ, π), an alternative state function describing a partially saturated deformable porous skeleton is obtained as $G_s(\varepsilon, \pi)$ where π is an equivalent pore pressure described below. The corresponding state equations are the constitutive laws that account for the tensile effect of the interfaces on the pore walls. The material properties which specify the linear poroelastic model are typically identified through experimental investigations.

Without resorting to exhaustive derivations, below we recall briefly these relations under an overarching assumption of isotropic linear elastic homogeneous porous medium undergoing isothermal transformations. The primary unknowns chosen for this purpose are the displacement of the solid skeleton, u, and the fluid pressures, p_α, $\alpha \in \{w, nw\}$.

Fluid density

The state equations for the fluid phases, $\alpha \in \{w, nw\}$, relate their intrinsic densities to their averaged fluid pressures p_α assuming simplistic barotropic fluid phases,

$$\rho_\alpha = \rho_\alpha(p_\alpha). \tag{3.23}$$

Under the HSP in-compressible fluids are assumed and the above simply reduces to $\rho_\alpha = \rho_\alpha^0$, where ρ_α^0 is the corresponding initial intrinsic fluid mass density.

Capillary pressure & interfacial energy

At a pore-scale, the menisci formed between the wetting and non-wetting fluids have certain curvature depending on the surface tension between the two fluids, their wettability w.r.t the pore walls and the geometry of the pores. The pressure difference between the two fluids, that is the pore-scale capillary pressure, governs the volume fractions of those fluids within the pore space. Classical poromechanical practice involves assuming a simplistic geometry of the pore space and specifying that the work done by the pore-scale capillary pressure in causing infinitesimal variation in the volume content of the wetting fluid occupying the pore, is equivalent to the infinitesimal variation of interfacial energy (Coussy, 2010). Thus a continuum scale constitutive relation is determined between the interfacial energy, $U(S_w)$, and the saturation degree of the wetting fluid, S_w. See Fig.(3.1). This relation is called the retention relation or the retention curve, that at equilibrium allows for the retention of a given volume of wetting fluid at a prescribed pressure difference between the two phases, $(p_{nw} - p_w) = p_c(S_w)$, within a porous skeleton. In this sense, it accounts not only for the surface tension between the two fluids but also for the retention effect provided by the pore walls due their texture.

The functional form of $p_c(S_w)$ usually is empirical (van Genuchten, 1980; Brooks and Corey, 1964) in order to fit the experimental data and can

generally be hysteretic. In the current study the widely used van Genuchten form (van Genuchten, 1980),

$$U(S_w) = \int_{S_w}^{1} p_c(s)ds, \tag{3.24}$$

$$p_c(S_w) = -\frac{\partial U}{\partial S_w} = \pi_0 \left(\left(\frac{S_w - S_w^{res}}{1 - S_w^{res}} \right)^{-\frac{1}{m}} - 1 \right)^{1-m}, \tag{3.25}$$

is adopted where, π_0 scales as $\rho_w g \ell_c$. ℓ_c [L] is the porous media counterpart of capillary length scale that relates intensity of capillary forces in the porous medium to gravity. S_w^{res} is the saturation degree of the residual wetting fluid that is immobile and is always attached to the pore walls. Also, as can be observed from Fig.(3.1), $p_c(S_w)$ is a non-negative function of $S_w \in [S_w^{res}, 1]$ that monotonically decreases from $+\infty$ at $S_w = S_w^{res}$ to 0 at $S_w = 1$. So, $U(S_w)$ has a unique minimum within $S_w \in [S_w^{res}, 1]$ at $S_w = 1$.

It is to be noted that since fluid pressures, p_α, are chosen as the primary unknowns, saturation degree of the wetting fluid can be obtained by the inverse relation associated to Eq.(3.25),

$$S_w(p_w, p_{nw}) = p_c^{-1}(p_{nw} - p_w), \tag{3.26}$$

written with an abuse of notation. The saturation degree of the non-wetting fluid can then be obtained as, $S_{nw} = 1 - S_w$.

Also, as a cautionary note, the above relation assumes a homogeneous retention property, whereas spatial variations of porosities due to skeleton deformation could invalidate such an assumption. The validity of uniform retention properties is related to the HSP and is applicable only to the framework of linear poroelasticity.

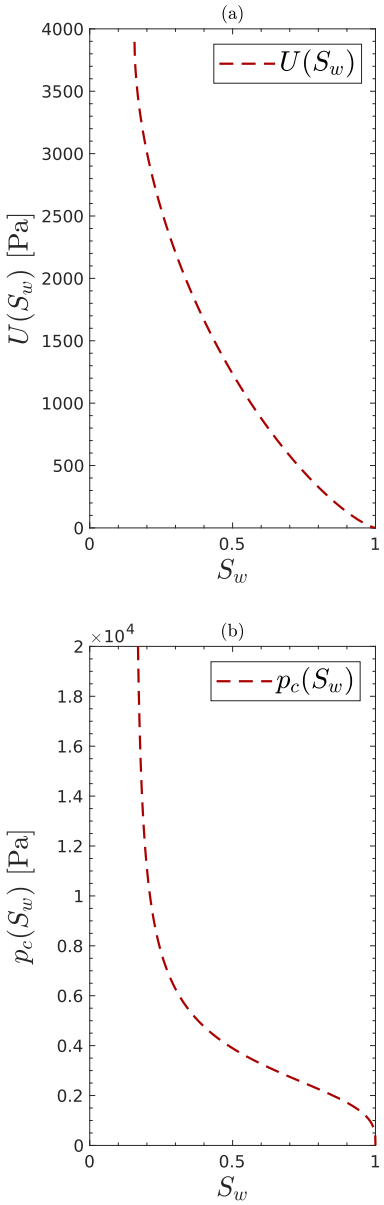

Figure 3.1: Graphs of (a) interfacial energy and (b) capillary pressure functions given by Eqs.(3.24 & 3.25) respectively, with $S_w^{res} = 0.1567$, $\pi_0 = 2840.91$ Pa and the van Genuchten model parameter $m = 0.685$ typical to silica sand saturated by air-water mixture.

Equivalent pore pressure & average fluid pressure

In full saturation where a single fluid completely saturates the pore spaces, the pore pressure is equivalent to the fluid pressure. In partial saturation however, due to the presence of two fluids phases superposed with the solid phase in the current configuration, a need for an equivalent pore pressure, π, arises. This equivalent pore pressure should properly take into account the contributions of fluid pressures of each fluid phase supposedly acting in unison on the pore walls.

While various possibilities for such an equivalent pore pressure were proposed over the years, we follow here the thermodynamically justified version by Coussy (2004),

$$\pi(p_w, p_{nw}) = p_w S_w + p_{nw} S_{nw} - U(S_w). \tag{3.27}$$

Such a definition accounts not only the effect of an average fluid pressure , $p^* = p_w S_w + p_{nw} S_{nw}$, but also for the tensile effect on the pore walls due to the capillary interface.

Effective stress

Since the early works of Terzaghi (Terzaghi, 1943) in soil mechanics and of Biot (Biot, 1941) in rock mechanics the concept of an effective stress is introduced that is assumed responsible for the entirety of the deformations of the solid skeleton, while taking into account the contribution due to the fluid pressure in the case of full saturation. An extension to the case of partial saturation for in-compressible solid matrix proposed by Bishop (Bishop, 1959) takes into account the concept of equivalent pore pressure, π. While originally proposed phenomenologically, the effective stress, σ_e, can

be derived also through thermodynamic considerations as done in Coussy (2004). Following the notation in the latter it is defined through,

$$\sigma - \sigma_0 = \sigma_e - b(\pi - \pi_0)I, \tag{3.28}$$

where σ_0 is the total pre-stress and π_0 is the equivalent pre-pressure if any. b is the so-called Biot's coefficient which in the case of homogeneous isotropic solid skeleton can be obtained (Biot and Willis, 1957) from the bulk modulus of the empty skeleton K and the bulk modulus of the solid matrix K_s,

$$b = 1 - \frac{K}{K_s}. \tag{3.29}$$

Assuming an isotropic linear poroelastic skeleton results in the effective stress being related to the linearized strain tensor, $\varepsilon(u)$, through the fourth order stiffness tensor $\mathbb{C}$ as follows,

$$\sigma_e = \mathbb{C} : (\varepsilon - \varepsilon_0), \tag{3.30}$$

which is equivalent to an isotropic Hooke's law for classical materials. ϵ_0 is the pre-strain if any. Due to the said assumption the stiffness tensor can be fully determined with the knowledge at least two material constants related to the empty porous skeleton, say the first, $\lambda = K - \frac{2}{3}\mu$, and the second μ Lamé parameters, μ being the corresponding shear modulus. Thus the following classical relation holds,

$$\sigma_e = \lambda\epsilon(u)I + 2\mu\varepsilon(u), \tag{3.31}$$

with $\epsilon(u) = \mathrm{tr}(\varepsilon(u))$.

Porosity

Again adopting an isotropic linear poroelastic solid, change in the total Lagrangian porosity, $\Delta\phi$, is obtained as a sum of contributions due to variations in solid strain and in equivalent pore pressure. This is given by the relation,

$$\Delta\phi = \phi(u, p_w, p_{nw}) - \phi_0 = b(\epsilon - \epsilon_0) + \frac{1}{N}(\pi - \pi_0), \tag{3.32}$$

where N is the so-called Biot's modulus that can be related to the properties of the macroscopic skeleton and of the matrix through,

$$\frac{1}{N} = \frac{b - \phi_0}{K_s}. \tag{3.33}$$

Remark: In soils the individual grains are typically in-compressible implying K_s goes to infinity, $b \approx 1$ and $1/N \approx 0$. Consequently, changes in porosity are entirely owing to skeleton strains, $\Delta\phi \approx \epsilon(u)$. The effective stress, σ_e, reduces to the Bishop's effective stress, $\sigma + \pi I$. In the case of full saturation this is equivalent to the simplification of Biot's effective stress to the celebrated Terzaghi's effective stress.

Darcy's law

The biphasic fluid flow accounting for dissipations of the fluid phases is described by an extension of Darcy flow to the partially saturated conditions. This is a relation between the volumetric flux of each fluid phase w.r.t the solid skeleton and the driving force which usually is the gradient of the fluid pressure of the respective phases and gravity (if considered). This is given for the each fluid phase as,

$$\frac{w_\alpha}{\rho_\alpha} = V_\alpha = nS_\alpha(v_\alpha - v_s) = \frac{\varkappa}{\eta_\alpha}k_\alpha(S_\alpha)\left(-\nabla p_\alpha + \rho_\alpha g\right), \tag{3.34}$$

where $\varkappa$ and η_α are respectively the intrinsic permeability of the porous skeleton and the dynamic viscosity of the fluid phase α. g is the acceleration due to gravity. V_α is the so-called filtration vector that represents the volumetric flux of each phase relative to the solid skeleton. $k_\alpha(S_\alpha)$ represents the relative permeability function for each phase which is a non-linear and typically empirical relation that modulates the flow of the particular fluid phase in accordance to its local saturation degree. In the current work we adopt empirical relations given by the van Genuchten model (van Genuchten, 1980; Luckner et al., 1989),

$$k_w(S_w) = \sqrt{S_w}\left[1 - \left(1 - S_w^{\frac{1}{m}}\right)^m\right]^2, \tag{3.35}$$

$$k_{nw}(S_{nw}) = \sqrt{S_{nw}}\left[1 - (1 - S_{nw})^{\frac{1}{m}}\right]^{2m}. \tag{3.36}$$

The above relations are smooth functions, see Fig.(3.2), that behave such that the more saturated the porous network is with a particular phase α the closer to one the relative permeability, $k_\alpha(S_\alpha)$, of that phase will be. It is to be noted that the function $k_w(S_w)$ is typically purely convex within $S_w \in [0, 1]$.

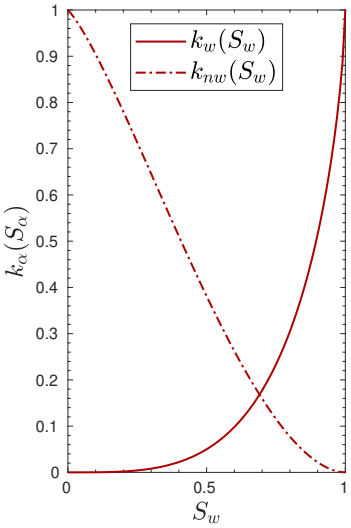

Figure 3.2: Graphs of the relative permeability functions in Eqs.(3.35 & 3.36) with the van Genuchten model parameter $m = 0.685$ typical to silica sand saturated by air-water mixture.

3.1.6 Summary of Governing equations under HSP

Under the simplifications provided by HSP, the governing equations are linearized to an extent. The residual non-linearity comes from the constitutive relations related to the fluids and the unsteady term within the balance of mass.

- The mass balance of the fluid phases, $\alpha \in \{w, nw\}$, given by Eq.(3.11) reduces to,

$$\frac{\partial(\phi S_\alpha)}{\partial t} + \nabla \cdot V_\alpha = 0, \tag{3.37}$$

  with V_α given by the Darcy's law with $\rho_\alpha = \rho_\alpha^0$, recapitulated below for convenience,

$$V_\alpha = \frac{\varkappa}{\eta_\alpha} k_\alpha(S_\alpha)\left(-\nabla p_\alpha + \rho_\alpha^0 g\right). \tag{3.38}$$

- The evolution of intrinsic mass density of the solid skeleton given by Eq.(3.13) reduces to,

$$\rho_s = \rho_s^0 \frac{(1 - \phi_0)}{(1 - \phi)}. \tag{3.39}$$

  Since this is an algebraic relation, ρ_s could be derived once ϕ is known from the solution of the problem through Eq.(3.32).

- The linear momentum balance or the equilibrium equation given by Eq.(3.16) with the help of classical localization arguments reduces to the differential form,

$$\nabla \cdot \sigma + \rho f_b = 0, \tag{3.40}$$

  with appropriate boundary conditions listed further. The total stress, σ, is given by Eq.(3.28) and the effective stress, σ_e, by Eq.(3.30) which have already been stated under HSP. The overall mass density of the porous medium is now given by $\rho = \rho_s^0(1 - \phi_0) + (\rho_w^0 S_w + \rho_{nw}^0 S_{nw})\phi$. f_b in principle accounts for the ensemble of body forces acting the porous medium which could also account for gravity.

3.1.7 Boundary & initial conditions

Appropriate boundary (BC) and initial (IC) conditions are needed to close the system of equations that form a boundary-initial value problem (BIVP). Typically the ICs relating to the state of the porous medium are assumed to be homogeneous ones. For instance, in soil hydrology one would usually come across initially dry or fully saturated conditions. The initial displacement corresponds to pre-strain of the solid skeleton if any. These set of ICs read as follows at $t = 0$ and for any $x \in \Omega$,

$$u(x,0) = u^0, \quad p_\alpha(x,0) = p_\alpha^0, \quad \alpha \in \{w, nw\}. \tag{3.41}$$

The BCs typically appear as essential (Dirichlet), natural (Neumann) and mixed (Robin) conditions. For the purpose of the current work we only consider the first two types of BCs. Parts of the full boundary, $\partial\Omega$, where these two types of BCs are applied are designated with a subscript 'D' and 'N' respectively. The mechanical BCs complimenting the equilibrium, Eq.(3.40), of the porous medium are designated with a superscript 's' and those complimenting the balances of fluid mass, Eq.(3.37), are designated with a superscript 'α' corresponding to the fluid phase concerned, $\alpha \in \{w, nw\}$. Further, we assume that all the BCs are independent of time and are uniformly applied to their corresponding parts of the boundary. These set of BCs read as follows for all $t > 0$,

$$u(x,t) = u_D, \quad x \in \partial\Omega_D^s, \tag{3.42}$$
$$\sigma \cdot \hat{n} = f_N, \quad x \in \partial\Omega_N^s \tag{3.43}$$
$$p_\alpha(x,t) = p_\alpha^D, \quad x \in \partial\Omega_D^\alpha, \quad \alpha \in \{w, nw\}, \tag{3.44}$$
$$V_\alpha \cdot \hat{n} = q_\alpha^N, \quad x \in \partial\Omega_N^\alpha, \quad \alpha \in \{w, nw\}. \tag{3.45}$$

With an abuse of notation $\hat{n}$ denotes the outward unit normal to the boundary wherever invoked. σ and V_α are given by their constitutive relations, Eq.(3.28) and Eq.(3.34) respectively. u_D, f_N, p_α^D and q_α^N are respectively prescribed values, on the corresponding boundaries, of displacement, surface traction, fluid pressures and volumetric fluid fluxes in the direction of $\hat{n}$.

3.1.8 Soil hydrology & Richards' equation

Typically in soil hydrology the two fluids involved are water and wet-air (or water vapor). Water in its liquid state is considered in-compressible, $\rho_w(x,t) = \rho_w^0$, which is already taken into account until this moment. Air on the other hand is naturally incompatible with such an assumption and rather can be modeled as an ideal gas,

$$\rho_{nw}(x,t) = \frac{p_{nw}(x,t)}{R\,T}, \quad x \in \Omega \tag{3.46}$$

where R and T are respectively the specific gas constant and absolute temperature assumed uniform and constant. As a first approximation considering air to be highly rarefied implies that its density is vanishing, $\rho_{nw}(x,t) \approx 0$ and an assumption of continuous connection of the air phase to the exterior ensures that any gradients in pressure are instantaneously vanishing. In fact, from the above equation one gets $p_{nw}(x,t) \approx 0$. Introducing these into the Darcy's law for air phase in Eq.(3.38) gives $V_\alpha \approx 0$. Thus the unknowns related to the air phase are eliminated and its saturation degree can be obtained trivially, $S_{nw} = 1 - S_w$, once the problem related to the water phase is resolved. Concurrently, the capillary pressure reduces to $p_c = -p_w$ and the equivalent pore pressure to,

$$\pi = p_w S_w - U(S_w). \tag{3.47}$$

The overall mass density of the porous medium is now approximated by $\rho = \rho_s^0(1-\phi_0) + \rho_w^0 S_w \phi$.

Now coming to the problem related to the water phase, inserting the Darcy's law Eq.(3.38) into the balance of mass, Eq.(3.37) gives Richards' equation,

$$\frac{\partial(\phi S_w)}{\partial p_w}\frac{\partial p_w}{\partial t} + \frac{\varkappa}{\eta_w}\nabla\cdot\hat{k}_w(p_w)\left(-\nabla p_w + \rho_w^0 g\right) = 0, \tag{3.48}$$

typically attributed to Richards (1931) but first published by Richardson (1922). In the above writing the dependency on the primary fluid unknown, i.e. p_w, is explicitly shown and hence this is referred to as the "head" form of Richards' equation. Note that $S_w(p_w)$ is obtained through the inverse retention relation, Eq.(3.26) and the relative permeability function is rewritten with p_w as the argument, hence is denoted $\hat{k}_w(p_w)$.

The Richards' equation can also be written in the "mixed water content" form by considering S_w as the primary unknown and water pressure as its function, $p_w(S_w) = -p_c(S_w)$ wherever it appears, leading to,

$$\frac{\partial(\phi S_w)}{\partial t} + \frac{\varkappa}{\eta_w}\nabla\cdot k_w(S_w)\left(\nabla p_c(S_w) + \rho_w^0 g\right) = 0. \tag{3.49}$$

In practical applications where soil is made up of layers with different properties, the water content among these layers undergoes sharp changes while the pressure remains continuous. This renders the head form more suitable. Whereas, in uniform soils the mixed water content form is more amenable, especially because use of the head form requires high accuracy time integration to avoid mass balance errors (Tocci et al., 1997) due to the high non-linearity involved in the coefficient of the unsteady term, $\partial(\phi S_\alpha)/\partial p_w$. Either of these forms are solved in tandem with the equilibrium equation Eq.(3.40), appropriate ICs and BCs (except those of air phase) to address water movement in deformable soils. In the case of non-deformable skeleton the porosity remains unchanged ($\phi = \phi_0 = \text{const}$) and the only problem to be resolved is of the flow of water and Richards' equation reduces to,

$$\phi\frac{\partial S_w}{\partial t} + \frac{\varkappa}{\eta_w}\nabla\cdot k_w(S_w)\left(\nabla p_c(S_w) + \rho_w^0 g\right) = 0. \tag{3.50}$$

3.1.9 Criticism and extensions of Richards' equation

While this approach has been widely accepted, over the years Richards' equation has faced criticisms on several fronts even though it reduces the complexity involved. These criticisms surround: the rough up-scaling law that is involved to model the retention effect of the pore walls on the fluids (Morrow, 1970; Gray and Hassanizadeh, 1991a), inability to reproduce physically observed fingering phenomenon (Egorov et al., 2003; Nieber et al., 2005) and complexities involved in numerical implementations Miller et al. (1998); Farthing and Ogden (2017). Concerning the latter, one can notice that the two empirical constitutive relations for the relative permeability, $k_w(S_w)$, and the capillary pressure, $p_c(S_w)$, are highly non-linear and are degenerate. $k_w(S_w)$ can behave as a constant close to full saturation or vanish in close to dry conditions. $p_c(S_w)$ as well takes arbitrarily small values close to full saturation and behaves asymptotically when tending to residual saturation. In reality these relations can as well be found to be hysteretic. In the case of infiltration in to dry soils two main features have been observed of the wetting phenomenon: sharp wetting front and fingering type instability as the front propagates through the soil mass (see Sec.(2.1.1)). The extremely large spatial gradients of the solution render a

high degree of non-linearity in Richards' equation making the design of numerical schemes complicated (Miller et al., 2013). In terms of stability, the works of Egorov et al. (2003); Nieber et al. (2005) revealed that Richards' equation is unconditionally stable against traversal perturbations thus being unable to produce experimentally observed fingering type instabilities.

In addition to the above criticisms, one needs to practice caution when using Richards' equation or its associated assumptions. The continuous connectivity of air phase to the exterior and the absence of impermeable layers is critical for neglecting the flow of air. Moreover, in the degenerate case of vanishing saturation degree of water, $S_w \to 0$, the equivalent pore pressure does not vanish. On the contrary it tends to negative infinity in accordance with the behavior of capillary energy, $\pi = -p_c(S_w)S_w - U(S_w) \to -\infty$, and with respect to the infinitely thin residual pore water films attached to the grains. However, the pore pressure within the dry soil should be equal to the atmospheric pressure due to the continuous connectivity of the air phase which is not compatible with the behavior of equivalent pore pressure.

While various extensions have been proposed intending to remedy these inadequacies, we mention here a few of them which focus on enriching the retention relation and enabling the description of fingering phenomenon. Hassanizadeh and Gray (1990); Gray and Hassanizadeh (1991a,b) introduced the specific interfacial area, which is a cumulative measure of fluid interfaces within an REV, as an internal state variable thus providing a corrective term to otherwise coarsely defined retention relation, $p_c(S_w)$. As part of their 'hold-back-pile-up' postulate Eliassi and Glass (2002) drew parallels to this corrective term, introducing the so-called 'hypo-diffusive' term and showed (Eliassi and Glass, 2003) that if this correction results in a non-monotonic retention relation then non-monotonic overshoot saturation profiles are possible in gravity driven infiltration. Eliassi and Glass (2002) also introduced a mixed 'relaxation' term, which is second-order in space and first-order in time, as an extension to standard Richards' equation and interpreted this as a consequence of the rate-dependent capillary pressure function introduced by Hassanizadeh and Gray (1993). Egorov et al. (2003); Nieber et al. (2005) have shown that such an extension of Richards' equation can produce instabilities for non-monotonic solution profiles. DiCarlo et al. (2008) used this relaxation term to introduce regularization to Richards' equation with non-monotonic capillary pressure function from (Eliassi and Glass, 2003) and showed similar overshoot solutions. Cueto-Felgueroso and Juanes (2009a) introduced a phase field model with a fourth-order in space term to the standard Richards' equation producing non-monotonic solution profiles and proposed a relevant heuristic scaling of the fourth-order coefficient that resulted in favorable comparison with some experimental observations. The caveat of this model is the use of a nonphysical 'compressibility' term of an exponential form thus modifying the behavior of the capillary energy. Stability analysis (Cueto-Felgueroso and Juanes, 2009b) of this model as well has revealed instabilities when saturation profiles are non-monotonic.

3.2 A PHASE FIELD APPROACH TO PARTIAL SATURATION

More recently in the work of Sciarra (2016), a framework has been built that is thermodynamically consistent and naturally allows for modeling possible localized deformations of the porous skeleton (Vardoulakis et al., 1978; Desrues and Viggiani, 2004; Desrues and Andò, 2015) and its coupling to the fluid flow. Concerning the fluid description, while the standard retention relation describes the confining effect due to the pore walls, an enhanced description of surface tension between the fluids is obtained by considering

the two immiscible fluids as a single non-uniform biphasic fluid in the spirit of Cahn and Hilliard (1958, 1959). In this sense it can be viewed as a phase field approach to model multi-phase fluid flow while accounting for the fact that the porous network, through which the non-uniform fluid is flowing, provides additional interfacial energy due to the solid-fluid interfaces. Such a description of fluids is adopted in Chp.(4). Naturally within such a framework, coexistence of isopotential phases is possible thanks to the Van der Waals-like double-well form of the fluid energy density. This gives rise to a non-monotonic effective retention curve when the confining effect given by the standard retention curve is added to it. This is elaborated further in this chapter. Parallels may be drawn to the 'hypo-diffusive' term (Eliassi and Glass, 2002; DiCarlo et al., 2008) which resulted in a non-monotonic retention relation, but the mixed 'relaxation' term is not employed in the current model. Instead, as usual in Cahn-Hilliard type phase field models (Lowengrub and Truskinovsky, 1998; Jacqmin, 2000; Boyer and Lapuerta, 2006; Kim, 2012), coarsening of the fluid domains and pattern formation is made possible due to a non-local gradient energy contribution giving rise to an extension to Richards equation which is now fourth-order in space. In this sense parallels may be as well drawn to the higher order model introduced by Cueto-Felgueroso and Juanes (2009a), which, however, does not account for coexistence of isopotential phases and phase segregation due to its lack of a bulk energy contribution that has a double-well structure.

In the following sections a derivation of this model is done following Sciarra (2016), however neglecting the description of a second-gradient solid through a simplifying assumption on the relation between solid and fluid double forces.

3.2.1 Kinematics & preliminaries

A macroscopic approach is adopted for treating the kinematics of a porous medium, which is understood, similar to classical poromechanics, as a superposition of the solid skeleton and the mixture of constituent fluids (water and air). As detailed further, the binary fluid mixture is assumed to be a single non-unfiorm fluid in the same sense as Cahn-Hilliard fluids, wherein possible spatial variations of an intensive scalar property is expected to describe the distribution of the constituent fluids. With such an assumption, the current kinematic description is closer to the classical one describing full saturation of the pore spaces with a single fluid (see Coussy (2004)). As a consequence and in view of being concise, the kinematics of classical partial saturation as described in Sec.(3.1.1) is adapted for the following. Specifically, the two constituents, $c \in \{s, f\}$, of the porous medium are considered the solid phase (subscript 's') representing the skeleton and the fluid phase (subscript 'f') representing the non-uniform fluid. With this, all the developments of Sec.(3.1.1) can be applied with subscript 'α' replaced with subscript 'f'.

As mentioned earlier, an intensive property is needed to delineate the constituent phases (water and air) within the non-uniform fluid,thus giving their spatial distribution. Following Sciarra (2016), this property is chosen as the ratio of volume density of the liquid phase (water) to the available porous volume, which is the nothing but the saturation degree of the liquid phase. This is denoted as S_r whose notational counterpart in the classical approach is S_w. In the spirit of Cahn-Hilliard modeling, S_r acts as a phase field/order parameter distinguishing the two phases. This particular choice puts a physically motivated restriction on the range of values this phase field parameter can take, as such $S_r \in [0, 1]$. $S_r = 0$ represents pure phase of air(non-wetting fluid) and $S_r = 1$ represents water(wetting fluid). Moreover,

it allows to invoke the assumptions (Hilfer and Steinle, 2014) that lead to Richards' equation. For an $S_r \in [0,1]$, a simple linear interpolation of individual densities of pure phases can be assumed for the apparent mass density, ρ_f, of the non-uniform fluid (Kim, 2012). A non-uniform fluid composed of in-compressible water ($\rho_w = const$) and highly rarefied air, the latter being continuously connected to the atmosphere, implies that pure air phase is of infinite mobility. Thus any pressure differences in this phase ($S_r = 0$) are instantaneously vanishing and the pressure itself equates to that of reference atmospheric pressure, assumed 0 for convenience. Concurrently invoking an ideal gas law for air implies that its density, ρ_{nw}, is negligible compared to that of water ($\rho_w \gg \rho_{nw} \approx 0$) leading to,

$$\rho_f = \rho_w S_r + \rho_{nw}(1 - S_r) \approx \rho_w S_r. \tag{3.51}$$

3.2.2 Balance of Mass

Similar to the developments in Sec.(3.1.2), the balance of masses written for the non-uniform fluid and the solid phases would result in,

$$\frac{dm_f}{dt} + \nabla_s \cdot M = 0, \quad \text{with } M = m_f F_s^{-1} \cdot (v_f - v_s) = m_f F_s^{-1} \cdot w, \tag{3.52}$$

as the pull-back in the solid reference configuration of the fluid mass balance and Eq.(3.13) as the relation for the current mass density of the solid.

3.2.3 Power of external forces & balance of momentum

According to the classical gradient theories, the power of external forces is written as a linear functional of the velocity fields of the non-uniform fluid and the solid,

$$\mathcal{P}^{ext} = \sum_c \left[\int_{\Omega^t} b_c \cdot v_c \, d\Omega^t + \int_{\partial\Omega^t} t_c \cdot v_c \, dS^t + \int_{\partial\Omega^t} \tau_c \cdot \frac{\partial v_c}{\partial \hat{n}} \, dS^t \right], \tag{3.53}$$

with $c = \{s, f\}$. $\partial\Omega^t$ is the smooth boundary of Ω^t such that the outward normal $\hat{n}$ to the boundary does not suffer jumps. Note that even though the deformations of the solid skeleton are eventually expected to be described using the standard first gradient formulation, we start the deductions by taking into account the contribution of a solid double force, τ_s, in the expression above, in addition to the bulk force, b_s, and the surface traction, t_s. Whereas a contribution due to the fluid double force, τ_f, is considered in addition to its bulk force, b_f, and surface traction, t_f, owing to its gradient nature elaborated further. In line with the extended Cauchy theorem (Dell'Isola and Seppecher, 1997) the surface tractions and double forces for each constituent can be related to the outward unit normal through tensorial quantities as follows,

$$(\Sigma_c - \nabla \cdot \Pi_c) \cdot \hat{n} - \nabla_s \cdot (\Pi_c \cdot \hat{n}) = t_c, \quad \text{on } \partial\Omega^t, \tag{3.54}$$

$$(\Pi_c \cdot \hat{n}) \cdot \hat{n} = \tau_c, \quad \text{on } \partial\Omega^t. \tag{3.55}$$

Σ_c and Π_c are respectively second-order apparent Cauchy stress and third-order apparent hyper-stress tensors per unit volume of the porous medium in the current configuration. Introducing these into Eq.(3.53) one gets,

$$\begin{aligned}\mathcal{P}^{ext} &= \sum_c \Bigg[\int_{\Omega^t} b_c \cdot v_c \, d\Omega^t + \int_{\partial\Omega^t} [(\Sigma_c - \nabla \cdot \Pi_c) \cdot \hat{n}] \cdot v_c \, dS^t \\ &\quad + \int_{\partial\Omega^t} (\Pi_c \cdot \hat{n}) : \nabla v_c \, dS^t \Bigg], \\ &= \sum_c \Bigg[\int_{\Omega^t} b_c \cdot v_c \, d\Omega^t + \int_{\Omega^t} \Big\{ [\nabla \cdot (\Sigma_c - \nabla \cdot \Pi_c)] \cdot v_c + \Sigma_c : \nabla v_c \Big\} \, d\Omega^t \\ &\quad + \int_{\Omega^t} \Pi_c \vdots \nabla\nabla v_c \, d\Omega^t \Bigg].\end{aligned} \tag{3.56}$$

According to the classical poromechanical practice we define the overall stress acting on the porous medium as a sum of the individual stresses acting on the solid and the fluid, $\Sigma = \Sigma_s + \Sigma_f$, similarly for the overall hyper-stress, $\Pi = \Pi_s + \Pi_f$, and the overall bulk force as the sum of the individual bulk forces, $b = b_s + b_f$. A quasi-static overall balance of momentum of the porous medium taking into account the extended Cauchy theorem reads in its local form,

$$\nabla \cdot (\Sigma - \nabla \cdot \Pi) + b = 0, \quad \text{in } \Omega^t. \tag{3.57}$$

At this point we make a couple of simplifying assumptions. Firstly, we assume that the structure of the hyper-stress tensor for both constituents is such that $\Pi_c = I \otimes \pi_c$, where π_c is equivalent to an hyper-stress vector. Such an assumption amounts to a restriction on the double force such that it works only on differential elongation in the case of the solid phase and on differential saturation ratio in the case of the fluid. This means that the skew-symmetric couples working on the vorticity on the boundary due to τ_c are assumed to be negligible. The second assumption concerns the overall hyper-stress itself, which is vanishing by assuming $\Pi_f = -\Pi_s$. The effect of this assumption as seen further is the absence of second-gradient solid contribution in the expression of strain working. Consequently the balance of momentum reduces to the classical one,

$$\nabla \cdot \Sigma + b = 0, \quad \text{in } \Omega^t. \tag{3.58}$$

Employing the principal of virtual power ($\mathcal{P}^{ext} = \mathcal{P}^{int}$) and introducing Eq.(3.58) into Eq.(3.56) we can get, following a trivial manipulation, an expression for the power of internal forces or the strain working as,

$$\mathcal{P}^{int} = \int_{\Omega^t} \Big\{ b_f \cdot w + \nabla \cdot \big(\Sigma_f - \nabla \cdot \Pi_f\big) \cdot w + \Pi_f \vdots \nabla\nabla w + \Sigma : \nabla v_s \Big\} d\Omega^t. \tag{3.59}$$

In order to perform a pull-back of the power of internal forces onto the solid reference configuration one needs to introduce appropriate Lagrangian quantities. The overall second Piola-Kirchhoff stress tensor, S, as a counter part to the overall Cauchy stress, Σ, is obtained such that,

$$\frac{J_s}{2} \Sigma : (\nabla v_s + \nabla^T v_s) = S : \dot{E} \implies \Sigma = J_s^{-1} F_s \cdot S \cdot F_s^T, \tag{3.60}$$

where $\dot{(\,)}$ represents time derivative w.r.t to the solid particle fixed in the solid reference configuration. The pull-back into the solid reference configuration of the fluid bulk forces is obtained as $\mathfrak{b}_f = J_s F_s^T b_f$. Further the fluid stress

tensor can be decomposed into its spherical and deviatoric parts as, $\Sigma_f = -p_f I + \Sigma_f^d$. Since the fluid hyper-stress vector is defined such that $\pi_f = \Pi_f/3$, its pull-back, γ_f, is obtained in accordance with $\pi_f = J_s^{-1} F_s \cdot \gamma_f$.

Introducing these quantities, the Lagrangian writing of $\mathcal{P}^{int}$, is obtained as,

$$\begin{aligned}\mathcal{P}_0^{int} = \int_{\Omega_s^0} \Bigg\{ \mathfrak{b}_f \cdot \frac{M}{m_f} - \nabla_s \cdot \left(J_s p_f \frac{M}{m_f} \right) + \nabla_s \cdot \left(J_s F_s^{-1} \cdot \Sigma_f^{d\,T} \cdot F_s \frac{M}{m_f} \right) \\ - \nabla_s \cdot \left[\left(\nabla_s \cdot \gamma_f \right) \frac{M}{m_f} - \frac{\gamma_f}{J_s} \nabla_s \cdot \left(J_s \frac{M}{m_f} \right) \right] + S : \dot{E} \Bigg\} d\Omega_s^0 .\end{aligned} \tag{3.61}$$

3.2.4 Thermodynamics

As mentioned earlier (Sec.(3.1.5)), the classical approach to unsaturated poromechanics, as detailed in Coussy (2004, 2010), involves a rough up-scaling of a simplistic pore-scale mechanism: energy stored due to creation of additional infinitesimal interfacial area within the pore is due to the work done by the capillary pressure difference causing infinitesimal variations in the volume content of the wetting fluid with the pore. Criticism concerning this approach and the particular extensions to remedy this lacking are detailed in Sec.(3.1.9).

Fluid & interfacial energies

In the current thesis we follow a novel approach proposed by Sciarra (2016) that involves a separation of the fluid-fluid and solid-fluid interfacial energies. The former is taken into account in the macroscopic constitutive prescription by describing the fluid mixture (air and water) as a single bi-phasic non-uniform fluid analogous to a Cahn-Hilliard (Cahn and Hilliard, 1958) like (Lowengrub and Truskinovsky, 1998; Jacqmin, 2000; Boyer and Lapuerta, 2006; Kim, 2012) fluid modeling. Accordingly the non-uniform fluid's internal energy is assumed to be a sum of local and non-local contributions,

$$\mathcal{E}_f = n\rho_f e_f \left(\frac{1}{\rho_f}, s_f \right) + \kappa_f(f_p), \quad f_p = \left(\nabla(n\rho_f) \cdot \nabla(n\rho_f) \right). \tag{3.62}$$

e_f is the fluid-specific internal energy. $\rho_f e_f$ is assumed to be a double-well potential dependent on the specific density, ρ_f and specific entropy, s_f of the non-uniform fluid. $\kappa_f(f_p)$ is the non-local energy dependent on the gradient of the non-uniform fluid content, so is responsible for regularization of the non-convex local energy and penalization allowing formation of interfaces.

With ψ_f as the fluid-specific Helmholtz free energy and according to the Legendre transformation $\psi_f = e_f - T s_f$, thermodynamic pressure, P, and chemical potential, μ, of the fluid can be defined such that,

$$P = -\frac{\partial e_f}{\partial \left(1/\rho_f\right)}\bigg|_{s_f=const} = -\frac{\partial \psi_f}{\partial \left(1/\rho_f\right)}\bigg|_{T=const}, \quad \mu = \frac{\partial(\rho_f e_f)}{\partial \rho_f}\bigg|_{T=const}, \tag{3.63}$$

where T is the absolute temperature, conjugate to s_f.

In view of the constitutive prescription of the fluid, Eq.(3.62), the following expressions for fluid stress and hyper-stress are derived,

$$p_f = nP - \kappa_f + 2\left(1 + \frac{1}{\mathrm{tr}I}\right)\frac{\partial \kappa_f}{\partial f_p} f_p, \tag{3.64}$$

$$\Sigma_f^d = -2\frac{\partial \kappa_f}{\partial f_p}\left(\nabla(n\rho_f) \otimes \nabla(n\rho_f) - \frac{1}{\mathrm{tr}I}\nabla(n\rho_f)\cdot\nabla(n\rho_f)I\right), \tag{3.65}$$

$$\pi_f = -2\frac{\partial \kappa_f}{\partial f_p}(n\rho_f)\nabla(n\rho_f). \tag{3.66}$$

The local double-well energy, similar to Van der Waals' isotherms in phase transition, is intended to allow for coexistence of the immiscible phases corresponding to isopotential minima. In view of the assumptions leading to the definition Eq.(3.51) for mass density of the non-uniform fluid in terms of the saturation degree of the wetting fluid, a possible form of the double-well energy potential is chosen as a function of S_r,

$$\rho_f e_f = \frac{C\gamma}{R} S_r^2 (1 - S_r)^2 . \tag{3.67}$$

This form has a symmetric double-well structure whose isopotential minima correspond to the pure phases of air ($S_r = 0$) and water ($S_r = 1$). See Fig.(3.3). The characteristic radius of channels within which the fluid menisci form, R, is an intrinsic property of the porous skeleton and according to Leverett (1941) it scales with $\sqrt{\varkappa/\phi_0}$. With $\Psi_f(S_r)$ as the free-energy counterpart of the above local internal energy,

$$\mu_f(S_r) = \left.\frac{\partial \Psi_f(S_r)}{\partial S_r}\right|_{T=const} = \left.\frac{\partial(\rho_f e_f)}{\partial S_r}\right|_{T=const} = \frac{2C\gamma}{R} S_r\left(1 - 3S_r + 2S_r^2\right), \tag{3.68}$$

defines a chemical potential that is identical to $\rho_w \mu$.

The non-local gradient energy contribution allowing the formation of diffuse interface between the two phases and providing regularization of the non-convex local energy, is typically assumed to be quadratic in the gradient of fluid content, $\nabla(nS_r)$, as follows:

$$\kappa_f(f_p) = \frac{C_k}{2}\left(\nabla(nS_r)\cdot\nabla(nS_r)\right). \tag{3.69}$$

The magnitude of C_k determines the spatial influence of this non-local energy. The significance and choice of scaling of this term is reserved for later analysis. However, in the case of a homogeneous evolution of S_r this term vanishes. Introducing Ψ_{NL} as the free-energy counterpart of $\kappa_f(f_p)$,

$$\mu_{NL}(\nabla(nS_r)) = \nabla\cdot\left.\frac{\partial \Psi_{NL}}{\partial \nabla(nS_r)}\right|_{T=const} = \nabla\cdot\left.\frac{\partial \kappa_f}{\partial \nabla(nS_r)}\right|_{T=const} = -\nabla\cdot\frac{\pi_f}{nS_r}, \tag{3.70}$$

defines the non-local chemical potential that is written here in view of its future use in Sec.(3.2.5).

Concerning the solid-fluid interfacial energy, $\mathcal{E}_{sf}$, a priori no constitutive prescription is done. This interfacial energy is thought of as responsible for the confining effect on the non-uniform fluid, provided by the pore walls due to their texture. Following the thermodynamic restrictions this contribution is to be found equivalent to the classical interfacial energy, $U(S_r)$.

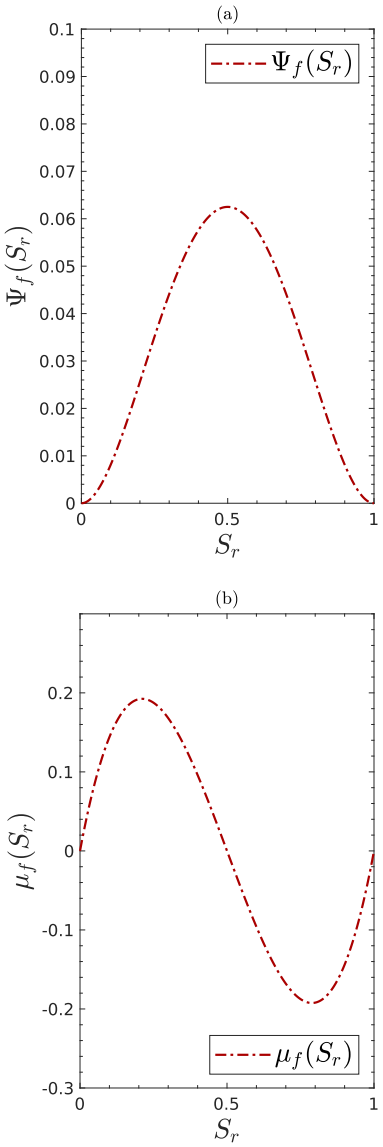

Figure 3.3: The double-well structure of the energy densities in (a) means that the pure fluid phases can coexist, since they are the isopotential, (b), minima. All functions plotted are dimensionless according to the scheme presented in Chp.(4)

The first principle of thermodynamics

Assuming the postulate of local state extended to porous continua (see Coussy (2004)) and introducing $\mathcal{E}_s = \rho_s(1-n)e_s$ as the internal energy of the solid skeleton per unit volume of the porous medium, the first principle of thermodynamics amounts to a balance of energy that reads as,

$$\frac{d^s}{dt}\int_{\Omega^t}\left(\mathcal{E}_s + \frac{1}{2}\mathcal{E}_{sf}\right)d\Omega^t + \frac{d^f}{dt}\int_{\Omega^t}\left(\mathcal{E}_f + \frac{1}{2}\mathcal{E}_{sf}\right)d\Omega^t = \mathcal{P}^{int} + \dot{\mathcal{Q}}. \tag{3.71}$$

Note that the solid-fluid interfacial energy is assumed to be equally decomposed in such way as to associate half of it to the displacement of solid matrix and the other half to the motion of the non-uniform fluid. Assuming no volume heat rate supply, $\dot{\mathcal{Q}}$ denotes the rate of heat supply from the exterior through the surface of Ω^t. This can be defined, employing the flux-density lemma, in terms of a rate of surface flux density, q, supplied through $\partial\Omega^t$ along its outward unit normal as,

$$\dot{\mathcal{Q}} = -\int_{\partial\Omega^t} q\cdot\hat{n}\, dS^t = -\int_{\partial\Omega_s^0}\mathfrak{q}\cdot\hat{N}_s\, dS_s^0 = -\int_{\Omega_s^0}\nabla_s\cdot\mathfrak{q}\, d\Omega_s^0, \tag{3.72}$$

where $\mathfrak{q}$ is introduced as the pull-back into the solid reference configuration of q.

An overall internal energy per unit volume of the porous medium can be defined as $\mathcal{E} = \mathcal{E}_s + \mathcal{E}_f + \mathcal{E}_{sf}$. Employing the definitions of particle derivative of an integral, Eq.(3.8), and the relative fluid mass flow vector, $w(x,t)$, the following can be derived,

$$\begin{aligned}
&\frac{d^s}{dt}\int_{\Omega^t}\left(\mathcal{E}_s + \frac{1}{2}\mathcal{E}_{sf}\right)d\Omega^t + \frac{d^f}{dt}\int_{\Omega^t}\left(\mathcal{E}_f + \frac{1}{2}\mathcal{E}_{sf}\right)d\Omega^t\\
&= \int_{\Omega^t}\left\{\frac{d^s\mathcal{E}}{dt} + \mathcal{E}\nabla\cdot v_s + \nabla\cdot\left(\frac{1}{\rho_f n}\left(\mathcal{E}_f + \frac{1}{2}\mathcal{E}_{sf}\right)w\right)\right\}d\Omega^t,\\
&= \int_{\Omega_s^0}\left\{\frac{d\mathbb{E}}{dt} + \nabla_s\cdot\left(\frac{1}{\rho_f n}\left(\mathcal{E}_f + \frac{1}{2}\mathcal{E}_{sf}\right)M\right)\right\}d\Omega_s^0,
\end{aligned} \tag{3.73}$$

where in the last step a pull-back into the solid reference configuration is performed with the introduction of corresponding overall internal energy per unit volume of the porous medium such that $\mathbb{E}d\Omega_s^0 = \mathcal{E}d\Omega^t$.

Finally rewriting Eq.(3.71) in the solid reference configuration using, Eqs.(3.61,3.72 & 3.73) gives a Lagrangian writing of the energy balance in the local form,

$$\begin{aligned}
\frac{d\mathbb{E}}{dt} &= S:\dot{E} + \mathfrak{b}_f\cdot\frac{M}{m_f} - \nabla_s\cdot\left(J_s p_f\frac{M}{m_f}\right) + \nabla_s\cdot\left(J_s F_s^{-1}\cdot\Sigma_f^{d^T}\cdot F_s\frac{M}{m_f}\right)\\
&\quad - \nabla_s\cdot\left[\left(\nabla_s\cdot\gamma_f\right)\frac{M}{m_f} - \frac{\gamma_f}{J_s}\nabla_s\cdot\left(J_s\frac{M}{m_f}\right)\right] - \nabla_s\cdot\left(\frac{1}{\rho_f n}\left(\mathcal{E}_f + \frac{1}{2}\mathcal{E}_{sf}\right)M + \mathfrak{q}\right).
\end{aligned} \tag{3.74}$$

The second principle of thermodynamics

The second principle of thermodynamics entails a fundamental inequality related to entropy evolution thus establishing a distinction between reversible and irreversible processes. For a porous medium saturated with a non-uniform fluid this inequality can be written as,

$$\frac{d^s}{dt}\int_{\Omega^t}\rho_s(1-n)s_s d\Omega^t + \frac{d^f}{dt}\int_{\Omega^t}\rho_f n s_f d\Omega^t \geq -\int_{\partial\Omega^t}\frac{q\cdot\hat{n}}{T}dS^t, \tag{3.75}$$

where s_s has been introduced as the specific entropy of the solid matrix. Employing similar steps as used for the first principle, the pull-back into the solid reference configuration of the entropy inequality reads in its local form,

$$\frac{d\mathbb{S}}{dt} + \nabla_s \cdot \left(s_f M + \frac{\mathfrak{q}}{T} \right) \geq 0, \tag{3.76}$$

where $\mathbb{S} = J_s \left(\rho_s (1-n) s_s + \rho_f n s_f \right)$ denotes the Lagrangian overall entropy per unit volume of the porous medium.

The Clausius-Duhem inequality & dissipation

Introducing the overall Helmholtz free energy of the porous medium, Ψ, though the Legendre transformation

$$\Psi = \mathbb{E} - T\mathbb{S}, \tag{3.77}$$

one can transform the rate of overall entropy within Eq.(3.76) to obtain,

$$\frac{d\mathbb{E}}{dt} - \mathbb{S}\frac{dT}{dt} - \frac{d\Psi}{dt} + T\, \nabla_s \cdot \left(s_f M + \frac{\mathfrak{q}}{T} \right) \geq 0. \tag{3.78}$$

Using the expression for rate of overall internal energy from Eq.(3.74) in Eq.(3.78) once can obtain the Clausius-Duhem inequality,

$$\begin{aligned} & S : \dot{E} + \mathfrak{b}_f \cdot \frac{M}{m_f} - \nabla_s \cdot \left(J_s p_f \frac{M}{m_f} \right) + \nabla_s \cdot \left(J_s F_s^{-1} \cdot \Sigma_f^{dT} \cdot F_s \frac{M}{m_f} \right) \\ & - \nabla_s \cdot \left[\left(\nabla_s \cdot \gamma_f \right) \frac{M}{m_f} - \frac{\gamma_f}{J_s} \nabla_s \cdot \left(J_s \frac{M}{m_f} \right) \right] - \nabla_s \cdot \left(\frac{1}{\rho_f n} \left(\mathcal{E}_f + \frac{1}{2} \mathcal{E}_{sf} \right) M + \mathfrak{q} \right) \\ & + T\, \nabla_s \cdot \left(s_f M + \frac{\mathfrak{q}}{T} \right) - \mathbb{S}\frac{dT}{dt} - \frac{d\Psi}{dt} \geq 0. \end{aligned} \tag{3.79}$$

Following a classical approach owing to the additive nature of energy and entropy, the Lagrangian densities of free energy, Ψ_s, and entropy, $\mathbb{S}_s$, of the porous solid are deduced by subtracting respective bulk contributions of the fluid from those of the overall porous medium,

$$\Psi_s = \Psi - m_f \psi_f, \quad \mathbb{S}_s = \mathbb{S} - m_f s_f. \tag{3.80}$$

As mentioned at the beginning of this chapter, the above terminology is due to the work of Biot (1972), according to which the porous solid is understood as a 'wetted' porous skeleton, with a thin layer of immobile fluid attached to the pore walls and thus accounting for the associated solid-fluid interfaces. This allows one to model Ψ_s as a state function in the context of thermo-poroelasticity, where dissipation is only attributed to flow of mobile fluid and thermal effects.

Introducing Eq.(3.80) into Eq.(3.79), while employing the balance of fluid mass, Eq.(3.52) and constitutive prescription of the non-uniform fluid, Eq.(3.64) the Clausius-Duhem inequality can be rephrased identifying an the overall dissipation of the porous medium Φ as,

$$\begin{aligned} \Phi = & -\left\{ \frac{1}{S_r} \nabla_s P + \nabla_s \left[\nabla_s \cdot \left(\frac{\gamma_f}{\phi S_r} \right) + \frac{1}{S_r} \left(\frac{1}{2n} \mathcal{E}_{sf} + \frac{\gamma_f}{\phi} \cdot \frac{\nabla_s J_s}{J_s} \right) \right] - \frac{\mathfrak{b}_f}{\phi S_r} \right\} \frac{M}{\rho_w} \\ & + S : \dot{E} + \left(P + \frac{1}{2n} \mathcal{E}_{sf} + \frac{\gamma_f}{\phi} \cdot \frac{\nabla_s J_s}{J_s} \right) \frac{d\phi}{dt} + \frac{\phi}{S_r} \left(\frac{1}{2n} \mathcal{E}_{sf} + \frac{\gamma_f}{\phi} \cdot \frac{\nabla_s J_s}{J_s} \right) \frac{dS_r}{dt} \\ & - \frac{\gamma_f}{\phi S_r} \cdot \frac{d \nabla_s (\phi S_r)}{dt} - \mathbb{S}_s \frac{dT}{dt} - \frac{d\Psi_s}{dt} - \frac{\mathfrak{q}}{T} \nabla_s T \geq 0. \end{aligned} \tag{3.81}$$

As a general practice in poromechanics (Coussy, 2004) the individual contributions by the solid skeleton (Φ_s), non-uniform fluid flow (Φ_f) and thermal effects (Φ_T), to the overall dissipation are identified and are independently assumed non-negative in order to satisfy the above inequality so that,

$$\begin{aligned}\Phi_s &= S : \dot{E} + P\frac{d\phi}{dt} + \frac{1}{S_r}\left(\frac{1}{2n}\mathcal{E}_{sf} + \frac{\gamma_f}{\phi}\cdot\frac{\nabla_s J_s}{J_s}\right)\frac{d(\phi S_r)}{dt} \\ &\quad - \frac{\gamma_f}{\phi S_r}\cdot\frac{d\nabla_s(\phi S_r)}{dt} - \mathbb{S}_s\frac{dT}{dt} - \frac{d\Psi_s}{dt} \geq 0, \end{aligned} \tag{3.82}$$

$$\Phi_f = -\left\{\frac{1}{S_r}\nabla_s P + \nabla_s\left[\nabla_s\cdot\left(\frac{\gamma_f}{\phi S_r}\right) + \frac{1}{S_r}\left(\frac{1}{2n}\mathcal{E}_{sf} + \frac{\gamma_f}{\phi}\cdot\frac{\nabla_s J_s}{J_s}\right)\right] - \frac{\mathfrak{b}_f}{\phi S_r}\right\}\frac{M}{\rho_w} \geq 0, \tag{3.83}$$

$$\Phi_T = -\frac{\mathfrak{q}}{T}\nabla_s T \geq 0. \tag{3.84}$$

Eq.(3.82) in addition to the postulate of local state leads to the free energy density of the solid being a rate independent function of the state variables: solid strain, Lagrangian porosity, saturation degree, spatial gradient of Lagrangian water content and absolute temperature, so that we obtain,

$$\Psi_s := \Psi_s(E, \phi, S_r, \nabla_s(\phi S_r), T). \tag{3.85}$$

The dissipation due to fluid flow is encompassed within Eq.(3.83). The essence of this restriction is that the generalized force, coefficient of M/ρ_w, causing the fluid flow must be related to the fluid velocity vector in such a way as to satisfy the dissipation inequality. Eq.(3.84) as usual states that heat flows from regions of higher temperature to those of lower temperature along the direction of negative spatial gradient of T.

3.2.5 Poroelastic constitutive relations

In what follows we assume isothermal conditions. Consequently the thermal dissipation is vanishing and the dependency of free energy density of the solid in Eq.(3.85) reduces to,

$$\Psi_s := \Psi_s(E, \phi, S_r, \nabla_s(\phi S_r)). \tag{3.86}$$

Solid state equations

Poroelasticity amounts to vanishing solid dissipation and absence of any frozen contributions to the free energy. Within this framework, using Eq.(3.86) in Eq.(3.82) gives the following restriction on Ψ_s,

$$\begin{aligned}\Phi_s &= \left(S - \frac{\partial\Psi_s}{\partial E}\right)\frac{dE}{dt} + \left[P + \left(\frac{1}{2n}\mathcal{E}_{sf} + \frac{\gamma_f}{\phi}\cdot\frac{\nabla_s J_s}{J_s}\right) - \frac{\partial\Psi_s}{\partial\phi}\right]\frac{d\phi}{dt} \\ &\quad + \left[\frac{\phi}{S_r}\left(\frac{1}{2n}\mathcal{E}_{sf} + \frac{\gamma_f}{\phi}\cdot\frac{\nabla_s J_s}{J_s}\right) - \frac{\partial\Psi_s}{\partial S_r}\right]\frac{dS_r}{dt} \\ &\quad - \left[\frac{\gamma_f}{\phi S_r} + \frac{\partial\Psi_s}{\partial\nabla_s(\phi S_r)}\right]\cdot\frac{d\nabla_s(\phi S_r)}{dt} \geq 0, \end{aligned} \tag{3.87}$$

wherein variations of the state variables can occur independent of each other. Similar to classical approach, the following set of dual relations can

be obtained as state equations of the porous solid,

$$\frac{\partial \Psi_s}{\partial E} = S, \tag{3.88}$$

$$\frac{\partial \Psi_s}{\partial \phi} = P + \left(\frac{1}{2n}\mathcal{E}_{sf} + \frac{\gamma_f}{\phi}\cdot\frac{\nabla_s J_s}{J_s}\right), \tag{3.89}$$

$$\frac{\partial \Psi_s}{\partial S_r} = \frac{\phi}{S_r}\left(\frac{1}{2n}\mathcal{E}_{sf} + \frac{\gamma_f}{\phi}\cdot\frac{\nabla_s J_s}{J_s}\right), \tag{3.90}$$

$$\frac{\partial \Psi_s}{\partial \nabla_s(\phi S_r)} = -\frac{\gamma_f}{\phi S_r}. \tag{3.91}$$

Eq.(3.88) is classical in poromechanics giving rise to a constitutive relation for total stress tensor. Eqs.(3.89, 3.90) are reminiscent of the standard relations in unsaturated poromechanics (see Sec.(6.2.2) of Coussy (2004)) with additional contributions due to the hyper stress of the fluid, which itself is restricted through Eq.(3.91).

In fact, in the absence of gradients of fluid content, Eq.(3.90) reduces, allowing a direct comparison with the classical relation involving macroscopic capillary pressure, p_c, (Eq.(3.25)) as follows,

$$\frac{\partial \Psi_s}{\partial S_r} \approx \frac{\phi}{S_r}\frac{1}{2n}\mathcal{E}_{sf} = -\phi p_c = \phi\frac{\partial U}{\partial S_r}. \tag{3.92}$$

Assuming such comparison to be valid, Eqs.(3.89, 3.90) can be rephrased introducing p_c,

$$\frac{\partial \Psi_s}{\partial \phi} = P + -S_r p_c + \frac{\gamma_f}{\phi}\cdot\frac{\nabla_s J_s}{J_s}, \tag{3.93}$$

$$\frac{\partial \Psi_s}{\partial S_r} = -\phi p_c + \frac{\gamma_f}{\phi}\cdot\frac{\nabla_s J_s}{J_s}. \tag{3.94}$$

Generalized Darcy's law

Coming to the fluid dissipation, Eq.(3.83), a way to satisfy this restriction, which is a usual practice in poromechanics, is to assume that the dissipation is a quadratic function of fluid velocity vector, $V = M/\rho_w$, the coefficient of proportionality being the inverse of the second-order permeability tensor, $\mathbb{K}$. With such an assumption, M is constitutively restricted to

$$M = -\rho_w \mathbb{K}\cdot\left\{\frac{1}{S_r}\nabla_s P + \nabla_s\left[\nabla_s\cdot\left(\frac{\gamma_f}{\phi S_r}\right) + \frac{1}{S_r}\left(\frac{1}{2n}\mathcal{E}_{sf} + \frac{\gamma_f}{\phi}\cdot\frac{\nabla_s J_s}{J_s}\right)\right] - \frac{\mathfrak{b}_f}{\phi S_r}\right\}. \tag{3.95}$$

Introducing Eqs.(3.63, 3.70, 3.91 & 3.92) into the above results in a generalization of the unsaturated Darcy's law,

$$M = \rho_w V = -\rho_w \mathbb{K}\cdot\left\{\nabla_s\left[\frac{\partial \Psi_f}{\partial S_r} + \frac{\partial U}{\partial S_r} - \nabla_s\cdot\left(\frac{\partial \Psi_{NL}}{\partial \nabla_s(\phi S_r)}\right)\right] - \frac{\mathfrak{b}_f}{\phi S_r}\right\}. \tag{3.96}$$

In the case of isotropic porous medium the permeability tensor reduces: $\mathbb{K} = (\varkappa/\eta_w)K(S_r)I$, where $K(S_r)$ is called a flux function and is assumed to play an equivalent role as the relative permeability of wetting fluid $k_w(S_w)$ in classical partial saturation introduced in Sec.(3.1.5). This equivalency in part is justified due to the choice of the phase field parameter S_r as the saturation degree of the wetting fluid. With the above setup, the fluid dissipation in Eq.(3.83) now reads,

$$\Phi_f = \frac{\eta_w}{\varkappa\, K(S_r)}\frac{(M\cdot M)}{\rho_w^2} \geq 0. \tag{3.97}$$

This results in a restriction on the function $K(S_r)$ to be positive in order to ensure the positiveness of the dissipation associated to the fluid flow. Moreover, it is worth to note at this point that there is no restriction due to thermodynamic principles on the convexity of the function $K(S_r)$. The particular form employed for this function in the current work is motivated further in Chp.(4).

Towards a non-uniform pore fluid

Looking at Eq.(3.96), in the absence of a bulk force acting on the fluid, $\mathfrak{b}_f = 0$, the generalized force driving the flow is the negative spatial gradient of a chemical potential identified as,

$$\mu_{pf} = \frac{\partial \Psi_f}{\partial S_r} + \frac{\partial U}{\partial S_r} - \nabla_s \cdot \left(\frac{\partial \Psi_{NL}}{\partial (\nabla_s (\phi S_r))} \right), \tag{3.98}$$

where a new sub-script 'pf' is introduced that represents a supposed 'non-uniform pore fluid' that is understood as a non-uniform fluid, as introduced in Sec.(3.2.4), that is confined within a porous network characterized by the capillary energy $U(S_r)$. As usual in Cahn-Hilliard type modeling, this chemical potential, μ_{pf}, can be derived from the variational derivative w.r.t S_r of an overall free energy of the non-uniform pore fluid when $\phi = const$, i.e., when the porous skeleton is rigid. The density of such an overall free energy, Ψ_{pf}, in the current case can clearly be identified by the overall free energy density of the porous medium, Ψ, assuming a rigid porous skeleton given by,

$$\Psi_{pf} = \phi\, \Psi_f(S_r) + \phi\, U(S_r) + \Psi_{NL}(\nabla(\phi S_r)). \tag{3.99}$$

It is worth noting that unlike $\Psi_f(S_r)$, the local part of this new energy density, $(\Psi_f(S_r) + U(S_r))$, has no more a symmetric double-well structure between $S_r = 0$ and 1. Instead, the minimum associated to $S_r = 0$ no more exists and only one global minimum remains at $S_r = 1$. See Fig.(3.4). Moreover, depending on the relative intensities of bulk and capillary energy densities it is possible also that a minimum associated to lower S_r exists, but is shifted inwards of the original range of S_r thus changing the corresponding local preferential states at equilibrium. However, these two minima would not be isopotential. In both these cases, when the chemical potential is non-monotonic, Maxwell construction (equal-area rule) can be understood as a search for the line bi-tangent to this new energy density at equilibrium conditions of the non-uniform pore fluid. This is equivalent to construction of a linear potential due to external forces which once accounted for brings back the double-well structure with two isopotential minima. Now these two minima, both shifted inwards of original range of S_r, being isopotential allows for coexistence between the corresponding phases. The inward shift of the minima can be understood as a correction to account for wetting properties of the skeleton at equilibrium in the case of lower minimum and as a correction to account for trapped air in the case of higher minimum shifted from $S_r = 1$. Owing to this significance of physical interpretation, this local contribution in Eq.(3.99) is further referred to as the effective energy density, $\Psi_e(S_r) = \Psi_f(S_r) + U(S_r)$, of the non-uniform pore fluid and its partial derivative w.r.t S_r, the effective chemical potential, see Fig.(3.4),

$$\mu_e(S_r) = \frac{\partial \Psi_f}{\partial S_r} + \frac{\partial U}{\partial S_r} = \mu_f(S_r) - p_c(S_r). \tag{3.100}$$

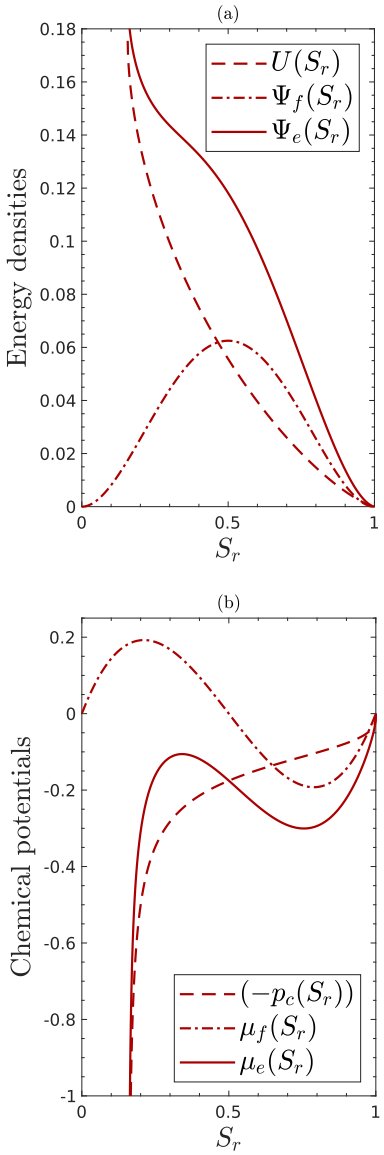

Figure 3.4: (a) The effective energy density is no more a symmetric double-well function. (b) The pure fluid phases are no more the isopotential minima of the effective energy density. All functions plotted are dimensionless according to the scheme presented in Chp.(4)

3.2.6 Extended Richards' equation: Rigid porous skeleton

Now that a framework resulting in thermodynamic restrictions has been recalled in sufficient detail, we move forward with simplifying assumptions. Restricting ourselves to the scope of the current thesis, we assume a rigid porous skeleton ($\phi = \phi_0 = \text{const}$) that is saturated with the non-uniform pore fluid. Such an assumption encompasses the hypothesis of small perturbations as already introduced in Sec.(3.1.4). Moreover we assume isotropic linear properties of the porous medium.

Assumption of a rigid porous skeleton allows one to neglect the power of external forces acting to deform the skeleton itself and consequently any power of internal forces acting to generate solid strains. So, any dissipative phenomena should be restricted to the fluid flow and interfacial changes. It is to be noted that with the introduction of the non-uniform pore fluid, the interfacial energy contributions, which were previously accounted for within the free energy of the porous solid, Eq.(3.80), are now part of Ψ_{pf}, given by Eq.(3.99). This allows to describe the dissipation within the system solely by flow of this non-uniform pore fluid through Eq.(3.96) and the evolution of S_r using the mass balance, Eq.(3.52). Both of these read respectively as follows under the said assumptions,

$$M = \rho_w V = -\rho_w \frac{\varkappa}{\eta_w} K(S_r) \cdot \left\{ \nabla \left[\frac{\partial \Psi_f}{\partial S_r} + \frac{\partial U}{\partial S_r} - \nabla \cdot \left(\frac{\partial \Psi_{NL}}{\partial \nabla(\phi S_r)} \right) \right] - \frac{\mathfrak{b}_f}{\phi S_r} \right\}, \tag{3.101}$$

$$\phi \frac{\partial S_r}{\partial t} + \nabla \cdot V = 0. \tag{3.102}$$

Similar to the developments in Sec.(3.1.8), an extension to Richard's equation, Eq.(3.50), can be derived in the current phase field context by substituting Eq.(3.101) into Eq.(3.102),

$$\phi \frac{\partial S_r}{\partial t} - \nabla \cdot \left(\frac{\varkappa}{\eta_w} K(S_r) \cdot \left\{ \nabla \left[\frac{\partial \Psi_f}{\partial S_r} + \frac{\partial U}{\partial S_r} - \nabla \cdot \left(\frac{\partial \Psi_{NL}}{\partial \nabla(\phi S_r)} \right) \right] - \frac{\mathfrak{b}_f}{\phi S_r} \right\} \right) = 0. \tag{3.103}$$

The appropriate boundary and initial conditions that supplement the above equation to form the BIVP are detailed further in Part II in specific contexts of imbibition and drainage.

3.3 SYNOPSIS

The current chapter serves as a basis for further developments in this thesis. The developments of Sec.(3.1) are utilized for the study mechanical instabilities through damage gradient modeling in Part III. The extended Richards' equation developed in the context of the phase field approach to partial saturation in Sec.(3.2) is analyzed in detail for it ability to predict fluid fingering phenomenon in Part II.

PART II
HYDRAULIC INSTABILITIES

4

ONE-DIMENSIONAL ANALYSIS: IMBIBITION & DRAINAGE

CONTENTS

4.1 Summary of the model - Governing equations 38
4.2 Dimensional analysis & scaling 39
4.3 Limit of vanishing diffusion & the flux function 40
4.4 PDE simulations 42
4.4.1 Imbibition 43
4.4.2 Drainage 45
4.5 Traveling wave analysis 49
4.5.1 Imbibition 50
4.5.2 Drainage 54
4.6 Synopsis 57

ABSTRACT

In the previous chapter a phase field approach has been introduced to treat partially saturation and an extended Richards' equation has been derived in the context of non-deformable porous skeleton. A one-dimensional analysis and resolution of solutions is presented in the current chapter for the extended Richards' equation. One-dimensional PDE simulations reveal that the model is able to describe both imbibition and drainage fronts when employing a non-convex flux function. Further these moving fronts are resolved using a traveling wave analysis thus setting the stage for a linear stability analysis against imposed perturbations which is the intent of the next chapter.

4.1 SUMMARY OF THE MODEL - GOVERNING EQUATIONS

The current analysis starts from the extended Richards' equation, Eq.(3.103), derived under the assumption of a rigid porous skeleton ($\phi = \phi_0 = \text{const}$). In soil hydrology and various other practical applications like CO_2 sequestration, the bulk force acting on the fluid is due to gravity. If we consider gravitational acceleration to be acting in the positive x-direction, then $\mathfrak{b}_f = m_f g e_x \approx \rho_w S_r \phi g e_x$ in accordance with Eq.(3.51). The structure of Eq.(3.103) closely resembles that of the classical Richards equation, Eq.(3.50). The difference lies in the constitutive prescription that lead to the particular expression of μ_{pf}, Eq.(3.98), compared to that of $p_c(S_w)$ in Eq.(3.50).

In what follows, a more general case is considered by introducing an additional linear pressure distribution which potentially allows to describe an initial uniform background mean flow. This state can then be perturbed by modifying the boundary conditions in order to investigate the evolution of either a drainage or an imbibition front. Thus an augmented chemical

potential incorporating both the effects of initial background mean flow and of gravity forces is written as,

$$\mu = \mu_{pf} + P, \tag{4.1}$$

where the pressure distribution $P = -\lambda x$. In the case when only gravity forces are considered P is just proportional to $\lambda = \rho_w g$. Both these scenarios may coexist in which case gravity can act to either stabilize or destabilize the motion of an air-water front depending on their relative directions.

Introducing the above mentioned augmented chemical potential, μ, the governing equation for S_r, Eq.(3.103), can be re-written as follows,

$$\phi \frac{\partial S_r}{\partial t} + \frac{\varkappa \lambda}{\eta_w} \frac{\partial K(S_r)}{\partial x} - \frac{\varkappa}{\eta_w} \nabla \cdot \left[K(S_r) \left(\nabla \mu_{pf} \right) \right] = 0, \tag{4.2}$$

with μ_{pf} given by Eq.(3.98) and reported again below for the sake of clarity,

$$\mu_{pf} = \frac{\partial \Psi_f}{\partial S_r} + \frac{\partial U}{\partial S_r} - \nabla \cdot \left(\frac{\partial \Psi_{NL}}{\partial (\nabla (\phi S_r))} \right). \tag{4.3}$$

The quantity $\varkappa\lambda/\eta_w$ [LT^{-1}] can be identified as the magnitude of a saturated mean velocity, V_m, in the porous medium. In essence this quantity represents the intensity of advection of non-uniform pore fluid, in other words that of the phase field parameter S_r. Appropriate boundary conditions will be introduced in Secs.(4.4.1 & 4.4.2) to close the problem.

4.2 DIMENSIONAL ANALYSIS & SCALING

The effective dimension of Eq.(4.2) is [T^{-1}]. To render the equation dimensionless the following dimensionless variables ($\tilde{.}$) and corresponding characteristic scaling numbers (sub-scripted 'h') are introduced:

$$\tilde{x} = \frac{x}{x_h}, \quad \tilde{\mu}_{pf} = \frac{\mu_{pf}}{p_h} = \frac{\mu_{pf} R}{C\gamma}, \quad \tilde{t} = \frac{t}{t_h} = \frac{t V_m}{x_h}. \tag{4.4}$$

The time scale is chosen to make unity the coefficient in front of advection term, $t_h = x_h/V_m$. And a particular grouping of parameters results in the dimensionless equation,

$$\phi \frac{\partial S_r}{\partial \tilde{t}} + \frac{\partial K(S_r)}{\partial \tilde{x}} - \frac{\delta_R}{C_a} \tilde{\nabla} \cdot \left[K(S_r) \left(\tilde{\nabla} \tilde{\mu}_{pf} \right) \right] = 0. \tag{4.5}$$

The dimensionless effective chemical potential of the non-uniform pore fluid, $\tilde{\mu}_{pf}$, along with the linear pressure contribution, $\tilde{P}$, can be written, employing the particular expressions introduced in Secs.(3.1.5 & 3.2.4), as,

$$\begin{aligned} \tilde{\mu} &= \tilde{\mu}_{pf} + \tilde{P} \\ &= 2S_r \left(1 - 3S_r + 2S_r^2 \right) - D_U \left(\left(\frac{S_r - S_r^{res}}{1 - S_r^{res}} \right)^{-\frac{1}{m}} - 1 \right)^{1-m} \\ &- D_{NL} \tilde{\nabla} \cdot \left(\tilde{\nabla} (\phi S_r) \right) - \frac{C_a}{\delta_R} \tilde{x}. \end{aligned} \tag{4.6}$$

The dimensionless numbers C_a, δ_R , D_U and D_{NL} are identified as follows:

$$\begin{aligned} C_a &= \frac{V_m \eta_w R^2}{\varkappa C\gamma}, \quad \delta_R = \frac{R}{x_h}, \\ D_U &= \frac{\pi_0 R}{C\gamma}, \quad D_{NL} = \frac{C_k R}{C\gamma x_h^2} = \frac{\pi_k R}{C\gamma} \left(\frac{\ell}{x_h} \right)^2. \end{aligned} \tag{4.7}$$

Here, C_a is the Capillary number signifying the competition between viscous forces and capillary forces at the air-water interface. δ_R is the ratio of characteristic radius of porous channels to the reference length scale. D_U is a measure of relative strength of the coefficients of capillary interfacial energy and the air-water interfacial energy. And D_{NL} is the so-called Cahn number, signifying intensity of the gradient energy with respect to the diffusive term. Above in Eq.(4.7) it is shown that the expression of D_{NL} can be recast such that the interface thickness, ℓ, is introduced into the equations and a free parameter, π_k [$\mathrm{ML^{-1}T^{-2}}$], appears. This allows an input to the model from experimental measurements of observed macroscopic transition lengths. Further in this work, the length scale, x_h, is chosen to be the characteristic physical length of the domain under consideration. These choices are shown further to produce transition lengths of order ℓ in the numerical solutions when flow is driven by gravity. The full dimensionless form using Eq.(4.6) in Eq.(4.5), with the above choices of dimensionless numbers is as follows,

$$\begin{aligned}\phi\frac{\partial S_r}{\partial t}+\frac{\partial K(S_r)}{\partial x}-\frac{\delta_R}{C_a}\nabla\cdot\Bigg[K(S_r)\Bigg(\nabla\Bigg[2S_r\left(1-3S_r+2S_r^2\right)\\ -D_U\left(\left(\frac{S_r-S_r^{res}}{1-S_r^{res}}\right)^{-\frac{1}{m}}-1\right)^{1-m}\Bigg]-D_{NL}\nabla\Delta(\phi S_r)\Bigg)\Bigg]=0.\end{aligned} \tag{4.8}$$

It is to be noted that $(\tilde{.})$ has been dropped in Eq.(4.8) and is done so further in this work. So, from this point all the variables are dimensionless unless either mentioned otherwise or referred to from earlier sections.

4.3 LIMIT OF VANISHING DIFFUSION & THE FLUX FUNCTION

In the work of Saffman and Taylor (1958), a fundamental study of the stability of fluid-fluid interface has been done in an analogous Hele-Shaw flow context. In order to perform this, an horizontal sharp interface has been assumed to separate two fluids of different viscosities moving within a Hele-Shaw cell, under the forces of gravity and pressure gradient. Upon this horizontal interface, wave like disturbances of variable wavelengths have been assumed and their growth in time has been understood as the typical fingering instability. Furthermore, surface tension has been shown to introduce a lower bound for the range of wavelengths of disturbances for which the interface is unstable.

It our intention here, to characterize within the framework of the adopted model, propagation of an air-water interface both in the case of imbibition and in drainage. And in the Chp.(5) the stability/instability of these interfaces will be investigated. Therefore, as a first step transversely homogeneous solutions of Eq.(4.8) that represent such interfaces need to be built.

In this section we observe that solutions assuming transverse homogeneity in y and z-directions but evolving longitudinally along x-coordinate, are composed of similarity solutions of the one-dimensional equation

$$\begin{aligned}\phi\frac{\partial S_r}{\partial t}+\frac{\partial K(S_r)}{\partial x}-\frac{\delta_R}{C_a}\frac{\partial}{\partial x}\left(K(S_r)\mu_e'(S_r)\frac{\partial S_r}{\partial x}\right)\\ +\frac{\delta_R}{C_a}\phi D_{NL}\frac{\partial}{\partial x}\left(K(S_r)\frac{\partial^3 S_r}{\partial x^3}\right)=0.\end{aligned} \tag{4.9}$$

In the above, the definition of effective chemical potential of non-uniform pore fluid, $\mu_e(S_r)$ (Eq.(3.100)), is invoked. $(.)'$ denotes a partial derivative w.r.t S_r throughout this Part II.

At larger spatial scales compared to both the length scale of the air-water interface and that of diffusion, the solutions of Eq.(4.9) are regularized solutions of the corresponding scalar hyperbolic conservation law (LeFloch, 2002) in the limit of vanishing diffusion. Assuming such limit, Eq.(4.9) simplifies as

$$\phi \frac{\partial S_r}{\partial t} + \frac{\partial K(S_r)}{\partial x} = 0. \tag{4.10}$$

Here, the function $K(S_r)$ plays the role of an advective flux. A class of weak solutions of a Riemann problem governed by Eq.(4.10), given a piece-wise uniform initial condition with a jump between S_- and S_+ at $x = 0$, that represent sharp displacement of one fluid by another, are piece-wise uniform functions known as shocks,

$$S_r(x,t) = \begin{cases} S_- & if \quad x < ct \\ S_+ & if \quad x > ct, \end{cases} \tag{4.11}$$

that move with a characteristic speed, c. These solutions are self-similar in nature with respect to the transformation $\xi = x - ct$ and propagate along the x-coordinate while satisfying the Rankine-Hugoniot jump condition,

$$K(S_+) - K(S_-) = c\phi(S_+ - S_-), \tag{4.12}$$

that relates the speed of the shock wave to the uniform solution values on either side of the shock. A shock is considered classical or 'compressive' if the characteristics on either side of the shock impinge onto it. This condition is given by the celebrated Lax Entropy condition, which in the current case can be written as

$$K'(S_+) \leqslant \phi c \leqslant K'(S_-). \tag{4.13}$$

Apart from shocks, the class of smooth monotone weak solutions of the Riemann problem governed by Eq.(4.10) are rarefaction waves connecting S_- to S_+. These solutions are expansive and self-similar with respect to the transformation $\xi = x/t$. These are described by the following form:

$$S_r(x,t) = \begin{cases} S_- & if \quad \phi x < t\, K'(S_-) \\ K'^{-1}(\phi x/t) & if \quad t\, K'(S_-) < \phi x < t\, K'(S_+) \\ S_+ & if \quad \phi x > t\, K'(S_+). \end{cases} \tag{4.14}$$

When the flux function, $K(S_r)$, is purely convex and increasing, the only possible weak solutions are either classical shocks (if $S_- > S_+$) or rarefaction waves (if $S_- < S_+$) and analogously for purely concave flux function (LeFloch, 2002). In the presence of diffusion these sharp classical shock solutions satisfying Eq.(4.13), tend to be smeared up to a finite distance. On the other hand, for flux functions that have inflection points the structure of solutions is much more rich in the presence of higher order diffusion/dispersion. For instance smeared shock solutions that violate Eq.(4.13) can exist, which are considered to be non-classical (Bertozzi et al., 1999; Hayes and Shearer, 1999). The class of non-classical shocks for which the characteristics on either side pass through the shock are termed 'under-compressive' (Dukler et al., 2020) and they satisfy either of

$$K'(S_\pm) \leqslant \phi c \; ; \quad K'(S_\pm) \geqslant \phi c. \tag{4.15}$$

And those for which the characteristics behind and in the front seem to expand the shock itself are termed 'expansion' shocks (El et al., 2016) and they violate Eq.(4.13) as

$$K'(S_-) \leqslant \phi c \leqslant K'(S_+). \tag{4.16}$$

Presence of these solutions and their manifestation as traveling waves in the solution structure of imbibition and drainage problems governed by Eq.(4.9) are shown in the following section. Further in Sec.(4.5), the traveling wave part of these solutions are resolved in a one-dimensional setting.

As mentioned earlier, the nature of the flux function, $K(S_r)$, has an important effect on the structure of solutions that represent air-water displacements. In classical partial saturation, Sec.(3.1), the role of modulating the individual fluid velocities in space accordingly to their respective saturation degree is played by the relative permeability function. In the current study we intend to use the functional form of such a relative permeability of water for the flux function, owing to the phase field parameter, S_r, of the current model being representative of the saturation degree of water.

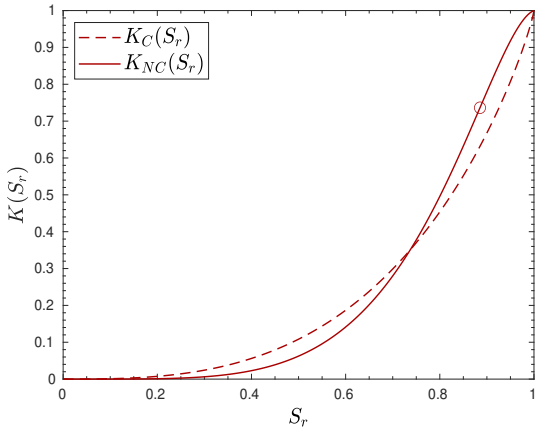

Figure 4.1 – Relative permeability functions $K(S_r)$, Eq.(4.17), for different values of van Genuchten parameters (a, b, c). K_C:$(1.175, 0.85, 2.0)$, K_{NC}:$(8.0, 2.0, 0.5)$. Inflection point is shown as a circle on curve $K_{NC}(S_r)$.

Typically unsaturated relative permeability functions used for various soils and fluid combinations are parametric models in order to fit experimental data. Especially in soil hydrology when fluid combination is water and wet air the well known van Genuchten model is widely use as introduced in Sec.(3.1.5). The expression of relative permeability of wetting fluid is recapitulated below with a change of notations for convenience,

$$K(S_r) = \sqrt{S_r}\left[1 - (1 - {S_r}^a)^b\right]^c, \tag{4.17}$$

where a, b and c are real constants obtained through fitting with experimental results. As can be seen in Fig.(4.1), this functional form has the possibility to model a purely convex behavior, $K_C(S_r)$, and as well a convex-concave behavior, $K_{NC}(S_r)$. In what follows, in order to account for consolidation of the porous skeleton (Bear, 1972) and to demonstrate in the context of the current phase field model the possibility of modeling air-water displacements representing both imbibition and drainage, we employ the convex-concave function, $K(S_r) = K_{NC}(S_r)$, with $a = 8.0$, $b = 2.0$ and $c = 0.5$.

4.4 PDE SIMULATIONS

In the current section we characterize the spatio-temporal evolution of solutions both in imbibition and drainage scenarios. To do this we choose the primary unknowns as the Saturation degree, S_r, and the regularized effective chemical potential with known spatially linear pressure contribution, μ. Then the coupled system of equations formed by Eq.(4.5) and Eq.(4.6) is

resolved. We acknowledge at this point that since our focus is to analyze the general structure and evolution of the solutions, we have adopted a simplest numerical discretization. One can definitely extend this to more sophisticated techniques of the likes of adaptive refinement (Martin et al., 2005; Boyer et al., 2009) and non-local operator methods (Ren et al., 2021).

Spatial discretization is done employing a standard Galerkin formulation and linear Lagrange finite elements. Time discretization is done using the implicit Euler scheme of first-order. The discrete solutions at n^{th} time step, S_r^n and μ^n, are obtained by searching in the Hilbert space of admissible functions given by the Cartesian product $\mathcal{H}_s \times \mathcal{H}_\mu$, with

$$\begin{aligned} \mathcal{H}_s &:= \left\{ S_r^n \in H^1(\Omega) : S_r^n = \bar{S}_r^n \ on \ \partial\Omega_s \right\} \\ \mathcal{H}_\mu &:= \left\{ \mu^n \in H^1(\Omega) : \mu^n = \bar{\mu}^n \ on \ \partial\Omega_\mu \right\} \end{aligned} \tag{4.18}$$

defined over the discretized domain Ω, so that the ordered couple (S_r^n, μ^n) solve the non-linear coupled variational system,

$$\begin{aligned} &\int_\Omega \widehat{q} \left(\frac{\phi \left(S_r^n - S_r^{n-1} \right)}{\Delta t} \right) d\Omega + \int_\Omega \frac{\delta_R}{C_a} K(S_r^n) \left(\nabla \widehat{q} \cdot \nabla \mu^n \right) d\Omega \\ &\qquad - \int_{\Omega_{N\mu}} \widehat{q} \left(\frac{\delta_R}{C_a} K(S_r^n) \nabla \mu^n \right) \cdot \widehat{n} \, d\Omega_{N\mu} = 0, \\ &\int_\Omega \widehat{S} \left(\mu^n - \mu_e(S_r^n) + \frac{C_a}{\delta_R} x \right) d\Omega - \int_\Omega \phi D_{NL} \left(\nabla \widehat{S} \cdot \nabla S_r^n \right) d\Omega \\ &\qquad + \int_{\Omega_{Ns}} \widehat{S} \left(\phi D_{NL} \nabla S_r^n \right) \cdot \widehat{n} \, d\Omega_{Ns} = 0. \end{aligned} \tag{4.19}$$

Here $\widehat{q}$ and $\widehat{S}$ are test functions belonging to the Hilbert space $(\mathcal{H}_s)_0 \times (\mathcal{H}_\mu)_0$ of functions which vanish on $\partial\Omega_s$ and $\partial\Omega_\mu$ where the values of S_r and μ are specified respectively. $\widehat{n}$ is the outward unit normal vector to the boundary where it is referred to. $\Omega_{N\mu}$ is the part of the boundary where normal derivative of μ is specified, which translates to imposing at that part of the boundary an injection or extraction velocity of the fluid with a natural form,

$$V_f \Big|_{\Omega_{Ns}} = -\frac{\delta_R}{C_a} K(S_r) \nabla \mu. \tag{4.20}$$

Ω_{Ns} is part of the boundary where normal derivative of S_r is specified. For one-dimensional simulations the computational domain is chosen along the positive x-direction such that $x \in [0, 1]$. The corresponding physical length, $L = 100$m, is chosen to be sufficiently large such that the analysis is satisfactorily close to the limit of vanishing diffusion mentioned earlier. The material properties of the porous medium and the parameters of the model chosen for the purpose of demonstration are listed in Table.(4.1), which are in the range typical of silica sands saturated with air-water mixture. The corresponding dimensionless numbers defined in Sec.(4.2) are listed in Table.(4.2).

Mesh convergence behavior has been tested, once chosen initial and boundary conditions corresponding to an imbibition and a drainage problem, which are elaborated in Secs.(4.4.1 & 4.4.2), to validate the numerical solution. In particular successively refined discretization steps have been considered. The results of this analysis are reported in Appendix A1.

Table 4.1: Material properties, model parameters used through Part II, unless mentioned otherwise.

property/ parameter	Sand
$\varkappa$ [m^2]	1.0E-12
η_w [Pa.s]	8.9E-04
ϕ [−]	0.37
C [−]	0.5
γ [N.m^{-1}]	0.073
R [m]	1.64E-06
π_0 [Pa]	2840.91
m [−]	0.685
S_r^{res} [−]	0.1567
C_k [N]	113.66
ℓ [m]	0.2

Table 4.2: Dimensionless numbers corresponding to the material properties and model parameters in Table.(4.1) used through Part II, unless mentioned otherwise.

Dimensionless number	Value
C_a	7.4E-07
δ_R	1.64E-08
D_U	0.128
D_{NL}	5.12E-07

4.4.1 Imbibition

Displacement of air by water representing imbibition can be understood as a solution which transitions from a higher degree of saturation to a lower

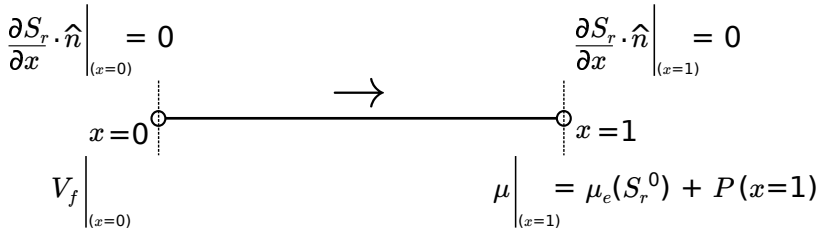

Figure 4.2: Schematic of the imbibition simulations showing boundary conditions applied on the one-dimensional domain. The arrow indicates the direction of motion of the self-similar interface. The form of natural boundary condition $V_f(x=0)$ is given in Eq.(4.21).

one and moves in the direction of the lower saturation. According to characteristic water retention properties of the porous skeleton, see Table.(4.1), the appropriate initial condition for imbibition is set to $S_r^0 = 0.20$ throughout the domain, which is close to the residual saturation, S_r^{res}, and $\mu^0 = \mu_{pf}(S_r^0) + P$. For all $t > 0$, the normal derivative of S_r is set to vanish at both the boundaries, $x = 0$ and $x = 1$. See schematic Fig.(4.2). At the left boundary an injection velocity,

$$V_f\Big|_{(x=0)} = -\frac{\delta_R}{C_a}K(S_-)\nabla P = K(S_-)e_x, \tag{4.21}$$

is imposed. This has an effect of perturbing the saturation degree at the left boundary towards $S_- > S_r^0$, inducing imbibition, while the normal derivative of μ_{pf} vanishes. The boundary at the right, $x = 1$, is drained with a Dirichlet boundary condition on μ such that,

$$\mu\Big|_{(x=1)} = \mu_e(S_r^0) + P(x=1). \tag{4.22}$$

The results of simulations for various values of S_- and $\lambda = \rho_w g$ are shown in Fig.(4.3). The diffused interface in the solution connecting a higher value of S_r to a lower value represents the infiltration of water into a fluid-poor domain under the presence of gravity acting in the positive x-direction. The profile within the domain, of the regularized effective chemical potential, μ_{pf}, follows that of the S_r solution according to Eq.(3.98), with a strong gradient effect due to the interface. While all the saturation profiles are non-monotonic in the vicinity of S_r^0, there exist overshoot and non-overshoot behaviors behind the invading front. The reasoning for presence or absence

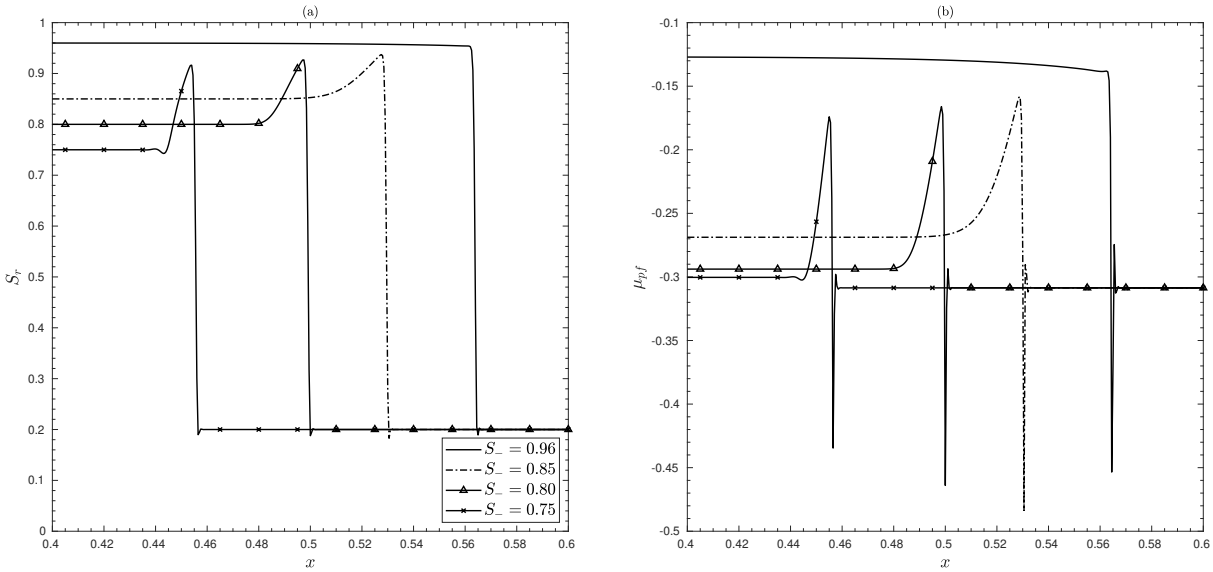

Figure 4.3: One dimensional imbibition solutions of the coupled system Eq.(4.19), for $\lambda = \rho_w g$, with initial condition $S_r^0 = 0.20$ and boundary conditions corresponding to a constant rate of injection Eq.(4.21) with $S_- = 0.96, 0.85, 0.80, 0.75$, Δt = 1E-05, Δx = 5E-04, (a) Saturation degree, S_r, (b) regularized effective chemical potential, μ_{pf}. Solutions are shown at different time-steps and restricted spatial range for clarity. Out of this range, solutions are continuous and uniform extensions up to their respective boundary conditions.

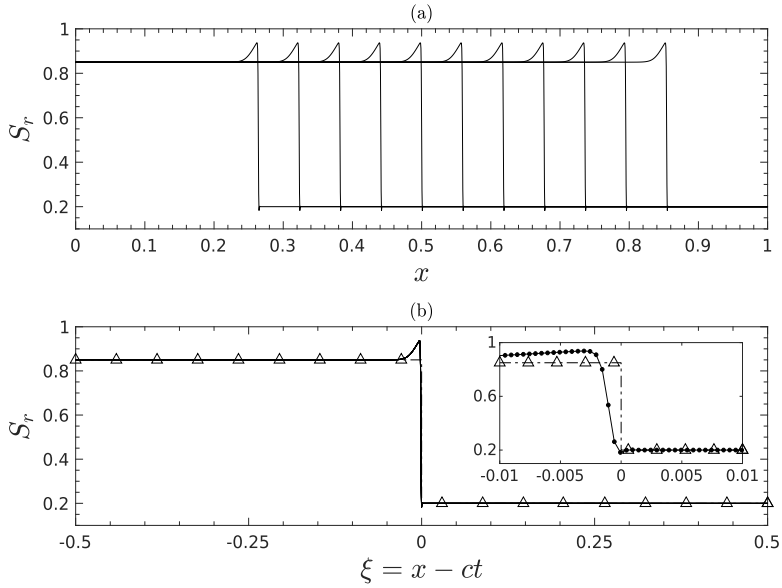

Figure 4.4: One dimensional imbibition solution S_r of the coupled system Eq.(4.19), for $\lambda = \rho_w g$, $S_r^0 = 0.20$ and $S_- = 0.85$; (a) Solution at various time steps, (b) Solutions in (a) transformed into the TW-coordinate $\xi = x - ct$ with $c \approx 2.63$ given by Eq.(4.12). Shock solution, Eq.(4.11), for $S_- = 0.85$ and $S_+ = S_r^0 = 0.20$ is shown with triangle markers. Inset in (b) shows the solution, now with the finite element nodes depicted as black dots, and the shock solution in the immediate vicinity of $\xi = 0$.

of such overshoots and the oscillatory behavior around S_r^0 is reserved for analysis in the further sections.

However, in all these solutions the transition from S_- to S_r^0 seems to translate self-similarly in space suggesting the presence of traveling wave type higher order approximations of shock solutions. This observation is justified by a transformation into a TW-coordinate, $\xi = x - ct$, where c is given by Eq.(4.12) with $S_+ = S_r^0$, see Fig.(4.4). This results in the transition region of the solution to collapse into the vicinity of a single location, $\xi = 0$. The self-similar shock solution, Eq.(4.11), of the hyperbolic equation, Eq.(4.10), as well is plotted in the same TW-coordinate in Fig.(4.4). In Sec.(4.5.1) these TW-solutions are resolved and are shown to be classical or compressive in the sense of shocks.

4.4.2 Drainage

Drainage of water by air is understood as the contrary of imbibition, which is a transition from lower saturation degree to higher, moving in the direction of the higher saturation. So the initial condition is chosen as $S_r^0 = 0.99$ which is close to fully saturated condition, and $\mu^0 = \mu_{pf}(S_r^0) + P$. Owing to the phase field parameter, S_r, of the current model being representative of the saturation degree of water, an injection flux of the form Eq.(4.20) at the boundary would not be appropriate to induce drainage. Instead the initial condition is perturbed at the left boundary, $x = 0$, by imposing gradually decreasing Dirichlet boundary conditions on S_r and μ until the intended air saturation, S_r^d and $\mu^d = \mu_e(S_r^d)$ are achieved within a finite time, t_d, and then those boundary conditions are kept constant for all $t > t_d$. See schematic Fig.(4.5). The boundary at $x = 1$ is drained with a Dirichlet boundary condition on μ, Eq.(4.22), and the normal derivative of S_r is set to vanish for all $t > 0$ similar to the imbibition case.

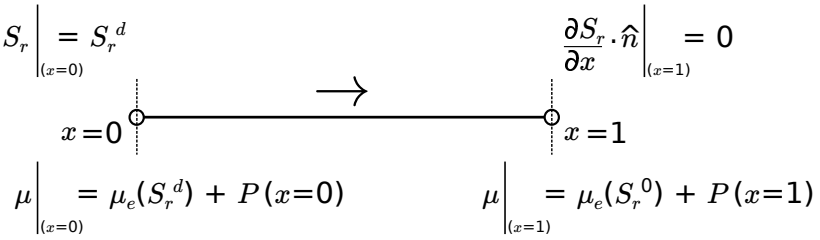

Figure 4.5: Schematic of the drainage simulations showing boundary conditions applied on the one-dimensional domain for $t > t_d$. The arrow indicates the direction of motion of the self-similar interface.

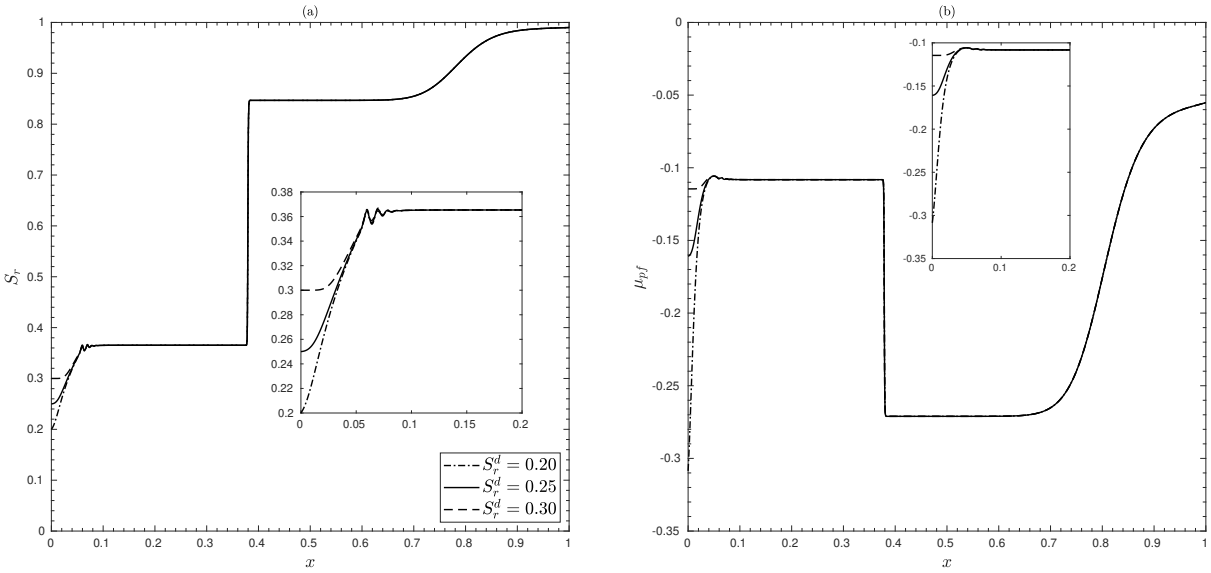

Figure 4.6: One dimensional drainage solutions of the coupled system Eq.(4.19), for $\lambda = \rho_w g$, with initial condition $S_r^0 = 0.99$ and boundary conditions corresponding to drainage reaching $S_r^d = 0.20, 0.25, 0.30$ in $t_d = 100\Delta t$, with Δt = 1E-05, Δx = 5E-04, (a) Saturation degree, S_r, with the pair of intermediate states $(S_a, S_b) \approx (0.847, 0.365)$, (b) regularized effective chemical potential, μ_{pf}. Solutions are shown at the same time-step. Insets focus on the oscillatory junction between the bottom rarefaction wave and the uniform solution state (a) $S_b \approx 0.365$, (b) $\mu_e(S_b)$.

Fig.(4.6) shows the solutions for various values of S_r^d and $\lambda = \rho_w g$. We note that the solution at later times is composed of an expanding part connecting S_r^d to a uniform state, S_b, which is then connected by a sharper transition to another uniform state S_a. S_a then connects to S_r^0 through a second expanding part. It is interesting to observe that for all values of S_r^d chosen, the solution settles down to the same values of $S_a \approx 0.847$ and $S_b \approx 0.365$, see Fig.(4.6). The solution, μ_{pf}, has a similar structure with uniform states corresponding to $\mu_e(S_a)$ and $\mu_e(S_b)$ with a diffused transition in between.

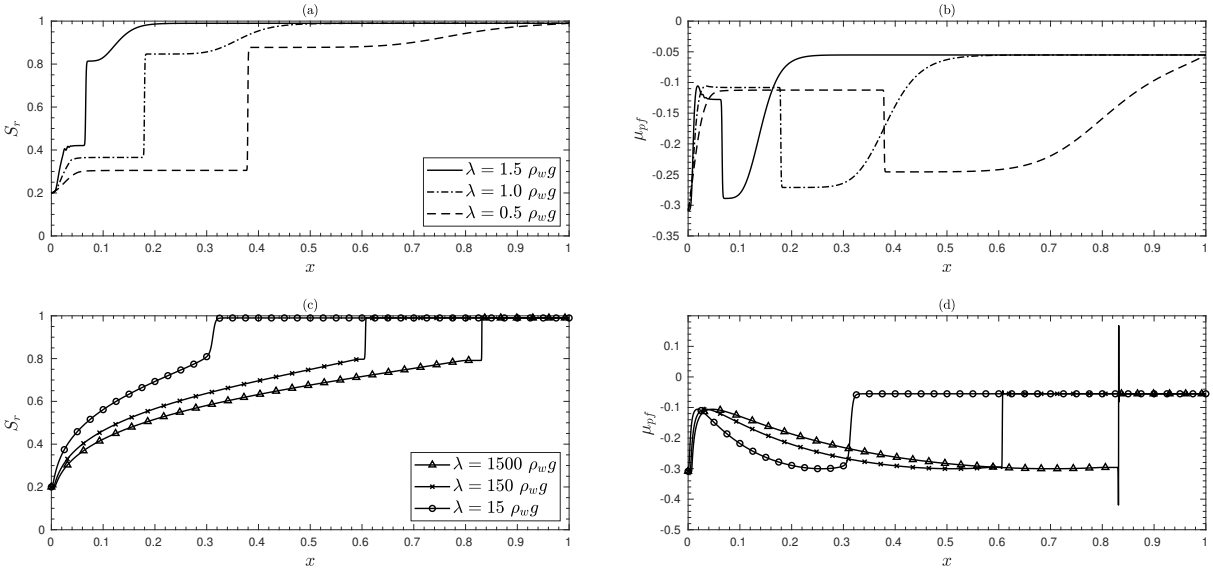

Figure 4.7: One dimensional drainage solutions of the coupled system Eq.(4.19), with initial condition $S_r^0 = 0.99$ and boundary conditions corresponding to drainage reaching $S_r^d = 0.20$, in $t_d = 100\Delta t$, with $\lambda = 0.5\rho_w g, \rho_w g, 1.5\rho_w g$, Δt = 1E-05, Δx = 5E-04, (a) Saturation degree, S_r, with pairs of intermediate states, in the same order as that of λ values, $(S_a, S_b) \approx (0.878, 0.305), (0.847, 0.365), (0.814, 0.421)$, (b) regularized effective chemical potential, μ_{pf}; And with $\lambda = 15\rho_w g, 150\rho_w g, 1500\rho_w g$, Δt = 1E-06, Δx = 1E-04, (c) Saturation degree, S_r, with the intermediate states $S_b \approx 0.797, 0.791$ for $\lambda = 150\rho_w g, 1500\rho_w g$ respectively, (d) regularized effective chemical potential, μ_{pf}; Solutions are shown at different time-steps for clarity.

Akin to the imbibition case, the sharper transitions between S_b and S_a translate self-similarly in space. See, Fig.(4.8(b)) where one of the solutions from Fig.(4.6) is plotted in the TW-coordinate $\xi = x - ct$, where c is given by Eq.(4.12) with $S_- = S_b$ and $S_+ = S_a$. The transition region collapses into the vicinity of $\xi = 0$ as expected for the associated shock solution, Eq.(4.11), which is also plotted. The corresponding TW-solutions of Eq.(4.9) will be looked for in Sec.(4.5.2), which are shown to be non-classical in the sense of shocks violating the entropy condition such that Eq.(4.16).

The expanding parts of the solution in front of and behind the sharper transition do not translate in the same fashion. Under a transformation of variable $\xi = x/t$, the part connecting S_r^d to S_b tends to collapse into the corresponding rarefaction solution, Eq.(4.14), of the hyperbolic equation, Eq.(4.10), with $S_- = S_r^d$ and $S_+ = S_b$, see Fig.(4.8(c)). In fact the flux function is convex within the interval $(S_-, S_+) = (S_r^d, S_b) = (0.20, 0.365)$ and since $S_- < S_+$ the rarefaction wave that is observed is expected. On the other hand, it can be observed that for the same transformation the part connecting S_a to S_r^0 does not collapse into a similarity type solution. In fact, the flux function is non-convex within the interval $(S_a, S_r^0) = (0.847, 0.99)$ and so a rarefaction wave with $S_- = S_a$ and $S_+ = S_r^0$ is not an associated weak solution.

At the junction of the expanding part of the solution and the uniform state, S_b, longitudinal oscillations are observed which seem to grow with time, see Fig.(4.6). It is explained in Sec.(4.5.2) with the help of dynamical systems analysis that these oscillations are triggered due to the nature of the equilibrium state associated to S_b. The growth of such oscillations with time on the other hand, is justified in Chp.(5) by analyzing the linear stability of one-dimensional uniform saturation states against longitudinal perturbations.

The overall solution structure represents a drainage scenario in which ahead of the macroscopic air-water interface, the air phase can start invading the pores. And behind such interface there exists a uniform saturation state of the water phase corresponding to S_b, that is not displaced.

Now, for $S_r^d = 0.20$, we vary λ, see Fig.(4.7). For lower values of $\lambda = 0.5\rho_w g, 1.5\rho_w g$, and thus of C_a, the solution structure is similar to that of $\lambda = \rho_w g$ with two intermediate uniform states S_a and S_b appearing at later times. However, for relatively higher values of $\lambda = 150\rho_w g$, $1500\rho_w g$ a single uniform state, $S_b \approx 0.797, 0.791$ respectively, appears which connects to the right directly to S_r^0 through a sharper transition representing the air-water front. This intermediate state, S_b, connects to S_r^d to the left through an expanding part. The regularized effective chemical potential, μ_{pf}, follows a similar structure in accordance with Eq.(4.3).

A transformation into the TW-coordinate $\xi = x - ct$, where c is given by Eq.(4.12) with $S_- = S_b$ and $S_+ = S_r^0$ reveals the self-similar nature of the sharper transition, see Fig.(4.9(b)). In Sec.(4.5.2) the corresponding TW-solutions of Eq.(4.9) will be looked which are also non-classical in the sense of shocks violating the entropy condition such that Eq.(4.15). Whereas under a transformation of variable $\xi = x/t$, the part connecting S_r^d to S_b tends to collapse into the corresponding rarefaction solution, Eq.(4.14), of the hyperbolic equation, Eq.(4.10), with $S_- = S_r^d$ and $S_+ = S_b$, see Fig.(4.9(c)).

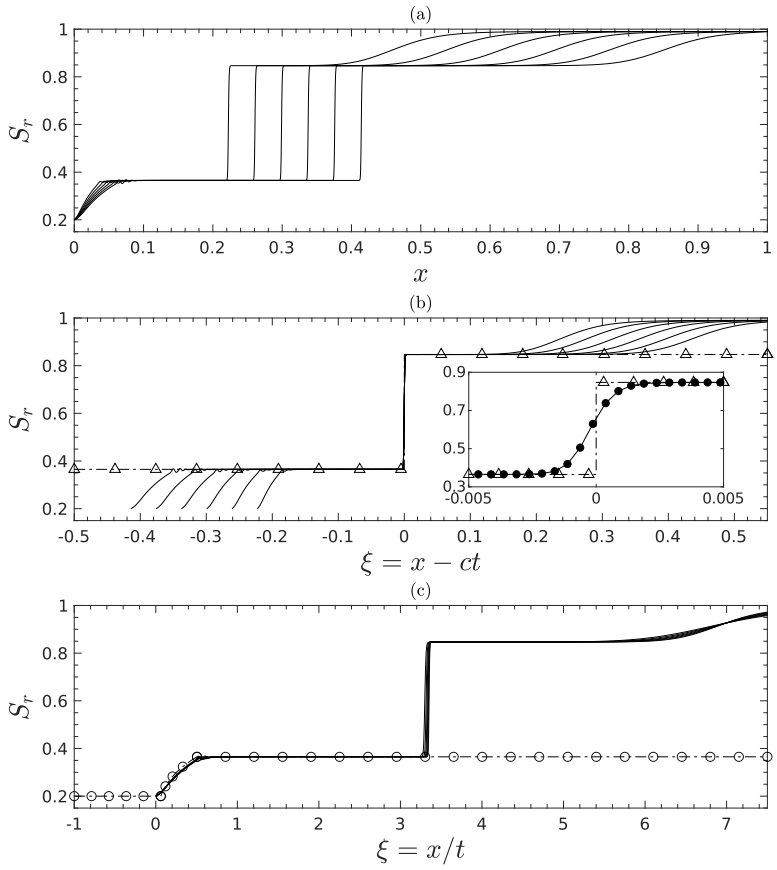

Figure 4.8: One dimensional drainage solution S_r of the coupled system Eq.(4.19), for $\lambda = \rho_w g$, $S_r^0 = 0.99$ and $S_r^d = 0.20$; (a) Solution at various time steps, (b) Solutions in (a) transformed into the TW-coordinate $\xi = x - ct$ with $c \approx 3.41$ given by Eq.(4.12). Shock solution, Eq.(4.11), for $S_- = S_b \approx 0.365$ and $S_+ = S_a \approx 0.847$ is shown with triangle markers. Inset in (b) shows the solution, now with the finite element nodes depicted as black dots, and the shock solution in the immediate vicinity of $\xi = 0$. (c) Solutions in (a) transformed into the coordinate $\xi = x/t$. Rarefaction solution, Eq.(4.14), for $S_- = S_r^d$ and $S_+ = S_b \approx 0.365$ is shown in circle markers.

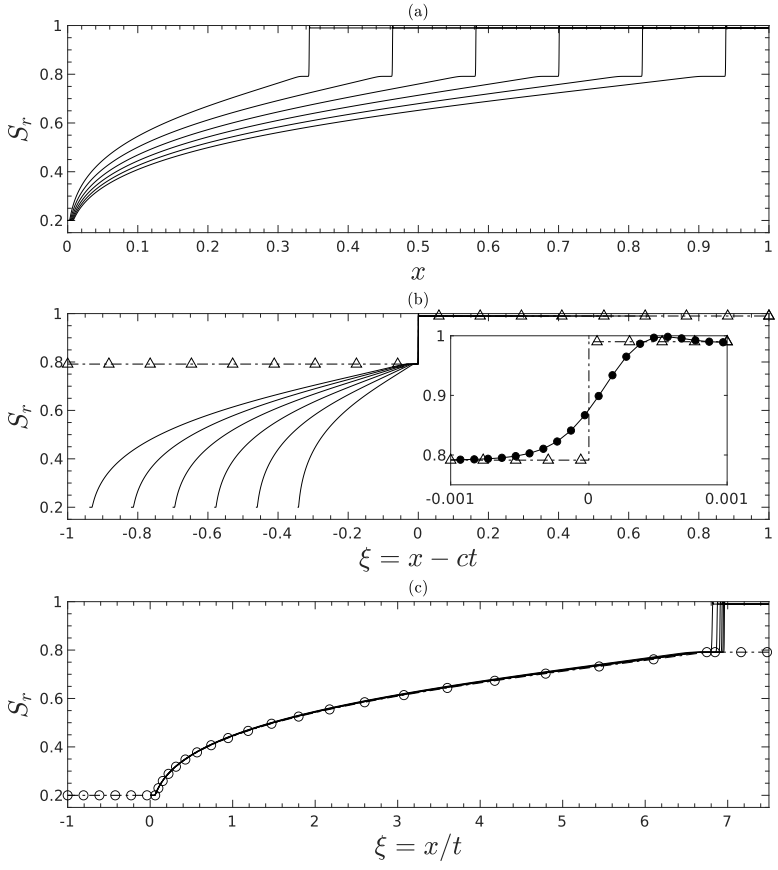

Figure 4.9: One dimensional drainage solution S_r of the coupled system Eq.(4.19), for $\lambda = 1500\rho_w g$, $S_r^0 = 0.99$ and $S_r^d = 0.20$; (a) Solution at various time steps, (b) Solutions in (a) transformed into the TW-coordinate $\xi = x - ct$ with $c \approx 7.05$ given by Eq.(4.12). Shock solution, Eq.(4.11), for $S_- = S_b \approx 0.791$ and $S_+ = S_r^0 = 0.99$ is shown with triangle markers. Inset in (b) shows the solution, now with the finite element nodes depicted as black dots, and the shock solution in the immediate vicinity of $\xi = 0$. (c) Solutions in (a) transformed into the coordinate $\xi = x/t$. Rarefaction solution, Eq.(4.14), for $S_- = S_r^d$ and $S_+ = S_b \approx 0.791$ is shown in circle markers.

4.5 TRAVELING WAVE ANALYSIS

In this section we intend to resolve the TW part of the solutions observed in Sec.(4.4). With this intent we make a transformation of the independent variables into a moving coordinate,

$$S_r(x,t) = s(x-ct) = s(\xi) \qquad \forall x \in \Re \; ; \; \forall t > 0. \tag{4.23}$$

Where the TW-solution, $s(\xi)$, and speed, c, are a priori not known. The TW-coordinate, ξ, is assumed to have the same speed as that of a shock representative of the transition within the solution $S_r(x,t)$. And so the TW-solution is independent of time and the transition within it is always centered at $\xi = 0$. Introducing Eq.(4.23) into Eq.(4.9) yields an ordinary differential equation (ODE) that $s(\xi)$ needs to satisfy:

$$-\phi c\frac{ds}{d\xi} + \frac{dK(s)}{d\xi} - \frac{\delta_R}{C_a}\frac{d}{d\xi}\left(K(s)\mu_e'(s)\,\frac{ds}{d\xi}\right) + \frac{\delta_R}{C_a}\phi D_{NL}\frac{d}{d\xi}\left(K(s)\,\frac{d^3s}{d\xi^3}\right) = 0, \tag{4.24}$$

The existence of such traveling wave type similarity solutions for Eq.(4.9) can qualitatively explain part of the complete saturation solution, $S_r(x,t)$, ranging between the two uniform states (see figures in Sec.(4.4)). In other words the TW-solution, $s(\xi)$, of Eq.(4.24) can represent a branch of the PDE solution $S_r(x,t)$, with the corresponding boundary conditions on an infinite domain:

$$\begin{aligned} s\Big|_{(\xi=+\infty)} &= s_+\,, \quad \frac{ds}{d\xi}\Big|_{(\xi=+\infty)} = 0, \\ s\Big|_{(\xi=-\infty)} &= s_-\,, \quad \frac{ds}{d\xi}\Big|_{(\xi=-\infty)} = 0. \end{aligned} \tag{4.25}$$

Integrating Eq.(4.24) once w.r.t ξ, using the boundary conditions at $\xi = +\infty$ and assuming higher derivatives of the solution vanish as $\xi \to +\infty$ yields in a canonical form:

$$\frac{d^3s}{d\xi^3} = \frac{C_a}{\delta_R\phi D_{NL}K(s)}\left(\phi c(s-s_+) - K(s) + K(s_+) + \frac{\delta_R}{C_a}K(s)\mu_e'(s)\,\frac{ds}{d\xi}\right). \tag{4.26}$$

The Rankine-Hugoniot jump condition, Eq.(4.12), for the speed, c, of the representative shock can be recovered by employing Eq.(4.25) as $\xi \to -\infty$. Since we are looking for TW-solutions satisfying boundary conditions Eq.(4.25), the states s_- and s_+ are two known equilibria of Eq.(4.26). In order to analyze their properties and the possibility of existence of other such equilibria it is convenient to rewrite Eq.(4.26) into a system of first-order ODEs:

$$\begin{aligned} s_\xi &= v, \\ v_\xi &= w, \\ w_\xi &= \frac{C_a\left(\phi c(s-s_+) - K(s) + K(s_+)\right)}{\delta_R\phi D_{NL}K(s)} + \frac{\mu_e'(s)}{\phi D_{NL}}v. \end{aligned} \tag{4.27}$$

In the above sub-script ξ is used to represent derivative of a variable w.r.t to ξ. In the sense of a dynamical system with ξ playing the role of a time-like independent variable, the TW-solutions can viewed as trajectories connecting associated equilibria, $(s_e, 0, 0)$, of such system. The local stability properties of such equilibria determine the nature of the connection between them, (Bertozzi and Shearer, 2000). The eigen values of a corresponding linearized system in the vicinity of an equilibrium reveals the behavior of a

small perturbation to it. These eigen values are the roots of the depressed cubic equation,

$$\beta^3 - \frac{\mu_e'(s_e)}{\phi D_{NL}}\beta - \frac{C_a\left(\phi c - K'(s_e)\right)}{\delta_R \phi D_{NL} K(s_e)} = 0. \tag{4.28}$$

A detailed deduction of the above linearization is done in Appendix A2. According to the classical Cardano-Tartaglia formula for roots of depressed cubic equations, for $\mu_e'(s_e) > 0$, if the discriminant of Eq.(4.28) is negative, then all three eigen values corresponding to the equilibrium are real. This condition can be simplified to,

$$\frac{C_a\sqrt{\phi D_{NL}}}{\delta_R}\frac{\left(\phi c - K'(s_e)\right)}{K(s_e)} < \left(\frac{4}{27}(\mu_e'(s_e))^3\right)^{\frac{1}{2}}. \tag{4.29}$$

Else, only one eigen value of the three is real and the other two are complex conjugates giving rise to oscillatory behavior in the vicinity of such equilibria. On the other hand, for a $\mu_e'(s_e) < 0$, one eigen value of the three is real and other two are complex conjugates, irrespective of the sign of the discriminant. These relations form the basis for understanding the behavior of TW-solutions in the vicinity of their respective equilibrium states, $(s_e, 0, 0)$.

4.5.1 Imbibition

As observed in Sec.(4.4.1), the imbibition solutions are self-similar in the whole of the domain such that the uniform saturation states observed in the PDE solutions correspond to the imposed boundary conditions, S_-, on the left and initial conditions, S_r^0, on the right. Hence, saturation states at the boundaries of TW-solutions in Eq.(4.25) are chosen as $s_+ = S_r^0$ and $s_- = S_-$. And then the third order ODE Eq.(4.26) is numerically resolved over a domain of finite physical length, $L = 100$m, that is sufficiently large in comparison to the characteristic interface thickness, ℓ, such that we get a satisfactory approximation of an unbounded domain. Within this domain, the transition region from s_- to s_+ would be centered at $\xi = 0$. We discretize this domain using a uniform finite difference grid and use a second-order accurate central difference scheme to approximate the derivatives in Eq.(4.25) and (4.26). Then the solutions are obtained solving the non-linear problem

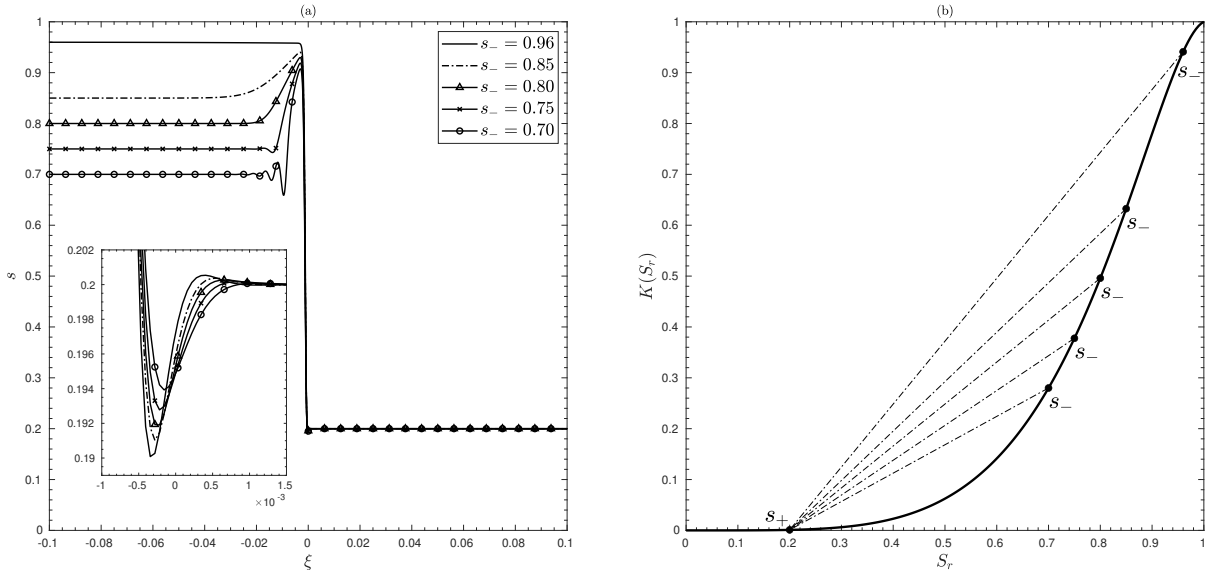

Figure 4.10: (a)TW-solutions of Eq.(4.26) for $\lambda = \rho_w g$, with boundary conditions $s_+ = 0.20$, $s_- = 0.96, 0.85, 0.80, 0.75, 0.70$. Solutions are shown in a restricted range of ξ for clarity. (b) the corresponding connections shown on the curve $K(S_r)$.

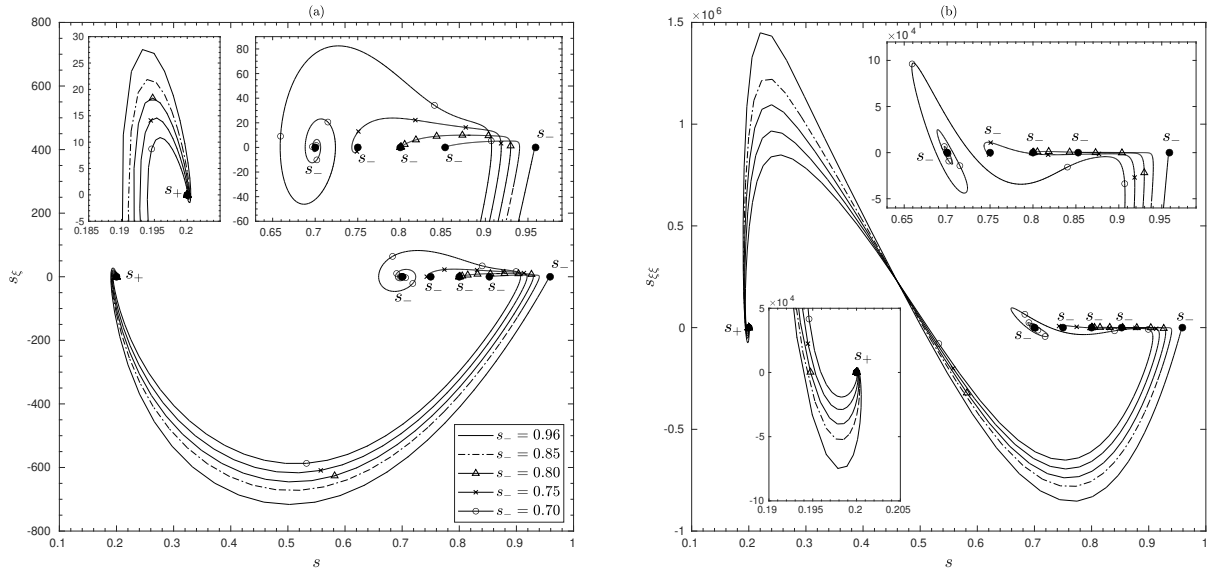

Figure 4.11: TW-solutions shown as trajectories in the phase space defined by of Eq.(4.27) for $\lambda = \rho_w g$, with boundary conditions $s_+ = 0.20$, $s_- = 0.96, 0.85, 0.80, 0.75, 0.70$; phase plane views (a) (s, s_ξ), (b) $(s, s_{\xi\xi})$.

starting from an initial guess that is a sharp transition at $\xi = 0$ between the intended saturation values on either side.

Fig.(4.10) shows these solutions and their corresponding transitions as connections on the graph of flux function, $K(S_r)$, for various values of s_- and $\lambda = \rho_w g$. The slope of these connections is the speed, c, of the corresponding shock that is represented by the TW-solution. As can be inferred from the plot, the relation between characteristic speed on either side of the connection, $K'(s_-)$, $K'(s_+)$, and the speed of the shock is such that these connections are representative of classical compressive shocks that satisfy the Lax entropy condition, Eq.(4.13). Moreover, similar to observations made in Sec.(4.4.1), there exist non-monotonicities of overshoot type and oscillatory type. These solutions are qualitatively comparable to the results of one-dimensional experiments done by DiCarlo (2004) for constant rate infiltration of water into initially dry sand. In those experiments, while for the highest imposed flux the water saturation profile was monotonic, for intermediate fluxes non-monotonicities were observed, which grew stronger as the flux is lowered within the intermediate range. It can observed in Fig.(4.10) the same trend as in the experiments, of the non-monotonicities with respect to varying flux, Eq.(4.21).

In order to aid the analysis of the behavior in the vicinity of equilibria, $(s_-, 0, 0)$ and $(s_+, 0, 0)$, these TW-solutions understood as trajectories running between the equilibria are plotted, see Fig.(4.11), in the phase space governed by the third order ODE system Eq.(4.27). For all s_- the solution close to s_+ is oscillatory. However, behind the front, for certain values of $s_- = 0.85, 0.80$, there is a non-oscillatory overshoot and for $s_- = 0.75, 0.70$ the overshoot is oscillatory as it leaves the equilibrium at s_-. For $s_- = 0.96$ there is neither an overshoot nor oscillations behind the front.

The oscillatory behaviors at both the equilibria can be explained analyzing the corresponding linearized eigen values. For all left equilibrium states, $(s_-, 0, 0)$, such that $\mu_e'(s_-) < 0$ results in oscillations, when leaving this state as seen in the case of $s_- = 0.75, 0.70$. The right equilibrium state, $(s_+ = 0.20, 0, 0)$, is such that $\mu_e'(s_+) > 0$. However, the condition on discriminant being negative, Eq.(4.29), is not satisfied for the choice of C_a and D_{NL} resulting in oscillations when arriving $s_+ = 0.20$.

The overshoot behavior on the other hand can be explained by employing singular perturbation techniques (Witelski, 1996). To do this we introduce a

small nonzero parameter, $\epsilon \approx O(\ell/x_h)$, and expand the solution using a perturbation series, $s(\xi) = s_0(\xi) + \epsilon s_1(\xi) + \epsilon s_2(\xi)\ldots$, which separates Eq.(4.24) into a cascade of problems each governing the solution at a particular order. As $\epsilon \to 0$ the leading order solution, $s_0(\xi)$, is governed by

$$-\phi c \frac{ds_0}{d\xi} + \frac{dK(s_0)}{d\xi} - \frac{\delta_R}{C_a}\frac{d}{d\xi}\left(K(s_0)\mu_e'(s_0)\,\frac{ds_0}{d\xi}\right) = 0. \tag{4.30}$$

Integrating once w.r.t ξ and employing boundary conditions, Eq.(4.25), at $\xi = +\infty$ gives,

$$-\phi c(s_0 - s_+) + K(s_0) - K(s_+) - \frac{\delta_R}{C_a}K(s_0)\mu_e'(s_0)\,\frac{ds_0}{d\xi} = 0. \tag{4.31}$$

This results in a smooth implicit solution valid outside the transition zone and so-called the 'outer' solution:

$$\begin{aligned}\xi(s_0) - \xi_m &= \int_{\xi_m}^{\xi} d\Xi \\ &= \int_{s_m}^{s_0} \frac{\frac{\delta_R}{C_a}K(S)\mu_e'(S)}{-\phi c(S - s_+) + K(S) - K(s_+)}dS,\end{aligned} \tag{4.32}$$

where ξ_m is a reference value, chosen to be 0.0, at which an arbitrary $s_m \in (s_+, s_-)$, chosen to be 0.5, occurs. This implicit solution is plotted in Fig.(4.12) for values $s_- = 0.96, 0.85$ and $s_+ = 0.20$. It is clear that in both cases the solution is non-monotonic in ξ for a range of s_0 within (s_+, s_-) and thus non-physical. Whereas, the parts of the solution for s_0 within $(s_-, 1.0)$ and (S_r^{res}, s_+) increase monotonically with s_0. Now, in order to resolve the non-physicality a weak solution can be constructed by traversing the non-physical region with a discontinuity. However, this jump in the saturation degree needs to comply with a continuity in the pressure whose gradient should exist. This condition can be met in the current model thanks to the double-well structure of the energy density which as explained earlier gives rise to isopotential saturation states. For the choice of parameters in the current study these isopotential states can be obtained as $(S_1^c, S_2^c) \approx (0.91, 0.23)$ using Maxwell construction. Now, exploiting the translational invariance

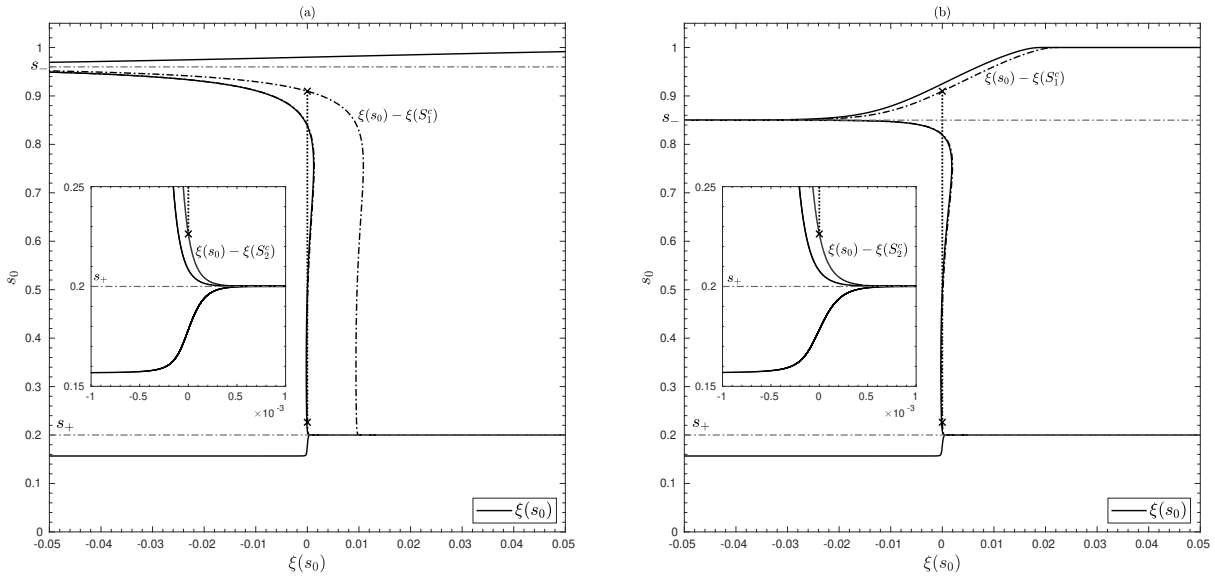

Figure 4.12: Implicit outer solutions, Eq.(4.32), shown as solid lines. Corresponding shifted solutions, $\xi(s_0) - \xi(S_1^c)$ and $\xi(s_0) - \xi(S_2^c)$, shown as dot-dashed lines. The jump part within the weak solution Eq.(4.33) shown as dotted connection between points $(0, S_1^c)$ and $(0, S_2^c)$ which are shown as crosses. Boundary conditions shown as dot-dashed horizontal reference lines for (a) $(s_-, s_+) = (0.96, 0.20)$, (b) $(s_-, s_+) = (0.85, 0.20)$. Solutions are shown in a restricted range of ξ for clarity.

of the implicit solution, Eq.(4.32), a weak implicit solution of the following form can be built using (S_1^c, S_2^c):

$$\widehat{\xi}(s_0) - \xi_m = \begin{cases} \xi(s_0) - \xi(S_1^c), & \forall \widehat{\xi} < \xi_m, \\ \xi(s_0) - \xi(S_2^c), & \forall \widehat{\xi} > \xi_m. \end{cases} \tag{4.33}$$

It is to be noted that the choice of boundary conditions on saturation degree, (s_-, s_+), is independent of the isopotential saturation states determined (S_1^c, S_2^c). Thus a combination of solutions is possible and accordingly the appropriate part of the outer solution, Eq.(4.32), needs to be chosen to further translate and construct the weak outer solution, Eq.(4.33). For instance, if $s_- > S_1^c$ and $s_+ < S_2^c$ the part of outer solution, $\xi(s_0)$, that is to be translated in the construction of $\widehat{\xi}(s_0)$ is the non-monotonic part within (s_+, s_-). See for example the case of $s_- = 0.96$ in Fig.(4.12(a)). On the other hand if $s_- < S_1^c$ and $s_+ < S_2^c$, the monotonically increasing outer solution, $\xi(s_0)$, within $(s_-, 1.0)$ is shifted to the right giving $\xi(s_0) - \xi(S_1^c)$, and the non-monotonic part within (s_+, s_-) is shifted to the right giving $\xi(s_0) - \xi(S_2^c)$. See the case of $s_- = 0.85$ in Fig.(4.12(b)). The jump part of the weak implicit solutions thus constructed traversing the non-physical zone can be seen as dotted vertical lines in Fig.(4.12). In this manner the presence of overshoots in the PDE solutions in Sec.(4.4.1) and in the TW-solutions can be rationalized comparing the left end boundary condition of saturation with the isopotential saturation state closest to it, S_1^c. Similarly two other combinations of solutions can be envisaged when $s_+ > S_2^c$, which involve undershoot when connecting to equilibrium state at s_+.

On the other hand, the structure of the 'inner' transition region can be resolved by making a transformation into a stretched variable, $\tilde{\xi} = (\xi - \xi_m)/\epsilon$, thus restricting the problem into the transition region. Under such transformation and further expanding the resulting solution, $\tilde{s}$, using a perturbation series w.r.t ϵ allows one to identify the leading order 'inner' problem,

$$-\mu_e'(\tilde{s}_0)\,\frac{d\tilde{s}_0}{d\tilde{\xi}} + \phi \frac{d^3\tilde{s}_0}{d\tilde{\xi}^3} = 0, \tag{4.34}$$

for $\tilde{s}_0$. Integrating Eq.(4.34) w.r.t $\tilde{\xi}$ using the boundary conditions that allow appropriate matching of the inner and outer solutions on one side, i.e., $\tilde{s}_0 = S_2^c$ and derivatives of $\tilde{s}_0$ vanish as $\tilde{\xi} \to \infty$, gives the implicit inner solution,

$$\begin{aligned} \tilde{\xi}(\tilde{s}_0) - \tilde{\xi}_m &= \int_{\tilde{\xi}_m}^{\tilde{\xi}} d\tilde{\Xi} \\ &= \int_{\tilde{s}_m}^{\tilde{s}_0} \left[\frac{2}{\phi} \int_{S_2^c}^{\tilde{s}_0} \left(\mu_e(\tilde{S}) - \mu_e(S_2^c)\right) d\tilde{S} \right]^{-\frac{1}{2}} d\tilde{S}, \end{aligned} \tag{4.35}$$

where $\tilde{\xi}_m = 0$ is a reference value where an arbitrary $\tilde{s}_m = 0.5$ is chosen to occur. This inner solution approaches smoothly on the other side, $\tilde{\xi} \to -\infty$, to $\tilde{s}_0 = S_1^c$, see Fig.(4.13). Thus the leading order inner solution is affected neither by the form of flux function, $K(s)$, nor by the boundary conditions chosen, Eq.(4.25). Once the implicit solutions Eq.(4.33) and Eq.(4.35) are determined, a solution valid over the full domain can be constructed using asymptotic matching techniques with appropriate assumption on the region of overlap of those solutions. One of such possible assumptions involves a uniform matching,

$$s(\xi) = \begin{cases} \widehat{s}_0(\xi) + \tilde{s}_0(\xi) - S_1^c, & \forall \xi < \xi_m, \\ \widehat{s}_0(\xi) + \tilde{s}_0(\xi) - S_2^c, & \forall \xi > \xi_m. \end{cases} \tag{4.36}$$

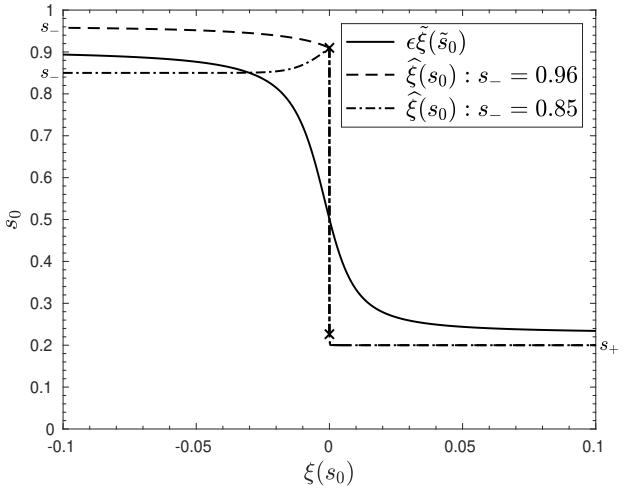

Figure 4.13: Implicit inner solution, Eq.(4.35), scaled back from the stretched variable space, $\epsilon\tilde{\xi}(\tilde{s}_0)$, shown as a solid line in the space $(\xi(s_0), s_0)$. This solution varies between $S_1^c \approx 0.91$ and $S_2^c \approx 0.23$. The weak implicit outer solution, Eq.(4.33), is shown for both the boundary conditions $(s_-, s_+) = (0.96, 0.20)$ (dashed) and $(s_-, s_+) = (0.85, 0.20)$ (dot-dashed). These involve a jump between $(0, S_1^c)$ and $(0, S_2^c)$ which are shown as crosses. Solutions are shown in a restricted range of ξ for clarity.

In the Eq.(4.36) above, $\widehat{s}_0(\xi)$ is the inverse mapping of $\widehat{\xi}(s_0)$ in Eq.(4.33), with an abuse of notation replacing $\widehat{\xi}$ with ξ noting that both take values from the real number line. $\tilde{s}_0(\xi)$ is the inverse mapping of the implicit inner solution that is scaled back from the stretched variable space, $\epsilon\tilde{\xi}(\tilde{s}_0)$. The accuracy of such solutions depends on the assumptions involved in the asymptotic matching procedure.

While, the weak implicit outer solution, Eq.(4.33), indicates whether the overshoot and undershoot behaviors are to be expected or not in the numerical solutions, it is prudent to note that the integrand in Eq.(4.32) diverges to $-\infty$ while approaching both s_- and s_+. And this is irrespective of the relation between s_- and s_+, i.e., either $s_- > s_+$ or $s_- < s_+$. Thus integrating backwards from $s_m \in (s_+, s_-)$ to $\min(s_+, s_-)$ always implies $\xi(s_0) \to \infty$ and integrating forwards from $s_m \in (s_+, s_-)$ to $\max(s_+, s_-)$ always implies $\xi(s_0) \to -\infty$. So, this implicit outer solution, is only representative of imbibition solutions and as such drainage solutions are not possible in the context of the leading order outer problem, Eq.(4.30). As we will see further, it is the second gradient term of the energy that is absent in the outer problem which is responsible for drainage solutions when $K(S_r)$ is non-convex.

With respect to imbibition, s_+ represents the initial saturation condition of the porous media into which injection of fluid is done with a velocity corresponding to s_- of the form Eq.(4.21). For fixed $\lambda = \rho_w g$, Fig.(4.14(a) & (b)) show respectively the effect of different left boundary conditions, s_-, with a given initial condition, $s_+ = 0.20$ and of different initial conditions, s_+, with a given left boundary condition, $s_- = 0.85$. In the latter, for larger values of s_+, the oscillatory non-monotonicity ahead of the interface are stronger and more spread-out along ξ, whereas the overshoot behind the interface tends to reduce slightly.

Fig.(4.14(c)) shows the imbibition solutions for various values of λ and for fixed boundary conditions, $s_- = 0.85, s_+ = 0.20$. Increasing λ tends to result in a reduced spread along ξ of the non-monotonicities within both behind and ahead of the interface. Also, the strength of these non-monotonicities tends to increase with λ.

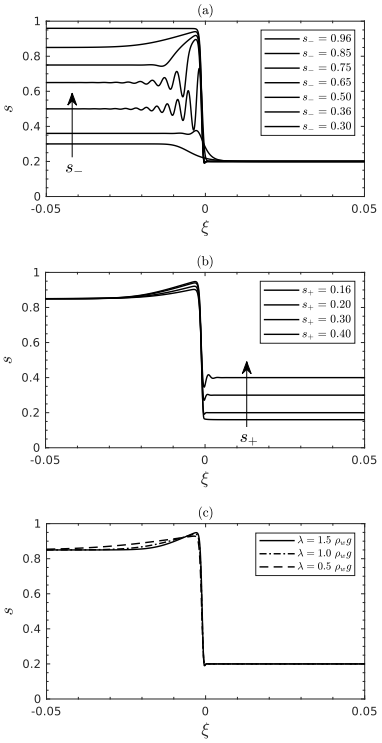

Figure 4.14: TW-solutions of Eq.(4.26) that represent imbibition, (a) for varying s_-, with $s_+ = 0.20$ and $\lambda = \rho_w g$, (b) for varying s_+, with $s_- = 0.85$ and $\lambda = \rho_w g$. (c) for varying λ, with $s_- = 0.85$ and $s_+ = 0.20$. All the solutions are shown in a restricted range of ξ for clarity.

4.5.2 Drainage

Contrary to the imbibition solutions in Sec.(4.4), the drainage solutions are not self-similar throughout the domain. Only a part of the solution seems to propagate as traveling waves with uniform intermediate saturation state/s appearing. For lower values of λ two intermediate states S_a and S_b form the traveling wave boundary conditions. And for higher values of λ only one

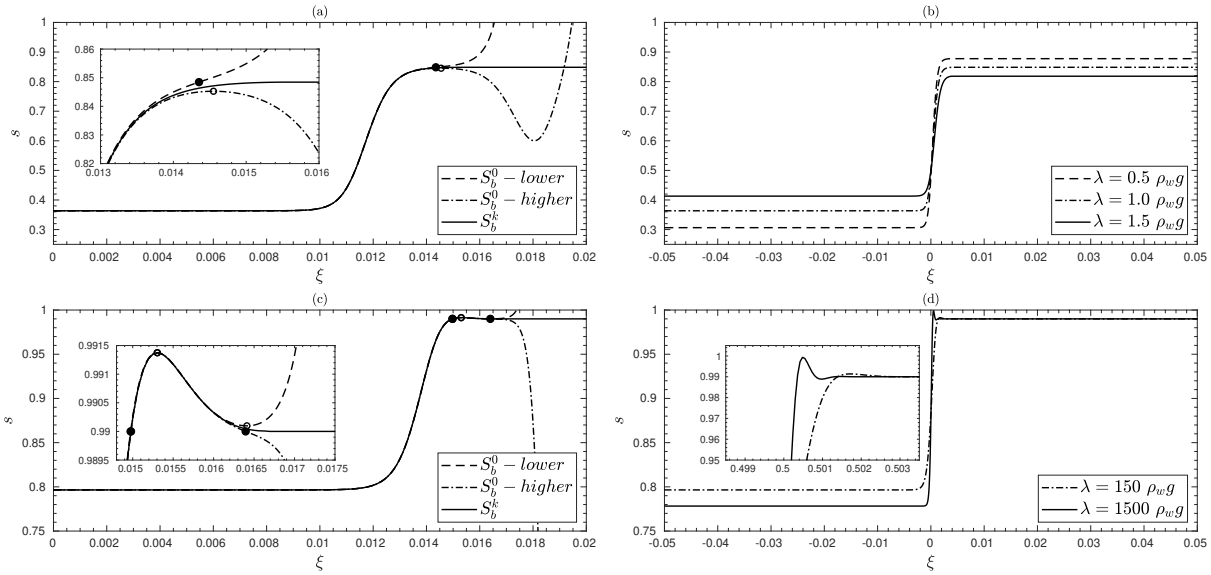

Figure 4.15: Trajectories of qualitatively different solutions with lower and higher starting equilibrium states, $(S_b^0, 0, 0)$, for (a) $\lambda = \rho_w g$, (c) $\lambda = 150\rho_w g$. Zero slope locations on the trajectories are shown as circles and locations where the trajectory crosses the target S_a are shown as filled dots. Solid lines represent the solution trajectory at the last iteration starting at equilibrium state $(S_b^k, 0, 0)$. Corresponding TW-solutions centered within the domain $\xi \in [-0.05, 0.05]$, for (b) lower values of $\lambda = 0.5\rho_w g$, $\rho_w g$, $1.5\rho_w g$ for which $(s_-, s_+) = (S_b^k, S_a)$ and $S_b^k \approx 0.30639, 0.36345, 0.413$ respectively with λ and for (d) higher values of $\lambda = 150\rho_w g$, $1500\rho_w g$ for which $(s_-, s_+) = (S_b^k, S_r^0)$ and $S_b^k \approx 0.79653, 0.77827$ respectively with λ. Solutions are shown in a restricted range of ξ, s and aspect ratio of insets adjusted for clarity.

intermediate state S_b connects directly to the initial condition S_r^0. Moreover, these intermediate state/s are not a priori known and hence the boundary conditions to resolve the corresponding TW-solutions are not known. However, it has been shown numerically, in the context of thin film flows, that non-classical 'under-compressive' shocks are unique (Bertozzi et al., 1999; Münch, 2000) in the sense that they represent traveling wave type solutions between unique combination of left and right boundary conditions. Also in the case of lower values of λ in Sec.(4.4.2), the intermediate states S_a and S_b remained unique irrespective of the changing boundary conditions. Taking cue from these observations, in what follows we consider one of the equilibrium states in the PDE solutions as a known. And then we use an iterative approach to find the unknown equilibrium state, employing a shooting method to integrate forward or backward in ξ, the dynamical system Eq.(4.27), until the target known equilibrium state is reached.

To do this in the case of lower values of λ we take as input from the 1D PDE results the higher equilibrium state, $(S_a, 0, 0)$, as the target and apply a small perturbation of the order 1E-6 to an initial guess of lower equilibrium state, $(S_b^0, 0, 0)$, in the direction of the eigen vector corresponding to an unstable eigen value at $(S_b^0, 0, 0)$. Then we proceed to integrate forward Eq.(4.27) using the MATLAB solver-ODE23s (Shampine and Reichelt, 1997) which is based on a modified Rosenbrock method and features adaptive step size. In order to provide stopping criteria for the integration and direction for the iterations we observe two qualitatively different types of trajectories starting from an $(S_b^0, 0, 0)$ in the vicinity of lower equilibrium state obtained in the 1D PDE results, $(S_b, 0, 0)$. See Fig.(4.15(a)). For lower values of S_b^0 the trajectory reaches the target S_a with a positive slope and then diverges towards full saturation. For higher values of S_b^0 on the other hand, it reaches a local maximum missing the target and then moves to a local minimum before diverging to full saturation. The required left equilibrium state would form a trajectory that reaches the target with a zero slope and curvature, up to a numerical error. Assuming such trajectory exists for an S_b^0 within the above two cases, we input them as starting points of iterations in a

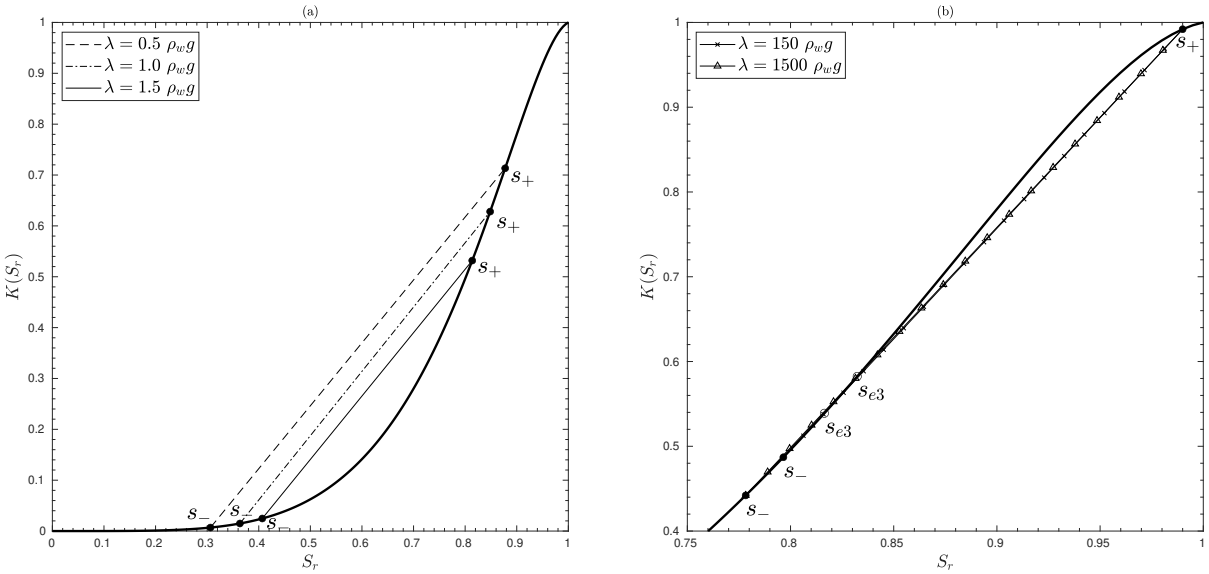

Figure 4.16: TW-solutions shown in Fig.(4.15b,d) shown as connections on the curve $K(S_r)$ for (a) lower values of $\lambda = 0.5\rho_w g,\ \rho_w g,\ 1.5\rho_w g$ for which $(s_-,\ s_+) = (S_b^k,\ S_a)$ and for (b) higher values of $\lambda = 150\rho_w g,\ 1500\rho_w g$ for which $(s_-,\ s_+) = (S_b^k,\ S_r^0)$ and $s_{e3} \approx 0.81641,\ 0.83232$ respectively with λ. The locations of $(s_{e3},\ K(s_{e3}))$ on the curve are shown as circle markers.

Regula-Falsi method (Galdino, 2011). The stopping criteria for the iterations is chosen as a tolerance to be satisfied by the difference between the target S_a and the saturation value at which a zero slope achieved. This tolerance is set to 1E-8 in this work. Fig.(4.15(b)) shows the TW-solutions thus obtained for different values of λ and the lower equilibrium state $(S_b^k, 0, 0)$ associated to the last iteration.

For the case of higher λ, where only one intermediate uniform saturation state, S_b, was observed in the 1D PDE results, we follow a similar approach and stopping criteria for the iterations, but with an a priori known target $(S_r^0, 0, 0) = (0.99, 0, 0)$. Again we observe two types of trajectories starting in the vicinity of equilibrium state $(S_b, 0, 0)$. In both cases we observe an oscillatory behavior while approaching the target. See Fig.(4.15(c)). However, for lower values of S_b^0, after oscillation, the trajectory reaches a local minimum without traversing the target and then diverges to full saturation. And for higher values of S_b^0, the trajectory reaches the target S_a with a negative slope and then diverges down towards residual saturation. With these new stopping criteria for integration we obtain TW-solutions shown in Fig.(4.15(d)) for different values of λ.

These drainage TW-solutions are shown as connections on the permeability curve $K(S_r)$ in Fig.(4.16). The connections for lower values of λ are representative of non-classical 'expansion' shocks that violate Lax entropy condition as Eq.(4.16). Since these solutions are connections between two equilibria, corresponding local stability properties can be analyzed in accordance with Sec.(4.5). In the current phase field model these non-classical 'expansion' connections occur between a left equilibrium state, $(s_-, 0, 0)$, which has locally one unstable real eigen value, two stable complex conjugate eigen values and a right equilibrium state, $(s_+, 0, 0)$, which has locally two unstable real eigen values, one stable real eigen value. And hence there are no oscillations observed neither when leaving the left equilibrium state along the unstable eigen vector nor when approaching the right equilibrium state along the stable eigen vector. In Sec.(4.4.2) it is observed that longitudinal oscillations appear at the junction of a rarefaction wave and the uniform intermediate saturation state associated to S_b. It can be inferred that these oscillations are due to the complex conjugate nature of the stable eigen pair in the vicinity of the left equilibrium state.

On the other hand, the connections for higher values of λ violate Lax entropy condition, Eq.(4.13), while satisfying the first relation in Eq.(4.15) and so are representative of non-classical 'under-compressive' shocks which travel faster than the characteristic speed on either side of the shock. For such connections the system governed by Eq.(4.27) has a third equilibrium, $(s_{e3}, 0, 0)$, such that,

$$\phi c(s_{e3} - s_+) - K(s_{e3}) + K(s_+) = 0. \tag{4.37}$$

However the solution only represents a connection directly from $(s_-, 0, 0)$ to $(s_+, 0, 0)$ that have the same local stability properties with one unstable real eigen value, two stable complex conjugate eigen values. And the later are responsible for the small oscillatory non-monotonicity when the solution approaches $(s_+, 0, 0)$. See inset in Fig.(4.15(d)).

Similar 'under-compressive' shocks have also been observed as solutions of thin film flow equations (Bertozzi et al., 1999; Bertozzi and Shearer, 2000). In fact, the dynamical system formed by such equations has a similar structure to Eq.(4.27). However, a significant difference is that the counterpart of the coefficient of v in Eq.(4.27)^3, $\mu_e'(s)$, in the case of thin film flow equations is a constant instead of a function of the unknown field that can change its sign as in the current context.

4.6 SYNOPSIS

Starting from the extended Richards' equation, we have presented an appropriate dimensional grouping and a one-dimensional analysis exploiting the hyperbolic structure of the governing conservation law. One-dimensional PDE simulations of the same have informed on the presence of similarity solutions for appropriate initial and boundary conditions. In particular the part of the solution which is a similarity solution of the traveling wave type was understood as the air-water displacement front. It has been demonstrated that both imbibition and drainage solutions are possible due to the non-convexity of the proposed flux function. Further with an intent to analyze their linear stability, the part of the solution that is a traveling wave type has been resolved by making a transformation into an appropriate moving coordinate system. These solutions were analyzed by exploiting the underlying dynamical system. The solutions corresponding to imbibition driven by gravity have been found to be non-monotonic under certain boundary conditions and the reason for such non-monotonicities has been analyzed. In the current model, the double-well structure of the non-uniform pore fluid energy has been found to cause overshoot type non-monotonicities depending on the boundary conditions chosen, whereas the oscillatory non-monotonicities are due to the dynamical nature of the equilibria associated to the boundary conditions. The solutions of imbibition under the influence of gravity have shown good qualitative agreement against one-dimensional infiltration experiments, with the trend of the relationship between infiltration flux and saturation degree overshoot being preserved. Drainage solutions connecting unknown boundary conditions as well were resolved using an iterative shooting method starting from left boundary condition taken from the PDE solutions.

5 LINEAR STABILITY ANALYSIS

CONTENTS

5.1 Stability against transverse perturbations 58
5.1.1 Perturbed problem 59
5.1.2 Discretization and Asymptotic growth/decay 60
5.2 Stability against longitudinal perturbations 65
5.3 Synopsis 67

ABSTRACT

In Chp.(4) we have done a one-dimensional analysis of the extended Richards' equation along with the resolution of traveling wave solutions. In the current study we present a linear stability analysis of its solutions which describe both imbibition and drainage. The essence of linear stability analysis performed is to understand if a small enough initial perturbation to the base solution grows or decays asymptotically in time by employing the principles of Lyapunov stability analysis. The results of stability against transverse perturbations sheds light on the sensitivity of the flow stability on injection flux, imposed pressure gradient and initial saturation degree. Further, a stability analysis against longitudinal perturbations reveals the instability of certain solutions that is associated to the non-monotonic structure of the fluid bulk energy.

5.1 STABILITY AGAINST TRANSVERSE PERTURBATIONS

Saffman and Taylor (1958), have studied the stability of an horizontal sharp interface separating two viscous fluids within a Hele-Shaw cell, driven by an imposed pressure gradient and under the influence of gravity. It has been shown that wave like disturbances of arbitrary wavelengths can grow in time and eventually destabilize the interface if the motion of the interface is towards the more viscous fluid and if the velocity is sufficiently large. Further the effect of surface tension has been suggested, referring to the work of Chuoke et al. (1959), to be acting to limit the range of wavelengths of the disturbances to which the interface is unstable. A study of stability of the diffused interface formed within the non-uniform pore fluid, that is modeled using the Eq.(4.8), is warranted, given the analogous nature of porous media flow with respect to Hele-Shaw flow. With this intention the base solutions, resolved as traveling waves are understood as plane wave solutions that are independent of the direction orthogonal to their propagation. Arbitrary wave like perturbations are then superposed to these base solutions and the growth in time of the former is understood as early time fingering phenomenon.

5.1.1 Perturbed problem

The base solutions in the physical domain are represented as $S_0(x,t)$ and they propagate along the x-direction. The physical solution itself is assumed to be a perturbed one, $S(x,y,t)$, that is composed of the base solution $S_0(x,t)$ at the leading order and superposed disturbances, resulting in a regular series expansion,

$$S(x,y,t) = S_0(x,t) + \epsilon S_1(x,y,t) + \epsilon^2 S_2(x,y,t)\ldots, \tag{5.1}$$

where ϵ represents the magnitude of the disturbance. This form of the perturbed solution is inserted back into Eq.(4.8) which is further linearized by ignoring quadratic and higher-order terms in ϵ. This leads to two problems, one of the leading order, $O(1)$, and another perturbed problem of order $O(\epsilon)$. This perturbed problem,

$$\begin{aligned}&\phi\frac{\partial S_1}{\partial t} + \frac{\partial(K_0' S_1)}{\partial x} - \frac{\delta_R}{C_a}\Delta\Big(K_0\mu_{e0}' S_1\Big)\\ &+\frac{\delta_R}{C_a}\phi D_{NL}\nabla\cdot\Big(K_0\nabla\Delta S_1 + K_0'\nabla\Delta S_0 S_1\Big) = 0,\end{aligned} \tag{5.2}$$

governs the evolution of a generic disturbance up to order $O(\epsilon)$. In the above and what follows, functions sub-scripted $(.)_0$ are to be understood as evaluated with the base solution. Noting that the base solution $S_0(x,t)$ is uniform along y-direction and subsequently employing $\xi = x - ct$ yields the $O(\epsilon)$ perturbed problem governing $s_1(\xi,y,t)$ in the TW-coordinate,

$$\begin{aligned}&\phi\frac{\partial s_1}{\partial t} - \phi c\frac{\partial s_1}{\partial \xi} + \frac{\partial(K_0' s_1)}{\partial \xi} - \frac{\delta_R}{C_a}\Bigg\{s_1\frac{d^2}{d\xi^2}\Big(K_0\mu_{e0}'\Big)\\ &+ 2\frac{\partial s_1}{\partial \xi}\frac{d}{d\xi}\Big(K_0\mu_{e0}'\Big) + K_0\mu_{e0}'\left(\frac{\partial^2 s_1}{\partial \xi^2} + \frac{\partial^2 s_1}{\partial y^2}\right)\Bigg\}\\ &+ \frac{\delta_R}{C_a}\phi D_{NL}\Bigg\{s_1\frac{d}{d\xi}\left(K_0'\frac{d^3 s_0}{d\xi^3}\right) + \frac{\partial s_1}{\partial \xi}\left(K_0'\frac{d^3 s_0}{d\xi^3}\right)\\ &+ \frac{dK_0}{d\xi}\left(\frac{\partial^3 s_1}{\partial \xi^3} + \frac{\partial^3 s_1}{\partial \xi \partial y^2}\right) + K_0\Bigg(\frac{\partial^4 s_1}{\partial \xi^4} + \frac{2\partial^4 s_1}{\partial \xi^2 \partial y^2}\\ &+ \frac{\partial^4 s_1}{\partial y^4}\Bigg)\Bigg\} = 0.\end{aligned} \tag{5.3}$$

Now since any generic disturbance can be resolved into its Fourier modes, modal stability analysis amounts to knowing the growth in time of individual Fourier modes composing the disturbance. If any one of these modes is found to be growing in time, the flow as a whole is to be understood as unstable since any physical disturbance would contain all of these modes. Following this approach a spatially periodic form is assumed for s_1:

$$s_1(\xi,y,t) = e^{iky+\sigma t}\,\widehat{s}(\xi), \tag{5.4}$$

where k is characteristic wave number of the disturbance in y-direction, σ is the exponential growth factor in time (with an abuse of notation used for the Cauchy stress tensor) and $\widehat{s}(\xi)$ is the amplitude of the wave-like disturbance allowing variation in direction of propagation, ξ. Introducing Eq.(5.4) in Eq.(5.3) yields:

$$A\frac{d^4\widehat{s}}{d\xi^4} + B\frac{d^3\widehat{s}}{d\xi^3} + C\frac{d^2\widehat{s}}{d\xi^2} + D\frac{d\widehat{s}}{d\xi} + E\widehat{s} - \sigma\widehat{s} = 0, \tag{5.5}$$

a linear homogeneous ODE with spatially varying coefficients identified as,

$$
\begin{aligned}
A &= -\frac{\delta_R}{C_a} D_{NL} K_0, \quad B = -\frac{\delta_R}{C_a} D_{NL} \frac{dK_0}{d\xi}, \\
C &= -\frac{1}{\phi}\frac{\delta_R}{C_a}\Big\{ -K_0\mu'_{e0} - 2\phi D_{NL} k^2 K_0 \Big\}, \\
D &= -\frac{1}{\phi}\Bigg\{ K'_0 - \phi c - 2\frac{\delta_R}{C_a}\frac{d}{d\xi}\Big(K_0\mu'_{e0}\Big) \\
&\quad + \frac{\delta_R}{C_a}\phi D_{NL}\left(K'_0\frac{d^3 s_0}{d\xi^3} - k^2\frac{dK_0}{d\xi}\right)\Bigg\}, \\
E &= -\frac{1}{\phi}\Bigg\{ -\frac{\delta_R}{C_a}\left(\frac{d}{d\xi}\Big(K_0\mu'_{e0}\Big) - k^2 K_0\mu'_{e0}\right) \\
&\quad + \frac{\delta_R}{C_a}\phi D_{NL}\left(\frac{d}{d\xi}\left(K'_0\frac{d^3 s_0}{d\xi^3}\right) + k^4 K_0\right) + \frac{dK'_0}{d\xi}\Bigg\}.
\end{aligned}
\tag{5.6}
$$

These coefficients are dependent on the base solution, s_0, its derivatives w.r.t ξ and the wave number of the disturbance, k. Since the base solution satisfies boundary conditions s_- and s_+ while approaching uniformly the boundaries $\xi \to -\infty$ and $\xi \to +\infty$ respectively, $\widehat{s}$ needs to vanish uniformly at those boundaries such that the $O(\epsilon)$ perturbed solution is admissible. This results in the following boundary conditions that any $\widehat{s}$ governed by Eq.(5.5) needs to satisfy,

$$
\begin{aligned}
\widehat{s}\Big|_{(\xi=+\infty)} &= 0\,, \quad \frac{d\widehat{s}}{d\xi}\Big|_{(\xi=+\infty)} = 0, \\
\widehat{s}\Big|_{(\xi=-\infty)} &= 0\,, \quad \frac{d\widehat{s}}{d\xi}\Big|_{(\xi=-\infty)} = 0.
\end{aligned}
\tag{5.7}
$$

5.1.2 Discretization and Asymptotic growth/decay

In the current section for each base solution, the pair $\widehat{s}$ and σ are determined numerically varying the value of k. We approximate using a second-order accurate central difference scheme the derivatives in Eq.(5.5) and (5.7). The physical domain is the same as that is used to resolve the base solutions, with $L_0 = 100$m and corresponding dimensionless domain $\xi \in (-0.5, 0.5)$. Subsequently the discretized problem for $\widehat{s}$ and σ can be posed as an eigen value problem,

$$
(\mathbb{A} - \sigma\mathbb{I})\widehat{s} = 0, \tag{5.8}
$$

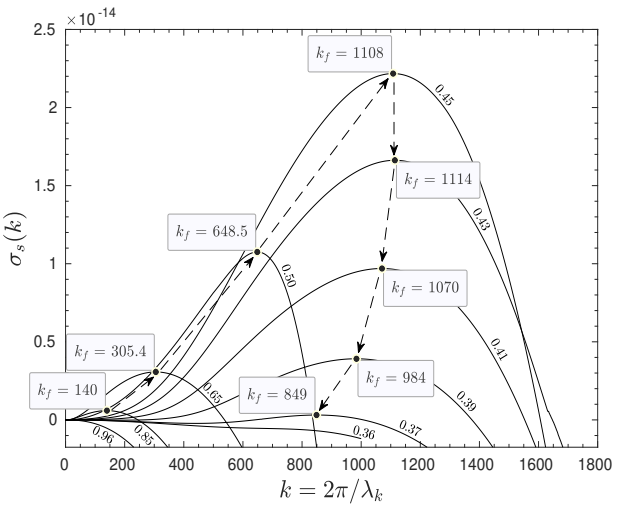

Figure 5.1: Dispersion curves of imbibition solutions for $\lambda = \rho_w g$, with boundary conditions $s_+ = 0.20$, a range of $s_- \in [0.36, 0.96]$. Respective s_- values are labeled on each curve. Peaks that represent maximal positive growth rate are shown as filled dots on the curves, with their respective wave number, k_f, labeled. Arrows trace the path followed by k_f for decreasing s_-.

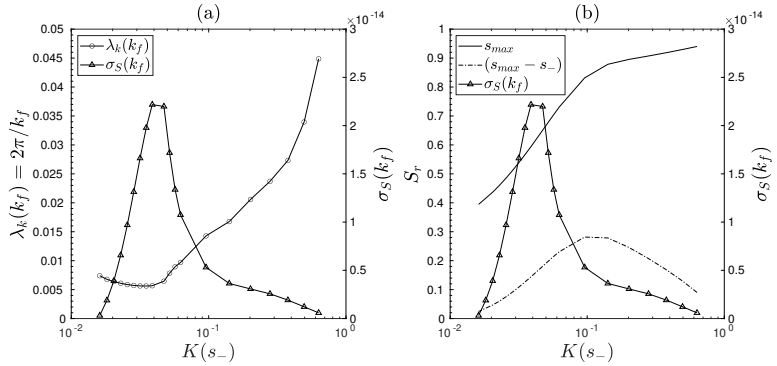

Figure 5.2: Plots indicating the correlation between the injection velocity and the non-monotonicities in the base solutions and their associated instability behavior. (a) Wavelength associated to the fastest growing wave number, $\lambda_k(k_f)$, and the corresponding growth rate, $\sigma_s(k_f)$, as functions of the magnitude of dimensionless injection velocity, $K(s_-)$. (b) Maximum value attained at the tip of the imbibition front in the base solutions, s_{max} and the intensity of the non-monotonicity represented by $(s_{max} - s_-)$, as functions of $K(s_-)$.

where $\mathbb{A}$ is a sparse matrix encompassing the coefficients at respective finite difference (FD) nodes and $\mathbb{I}$ is an identity matrix of the same size. Since for a non-trivial $\widehat{s}$, $|\mathbb{A} - \sigma\mathbb{I}| = 0$, the solution set for σ is given by the spectrum of $\mathbb{A}$, represented $\sigma_{\mathbb{A}}$. Following modal stability analysis, if $\sup\{\Re(\sigma_{\mathbb{A}})\} > 0$, then the corresponding perturbation grows exponentially in time according to Eq.(5.4). Whereas if $\sup\{\Re(\sigma_{\mathbb{A}})\} < 0$, then all the perturbations, $\widehat{s}$, decay exponentially with time. In order to numerically approximate this critical eigen value, $\sigma_s = \sup\{\Re(\sigma_{\mathbb{A}})\}$, for a given wave number, k, a Krylov-Schur algorithm available in MATLAB (Stewart, 2002) has been employed. This relation between k and $\sigma_s(k)$ is plotted as a dispersion curve for each base solution, s_0.

Fig.(5.1) shows the dispersion relation for base solutions which represent imbibition for various values of s_-, $s_+ = 0.20$ and $\lambda = \rho_w g$. The wave number of the fastest growing perturbation, k_f, is the one associated to the peak of the dispersion curve. For a large value of $s_- = 0.96$, representing large injection velocity according to Eq.(4.21), $\sigma_s(k)$ is found to be negative for all values k analyzed. This indicates an exponential decay of the arbitrary perturbations applied to those base solutions and thus a stable imbibition front which is the associated plane wave. As s_- is reduced the base solutions start to involve non-monotonicities and the growth rate $\sigma_s(k)$ is found to be positive for a range of k. This indicates that perturbations within those ranges can potentially grow in time, triggering fingering type instabilities. As s_- is reduced further, $s_- \leqslant 0.36$, the dispersion curves again indicate exponential stability of the base solutions. This is in qualitative agreement with the experimental observations by Shiozawa and Fujimaki (2004); DiCarlo (2004) and the related hypothesis that overshoot profiles of saturation result in an unstable wetting front in gravity driven infiltration (Nieber et al., 2000; Eliassi and Glass, 2001; Egorov et al., 2003; DiCarlo, 2013).

Also, indicated in Fig.(5.1) is the path followed by the wave number of the fastest growing perturbation, k_f, as s_- is reduced. The interpretation of this path is made clear in Fig.(5.2), with the understanding that the wave length associated to the fastest growing perturbation, $\lambda(k_f) = 2\pi/k_f$, is representative of the spacing between the early time fingers. And the intensity

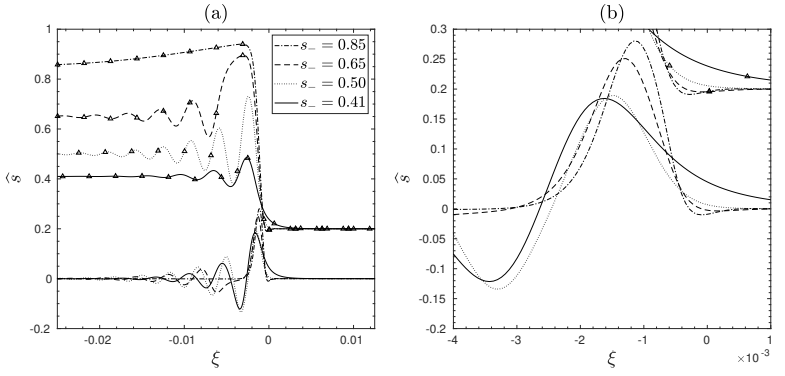

Figure 5.3: (a) Eigen functions, $\widehat{s}$, for $k = 140$, $\lambda = \rho_w g$, with boundary conditions $s_+ = 0.20$, $s_- = 0.41, 0.50, 0.65, 0.85$. The corresponding base solutions, s_0, shown with triangle markers, are also plotted here for reference, (b) close-up view showing the structure of eigen functions in the vicinity of their peaks.

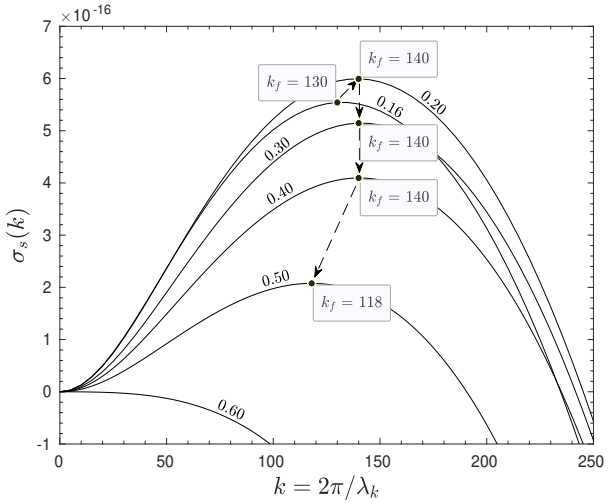

Figure 5.4: Dispersion curves of imbibition solutions for $\lambda = \rho_w g$, with boundary conditions $s_- = 0.85$, a range of $s_+ \in [0.16, 0.60]$. Peaks that represent maximal positive growth rate are shown as filled dots on the curves, with their respective wave number, k_f, labeled. Arrows trace the path followed by k_f for increasing s_+.

of the non-monotonicity is reflected by $(s_{max} - s_-)$, where s_{max} is the peak value of the saturation degree attained by the imbibition front. For intermediate range of injection velocities the intensity of overshoot in the base solutions is larger and the corresponding finger spacing is smaller, whereas the growth rate is larger. As the injection velocity either increases moving towards fully saturated conditions or decreases lower than the intermediate range, the intensity of overshoot reduces, the corresponding finger spacing increases and the growth rate decreases indicating a transition to the stable regime. This strongly indicates a correlation between the injection flux and the characteristics of the associated fingering instabilities as observed in experiments (Glass et al., 1989b; Yao and Hendrickx, 1996). A similar observation has been done in Cueto-Felgueroso and Juanes (2009a).

Also, it is interesting to compare the structure of the perturbation with maximum growth rate for a given wave number. Fig.(5.3) shows this normalized eigen function, $\widehat{s}$, determined by solving Eq.(5.8) with $k = 140$ and the associated base solutions, s_0, superposed. For all values of s_- the eigen function reaches a maximum within the diffused interface between s_- and s_+ of the base solution. However, there exists a relative difference in the peak values and the spread along ξ of these peaks among these eigen functions. As s_- reduces the peak value reduces and the spread along ξ increases. This indicates a shift towards weaker and more spread-out perturbations. It can be inferred from this observation that for base solutions that consist a stronger non-monotonicity (lower s_-), a relatively weaker perturbation is sufficient to render the flow unstable and vice versa.

Fig.(5.4) shows the dispersion relation for base solutions representing

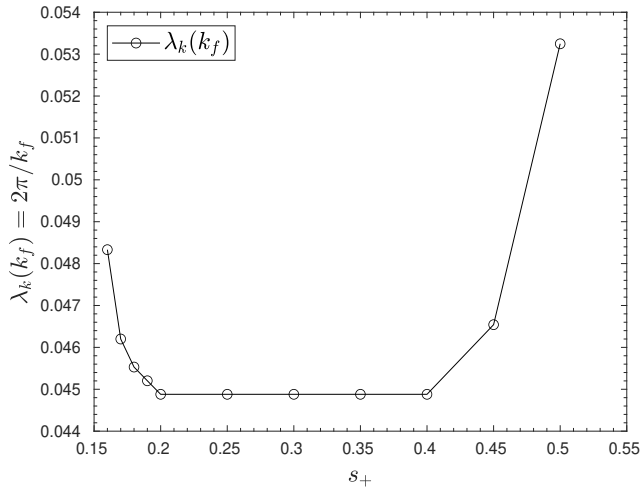

Figure 5.5: Plot indicating the correlation between initial saturation degree, s_+, in the imbibition solutions and their associated instability behavior. Wavelength associated to the fastest growing wave number, $\lambda_k(k_f)$ is plotted as a function of $s_+ \in [0.16, 0.60]$.

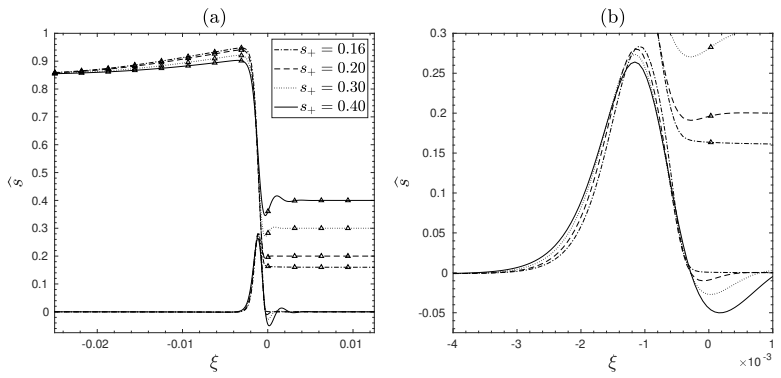

Figure 5.6: (a) Eigen functions, $\widehat{s}$, for $k = 140$, $\lambda = \rho_w g$, with boundary conditions $s_- = 0.85$, $s_+ = 0.16, 0.20, 0.30, 0.40$. The corresponding base solutions, s_0, shown with triangle markers, are also plotted here for reference, (b) close-up view showing the structure of eigen functions in the vicinity of their peaks.

imbibition for various values of s_+, $s_- = 0.85$ and $\lambda = \rho_w g$ and the path followed by the wave number of the fastest growing perturbation, k_f, as s_+ is increased. For high values of s_+ the base solution seems to be stable. The intermediate range of s_+ shows unstable behavior and as s_+ is reduced further the tendency seems to be towards stable behavior. However, it is to be noted that the lowest value of s_+ in this work is restricted by the residual saturation degree $S_r^{res} = 0.1567$. This behavior is also plotted in Fig.(5.5) showing the relation between the qualitative indicator of finger spacing, $\lambda_k(k_f)$, and s_+. A qualitatively similar observation was made in point-source infiltration experiments by Bauters et al. (2000), where water was injected into initially moist sand packs, albeit within a lower range of initial water content. It was observed that the ensuing finger sizes decreased slightly with increasing initial water content starting from a completely dry condition and after a certain value, the finger sizes increased exponentially.

For $k = 140$ the normalized eigen function, $\widehat{s}$, is more spread-out along ξ and has a lower maximum value of the peak when s_+ is increased, see Fig.(5.6). This indicates that for larger s_+ while a weaker and more diffused perturbation can invoke instability in the flow, it grows relatively slower in accordance with Fig.(5.4).

Fig.(5.7) shows the dispersion relation for base solutions in Fig.(4.14(c)) that represent imbibition for varying values of $\lambda = 0.5\rho_w g, \rho_w g, 1.5\rho_w g$ and with fixed boundary conditions $s_+ = 0.20$ and $s_- = 0.85$. For the range of λ studied it is clear that base solutions with a relatively narrower spread along ξ (larger λ) when leaving the equilibrium state, $(s_-, 0, 0)$ have a wider range of k for which the perturbations are unstable and also larger values of k_f and associated peaks, corresponding to a relatively faster growing perturbations.

Fig.(5.8) shows the normalized eigen functions, $\widehat{s}$, for $k = 140$ along with the corresponding base solutions. It can be inferred that for larger values of λ (accordingly larger C_a) the eigen function has a peak value which is

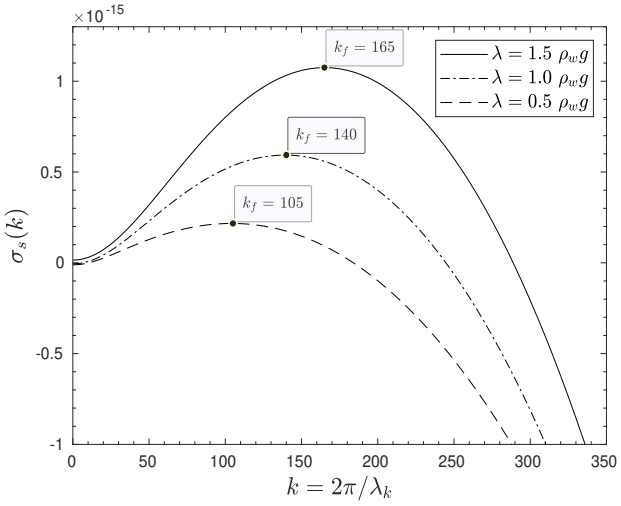

Figure 5.7: Dispersion curves of imbibition solutions for $\lambda = 0.5\rho_w g, \rho_w g, 1.5\rho_w g$, with boundary conditions $s_- = 0.85$, $s_+ = 0.20$. Peaks that represent maximal positive growth rate are shown as filled dots on the curves, with their respective wave number, k_f, labeled.

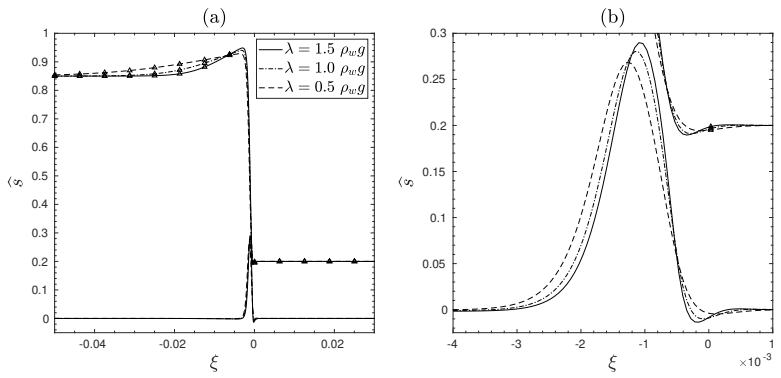

Figure 5.8: (a) Eigen functions, $\widehat{s}$, for $k = 140$, $\lambda = 0.5\rho_w g, \rho_w g, 1.5\rho_w g$, with boundary conditions $s_- = 0.85$, $s_+ = 0.20$. The corresponding base solutions, s_0, shown with triangle markers, are also plotted here for reference, (b) close-up view showing the structure of eigen functions in the vicinity of their peaks.

higher and relative spread along ξ which is narrower representing a stronger perturbation that is needed to generate an unstable flow and according to the dispersion relation, Fig.(5.7), this perturbation would grow relatively faster.

To summarize the case of imbibition, linear stability analysis of the infiltrating front provides results consistent with experimental evidence. Moreover, it tells us that for a given imposed pressure gradient, stronger the perturbation needed to destabilize the front, faster would be its growth and consequently faster would be the destabilized finger. And this condition is achieved when the non-monotonicity of the base solution is less pronounced.

For the drainage case, Fig.(5.9) shows the dispersion relation for base solutions in Fig.(4.15(b) & (d)) with varying λ. As mentioned earlier the drainage base solutions represent two qualitatively different type of TW-solutions. Those solutions representative of non-classical 'under-compressive' shocks, which were observed in the higher range of λ, are found to be stable towards transverse perturbations. Whereas, the solutions representative of non-classical 'expansion' shocks, at the lower range of λ, are found to be unstable within a particular range of wave numbers, k, in spite of those base solutions being monotonic. Among the latter, for the range of λ studied, as λ is increased the range of unstable wave numbers increased along with the wave number of the fastest growing perturbation, k_f. From Fig.(5.10) for $k = 150$, it can be observed that for higher values of λ the eigen function has a lower peak and a wider spread along ξ representing a weaker perturbation that renders the flow unstable. It can be noted that this tendency is contrary to what was observed in the imbibition case.

While the subsequent growth of an initial disturbance is governed by non-linearities inherent to the model, in the context of linearized analysis it can be expected that the wave number of the ensuing fingering instability at late times would be close to that of the fastest growing perturbation,

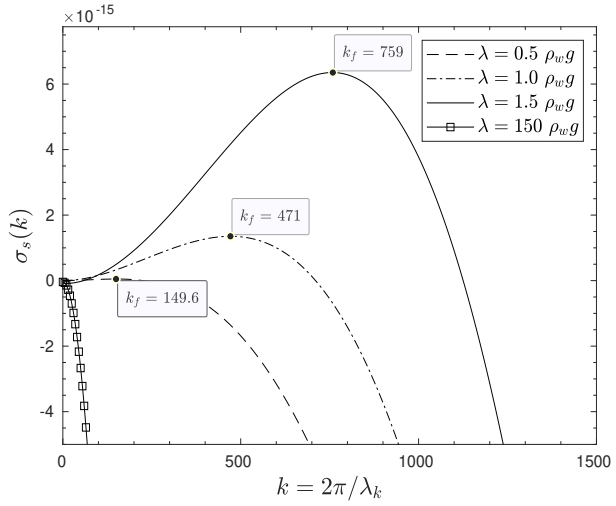

Figure 5.9: Dispersion curves of drainage solutions for $\lambda = 0.5\rho_w g, \rho_w g, 1.5\rho_w g, 150\rho_w g$. Peaks that represent maximal positive growth rate are shown as filled dots on the curves, with their respective wave number, k_f, labeled.

k_f. Also the upper bound of the range of unstable wave numbers serves as a critical wave number beyond which any perturbations decay. In this sense, linear stability analysis serves as tool to identify the minimum size of the transverse dimension of a porous medium domain in order to be able to invoke and observe fingering phenomenon. Taking cue from the above results, two-dimensional PDE simulations in Chp.(6) were initialized within appropriately sized domains and with an imposed transversal perturbation superposing a few random wave numbers in the neighborhood of k_f in order to accelerate the onset of instabilities.

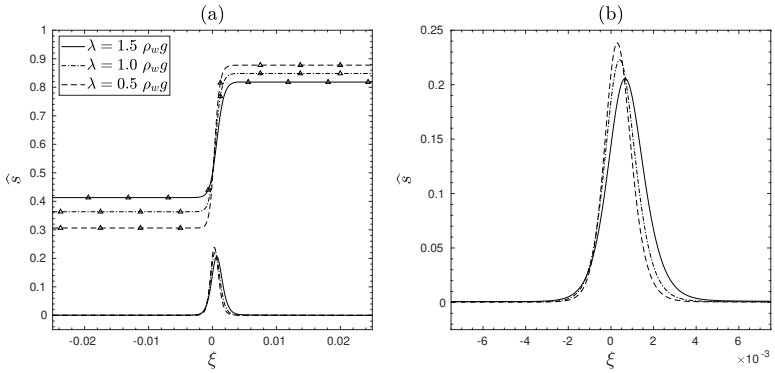

Figure 5.10: (a) Eigen functions, $\widehat{s}$, of the drainage solutions for $k = 150$, $\lambda = 0.5\rho_w g, \rho_w g, 1.5\rho_w g$. The corresponding base solutions, s_0, shown with triangle markers, are also plotted here for reference, (b) close-up view showing the structure of eigen functions in the vicinity of their peaks.

5.2 STABILITY AGAINST LONGITUDINAL PERTURBATIONS

As can be observed from the structure of the base solutions of the TW-problem, there exist regions of uniform saturation degree ahead and behind the front. The solution within these regions is subject to instability in the presence of longitudinal perturbations such as the oscillatory non-monotonicities observed in base solutions in the vicinity of the front, see Fig.(4.14). Such instability triggers the formation of banks of fluid perpendicular to the direction of motion of the front, which further destabilize transversely to form bubbles behind the front. Also, when a front destabilizes due to transverse perturbations, as analyzed in Sec.(5.1), their ensuing growth forms fingers, see Chp.(6). Along the length of those fingers, there is also a region behind their tips within which the saturation degree is uniform. The solution within this region can as well destabilize due to longitudinal perturbations resulting in breakup of those fingers into droplets. This is akin to the now well-studied Plateau-Rayleigh instability that explains jets of liquid destabilizing and forming coalesced droplets (Eggers and Villermaux, 2008). In order to analyze the onset of such instabilities in the current context, we consider a longitudinally perturbed solution, $S(x,t)$, of Eq.(4.9), in the vicinity of a constant and uniform base solution, S_0, and expand it in a regular series,

$$S(x,t) = S_0 + \epsilon S_1(x,t) + \epsilon^2 S_2(x,t)\ldots, \tag{5.9}$$

about the base solution, with ϵ now being the magnitude of longitudinal perturbation. Introducing such perturbed solution into Eq.(4.8), and further assuming that the perturbation is small compared to the base solution results in an $O(\epsilon)$ perturbed equation,

$$\phi\frac{\partial S_1}{\partial t} + K_0'\frac{\partial S_1}{\partial x} - \frac{\delta_R}{C_a}K_0\mu_{e0}'\frac{\partial^2 S_1}{\partial x} + \frac{\delta_R}{C_a}\phi D_{NL}K_0\frac{\partial^4 S_1}{\partial x^4} = 0, \tag{5.10}$$

that governs $S_1(x,t)$. Here as well, functions sub-scripted $(.)_0$ are to be understood as evaluated with the base solution.

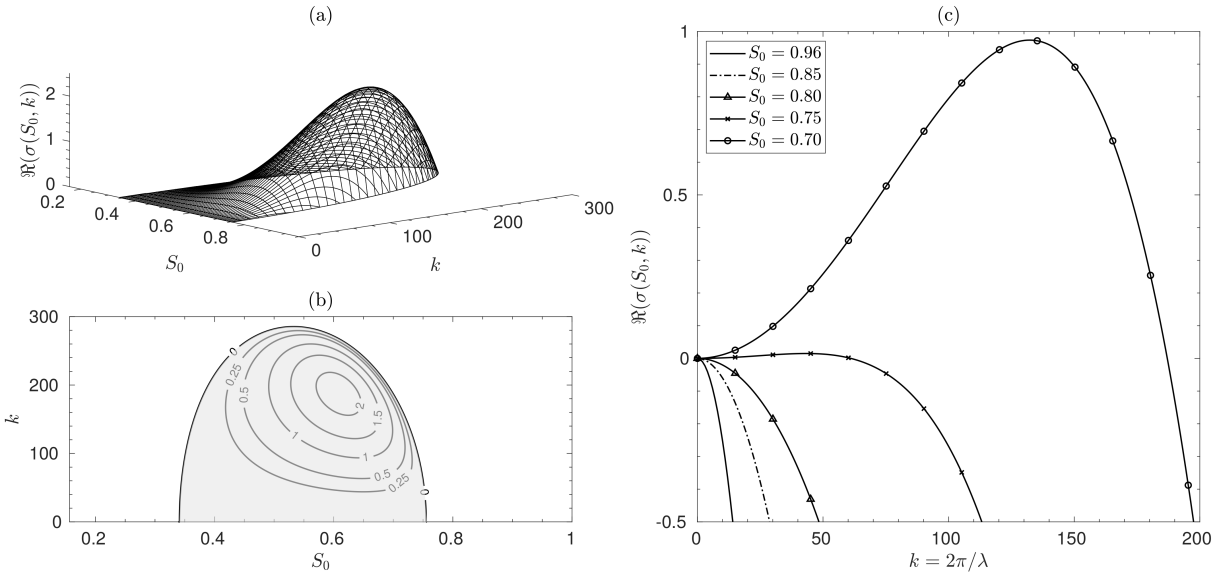

Figure 5.11: (a) The relation Eq.(5.12) plotted in the space of (S_0, k, $\Re(\sigma)$). Only the unstable region, $\Re(\sigma) > 0$, is shown. (b) Contour plot of the same relation projected on the plane (S_0, k). The unstable region satisfying Eq.(5.13) is shaded grey. (c) Dispersion curves plotted for uniform base solutions $S_0 = 0.96, 0.85, 0.80, 0.75, 0.70$.

In order to analyze if a longitudinally harmonic perturbation would grow/decay asymptotically in time, the following form is assumed for the $O(\epsilon)$ perturbation,

$$S_1(x,t) = e^{ikx+\sigma t}, \tag{5.11}$$

where k is characteristic wave number of the disturbance in x-direction and σ is its exponential growth factor in time. Introducing Eq.(5.11) into Eq.(5.10) results in an expression for the growth factor in terms of the base solution and the wave number,

$$\sigma(S_0,k) = \frac{1}{\phi}\left\{ -\frac{\delta_R}{C_a}K_0\left(\mu'_{e0}k^2 + \phi D_{NL}k^4\right) - ikK'_0\right\}. \tag{5.12}$$

Similar to what was noted in the Sec.(5.1) for transverse perturbations, any longitudinal perturbation resulting in $\Re(\sigma) > 0$ is to be understood as growing exponentially in time leading to instability about the uniform base solution. Fig.(5.11), shows the graph of the relation Eq.(5.12) in the space of $(S_0, k, \Re(\sigma))$. For certain values of S_0 there exist a range of wave numbers k for which $\Re(\sigma) > 0$. This region of instability, shaded grey in Fig.(5.11(b)), is given by the relation,

$$\mu'_{e0} < -\phi D_{NL}k^2, \tag{5.13}$$

between the slope of the effective chemical potential evaluated at S_0 and the square of the wave number. Fig.(5.11(c)) shows the dispersion relations in the space of $(k, \Re(\sigma))$ for uniform saturation values, S_0, observed as left boundary conditions, s_-, in the base solutions corresponding to imbibition in Fig.(4.14). For $S_0 = 0.70, 0.75$ there is a range of k for which $\Re(\sigma) > 0$. While the respective base solutions for both these cases exhibit oscillations when leaving the uniform equilibrium state $(s_-, 0, 0)$, it will be shown further using two dimensional simulations in Chp.(6) that only the oscillations in the case $s_- = 0.70$ are within the range of k that trigger the instabilities behind the front.

5.3 SYNOPSIS

In the current chapter a systematic linear stability analysis is presented of the solutions of the extended Richards' equation developed in Sec.(3.2). The solutions analyzed were both of imbibition and drainage. Transverse stability analysis of the imbibition solutions has indicated that they are sensitive to imposed infiltration flux as observed in the experiments. On the other hand for the drainage front a larger range of imposed pressure gradient was studied and the drainage front seemed to stabilize at very high pressure gradients. An analytical result was also presented for the stability of one-dimensional uniform base solutions against longitudinal perturbations in the direction of propagation of the front. This result indicated on the possibility of destabilization of the solutions within a particular range of uniform values of the base solutions which could result in the formation of trapped regions of dissimilar saturation in higher dimensions. In the following chapter two-dimensional simulations are done for that verify the results of the above stability analysis.

6 TWO-DIMENSIONAL SIMULATIONS

CONTENTS

6.1 Imbibition fronts 68
6.2 Drainage fronts 71
6.3 Synopsis 74

ABSTRACT

In the current chapter two-dimensional numerical simulations of the extended Richards' equation are presented with an intention to verify the results of stability analysis done in Chp.(5). The simulation results reveal fluid fingering phenomenon for the boundary and initial conditions which are found to be unstable in the stability analysis against transverse perturbations. Further due to the double-well nature of the fluid energy a rich structure of fluid invasion is revealed as predicted in the stability analysis against longitudinal perturbations.

In this chapter we use numerical simulations as a means to examine the non-linear growth of perturbations to a base solution in a two-dimensional spatial setting. To do this the two-dimensional domain is initiated with a field of $S_r(x, y)$ involving a smooth jump along the x-direction and extending homogeneously in the y-direction, that represents a transition from one fluid phase to another. To this field, perturbations dependent on y-direction are superposed, that are sinusoidal in nature involving a few randomized wave lengths. This perturbed initial condition is representative of physically realistic conditions where the air-water interface in a porous medium is not independent of y-direction owing to intrinsic heterogeneities. However, it is to be noted that these imposed perturbations are only spatial in nature and does not involve perturbations in the value of S_r itself.

The numerical method and discretization scheme are the same as that of the one-dimensional PDE simulations in Sec.(4.4) where the weak formulations are written in a general manner. The material properties and dimensionless numbers are as well utilized from Tables.(4.1 & 4.2) respectively. The details of the discretization domain, boundary and initial conditions for each case are detailed further.

6.1 IMBIBITION FRONTS

The computational domain used for imbibition simulations is a rectangle, such that $x \in [0, 1]$ and $y \in [0, 0.3]$, whose physical dimensions correspond to a length of $L = 20$m and a height of $H = 6$m. Displacement of air by water representing imbibition can be understood as a solution which transitions from a higher degree of saturation to a lower one and moves in the direction of the lower saturation. In order to realize this, the domain is initialized with a solution $S_r(t = 0)$ involving a smooth jump along the x-direction, between

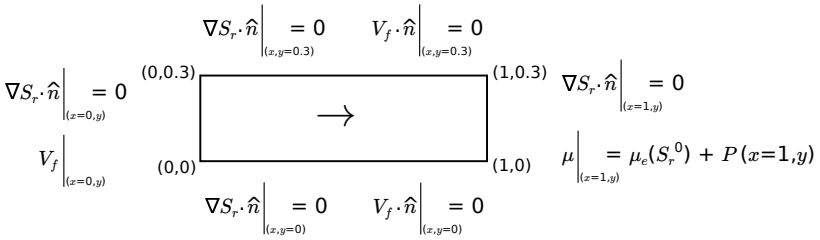

Figure 6.1: Schematic of the imbibition simulations showing boundary conditions imposed. The arrow indicates the direction of motion of the interface. The form of natural boundary condition $V_f(x = 0, y)$ is given in Eq.(6.1).

the saturation degree representing the infiltrating water, S_-, and that of an initial saturation degree of an almost dry domain, S_r^0, such that $S_- > S_r^0$. At $t = 0$, the region of the domain initialized with S_- is restricted to a thin layer at the infiltrating surface, $(x = 0, y)$ that is perturbed transversely in the y-direction with a few randomized wave lengths within the vicinity of the fastest growing wavelength, $\lambda_k(k_f)$, given by the linear stability analysis with boundary conditions $s_- = S_-$, $s_+ = S_r^0$. The initial condition for μ is such that $\mu(t = 0) = \mu_{pf}(S_r(t = 0)) + P$.

For all $t > 0$, the normal derivative of S_r is set to vanish at all the boundary surfaces. At the left boundary surface, $(x = 0, y)$, an injection velocity,

$$V_f\Big|_{(x=0,y)} = -\frac{\delta_R}{C_a} K(S_-)\nabla P, \tag{6.1}$$

is imposed. This has an effect of inducing imbibition with a uniform saturation degree of S_- while the normal derivative of μ_{pf} vanishes. The boundary at the right, $(x = 1, y)$, is drained with a Dirichlet boundary condition on μ such that

$$\mu\Big|_{(x=1,y)} = \mu_e(S_r^0) + P(x = 1, y). \tag{6.2}$$

The top, $(x, y = 0.3)$, and the bottom, $(x, y = 0)$, boundaries are impermeable. See schematic Fig.(6.1) for a summary of these boundary conditions.

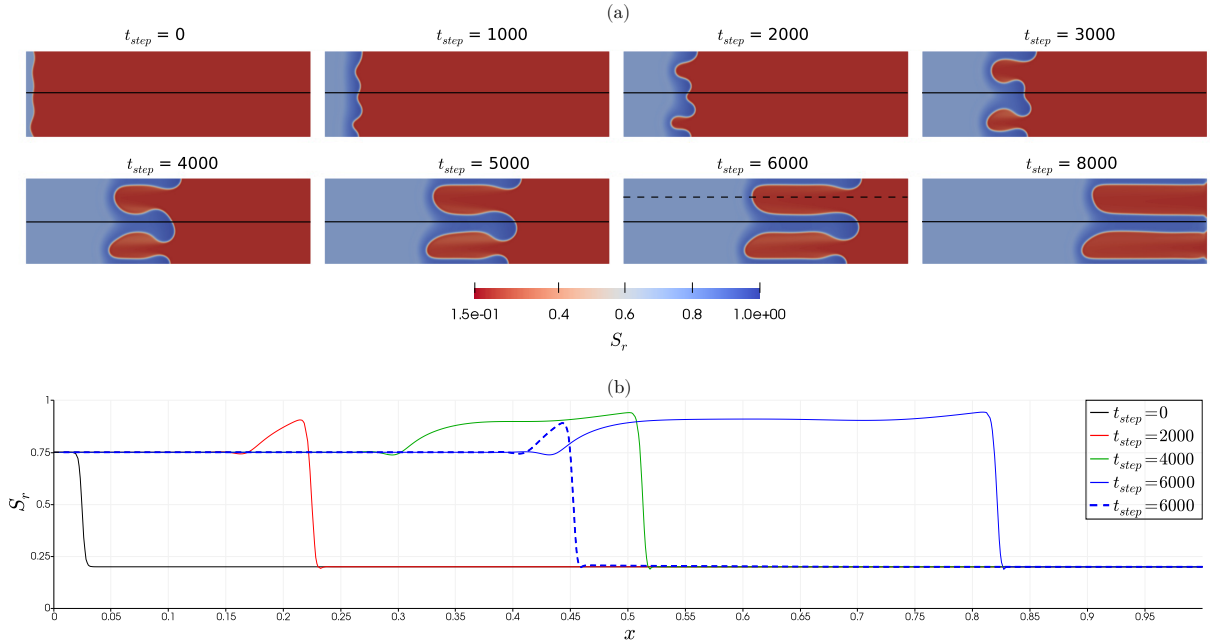

Figure 6.2: (a) Evolution of initial perturbation to an imbibition front for $S_- = 0.75$, $S_r^0 = 0.20$ on a domain $(x, y) \in ([0, 1], [0, 0.3])$, with time step size Δt = 2.0E-04, $\ell = 0.2$m and characteristic element size Δx = 2.5E-03 = $\ell/4$. Sequence shown is for increasing time step, t_{step}. The non-linear evolution involves formation of fingering like instability akin to observations in infiltration experiments. (b) Solution plotted along the length of the central finger in solid lines, $S_r(x, y = 0.15)$, and within the gap between the fingers in dashed line, $S_r(x, y = 0.23)$, at $t_{step} = 6000$.

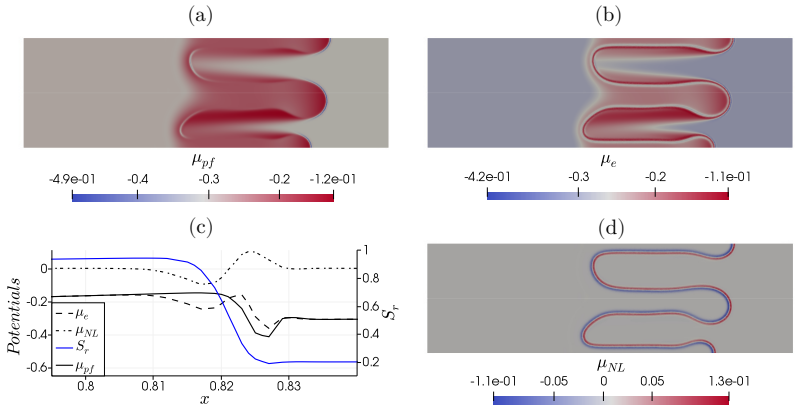

Figure 6.3: Dimensionless quantities corresponding to the imbibition front shown in Fig.(6.2) at $t_{step} = 6000$. (a) regularized effective chemical potential, μ_{pf}, (b) effective chemical potential, μ_e and (d) non-local potential, μ_{NL}. (c) These quantities plotted along the length of the central finger in the vicinity of its tip, ($x \in [0.795, 0.84]$, $y = 0.15$). The non-monotonicities in S_r and μ_{pf} are not apparent due to this restricted spatial view.

Fig.(6.2) shows such a perturbed initial condition for the case of $S_- = 0.75$, $S_r^0 = 0.20$ and its evolution for $t > 0$ under the above boundary conditions and $\lambda = \rho_w g$. The perturbations grow in time forming fingers within the domain that are similar to observations in infiltration experiments into initially dry sand (Glass et al., 1989b; Selker et al., 1992). This model indicates that these ensuing fingers are more saturated than the region behind. Also, the advancing tips of the fingers are of higher saturation than the region within the finger itself. These observations are inline with the experimental saturation profiles of fingers detected using light transmission by Glass et al. (1989a). The saturation profile within the space between the fingers, see Fig.(6.2(b)), is significantly different from that within the finger itself and is also closer to that of the one-dimensional base solution. These intricate comparisons of the saturation profiles are yet to be realized using meticulously designed experiments.

The solution of μ_{pf} along with its constituent local and non-local components is shown in Fig.(6.3) at $t_{step} = 6000$, along with a comparative plot within the vicinity of the tip of the central finger. It is clear that while the effective chemical potential, μ_e, is non-monotonic owing to the non-convex local fluid energy, the non-local chemical potential, μ_{NL}, compensates by following the convexity of S_r, in accordance with Eq.(4.3). Along the sides of the fingers, the fringe region, the solution indicates regions of higher μ_e. This is a consequence of higher saturation degree within this fringe region compared to that of the initially dry region, S_r^0, see Fig.(6.2(a)). This fringe region as well coincides with the passage of the distinctive swell of the finger tip at an earlier time step.

The linear stability analysis in Sec.(5.1) indicates that as the injection velocity, V_f, is increased from the intermediate range, the spacing between

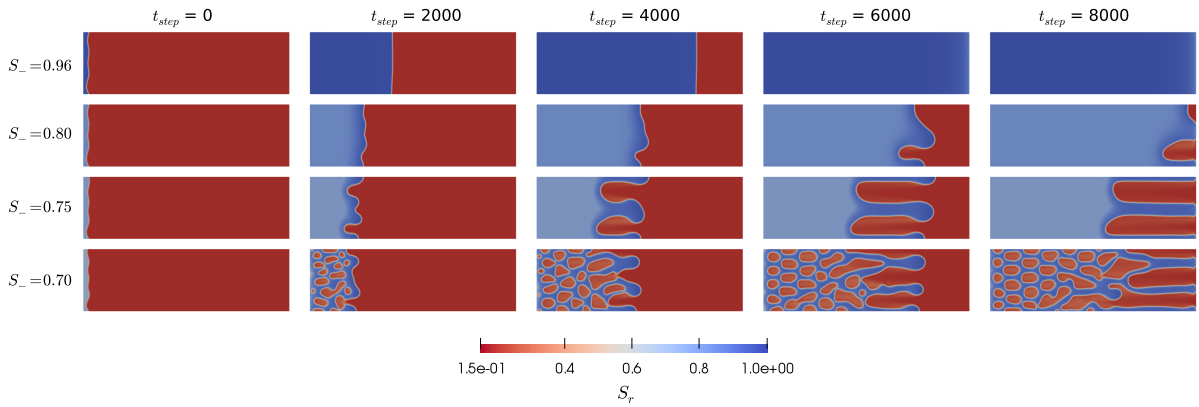

Figure 6.4: Evolution of initial perturbation to imbibition fronts for injection velocities corresponding to Eq.(6.1) for $S_- \in [0.70, 0.96]$ (to be read row-wise), $S_r^0 = 0.20$ on a domain $(x, y) \in ([0, 1], [0, 0.3])$, for increasing time step, t_{step}.

the fingers increases and their growth rate decreases, effectively suppressing the fingering phenomenon. This is verified in the two-dimensional problem, see Fig.(6.4), where as S_- in Eq.(6.1) is varied within the range $[0.70, 0.96]$, the same trend is observed. For the largest injection velocity, $S_- = 0.96$, the initial perturbations are completely suppressed and the imbibition front infiltrates the domain homogeneously.

An important correlation is observed between these solutions and the results of the linear stability analysis in Sec.(5.1). Specifically, the number of fingers that eventually appear after the non-linear growth for each S_-, see Fig.(6.4), is strikingly close to the predictions of linear stability analysis which, in principle, is applicable only in the early stages of growth of the perturbations. If this correlation is universally true for solutions of models that exhibit non-monotonic dispersion curves is a question that could potentially have important consequences.

For $S_- = 0.70$ the region behind the infiltrating front which is expected to have a uniform saturation degree of 0.70 is perturbed longitudinally due to the oscillations as seen in the one-dimensional solution, see Fig.(4.14). These oscillations are longitudinal in nature, as elaborated in Sec.(5.2), and grow in time while interacting non-linearly with the infiltrating front. The result of this kind of instability and the non-linear interactions is the formation of bubble like trapped regions of lower saturation, see last row of Fig.(6.4).

6.2 DRAINAGE FRONTS

The computational domain used for drainage simulations is a rectangle, such that $x \in [0, 1]$ and $y \in [0, 0.15]$, whose physical dimensions correspond to a length of $L = 20$m and a height of $H = 3$m. Drainage of water by air is understood as the contrary of imbibition, which is a transition from lower saturation degree to higher, moving in the direction of the higher saturation. So the initial condition, $S_r(t = 0)$, is chosen similar to that of imbibition, with a smooth jump along the x-direction in the saturation degree from S_- to S_r^0 such that $S_- < S_r^0$. The initially saturated region of the domain is assumed to be close to full saturation, $S_r^0 = 0.99$. The region that is relatively dry, $S_r(x, y) = S_-$, is restricted to a thin layer at the left boundary, $(x = 0, y)$. Similar to imbibition, this initial condition is perturbed with randomly chosen wave lengths within the vicinity of the fastest growing wave length indicated by the linear stability analysis. The initial condition for μ is such that $\mu(t = 0) = \mu_{pf}(S_r(t = 0)) + P$.

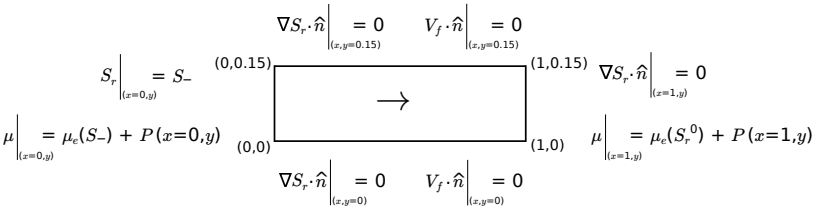

Figure 6.5: Schematic of the drainage simulations showing boundary conditions imposed. The arrow indicates the direction of motion of the interface.

Owing to the phase field parameter, S_r, of the current model being representative of the saturation degree of the wetting fluid, an injection flux of the form Eq.(4.20) at the boundary would not be appropriate to induce drainage. Instead the imposed linear pressure, P, is allowed to drive the drainage front across the domain by choosing appropriate boundary conditions. See schematic Fig.(6.5). For all $t > 0$, at the left boundary surface, $(x = 0, y)$, Dirichlet boundary conditions are setup with $S_r(x = 0, y) = S_-$ and

$$\mu\Big|_{(x=0,\,y)} = \mu_e(S_-) + P(x = 0, y). \tag{6.3}$$

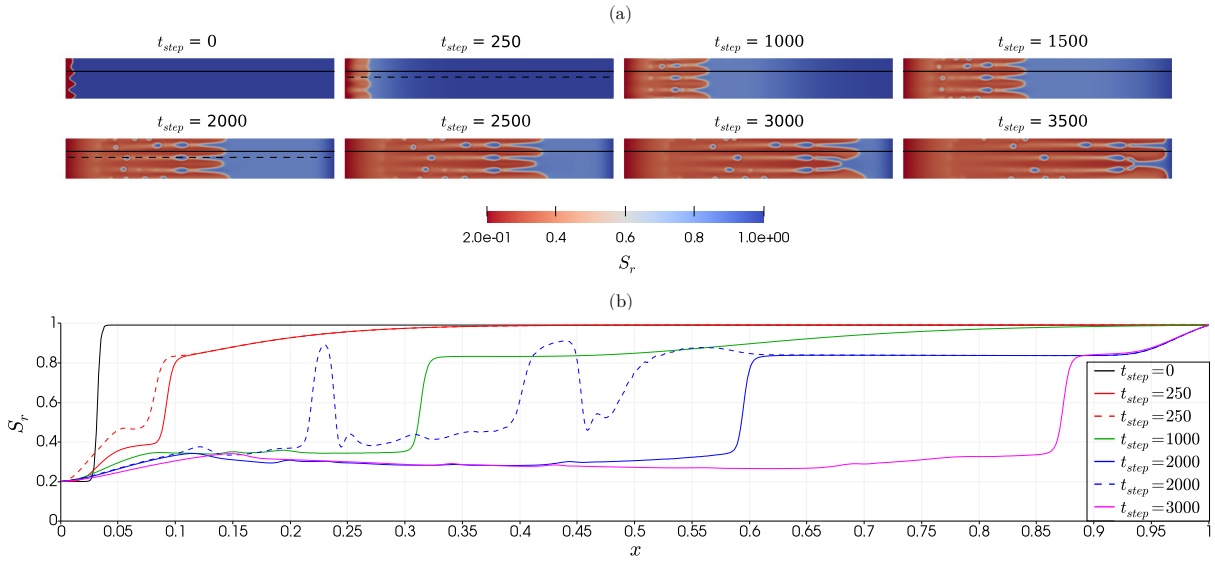

Figure 6.6: (a) Evolution of initial perturbation to a drainage front for $S_- = 0.20$, $S_r^0 = 0.99$ on a domain $(x, y) \in ([0, 1], [0, 0.15])$, with Δt = 5.5E-04, $\ell = 0.2$m and Δx = 2.5E-03 = $\ell/4$. Sequence shown is for increasing time step, t_{step}. (b) Solution plotted along the length of the second finger from top in solid lines, $S_r(x, y = 0.1)$, and within the gap between the fingers in dashed line, $S_r(x, y = 0.0775)$, at $t_{step} = 250, 2000$.

The boundary at the right, $(x = 1, y)$, is drained with a Dirichlet boundary condition on μ, Eq.(6.2), and the normal derivative of S_r is set to vanish, similar to the imbibition case. These set of boundary conditions have an effect of inducing extraction of water at the right boundary that is consistent with the imposed pressure gradient, while the normal derivative of μ_{pf} vanishes. The top, $(x, y = 0.15)$, and the bottom, $(x, y = 0)$, boundaries are impermeable and the normal derivative of S_r is as well set to vanish.

Fig.(6.6) shows the evolution of $S_r(x, y)$ for $t > 0$ of a perturbed initial condition, for the case of $S_- = 0.20$, under the above boundary conditions and for $\lambda = 1.5\rho_w g$. The solution along the length of the domain is consistent with one-dimensional PDE solutions in Chp.(4), with a self-similar traveling wave part connecting a lower saturation degree, S_b, to a higher, S_a, which represents a non-classical 'expansion' shock and this is connected on either side up to the boundary by expanding parts of the solution. However, the traveling wave part of the solution along the length of the finger has a different lower value compared to that of within the gap between the fingers, see Fig.(6.6(b)) $t_{step} = 250$, the latter being consistent with the one-dimensional base solution for the imposed boundary conditions in the current problem, see Fig.(4.15(b)). In fact, a one-dimensional traveling wave connecting S_b to S_a that correspond to the solution along the length of the finger would have a higher speed, approximated by Eq.(4.12), compared to that of within the gap between the fingers, which explains the higher speed of the advancing tip of the finger compared to its base.

As the solution evolves, formation and detachment of droplet like structures occurs between the fingers. This is due to the growth of longitudinal perturbations to the part of the solution, $S_r(x, y = 0.0775) = S_b \approx 0.45$,

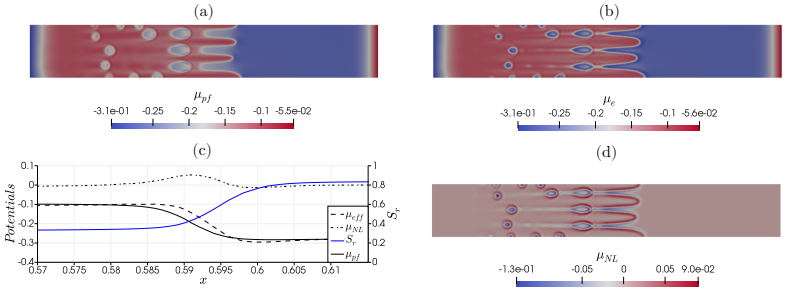

Figure 6.7: Dimensionless quantities corresponding to the drainage front shown in Fig.(6.6) at $t_{step} = 2000$. (a) regularized effective chemical potential, μ_{pf}, (b) effective chemical potential, μ_e and (d) non-local potential, μ_{NL}. (c) These quantities plotted along the length of the second finger from top in the vicinity of its tip, ($x \in [0.57, 0.615]$, $y = 0.1$).

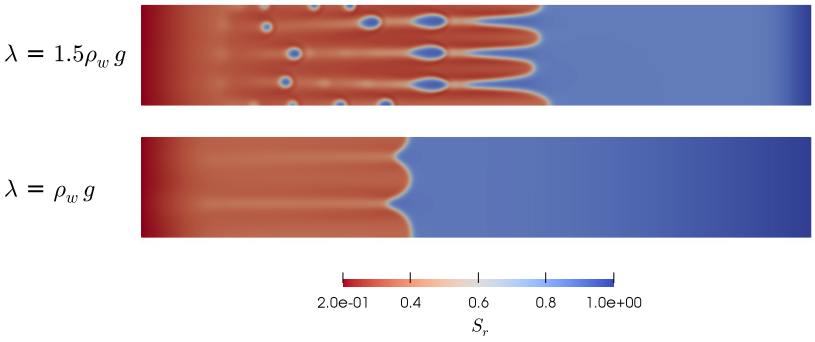

Figure 6.8: Evolution of initial perturbation to drainage fronts for gradient of imposed pressure distribution $\lambda = \rho_w g, 1.5\rho_w g$, $S_r^0 = 0.20$ on a domain $(x, y) \in ([0, 1], [0, 0.15])$, at $t_{step} = 2000$.

between the diffused interface and the expanding region on the left. As noted in Chp.(4), the origin of longitudinal oscillations in this region is related to the nature of the equilibrium state associated to S_b of the dynamical system formed by the ODE (4.26). These oscillations tend to grow because $S_b \approx 0.45$ is clearly within the unstable region of uniform base solutions dictated by Eq.(5.13), see Sec.(5.2). This is not true for the solution along the length of the finger because the corresponding $S_b \approx 0.35$.

Similar to the imbibition case, the effective chemical potential, μ_e, is non-monotonic and the non-local chemical potential, μ_{NL}, follows the convexity of S_r, taking positive values just behind the diffused interface as can be seen in Fig.(6.7). In order to verify the prediction of the linear stability analysis done in Sec.(5.1), we present here the evolution of the solution S_r for different values of the gradient of imposed pressure distribution, λ. Inline with the prediction, as λ is decreased from $1.5\rho_w g$, the finger spacing is reduced resulting in thicker fingers that grow slower, see Fig.(6.8).

However, if λ is increased drastically the arbitrary initial perturbations to the diffused drainage front decay in time, see Fig.(6.9). It is to be noted that for $\lambda = 150\rho_w g$ the diffused front connects between $S_r \approx 0.8$ and the initial saturation degree of $S_r = 0.99$, see Fig.(4.15(d)), which is indicative of non-classical 'under-compressive' shock. The decay of initial perturbation is revealed by the reduction, as the solution evolves, of the spatial gap at the diffused interface due to the imposed perturbation at $t_{step} = 0$. The

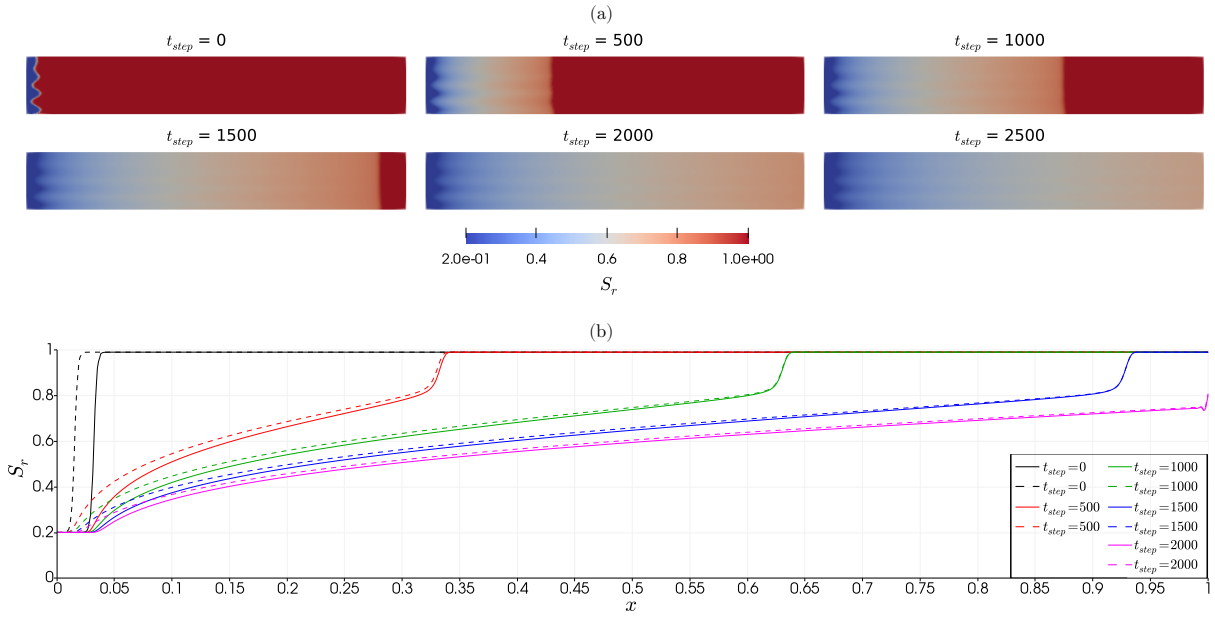

Figure 6.9: (a) Evolution of initial perturbation to a drainage front for $S_- = 0.20$, $S_r^0 = 0.99$ on a domain $(x, y) \in ([0, 1], [0, 0.15])$, with $\Delta t =$ 5.5E-04, $\ell = 0.2$m and $\Delta x =$ 2.5E-03 $= \ell/4$. Sequence shown is for increasing time step, t_{step}. (b) Solution, $S_r(x, y = 0.1)$ and $S_r(x, y = 0.0775)$, plotted along the length of the domain in solid lines and dashed lines respectively. The spatial gap between these two solutions represents the initial perturbation at $t_{step} = 0$ and its evolution for all $t_{step} > 0$.

expanding rarefaction part of the solution behind the diffused front does not seem to follow the same rate of decay resulting in persistence of the initial disturbance at the left end of this part of the solution.

6.3 SYNOPSIS

In this chapter two-dimensional numerical results were presented which were based on a finite element implementation. These results verify those of the linear stability analysis with respect to finger sizes observed and stabilization of the front when expected. The rich structure of the solutions is attributed to the various energy contributions that encompass the non-uniform fluid potential. While the results were inline with the existing experimental observations, the model predicts additional features that maybe observed during air-water displacements. Detailed experiments are warranted both in imbibition and drainage in order to investigate these predictions.

PART III
MECHANICAL INSTABILITIES

7

GRADIENT DAMAGE MODELING OF TENSILE FRACTURE

CONTENTS

7.1 Mathematical model 77
7.1.1 Gradient damage modeling setup 77
7.1.2 Transient hydraulic problem 79
7.1.3 Evolution problem 80
7.1.4 First-order stability & necessary conditions 81
7.1.5 Tension-Compression split 83
7.1.6 Fracture toughness & related assumptions 84
7.2 Numerical approximation & Algorithm 85
7.3 Two-dimensional desiccation problem 86
7.3.1 Problem setup 87
7.3.2 Results 88
7.4 Synopsis 90

ABSTRACT

Initiation and evolution of complex fracture networks is ubiquitous in geomaterials, especially during drainage. This chapter presents an application of gradient damage modeling in order to study initiation of fractures in the context of drainage induced partial saturation in porous media. The study starts with a modeling approach that envisages drainage induced mode-I fractures as caused by the build up of tensile stresses. Following this the evolution problem for damage is derived employing three principles underlying the variational approach to damage: irreversibility of damage, stability and energy balance. The governing equations of the problem are derived as the first-order optimality conditions of the evolution problem. A numerical discretization scheme and algorithm are presented followed by a two-dimensional test case. The results portray the bifurcation and eventual localization of the damage into a series of well-spaced fractures originating at the drainage boundary and propagating into the drying porous skeleton driven by desaturation. The results also show qualitative similarity with observations in experimental desiccation tests. While the presented modeling approach remains a simplistic one, it is contended in Ch.(8) regarding its applicability to fine-grained soils which do not sustain significant tensile stresses when close to full saturation and an alternative underlying phenomenon is explored.

In this chapter the phase field model of partial saturation is not adopted and the starting points of the current development are the classical poromechanical approach to partial saturation (see Sec.(3.1)), and the now well studied gradient damage modeling of brittle fracture (see Marigo et al. (2016) for an overview). In addition to this we work under an overarching

assumption of a hydrophilic porous skeleton whose pore spaces are filled by two fluids, air and water, between which air is considered passive and the hypothesis of small perturbations is assumed as detailed in Sec.(3.1.4).

7.1 MATHEMATICAL MODEL

Apart from the hydraulic problem related to the fluid flow, the modeling developed in this chapter is done specifically considering the porous skeleton. This is done adopting the hypothesis of energy separation as explained in Sec.(3.1.5). A free energy density of a partially saturated deformable porous skeleton is thus identified as a state function, $G_s(\varepsilon, \pi)$. The corresponding state equations are the constitutive laws Eq.(3.28) and Eq.(3.32), respectively for the dual variables total stress, $\sigma(\varepsilon, \pi)$, and Lagrangian porosity, $\phi(\varepsilon, \pi)$, recapitulated below for easy reference.

$$\sigma - \sigma_0 = \sigma_e - b(\pi - \pi_0)I, \qquad \text{with } \sigma_e(\varepsilon) = \mathbb{C} : (\varepsilon - \varepsilon_0), \tag{7.1}$$

$$\phi - \phi_0 = b(\epsilon - \epsilon_0) + \frac{1}{N}(\pi - \pi_0), \text{ with } \pi(p_w, S_w) = p_w S_w - U(S_w). \tag{7.2}$$

Notwithstanding this modeling choice, it is to be noted that an equivalent formulation can be derived considering the porous solid (the so-called 'wetted' porous skeleton which comprises the skeleton and a thin layer of fluid attached to it) starting from $\Psi_s(\varepsilon, \phi, S_w)$. This alternative approach is pursued in Ch.(8) to serve the investigation of a specific phenomenon.

7.1.1 Gradient damage modeling setup

We consider an n_d-dimensional domain, $\Omega \in \Re^{n_d}$, representing the initial configuration of a damaging isotropic partially saturated porous skeleton whose boundary is denoted by $\partial\Omega$. Now, in line with standard gradient damage modeling (Marigo et al., 2016) and the theory of partially saturated poroelasticity, the following considerations are done:

1. The scalar internal variable, $\alpha \in [0, 1]$, is assigned the role of describing the extent of damage. $\alpha = 0$ denotes an intact healthy skeleton. Whereas, $\alpha = 1$ denotes a fractured skeleton whose stiffness is degraded and can only sustain vanishing stresses.

2. For a given unit volume of the porous skeleton in its reference configuration the bulk energy density, W_s, is a state function characterized by: $(\varepsilon, \pi, \alpha, \nabla\alpha)$, respectively the linearized strain tensor, the equivalent pore pressure, the damage variable and the gradient of damage.

3. The porous skeleton is assumed to be dissipative in a non-local sense due to the dependency of the bulk energy density on the gradient of damage. The particular expression of the bulk energy density is assumed to be:

$$W_s(\varepsilon, \pi, \alpha, \nabla\alpha) = G_s(\varepsilon, \pi, \alpha) + w(\alpha) + \frac{1}{2} w_1 \ell^2 \nabla\alpha \cdot \nabla\alpha. \tag{7.3}$$

   The different terms of the above expression are explained below.

   (a) With an abuse of notation $G_s(\varepsilon, \pi, \alpha)$ now denotes the elastic energy density of the damaging porous skeleton which, as mentioned earlier, encompasses the contribution due to the deformation of the porous skeleton resulting in solid strains and changes in equivalent pore pressure accounting for the consequence of formation/annihilation of interfaces. A possible form this energy

density that gives back the proper constitutive relations as its state equations reads as,

$$G_s(\varepsilon, \pi, \alpha) = \frac{1}{2}a(\alpha)(\varepsilon - \varepsilon_0) : \mathbb{C} : (\varepsilon - \varepsilon_0) - b(\epsilon - \epsilon_0)\Delta\pi - \frac{1}{2N}\Delta\pi^2 - \phi_0\pi, \tag{7.4}$$

where the notations are borrowed from Sec.(3.1.5). $\Delta\pi$ represents the increment of equivalent pore pressure, $(\pi - \pi_0)$. α_0 is a priori assumed to be a null field associated to an initially undamaged skeleton. $\mathbb{C}$ is the stiffness tensor of the undamaged skeleton and its inverse, the compliance tensor, is denoted $\mathbb{S}$. $a(\alpha)$ denotes a damage law that, when α grows from 0 to 1, degrades the elastic energy density responsible for solid strains to a vanishing value. While various choices of the functional form of $a(\alpha)$ are possible, we make a specific choice following Pham et al. (2011a),

$$a(\alpha) = (1 - \alpha)^2 + k_\ell, \tag{7.5}$$

where k_ℓ is a small positive constant used solely for numerical purposes to govern the fully damaged state. The consequence on the damage evolution due to the above choices is discussed further.

(b) The second term in Eq.(7.3) is the local part of the dissipated energy,

$$w(\alpha) = w_1\alpha, \tag{7.6}$$

growing from 0 when $\alpha = 0$, to a positive constant $w_1 < +\infty$ when $\alpha = 1$. Thus in accordance with the developments in Pham et al. (2011a), since $w'(\alpha) > 0$ there exists an elastic phase preceding damage initiation and the finiteness of w_1 ensures that the energy dissipated during a homogeneous evolution of α from 0 to 1 is as well finite. The significance and possible motivation for the magnitude of this constant is discussed at a later moment.

(c) The last term in Eq.(7.3) is the non-local dissipation, which is assumed to be a quadratic function of the gradient of α, and is intended to regularize the local model allowing localizations of finite thickness. ℓ appears with the physical dimension of a length that in the context of gradient damage modeling is intended to control the localization thickness.

4. The dual relations associated to the state variables in Eq.(7.3) are obtained as follows,

$$\begin{aligned}
\frac{\partial W_s}{\partial \varepsilon} &= a(\alpha)\mathbb{C} : (\varepsilon - \varepsilon_0) - b\Delta\pi I, \\
\frac{\partial W_s}{\partial \pi} &= -b(\epsilon - \epsilon_0) - \frac{1}{N}\Delta\pi - \phi_0, \\
\frac{\partial W_s}{\partial \alpha} &= \frac{1}{2}a'(\alpha)(\varepsilon - \varepsilon_0) : \mathbb{C} : (\varepsilon - \varepsilon_0) + w'(\alpha), \\
\frac{\partial W_s}{\partial (\nabla\alpha)} &= w_1\ell^2\nabla\alpha.
\end{aligned} \tag{7.7}$$

According to the developments in Pham and Marigo (2013), the above choices of the functional forms of $a(\alpha)$ and $w(\alpha)$ result in a material behavior that is characterized by finiteness of the energy dissipated during a full

process of homogeneous damage and stress-softening. This latter property of stress-softening (resp. strain-hardening) requires that the elastic domain in the stress space (resp. strain space) is a decreasing (resp. increasing) function of α. These spaces within the current context can be written employing the local part of the energy density, $\widehat{W}_s(\varepsilon, \pi, \alpha) := W_s(\varepsilon, \pi, \alpha, \nabla\alpha = 0)$, as,

$$\mathcal{R}(\alpha) = \left\{\varepsilon \in \mathbb{M}_s : \frac{\partial \widehat{W}_s}{\partial \alpha} \geq 0\right\}, \quad \mathcal{R}^*(\alpha) = \left\{\sigma \in \mathbb{M}_s : \frac{\partial \widehat{W}_s^*}{\partial \alpha} \leq 0\right\}, \tag{7.8}$$

where $\mathbb{M}_s$ represents the space of symmetric second-order tensors. $\widehat{W}_s^*$ is the conjugate of $\widehat{W}_s$ obtained employing a Legendre-Fenchel transformation about the pair (σ, ε),

$$\widehat{W}_s^*(\sigma, \pi, \alpha) = \sup_{\bar{\varepsilon} \in \mathbb{M}} \{\sigma : \bar{\varepsilon} - \widehat{W}_s(\bar{\varepsilon}, \pi, \alpha)\}. \tag{7.9}$$

Utilizing the expression of $\widehat{W}_s(\varepsilon, \pi, \alpha)$ derived from Eq.(7.3) the transformation Eq.(7.9) can be identified as,

$$\begin{aligned}\widehat{W}_s^*(\sigma, \pi, \alpha) = \frac{1}{a(\alpha)}\left(\frac{1}{2}\sigma : \mathbb{S} : \sigma + b\mathrm{tr}(\mathbb{S} : \sigma)\Delta\pi + \frac{1}{2}b^2\mathrm{tr}(\mathbb{S} : I)\Delta\pi^2\right) \\ + \frac{1}{2N}\Delta\pi^2 + \phi_0\pi - w(\alpha),\end{aligned} \tag{7.10}$$

and the elastic domains Eq.(7.8) can be obtained explicitly,

$$\begin{aligned}\mathcal{R}(\alpha) &= \left\{\varepsilon \in \mathbb{M}_s : (\varepsilon - \varepsilon_0) : \mathbb{C} : (\varepsilon - \varepsilon_0) \leq \frac{w_1}{1-\alpha}\right\}, \\ \mathcal{R}^*(\alpha) &= \left\{\sigma \in \mathbb{M}_s : \sigma : \mathbb{S} : \sigma + 2b\ \mathrm{tr}(\mathbb{S} : \sigma)\Delta\pi + b^2\mathrm{tr}(\mathbb{S} : I)\Delta\pi^2 \leq w_1(1-\alpha)^3\right\},\end{aligned} \tag{7.11}$$

As α grows from 0, it is clear that the elastic domain in the total stress space reduces. This indicates a total stress-softening behavior of the model as damage evolves. As well, it is interesting to note the dependency of the elastic domain in the total stress space on the equivalent pore pressure, π, and consequently on the saturation degree of the wetting fluid, S_w. This is because the total stress, $\sigma(\varepsilon, \pi)$, as mentioned earlier, involves a negative contribution due to the equivalent pore pressure, along with the effective stress, $\sigma_e(\varepsilon)$, which is the same as that of an ordinary elastic solid. This dependency on the equivalent pore pressure can be recast into a dependency on the solution of the fluid flow problem which is discussed further.

7.1.2 Transient hydraulic problem

The hydraulic part of the problem involves the spatio-temporal evolution of the fluids within the porous skeleton under the influence of gradients within fluid pressures and imposed fluxes at the boundaries. Bulk force due to gravity is neglected for this purpose. Since, we assume a passive and rarefied air phase, the hydraulic problem reduces to the solution of the Richards' equation for deformable porous skeleton. The corresponding developments were detailed in Sec.(3.1.8).

In particular the governing PDE, Eq.(3.49), for the evolution of saturation degree of wetting fluid, $S_w(x, t)$, is recapitulated below,

$$\frac{\partial(\phi S_w)}{\partial t} + \frac{\varkappa}{\eta_w}\nabla \cdot k_w(S_w)\left(\nabla p_c(S_w)\right) = 0, \tag{7.12}$$

written in the "mixed water content" form and in the absence of gravity.

In the current chapter a specific choice is done in order to reduce the non-linearity of the otherwise highly non-linear equation above. This concerns the algorithm utilized to resolve it numerically. The negative capillary pressure is replaced by the wetting fluid pressure, $p_w(x,t) = -p_c(S_w)$, which is considered also as an unknown. See Sec.(3.1.8) for similar developments leading to the "head" form of the Richards' equation. Consequently, we arrive at the following PDE with two unknowns, $S_w(x,t)$ and $p_w(x,t)$,

$$\frac{\partial(\phi S_w)}{\partial t} - \frac{\varkappa}{\eta_w}\nabla \cdot k_w(S_w)\,(\nabla p_w) = 0. \tag{7.13}$$

As detailed further in Sec.(7.2), an iterative approach is taken by first considering $S_w(x,t)$ as a known quantity and solving the above equation for $p_w(x,t)$, in tandem with the mechanical problem for displacements of the solid skeleton. While doing this $k_w(S_w)$ is also a known function through Eq.(3.35) and $\phi(p_w, S_w)$ is given by the constitutive law Eq.(7.2).

Appropriate boundary conditions accompany the resolution of Eq.(7.13), which could be either an imposed flux representing a natural boundary condition or an imposed pressure representing an essential boundary condition. Once $p_w(x,t)$ is resolved, $S_w(x,t)$ is obtained algebraically through the inverse retention relation Eq.(3.26) recapitulated below,

$$S_w(p_w) = p_c^{-1}(p_w), \tag{7.14}$$

The iterations are then repeated until convergence.

> *Remark:* The state variable π of the problem related to the skeleton, see Eq.(7.3), is obtained from the solution pair, (p_w, S_w), of the dissipative fluid flow problem. Thus at every time $t > 0$, the solution of the hydraulic problem acts as an instantaneous input to the poromechanical damage problem through the parametrization of π. Consequently the bulk energy density in Eq.(7.3) can be rewritten as,
>
> $$W_s(\varepsilon, \alpha, \nabla\alpha; \pi) = G_s(\varepsilon, \alpha; \pi) + w(\alpha) + \frac{1}{2} w_1 \ell^2 \nabla\alpha \cdot \nabla\alpha. \tag{7.15}$$
>
> All the developments done earlier still hold true under such parametrization.

7.1.3 Evolution problem

Assuming that the transient hydraulic problem is resolved to obtain π, we now focus on the evolution problem for the pair, (u, α). This is written using a variational approach similar to the developments in Pham and Marigo (2010a,b). The principles governing the evolution are elaborated for the current problem which now concerns the porous skeleton.

The variational approach is based on a total energy of the porous skeleton associated to admissible pair of states $(v, \beta) \in \mathcal{C} \times \mathcal{D}$. These functional spaces are defined as,

$$\begin{aligned} \mathcal{C} &= \{v \in H^1(\Omega)^{n_d} : v = 0 \text{ on } \partial\Omega_D\}, \\ \mathcal{D} &= \{\beta \in H^1(\Omega) : 0 \leq \beta < 1 \text{ in } \Omega\}, \end{aligned} \tag{7.16}$$

where $H^1(\Omega)$ is the Sobolev space of square integrable functions whose weak gradients are also square integrable. $\partial\Omega_D \subseteq \partial\Omega$ where displacement, u, is imposed.

This definition of total energy at each time t is given as the integral over the whole domain of the bulk energy density minus the potential of external forces. In the absence of volume forces and surface forces acting respectively on Ω and its boundary $\partial\Omega$, the potential of external forces vanishes and the total energy at a given time t reads,

$$\mathcal{E}_t(v,\beta) = \int_\Omega W_s^t(v,\beta,\nabla\beta;\pi_t(p_t,S_t))\,dx, \tag{7.17}$$

Parametrization w.r.t π_t of $\mathcal{E}_t(v,\beta)$ is understood implicitly.[1]

> *Remark:* We assume that all the fields are sufficiently smooth in time allowing for the following developments. Also we consider only the states of damage where $\alpha < 1$ and the saturation degree $S_w > 0$. This is done so that in the following analysis the total energy remains finite.

The variational approach developed in Pham and Marigo (2010a,b) for the evolution in Ω of $(u_t,\alpha_t) \in \mathcal{C}\times\mathcal{D}$ for all $t \geq 0$ is then governed by the three principles of irreversibility of damage, stability and energy balance that read:

(a) *Irreversibility of damage:* $t \mapsto \alpha_t$ must be non-decreasing. Consequently the admissible states accessible from α_t can be defined as,

$$\mathcal{D}_t = \{\beta \in H^1(\Omega) : \alpha_t \leq \beta < 1 \text{ in } \Omega\}. \tag{7.18}$$

(b) *Stability:* The state (u_t,α_t) must be directionally stable in the sense that for all $(v,\beta)\in\mathcal{C}\times\mathcal{D}_t$, there exists $\overline{h} > 0$, such that,

$$\forall h \in [0,\overline{h}], \quad \mathcal{E}_t(u_t + h(v-u_t), \alpha_t + h(\beta-\alpha_t)) \geq \mathcal{E}_t(u_t,\alpha_t). \tag{7.19}$$

(c) *Energy Balance:* During the evolution $t \mapsto (u_t,\alpha_t)$ the following energy balance must hold,

$$\mathcal{E}_t(u_t,\alpha_t) = \mathcal{E}_0(u_0,\alpha_0) \tag{7.20}$$

where (u_0,α_0) denotes the state of the skeleton at time $t = 0$.

7.1.4 First-order stability & necessary conditions

The stability condition Eq.(7.19) essentially means that in the total energy landscape, within the immediate neighborhood of the state (u_t,α_t) all the admissible states are of either higher or equal energy compared to that of (u_t,α_t). Assuming this neighborhood, governed by h, to be small, one can expand the perturbed energy and rewrite Eq.(7.19) as,

$$h\mathcal{E}_t'(u_t,\alpha_t)(v-u_t,\beta-\alpha_t) + \frac{h^2}{2}\mathcal{E}_t''(u_t,\alpha_t)(v-u_t,\beta-\alpha_t)^2 + o(h^2) \geq 0. \tag{7.21}$$

$\mathcal{E}_t'$ and $\mathcal{E}_t''$ represent respectively the first and second directional derivatives of $\mathcal{E}_t$ further referred to as FDD and SDD respectively for compactness. The representation $\mathcal{E}_t''(u_t,\alpha_t)(\bullet)^2$ is to be understood as a shorthand for the quadratic form whereas the associated symmetric bi-linear form is represented $\mathcal{E}_t''(u_t,\alpha_t)\langle\bullet,\bullet\rangle$ i.e., the application of $\mathcal{E}_t''(u_t,\alpha_t)$ to the pair of

[1] Pore pressure, p_w, and Saturation degree, S_w, of the wetting fluid at time t are further denoted in this chapter by p_t and S_t respectively in order not to overload the notation.

directions $\langle \bullet, \bullet \rangle$. The directional derivatives in Eq.(7.21) have the following forms in the general direction $(\widehat{v}, \widehat{\beta})$,

$$\mathcal{E}_t'(u_t, \alpha_t)(\widehat{v}, \widehat{\beta}) = \int_\Omega \left\{ \frac{\partial W_s^t}{\partial \varepsilon} : \varepsilon(\widehat{v}) + \frac{\partial W_s^t}{\partial \alpha} \widehat{\beta} + \frac{\partial W_s^t}{\partial (\nabla \alpha)} \cdot \nabla \widehat{\beta} \right\} dx, \tag{7.22}$$

$$\begin{aligned} \mathcal{E}_t''(u_t, \alpha_t)(\widehat{v}, \widehat{\beta})^2 = \int_\Omega \Big\{ & a(\alpha_t)\varepsilon(\widehat{v}) : \mathbb{C} : \varepsilon(\widehat{v}) + 2a'(\alpha_t)(\varepsilon_t - \varepsilon_0) : \mathbb{C} : \varepsilon(\widehat{v})\widehat{\beta} \\ & + \frac{1}{2} a''(\alpha_t)(\varepsilon_t - \varepsilon_0) : \mathbb{C} : (\varepsilon_t - \varepsilon_0)\widehat{\beta}^2 + w_1 \ell^2 \nabla \widehat{\beta} \cdot \nabla \widehat{\beta} \Big\} dx. \end{aligned} \tag{7.23}$$

In Eq.(7.22) the partial derivatives of bulk energy density are functions of state (u_t, α_t) given by Eq.(7.7).

Dividing Eq.(7.21) by h and passing to the limit $h \longrightarrow 0$ gives,

$$\mathcal{E}_t'(u_t, \alpha_t)(v - u_t, \beta - \alpha_t) \geq 0, \tag{7.24}$$

which is the so-called first-order stability condition and can be viewed as characterizing stationarity of the state (u_t, α_t). In Eq.(7.24) testing with $\beta = \alpha_t$ and noting that C is a linear space can obtain the variational (weak) form of the classical equilibrium condition,

$$\int_\Omega \frac{\partial W_s^t}{\partial \varepsilon} : \varepsilon(v - u_t) dx = 0, \qquad \forall\, (v - u_t) \in C, \tag{7.25}$$

where the total stress tensor can obviously be identified as,

$$\sigma_t = \frac{\partial W_s^t}{\partial \varepsilon} = a(\alpha)\mathbb{C} : (\varepsilon_t - \varepsilon_0) - b\,[\pi_t - \pi_0]\, I. \tag{7.26}$$

Using Eq.(7.25) in Eq.(7.24) gives the variational form of the non-local damage criterion,

$$\int_\Omega \left\{ \frac{\partial W_s^t}{\partial \alpha} (\beta - \alpha_t) + \frac{\partial W_s^t}{\partial (\nabla \alpha)} \cdot \nabla (\beta - \alpha_t) \right\} dx \geq 0, \qquad \forall\, \beta \in \mathcal{D}_t \tag{7.27}$$

Employing classical localization arguments of calculus of variations one can obtain from Eq.(7.25) and Eq.(7.27) the following local (strong) forms respectively with corresponding boundary conditions,

$$\nabla \cdot \sigma_t = 0 \quad \text{in } \Omega, \quad \sigma_t \cdot \hat{n} = 0 \quad \text{on } \partial\Omega \backslash \partial\Omega_D, \tag{7.28}$$

$$\frac{1}{2} a'(\alpha_t)(\varepsilon_t - \varepsilon_0) : \mathbb{C} : (\varepsilon_t - \varepsilon_0) + w'(\alpha_t) - w_1 \ell^2 \Delta \alpha_t \geq 0 \text{ in } \Omega, \ \frac{\partial \alpha_t}{\partial \hat{n}} \geq 0 \text{ on } \partial\Omega, \tag{7.29}$$

where $\hat{n}$ denotes the outwards unit normal vector associated to part of the boundary wherever invoked. Note the absence of surface and volume forces in the equilibrium equation according to earlier assumption.

Since we have assumed the evolution is smooth in time, taking a time derivative of the *Energy balance* leads to,

$$\begin{aligned} 0 = & \frac{d}{dt} \mathcal{E}_t(u_t, \alpha_t) \\ = & \int_\Omega \left\{ \frac{\partial W_s^t}{\partial \varepsilon} : \varepsilon(\dot{u}_t) + \frac{\partial W_s^t}{\partial \alpha} \dot{\alpha}_t + \frac{\partial W_s^t}{\partial (\nabla \alpha)} \cdot \nabla \dot{\alpha}_t \right\} dx. \end{aligned} \tag{7.30}$$

Integrating by parts the gradient terms and further using the local form of the equilibrium equations Eq.(7.28) gives,

$$0 = \int_{\Omega} \left\{ \frac{\partial W_s^t}{\partial \alpha} - \nabla \cdot \frac{\partial W_s^t}{\partial (\nabla \alpha)} \right\} \dot{\alpha}_t dx + \int_{\partial\Omega} \left(\frac{\partial W_s^t}{\partial (\nabla \alpha)} \cdot \hat{n} \right) \dot{\alpha}_t dx. \tag{7.31}$$

Owing to the irreversibility of damage everywhere in Ω and the local inequalities Eq.(7.29), the two integrals on the right-hand side of the above equation are non-negative. So, both of them should vanish. Further using classical localization arguments we obtain the so-called consistency conditions or the Karush-Kuhn-Tucker (KKT) conditions applicable everywhere in Ω and on the boundary $\partial\Omega$ respectively,

$$\begin{aligned} \left(\frac{1}{2} a'(\alpha_t)(\varepsilon_t - \varepsilon_0) : \mathbb{C} : (\varepsilon_t - \varepsilon_0) + w'(\alpha_t) - w_1 \ell^2 \Delta \alpha_t \right) \dot{\alpha}_t = 0 \quad &\text{in } \Omega. \\ \frac{\partial \alpha_t}{\partial \hat{n}} \dot{\alpha}_t = 0 \quad &\text{on } \partial\Omega. \end{aligned} \tag{7.32}$$

These conditions can be read in tandem with the *Irreversibility of damage*. The first condition states that everywhere in Ω, damage increases only if the local form of the damage criterion Eq.(7.29) is an equality and if it is a strict inequality then damage does not increase. The second condition states that everywhere on the boundary, $\partial\Omega$, if damage increases then the spatial derivative normal to the boundary vanishes.

7.1.5 Tension-Compression split

The regularized model for fracture with unilateral contact at the fracture faces proposed in Amor et al. (2009) is adopted here with an intention to avoid possible interpretation of the fracture faces. This is based on the decomposition of the strain tensor into its spherical and deviatoric components,

$$\varepsilon = \frac{1}{n_d} \epsilon I + \varepsilon_D. \tag{7.33}$$

Further a decomposition of ϵ into positive, $\epsilon_+ = 0.5(\epsilon + |\epsilon|)$, and negative, $\epsilon_- = 0.5(\epsilon - |\epsilon|)$, parts is done to distinguish the contributions within elastic energy density due to dilation and compression. Affecting the degradation due to damage only to the contributions due to dilation and shear is shown (Amor et al., 2009) to avoid crack interpenetration by predicting asymmetric results under traction and compression tests. Such a split of energy density is adopted such that,

$$\begin{aligned} G_s(\varepsilon, \pi, \alpha) &= a(\alpha) G_s^+(\varepsilon) + G_s^-(\varepsilon, \pi), \\ G_s^+(\varepsilon) &= \frac{1}{2} K \epsilon_+^2 + \mu \varepsilon_D : \varepsilon_D, \\ G_s^-(\varepsilon, \pi) &= \frac{1}{2} K \epsilon_-^2 - b \epsilon \Delta\pi - \frac{1}{2N} \Delta\pi^2 - \phi_0 \pi, \end{aligned} \tag{7.34}$$

in the absence of pre-strain. K and μ are respectively the bulk and shear moduli of the intact skeleton.

While the earlier developments still remain valid, the above split amounts to two modifications. The first one concerns the state equations. Specifically, Eqs.(7.7(a) & (c)) are modified to,

$$\begin{aligned} \frac{\partial W_s}{\partial \varepsilon} &= a(\alpha) \left(K \epsilon_+ I + 2\mu \varepsilon_D \right) + K \epsilon_- I - b \Delta\pi I, \\ \frac{\partial W_s}{\partial \alpha} &= a'(\alpha) \left(\frac{1}{2} K \epsilon_+^2 + \mu \varepsilon_D : \varepsilon_D \right) + w'(\alpha). \end{aligned} \tag{7.35}$$

The total stress tensor and the effective stress tensor now read respectively as,

$$\begin{aligned} \sigma &= \sigma_e - b\Delta\pi I, \\ \sigma_e &= a(\alpha)\left(K\epsilon_+ I + 2\mu\varepsilon_D\right) + K\epsilon_- I. \end{aligned} \tag{7.36}$$

The resulting elastic domains within the stress and strain spaces, Eq.(7.11), are modified to,

$$\begin{aligned} \mathcal{R}(\alpha) =& \left\{ \varepsilon \in \mathbb{M}_s : K\epsilon_+^2 + 2\mu\varepsilon_D : \varepsilon_D \leq \frac{w_1}{1-\alpha} \right\}, \\ \mathcal{R}^*(\alpha) =& \left\{ \frac{\mathrm{tr}_+(\sigma)^2}{n_d^2 K} + \frac{1}{2\mu}\sigma_D : \sigma_D + \frac{2b}{n_d K}\left[\mathrm{tr}_-(\sigma)\Delta\pi_+ + \mathrm{tr}_+(\sigma)\Delta\pi\right] \right. \\ & \left. + \frac{b^2}{K}\Delta\pi_+^2 \leq w_1(1-\alpha)^3 \right\}, \end{aligned} \tag{7.37}$$

where $\Delta\pi_\pm = 0.5(\Delta\pi \pm |\Delta\pi|)$ and $\mathrm{tr}_\pm(\sigma) = 0.5(\mathrm{tr}(\sigma) \pm |\mathrm{tr}(\sigma)|)$.

The second modification concerns the damage criterion, Eq.(7.29), and the KKT conditions in the bulk, Eq.(7.32(a)). Due to the above split these conditions are now written respectively as,

$$a'(\alpha)\left(\frac{1}{2}K\epsilon_+^2 + \mu\varepsilon_D : \varepsilon_D\right) + w'(\alpha_t) - w_1\ell^2\Delta\alpha_t \geq 0 \text{ in } \Omega, , \tag{7.38}$$

$$\left(a'(\alpha)\left(\frac{1}{2}K\epsilon_+^2 + \mu\varepsilon_D : \varepsilon_D\right) + w'(\alpha_t) - w_1\ell^2\Delta\alpha_t\right)\dot{\alpha}_t = 0 \quad \text{in } \Omega. \tag{7.39}$$

7.1.6 Fracture toughness & related assumptions

Fracture in the context of gradient damage models is understood as the localization of damage over a finite length controlled by the internal length, ℓ. In the works of Pham and Marigo (2013); Marigo et al. (2016) a link between fracture toughness, G_c, of a material and damage localization has been derived by explicitly constructing the total energy of a non-homogeneous damage evolution in one-dimension and passing to the limit of zero stress within a localized zone representative of a fracture. The energy dissipated in the creation of a single fracture is then identified with G_c. The following relation is thus arrived at in a more general setting of damage laws,

$$G_c = c_w \frac{\ell w_1}{\sqrt{2}} \quad \text{with} \quad c_w = 4\int_0^1 \sqrt{\frac{w(\beta)}{w_1}}\, d\beta. \tag{7.40}$$

For the particular forms of the damage laws chosen, Eqs.(7.5 & 7.6), the above relation reads,

$$G_c = \frac{4\sqrt{2}}{3} w_1 \ell, \quad c_w = \frac{8}{3}. \tag{7.41}$$

A similar analysis in the current context would lead to an identification of G_c which is not just dependent on the damage laws chosen but also on the saturation degree through the dependency on equivalent pore pressure. Such a dependency was proposed in the work of Cajuhi et al. (2018). In fact, in the experimental work of Lakshmikantha et al. (2012) it has been observed that fracture toughness of soils decreases exponentially with increasing water content. Also, in a uni-axial tension test one can infer from Eq.(7.37) that the elastic limit stress, σ_e, beyond which damage starts to initiate is linked to π.

In the current work we make a simplifying assumption that the G_c remains constant and the above relations are used to rephrase the total energy as,

$$\mathcal{E}(u,\alpha) = \int_\Omega \left\{ a(\alpha)\left(\frac{1}{2}K\epsilon_+^2 + \mu\varepsilon_D : \varepsilon_D\right) + \frac{1}{2}K\epsilon_-^2 - b\epsilon\Delta\pi - \frac{1}{2N}\Delta\pi^2 - \phi_0\pi \right\} dx + \sqrt{2}\frac{G_c}{c_w}\int_\Omega \left\{ \frac{1}{\ell}\frac{w(\alpha)}{w_1} + \frac{\ell}{2}w_1\ell^2\nabla\alpha\cdot\nabla\alpha \right\} dx, \tag{7.42}$$

7.2 NUMERICAL APPROXIMATION & ALGORITHM

When it comes to numerical resolution, in standard gradient damage modeling the minimization problem for the non-convex total energy potential is recast into two separate minimizations problems, w.r.t u and α, both of which are convex when the other variable is considered a constant. A popular algorithm for this purpose is the alternating algorithm proposed by Bourdin et al. (2000). In the current context given that the total energy is formulated considering the hydraulic problem as providing instantaneous input through the resolution of π, one can see that the alternating algorithm can be adapted for the minimization of $\mathcal{E}(u,\alpha)$ given by Eq.(7.42), w.r.t u and α separately subject to the unilateral constraint of *irreversibility of damage* and appropriate boundary conditions.

Given the solution triplet $(u_{n-1}, \pi_{n-1}, \alpha_{n-1})$ of the solid and fluid problems at time-step $(n-1)$, Alg.(1) describes the alternating algorithm to obtain the solution at time-step n. At each alternating iteration i, the nonlinear coupled problem for solid displacement and equivalent pore pressure, (u_n^i, π_n^i), is resolved using an iterative approach (hereafter referred to as the poro-split iterations) as mentioned earlier in Sec.(7.1.2). Specifically this coupled problem is recast into two sub-problems at each poro-split iteration k: a linear coupled problem for $({u_n^i}^k, {p_n^i}^k)$ and an algebraic problem for $({S_n^i}^k)$.

The pair $({u_n^i}^k, {p_n^i}^k)$ are obtained by resolving the equilibrium equation, Eq.(7.28), in tandem with the transient fluid flow equation, Eq.(7.13), both with appropriate boundary conditions. The time derivative within Eq.(7.13) is discretized using the implicit Euler scheme of first-order with time-step size Δt. This coupled problem can be viewed as a saddle-point problem (Miehe et al., 2015) which demands a certain stability to the finite element approximation, especially in the case of undrained situations with Biot coefficient close to unity, $b \approx 1$, in which case the problem is closer to in-compressible elasticity. Even though we do not intend to encounter such a limit case, the stability issue can be resolved by adhering to the celebrated LBB condition (Brezzi and Fortin, 1991), which can be practically implemented by choosing a finite element interpolation with higher polynomial degree for u compared to p. While other choices are possible, we employ a Taylor-Hood element pair with quadratic and linear Lagrange finite elements for u and p respectively. In order to resolve the coupled problem a sparse LU decomposition routine available in the FEniCS suite (Alnaes et al., 2015) is employed. Once ${p_n^i}^k$ is resolved $({S_n^i}^k)$ is obtained trivially through the algebraic relation Eq.(7.14) at the corresponding nodes. At the end of each poro-split iteration, the equivalent pore-pressure, ${\pi_n^i}^k$, at each node is obtained using Eq.(7.2). These iterations are repeated until convergence of the ℓ^2-norm of the maximum difference among the solutions of successive iterations, $\max\{\|({u_n^i}^k - {u_n^i}^{k-1})\|, \|({\pi_n^i}^k - {\pi_n^i}^{k-1})\|\}$.

Algorithm 1: Alternating algorithm for poromechanical gradient damage model

Input: $(u_{n-1}, \pi_{n-1}, \alpha_{n-1})$

➢ *initialization:* $(u_n^0, \pi_n^0, \alpha_n^0) \leftarrow (u_{n-1}, \pi_{n-1}, \alpha_{n-1})$;

➢ $i = 0$;

while *alternate algorithm not converged* **do**

- *initialization:* $({u_n^i}^0, {\pi_n^i}^0) \leftarrow (u_n^{i-1}, \pi_n^{i-1})$;
- $k = 0$;

while *poro-split algorithm not converged* | $\alpha_n = \alpha_n^{i-1}$ **do**

∗ Solve $({u_n^i}^k, {p_n^i}^k) := \{$Equlibrium, Eq.(7.28) & pressure evolution, Eq.(7.13)$\}$;

∗ Compute $S_n^{i\,k}({p_n^i}^k) := \{$Inverse retention relation, Eq.(7.14)$\}$;

∗ Compute $\pi_n^{i\,k}({p_n^i}^k, {S_n^i}^k) := \{$Equivalent pore pressure, Eq.(7.14)$\}$;

∗ $k \leftarrow k + 1$;

end

- *update:* $(u_n^i, \pi_n^i) \leftarrow ({u_n^i}^k, {\pi_n^i}^k)$;
- Solve $\alpha_n^i := \underset{\alpha}{\operatorname{argmin}}\ \mathcal{E}_n(u_n^i, \alpha) \mid \alpha_{n-1} \leq \alpha \leq 1$ in Ω;
- $i \leftarrow i + 1$;

end

➢ *update:* $(u_n, \pi_n, \alpha_n) \leftarrow (u_n^i, \pi_n^i, \alpha_n^i)$;

Output: (u_n, π_n, α_n)

The minimization problem for damage within each alternate iteration is posed as,

$$\alpha_n^i = \underset{\alpha}{\operatorname{argmin}}\ \mathcal{E}_n(u_n^i, \alpha) \mid \alpha_{n-1} \leq \alpha \leq 1 \text{ in } \Omega, \tag{7.43}$$

where the unilateral constraint $\alpha_{n-1} \leq \alpha \leq 1$ is the time-discrete version of the irreversibility of damage. The spatial discretization is done employing linear Lagrange elements with characteristic element size equal to half of the internal length, $\Delta x = 0.5\ell$. The above minimization problem is resolved using a bound-constrained optimization solver routine available as part of the TAO library (Balay et al., 2021). The convergence criterion of the alternating algorithm, at each iteration i, is the comparison against a tolerance, the ℓ^2-norm of the difference between the damage solutions of successive iterations, $\|(\alpha_n^i - \alpha_n^{i-1})\|$.

Table 7.1: Material properties, model parameters used through Chp.(7), unless mentioned otherwise.

property/ parameter	Clay
ϕ [−]	0.3
E [Pa]	5.0E06
ν [−]	0.4
b [−]	0.7
N [Pa]	9.26E07
$\varkappa$ [m^2]	1.0E-16
η_w [Pa.s]	8.9E-04
π_0 [Pa]	12500
m [−]	0.5
S_r^{res} [−]	0.0
G_c [N.m^{-1}]	0.2
ℓ [m]	0.002
k_ℓ [−]	1.0E-06

7.3 TWO-DIMENSIONAL DESICCATION PROBLEM

The above modeling approach is now applied to study the desiccation of soils. Typical desiccation experiments are done by subjecting a certain mass of fully saturated soil to air drying under controlled temperature and relative humidity. A few test cases of desiccation experiments can be found in the literature, Peron et al. (2009); Shin and Santamarina (2010, 2011a); Stirling (2014) to name a few. In what follows, we intend to verify if the modeling approach above results in localization of damage solutions thus allowing fracturing in drying soils. In order to definitely verify this, one would need to consider homogeneous solutions, at least along one direction and look for bifurcations leading to localizations in that particular direction.

A test case similar in construction is that of a thermal shock as studied by Sicsic et al. (2014) in which homogeneous damage along the surface of a ceramic plunged into a cold bath has been studied for possible bifurcations as time passes. We take inspiration from this study, to impose boundary conditions, as detailed in Sec.(7.3.1), such that drying of an initially saturated sample occurs homogeneously along the drying surface at initial times.

Further we consider a plane-strain assumption owing to the transverse dimension of the samples in all the experiments being larger than the vertical depth. This assumption does not affect drastically the above developments. Specifically, the in-plane stress components can still be obtained from the relation Eq.(7.26) with the definition of stiffness tensor in index notation,

$$\mathbb{C}_{ijkl} = \lambda\delta_{ij}\delta_{kl} + \mu(\delta_{ik}\delta_{jl} + \delta_{il}\delta_{jk}), \quad i,j,k,l \in \{1,2\}. \tag{7.44}$$

λ and μ are respectively the first and second Lamé parameters related to the empty porous skeleton. So, the boundary value problem formed by the coupled system of equations Eqs.(7.13, 7.28) and the bound-constrained minimization w.r.t α, Eq.(7.43), are resolved with appropriately defined boundary condition and initial conditions as laid out further in Sec.(7.3.1) and following the algorithm described in Alg.(1). The material properties of the porous medium and the parameters of the model chosen for the purpose of the simulations are listed in Table.(7.1), which are in the range typical of clays saturated with air-water mixture.

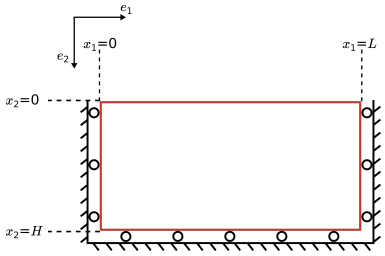

Figure 7.1: Reference configuration of the desiccation problem with mechanical boundary conditions depicted.

7.3.1 Problem setup

The reference initial configuration is a rectangular domain $\Omega = (0,L)\times(0,H)$ as shown in the Fig.(7.1) with the boundary $\partial\Omega = \{(x_1 = 0)\cup(x_1 = L)\cup(x_2 = 0)\cup(x_2 = H)\}$. At time $t = 0$ it is assumed that the porous skeleton is completely intact, stress free and fully saturated giving,

$$\alpha_0(x) = 0, \quad u_0(x) = 0, \quad \varepsilon_0(x) = 0, \quad \pi_0(x) = 0. \tag{7.45}$$

$x \in \Omega$ is the position vector given by $x = x_1e_1 + x_2e_2$. The horizontal and vertical displacements are set to vanish respectively on the lateral ($x_1 = 0$, $x_1 = L$) and the bottom ($x_2 = H$) faces along with the shear stresses at those boundaries. The top face at $x_2 = 0$ is a free surface. These set of mechanical boundary conditions $\forall t \geq 0$ read,

$$\begin{aligned} u_t \cdot e_1\big|_{(x_1=0)} = 0, \quad u_t \cdot e_1\big|_{(x_1=L)} = 0, \quad u_t \cdot e_2\big|_{(x_2=H)} = 0, \\ e_2 \cdot \sigma_t \cdot (-e_1)\big|_{(x_1=0)} = 0, \quad e_2 \cdot \sigma_t \cdot e_1\big|_{(x_1=L)} = 0, \\ \sigma_t \cdot (-e_2)\big|_{(x_2=0)} = 0, \quad e_1 \cdot \sigma_t \cdot e_2\big|_{(x_2=H)} = 0. \end{aligned} \tag{7.46}$$

Damage is not prescribed and is free to evolve at all the boundaries whenever the damage criterion is met. Accordingly the natural boundary condition on damage reads,

$$\left.\frac{\partial \alpha_t}{\partial \hat{n}}\right|_{x\in\partial\Omega} = 0 \quad \forall t \geq 0. \tag{7.47}$$

For the hydraulic problem, the lateral and bottom faces are set to be impermeable. The loading is done by a constant imposed suction, $\bar{p} < 0$, on the top face thus inducing a drying effect. These boundary conditions $\forall t \geq 0$ read,

$$\begin{aligned} \nabla p_t \cdot (-e_1)\big|_{(x_1=0)} = 0, \quad \nabla p_t \cdot e_1\big|_{(x_1=L)} = 0, \\ p\big|_{(x_2=0)} = \bar{p}, \quad \nabla p_t \cdot e_2\big|_{(x_2=H)} = 0. \end{aligned} \tag{7.48}$$

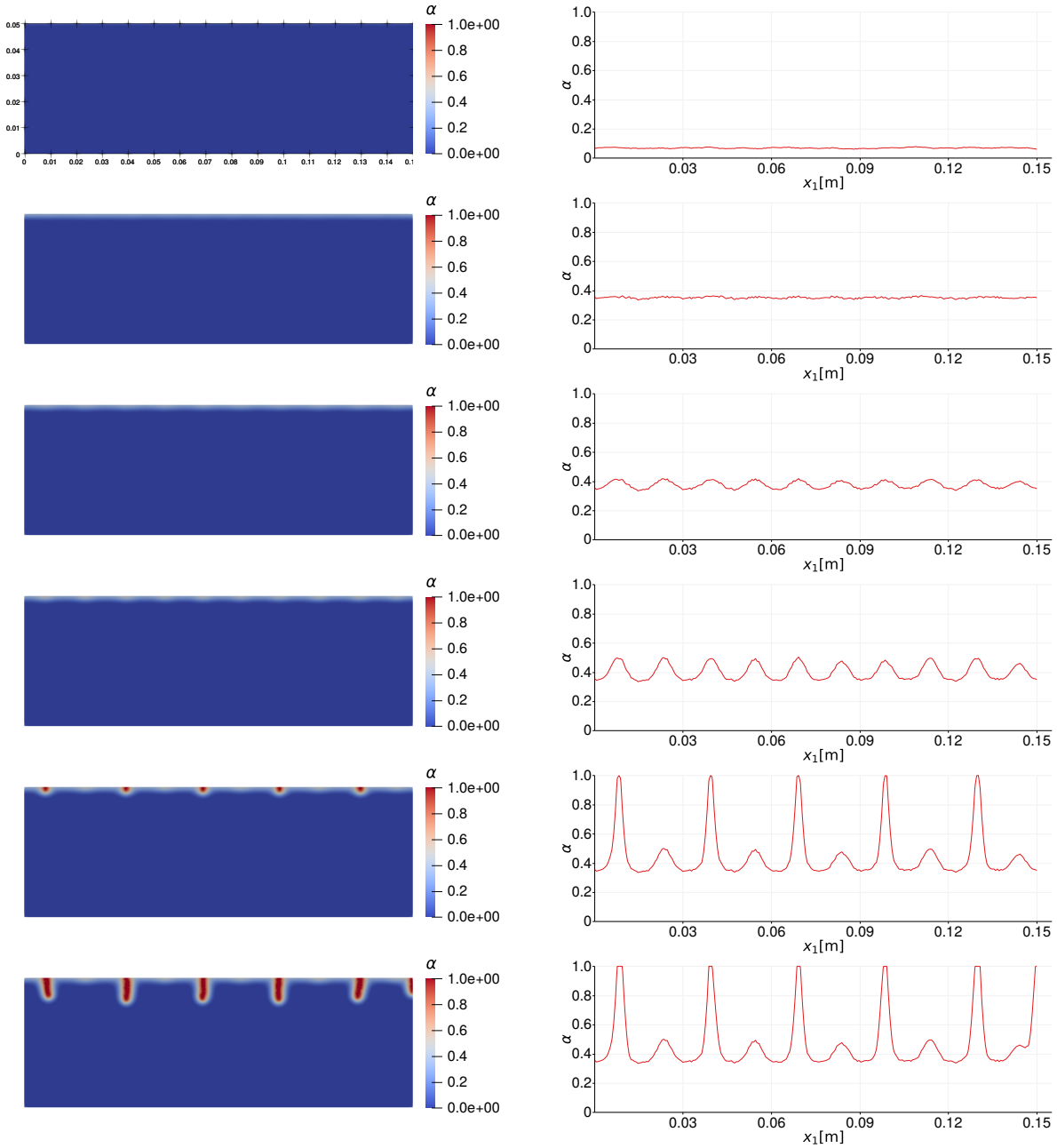

Figure 7.2: Evolution of the damage variable within the full domain (first column) and along the top boundary, $x_2 = 0$m (second column). The time corresponding to each row are $t = \{0.1, 0.8, 0.9, 1, 1.2, 10\}$s.

7.3.2 Results

It can be seen from the problem setup that the geometry, material properties and initial conditions are invariant along x_1-direction. The loading and boundary conditions on the top and bottom boundaries are as well invariant along x_1-direction. The boundary conditions on the lateral faces demand vanishing gradients of the solution along the x_1-direction. So, even though the problem does not render itself for obtaining an easy exact solution due to its non-linearity, one can a priori anticipate the existence of a particular class of solutions that are homogeneous in the x_1-direction and are dependent only on x_2. Bifurcation from such solutions would mean that at some time $t > 0$ a dependency of the solution on x_1 arises.

Fig.(7.2) shows the evolution of damage variable along the top surface $x_2 = 0$m, with $H = 0.05$m, $L = 0.15$m, $\bar{p} = -150$kPa. The discretization

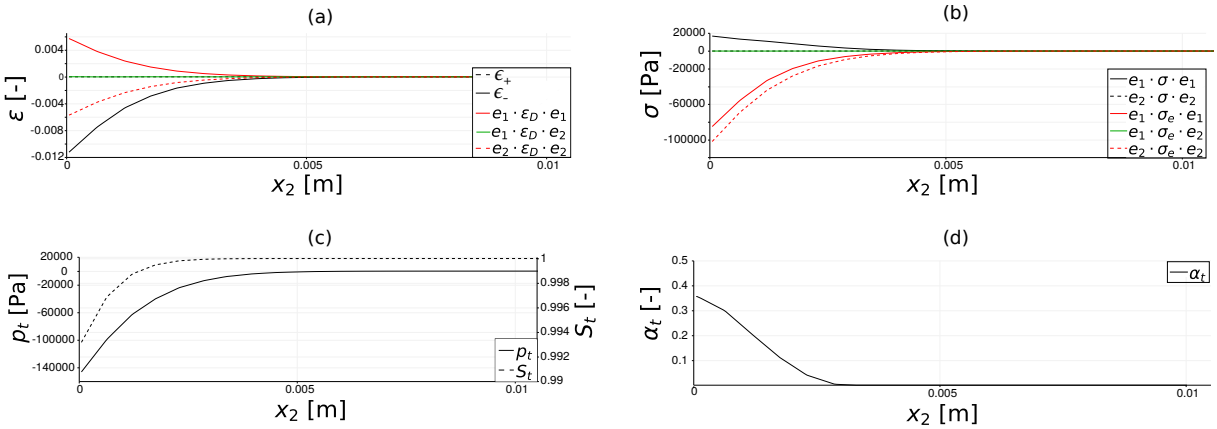

Figure 7.3: Spatial evolution of the solution along the depth of the domain at the location $x_1 = 0.069$m and at time $t = 0.8$s. (a) strains, (b) stresses, (c) pressure and saturation degree of the wetting fluid, (d) damage variable.

sizes are $\Delta x = 0.001$m and $\Delta t = 0.1$s. At the beginning damage evolves in a homogeneous manner along x_1 driven by desaturation. At $t = 0.9$s the solution starts to bifurcates with a periodic structure with almost 10 sinusoidal profiles along the length. As time passes damage grows within these sinusoidal profiles while the base of the profiles not showing any change. This leads to localization within these profiles with a so-called period doubling phenomenon observed in similar applications of gradient damage modeling (Bourdin et al., 2014; Sicsic et al., 2014; Marigo et al., 2016). In essence selective initiation and propagation of fractures occur resulting a complex fracture network in higher dimensions. These localized fractures propagate further into the domain as the desaturation progresses. The periodicity and spacing is qualitatively similar to what was observed in experimental desiccation tests as noted in Sec.(2.2.1).

When it comes to the driving force behind the damage growth in this problem setup, one needs to look at the x_1-homogeneous solution structure prior to any bifurcation. Fig.(7.3) shows the solution profiles along the depth of the domain at time $t = 0.8$s. While the pressure and the saturation profiles at the top boundary, $x_2 = 0$m, confirm to the boundary condition imposed, the solution within the profile is only affected up to a certain depth controlled by the fluid flow problem and this depth grows in time. The compression induced due to this desaturation is apparent looking at the profile of ϵ_-, whereas ϵ_+ remains vanishing. There is as well a significant contribution due to the deviatoric strain, ε_D, which in fact helps to drive the damage in accordance with Eq.(7.38). This can be seen in Fig.(7.3(d)) where damage

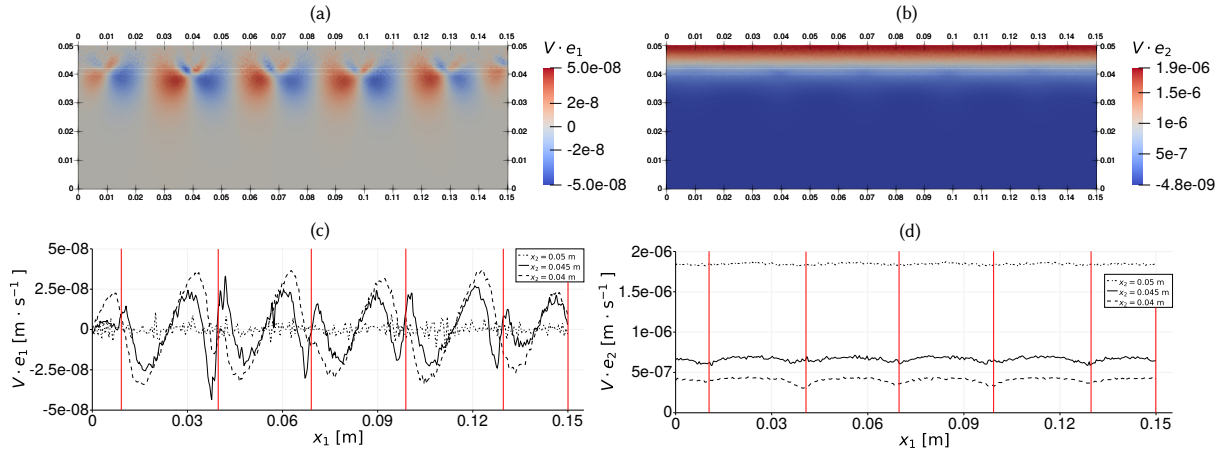

Figure 7.4: Spatial evolution of the components of the volumetric fluid flow vector V at time $t = 10$s, (a,b) within the domain and (c,d) along the length of the domain at the top boundary, $x_2 = 0.05$m, behind the tip of the fractures, $x_2 = 0.045$m and ahead of the tip, $x_2 = 0.04$m. The center of the fractures at $t = 10$s are approximately depicted as vertical red lines across the plots (c) & (d).

is largest at the top boundary and smoothly decreases with the depth. The components of the effective stress tensor, $e_1 \cdot \sigma_e \cdot e_1$ and $e_2 \cdot \sigma_e \cdot e_2$ are negative at the top boundary due to the negative contribution of ϵ_- and of $e_2 \cdot \varepsilon_D \cdot e_2$, in accordance with Eq.(7.36(b)). However, it is imperative to note that the contribution within the effective stress component $e_1 \cdot \sigma_e \cdot e_1$ that drives the damage evolution is tensile due to the positive contribution of $e_1 \cdot \varepsilon_D \cdot e_1$ even though ϵ_+ is vanishing. The component of the total stress tensor, $e_2 \cdot \sigma \cdot e_2$ remains vanishing as expected due to an unrestrained shrinkage along the vertical direction. $e_1 \cdot \sigma \cdot e_1$ however is positive at the top boundary due to the additional contribution of $\pi(x_2 = 0, t) < 0$ in accordance with Eq.(7.36(a)).

The flow of wetting fluid within the domain is governed by the gradient of pressure and the saturation degree according to the Darcy's law, Eq.(3.38). Fig.(7.4), shows both the components of the volumetric fluid flow vector, V and its evolution along x_1 at various depths when the series of fractures have already localized (approximate locations plotted as red vertical lines). It is clear that the vertical component of flow, $V \cdot e_2$, is not significantly affected due to the presence of a fracture within the domain. This is obviously not in line with the prevailing knowledge that fluid flows more freely along the fracture plane due to its higher permeability compared to intact porous solid. This is a direct consequence of the absence of coupling in the current modeling approach, between the damage field and the permeability of the material. The horizontal component of the flow, $V \cdot e_1$, indicates a tendency of asymmetric flow in the vicinity of the fracture tip where fluid seems to flow into the tip ahead of it and out of the tip in its wake. At the top boundary and along the length of the fracture there is not a significant effect.

7.4 SYNOPSIS

The presented modeling approach is similar in construction to the prevailing paradigm (Miehe and Mauthe, 2016; Cajuhi et al., 2018; Heider and Sun, 2020) that the creation of opening mode fracture in desiccating soils is due to the release of elastic energy. Apart from the two-dimensional test case presented, one can imagine as well partially constrained (bottom boundary fixed, lateral boundaries free) desiccation test cases which could generate also tensile effective stresses on the drying face as observed in the aforementioned literature. The choice of boundary conditions in the current study allowed us to confirm that x_1-homogeneous solutions could bifurcate in a periodic manner and localize as fractures.

8

GRADIENT DAMAGE MODELING OF 'CAPILLARY' FRACTURE

CONTENTS

8.1 Mathematical model 92
8.1.1 A 'damaged' porous solid 92
8.1.2 Transient hydraulic problem 94
8.1.3 Evolution problem 95
8.1.4 First-order stability & necessary conditions 96
8.2 Numerical approximation & Algorithm 99
8.3 Two-dimensional desiccation problem 100
8.3.1 Problem setup 101
8.3.2 One-dimensional base solutions 101
8.3.3 Bifurcation from and instability of the fundamental branch 104
8.3.4 Characterization of bifurcations 108
8.4 Synopsis 111

ABSTRACT

The intent of this chapter is to investigate a phenomenon of fracture initiation driven by capillarity, especially applicable to fine-grained soils close to full saturation. In order to do this in the framework of macroscopic porous continuum, the required ingredient is postulated as a damage mechanism described by a scalar damage variable, much like the gradient damage models that describe fractures in brittle materials. However, the driving force behind the damage evolution is revisited to replicate the capillary forces that are in action at the pore-scale. The analysis starts with the postulation of a damaged porous solid and its associated energy density. This postulate is a phenomenological one inspired by experimental observations and is designed to be simplistic in order to allow a detailed analysis. Following this, the evolution problem for damage is derived starting from a total energy of the porous solid and in accordance with the variational approach based on the three principles of irreversibility of damage, stability and energy balance, assuming a minimization principle to hold true at each time. This lays the foundation for investigation of the possibility of fracture initiation in a two-dimensional desiccation problem.

Similar to the previous chapter, the phase field model of partial saturation is not adopted. The starting points of the current development are the classical poromechanical approach to partial saturation (see Sec.(3.1)), and the variational approach underlying the gradient damage modeling of brittle fracture (see Marigo et al. (2016) for an overview). In addition to this we work under an overarching assumption of a hydrophilic porous skeleton whose pore spaces are filled by two fluids, air and water, between which air

is considered passive and the hypothesis of small perturbations is assumed as detailed in Sec.(3.1.4).

8.1 MATHEMATICAL MODEL

8.1.1 A 'damaged' porous solid

Damage of the porous solid is assumed to induce a reduction in its air-entry pressure and in particular to degrade its retention properties. Since according to the classical unsaturated poromechanics (see Coussy (2004)), a porous solid is understood as a so-called 'wetted' porous skeleton with a thin layer of fluid attached to the pore walls, the aforementioned degradation is equivalent to reduction of the cumulative interfacial energy stored at the interfaces between the fluids and the solid pore walls as well as at the fluid-fluid interfaces.

Accordingly the degraded retention relation between the saturation degree of the wetting fluid, S_w and the degraded macroscopic capillary pressure, p_c, reads,

$$p_c(S_w, \alpha) = a(\alpha)\, \widetilde{p}_c(S_w) = -a(\alpha)\, \widetilde{p}_w(S_w) = -p_w(S_w, \alpha), \tag{8.1}$$

where α plays the role of a scalar damage variable and $a(\alpha)$ is a damage law whose functional form is elaborated at a later point. With an abuse of notation $\widetilde{p}_c(S_w)$ now represents the standard retention relation of the form Eq.(3.25). Also, the assumptions leading to Richard's equation are adopted, in particular the hypothesis of a passive non-wetting phase is assumed, leading to $p_c \approx -p_w$, with p_w as the pore-water pressure in a degraded porous solid and $\widetilde{p}_w$ as its non-degraded counterpart. While the above serves as a reasonable first assumption for investigation, a complete modeling approach should also involve the degradation of the resistance to fluid flow within damaged zone and eventually along the localized fracture plane.

We consider again an n_d-dimensional domain, $\Omega \in \Re^{n_d}$, representing the initial configuration of a damaging isotropic partially saturated porous solid whose boundary is denoted by $\partial\Omega$. In line with standard gradient damage modeling (Marigo et al., 2016) and the theory of partially saturated poroelasticity, the following considerations are done:

1. The scalar internal variable, $\alpha \in [0, 1]$, is assigned the role of describing the extent of damage in the sense of loss of retention properties. $\alpha = 0$ denotes an intact healthy skeleton whose retention properties are described by the standard retention curve. Whereas, $\alpha = 1$ denotes a fully damaged skeleton whose retention properties are degraded and can only hold vanishing or residual amount of wetting fluid.

2. For a given unit volume of porous solid in its reference configuration the bulk energy density, W, accounting for the internal energy and the dissipation due to material degradation, is a state function characterized by: $(\varepsilon, \phi, S_w, \alpha, \nabla\alpha)$, respectively the linearized strain tensor, the Lagrangian porosity, the saturation degree of the wetting fluid, the damage variable and the gradient of damage.

3. In a similar way as the construction of the standard gradient damage model (Marigo et al., 2016) for the solid continuum, the porous solid is assumed to be dissipative in a non-local sense due to the dependency of the bulk energy density on the gradient of damage. The particular expression of the bulk energy density is assumed to be:

$$W(\varepsilon, \phi, S_w, \alpha, \nabla\alpha) = \Psi_s(\varepsilon, \phi, S_w, \alpha) + w(\alpha) + \frac{1}{2} w_1 \ell^2 \nabla\alpha \cdot \nabla\alpha. \tag{8.2}$$

The different terms of the above expression are explained below.

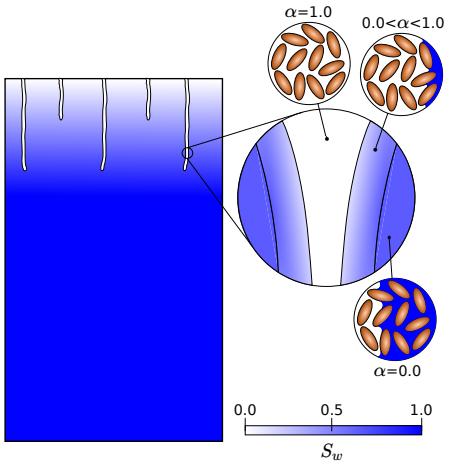

Figure 8.1: Conceptual schematic of a two-dimensional drying porous network along with the development of an opening mode fracture network originating on the drying face. Inset: zoomed-in view of the immediate vicinity of a conceptualized fracture

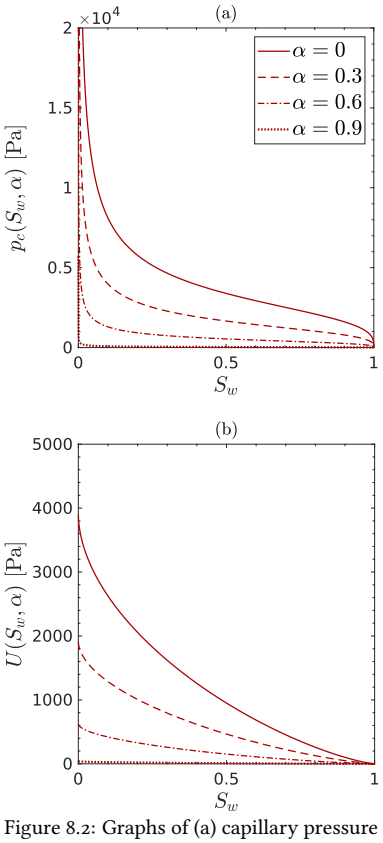

Figure 8.2: Graphs of (a) capillary pressure and (b) interfacial energy functions given by Eqs.(8.1 & 8.4) respectively, with $S_w^{res} = 0$, $\pi_0 = 2840.91$ Pa and the van Genuchten model parameter $m = 0.685$ typical to silica sand saturated by air-water mixture.

(a) The energy density of the porous solid, $\Psi_s(\varepsilon, \phi, S_w, \alpha)$, as elaborated in Ch.(3), encompasses the contributions due to the deformation of the porous skeleton, resulting in solid strains and changes in porosity and also, the interfacial energy contribution due to formation/annihilation of interfaces. Adopting the concept of energy separation (Coussy, 2004) between the free energy of the porous skeleton and the interfacial energy we obtain,

$$\Psi_s(\varepsilon, \phi, S_w, \alpha) = \psi_s(\varepsilon, \phi) + \phi\, U(S_w, \alpha). \tag{8.3}$$

Here a specific choice is done that would result in the aforementioned postulate that damage means the degradation of only the retention properties and not the poroelastic properties. The latter was the choice for modeling tensile mode fracture in Ch.(7). The choice done here allows to isolate the investigation of fracture formation just due to the 'release' of interfacial energy. Specifically, we assume a degradation of the form,

$$U(S_w, \alpha) = a(\alpha)\, \widetilde{U}(S_w), \tag{8.4}$$

consistent with the definition of the degraded capillary pressure in Eq.(8.1). Again with an abuse of notation $\widetilde{U}(S_w)$ now represents the undamaged interfacial energy given by,

$$\widetilde{U}(S_w) = \int_{S_w}^{1} \widetilde{p}_c(s) ds. \tag{8.5}$$

While various choices of the functional form of $a(\alpha)$ are possible, we make a specific choice following the standard gradient damage modeling,

$$a(\alpha) = (1-\alpha)^2 + k_\ell, \tag{8.6}$$

where k_ℓ is a small positive constant used solely for numerical purposes to govern the fully damaged state. Accordingly, when α grows from 0 to 1, the interfacial energy density degrades to a vanishing value. The behavior of the capillary pressure and interfacial energy density can be visualized in the Fig.(8.2). The consequence on the damage evolution due to the above choices is discussed further.

Now concerning the free energy density of the skeleton, a possible form that retrieves back the classical constitutive relations as its state equations reads as,

$$\begin{aligned} \psi_s(\varepsilon, \phi) =& \frac{1}{2}(\varepsilon - \varepsilon_0) : \mathbb{C} : (\varepsilon - \varepsilon_0) + \frac{1}{2} b^2 N (\epsilon - \epsilon_0)^2 \\ & - \Delta\phi (bN(\epsilon - \epsilon_0) - p_0^*) + \frac{1}{2} N \Delta\phi^2, \end{aligned} \tag{8.7}$$

where the notations are borrowed from Ch.(3). $\Delta\phi$ represents the increment of Lagrangian porosity, $(\phi - \phi_0)$. ϕ_0, ε_0 and p_0^* denote the initial reference states of the Lagrangian porosity, the linearized strain tensor and the average pore-pressure respectively.

(b) The second term in Eq.(8.2) is the local part of the dissipated energy,

$$w(\alpha) = w_1 \alpha, \tag{8.8}$$

growing from 0 when $\alpha = 0$, to a positive constant $w_1 < +\infty$ when $\alpha = 1$. Thus in accordance with the developments in Pham et al. (2011a), since $w'(\alpha) > 0$ there exists an elastic phase preceding damage initiation and the finiteness of w_1 ensures that the energy dissipated during a homogeneous evolution of α from 0 to 1 is as well finite. However, w_1 is not related to the fracture toughness in the classical sense. Rather it is to be viewed as related to a threshold beyond which the grains that form the skeleton start to 'slip' at their contacts thus characterizing a dissipative phenomenon that accompanies the release of built-up interfacial energy.

(c) The last term in Eq.(8.2) is the non-local dissipation, which is assumed to be a quadratic function of the gradient of α, and is intended to regularize the local model allowing localizations of finite thickness. ℓ appears with the physical dimension of a length that in the context of gradient damage modeling is intended to control the localization thickness.

4. The dual relations associated to the state variables in Eq.(8.2) are obtained as follows,

$$\begin{aligned}
\frac{\partial W}{\partial \varepsilon} &= \mathbb{C} : (\varepsilon - \varepsilon_0) + bN(b(\epsilon - \epsilon_0) - \Delta\phi)I, \\
\frac{\partial W}{\partial \phi} &= -bN(\epsilon - \epsilon_0) + p_0^* + N\Delta\phi + U(S_w, \alpha), \\
\frac{\partial W}{\partial S_w} &= \phi \frac{\partial U}{\partial S_w}(S_w, \alpha), \\
\frac{\partial W}{\partial \alpha} &= \phi a'(\alpha)\, \widetilde{U}(S_w) + w'(\alpha), \\
\frac{\partial W}{\partial (\nabla \alpha)} &= w_1 \ell^2 \nabla \alpha.
\end{aligned} \tag{8.9}$$

8.1.2 Transient hydraulic problem

Similar to the what was said in Sec.(7.1.2), the transient hydraulic problem governing the evolution the fluids within the porous solid is considered with the absence of bulk force due to gravity. This evolution can be determined by resolving Richards' equation for deformable porous skeleton, Eq.(3.48), that governs the pore pressure of the wetting fluid, p_w, recapitulated below for easy reference,

$$\frac{\partial(\phi S_w)}{\partial p_w}\frac{\partial p_w}{\partial t} + \frac{\varkappa}{\eta_w}\nabla \cdot \hat{k}_w(p_w)\,(-\nabla p_w) = 0. \tag{8.10}$$

Unlike the developments in Sec.(7.1.2), S_w is now obtained from the degraded inverse retention relation,

$$S_w(p_w, \alpha) = \widetilde{p}_c^{-1}\left(\frac{-p_w}{a(\alpha)}\right), \tag{8.11}$$

where $\widetilde{p}_c^{-1}(\bullet)$ is the undamaged inverse retention relation. The intrinsic permeability $\varkappa$ is assumed independent of α. However, since $\varkappa$ is expected to increase, in orders of magnitude, within a fracture we make a rather simplifying assumption of $\hat{k}_w(p_w) = 1$ to in part compensate for the lack of the aforementioned coupling. While this serves as a reasonable first assumption for investigation, a complete modeling approach should also involve the degradation of the resistance to fluid flow within damaged zone and eventually along localized fracture planes.

Appropriate boundary conditions compliment the above PDE which could be either an imposed flux representing a natural boundary condition or an imposed pressure representing a Dirichlet boundary condition.

Remark: u, the displacement of the solid, ϕ and α which are the solutions of the poromechanical damage problem are thus coupled to the hydraulic problem at each instant. Assuming a possible split between the resolution of both problems at each instant, the solution of the hydraulic problem can be viewed as providing instantaneous input to the poromechanical damage problem through the parametrization of S_w. Consequently the bulk energy density in Eq.(8.2) can be rewritten as,

$$W(\varepsilon, \phi, \alpha, \nabla\alpha; S_w) = \Psi_s(\varepsilon, \phi, \alpha; S_w) + w(\alpha) + \frac{1}{2} w_1 \ell^2 \nabla\alpha \cdot \nabla\alpha. \tag{8.12}$$

All the developments done earlier still hold true under such parametrization.

8.1.3 Evolution problem

Now we pose again the evolution problem for the solution triplet (u, ϕ, α) of the poromechanical damage problem using the variational approach similar to the developments in Sec.(7.1.3). At the risk of reintroducing this approach, the principles governing the evolution are elaborated for the current problem which now concerns the porous solid and not just the skeleton.

The variational approach starts again with the definition of a suitable total energy of the body under consideration (i.e., the porous solid), that is associated to the triplet of admissible states $(v, \varphi, \beta) \in \mathcal{C} \times \mathcal{P} \times \mathcal{D}$. These functional spaces $\mathcal{C}$ and $\mathcal{D}$ are as defined in Eq.(7.16) and $\mathcal{P}$ is defined as,

$$\mathcal{P} = \{\varphi \in L^2(\Omega) : 0 < \varphi < 1 \text{ in } \Omega\}, \tag{8.13}$$

where $L^2(\Omega)$ is the Lebesgue space of square integrable functions equipped with an L^2-norm. $\partial\Omega_D \subseteq \partial\Omega$ where displacement, u, is imposed.

This definition of total energy at each time t is given as the integral over the whole domain of the bulk energy density minus the work of external forces,

$$\mathcal{E}_t(v, \varphi, \beta) = \int_\Omega W_t(v, \varphi, \beta, \nabla\beta; S_t)\, dx - \mathcal{W}_t^e. \tag{8.14}$$

Since the focus here is on the porous solid, the external loading concerns not only bulk forces and tractions exerted on the solid skeleton, but also zeroth-order bulk actions tending to modify from inside the porosity of the solid. This time dependent bulk action is obviously related to the presence of fluids in the porous network and is therefore coupled with the solution of the hydraulic problem. In a similar way as in the case of fully saturated porous materials, working this action of the change of Lagrangian porosity it will coincide with the average pore pressure[1], $p_t^* = p_t S_t + p_{nw} S_{nw}$, for all $t > 0$. The assumption of a passive non-wetting phase leads to $p_t^*(S_t, \alpha_t) \approx p_t S_t$. Note the dependence of p_t^* on damage owing to the coupling of the fluid problem to the damage evolution within the domain. This contribution to the potential due to external efforts defined on the set of admissible porosity

[1]Pore pressure, p_w, and Saturation degree, S_w, of the wetting fluid at time t are further denoted in this chapter by p_t and S_t respectively in order not to overload the notation.

fields, $\varphi \in \mathcal{P}$, reads,

$$\mathcal{W}_t^e(\varphi) = \int_\Omega p_t^* \varphi dx. \tag{8.15}$$

Remark: We assume that all the fields are sufficiently smooth in time allowing for the following developments. Also we consider only the states of damage where $\alpha < 1$ and the saturation degree $S_w > 0$. This is done so that in the following analysis the total energy remains finite.

Now we are in a position to setup the principles of variational approach for the evolution in Ω of $(u_t, \phi_t, \alpha_t) \in \mathcal{C} \times \mathcal{P} \times \mathcal{D}$ for all $t \geq 0$ which read:

(a) *Irreversibility of damage:* $t \mapsto \alpha_t$ must be non-decreasing. Consequently the admissible states accessible from α_t belong to the space $\mathcal{D}_t$ defined in Eq.(7.18)

(b) *Stability:* The state (u_t, ϕ_t, α_t) must be directionally stable in the sense that for all $(v, \varphi, \beta) \in \mathcal{C} \times \mathcal{P} \times \mathcal{D}_t$, there exists $\overline{h} > 0$, such that,

$$\forall h \in [0, \overline{h}], \quad \mathcal{E}_t(u_t + h(v - u_t), \phi_t + h(\varphi - \phi_t), \alpha_t + h(\beta - \alpha_t)) \geq \mathcal{E}_t(u_t, \phi_t, \alpha_t). \tag{8.16}$$

(c) *Energy balance:* During the evolution $t \mapsto (u_t, \phi_t, \alpha_t)$ the following energy balance must hold,

$$\mathcal{E}_t(u_t, \phi_t, \alpha_t) = \mathcal{E}_0(u_0, \phi_0, \alpha_0) - \int_0^t \int_\Omega \phi_s \frac{\partial \pi}{\partial S_s} \dot{S}_s \, dx \, ds, \tag{8.17}$$

where the classical definition of equivalent pore-pressure has been adapted to the current context, $\pi(S_t, \alpha_t) = p_t^*(S_t, \alpha_t) - U(S_t, \alpha_t)$, and (u_0, ϕ_0, α_0) denotes the state of the skeleton at time $t = 0$. At any time $0 \leq s \leq t$, the second term on the left hand side of Eq.8.17 accounts for the time parametrization of the total energy through its dependency on S_t.

8.1.4 First-order stability & necessary conditions

As seen in Sec.(7.1.4), equilibrium equation and damage criterion can be obtained as first-order stability conditions starting from Eq.(8.16). In addition, since the solution now involves ϕ_t, an associated zeroth-order balance equation is expected to appear.

We start again by expanding the perturbed energy up to the second-order,

$$\begin{aligned} &h\mathcal{E}_t'(u_t, \phi_t, \alpha_t)(v - u_t, \varphi - \phi_t, \beta - \alpha_t) \\ &+ \frac{h^2}{2}\mathcal{E}_t''(u_t, \phi_t, \alpha_t)(v - u_t, \varphi - \phi_t, \beta - \alpha_t)^2 + o(h^2) \geq 0. \end{aligned} \tag{8.18}$$

$\mathcal{E}_t'$ and $\mathcal{E}_t''$ represent respectively the first and second directional derivatives of $\mathcal{E}_t$ further referred to as FDD and SDD respectively for compactness. The representation $\mathcal{E}_t''(u_t, \phi_t, \alpha_t)(\bullet)^2$ is to be understood as a shorthand for the quadratic form whereas the associated symmetric bi-linear form is represented $\mathcal{E}_t''(u_t, \phi_t, \alpha_t)\langle \bullet, \bullet \rangle$ i.e., the application of $\mathcal{E}_t''(u_t, \phi_t, \alpha_t)$ to the

pair of directions $\langle \bullet, \bullet \rangle$. The directional derivatives in Eq.(8.18) have the following forms in the general direction $(\widehat{v}, \widehat{\varphi}, \widehat{\beta})$,

$$\mathcal{E}_t'(u_t, \phi_t, \alpha_t)(\widehat{v}, \widehat{\varphi}, \widehat{\beta}) = \int_\Omega \left\{ \frac{\partial W_t}{\partial \varepsilon} : \varepsilon(\widehat{v}) + \left(\frac{\partial W_t}{\partial \phi} - p_t^* \right) \widehat{\varphi} + \left(\frac{\partial W_t}{\partial \alpha} - p_t^{*\prime} \phi_t \right) \widehat{\beta} + \frac{\partial W_t}{\partial (\nabla \alpha)} \cdot \nabla \widehat{\beta} \right\} dx, \tag{8.19}$$

$$\mathcal{E}_t''(u_t, \phi_t, \alpha_t)(\widehat{v}, \widehat{\varphi}, \widehat{\beta})^2 = \int_\Omega \left\{ \varepsilon(\widehat{v}) : \mathbb{C} : \varepsilon(\widehat{v}) + N \left(b\epsilon(\widehat{v}) - \widehat{\varphi} \right)^2 - \phi_t \pi_t'' \widehat{\beta}^2 - 2\pi_t' \widehat{\varphi} \widehat{\beta} + w_1 \ell^2 \nabla \widehat{\beta} \cdot \nabla \widehat{\beta} \right\} dx, \tag{8.20}$$

where for the sake of compactness of the notation we denoted the directions $(v - u_t, \varphi - \phi_t, \beta - \alpha_t)$ with $(\widehat{v}, \widehat{\varphi}, \widehat{\beta})$ and define their associated function spaces as $C \times \widehat{\mathcal{P}} \times \mathcal{D}$ with,

$$\widehat{\mathcal{P}} = \{ \widehat{\varphi} \in H^1(\Omega) : -1 < \widehat{\varphi} < 1 \text{ in } \Omega \}. \tag{8.21}$$

In Eq.(8.19) the partial derivatives of bulk energy density are functions of state (u_t, ϕ_t, α_t) given by Eq.(8.9).

Dividing Eq.(8.18) by h and passing to the limit $h \longrightarrow 0$ gives,

$$\mathcal{E}_t'(u_t, \phi_t, \alpha_t)(v - u_t, \varphi - \phi_t, \beta - \alpha_t) \geq 0, \tag{8.22}$$

which is the so-called first-order stability condition and can be viewed as characterizing stationarity of the state (u_t, ϕ_t, α_t). In Eq.(8.22) testing with $\varphi = \phi_t$, $\beta = \alpha_t$ and noting that C is a linear space one can obtain the variational (weak) form of the classical equilibrium condition,

$$\int_\Omega \frac{\partial W_t}{\partial \varepsilon} : \varepsilon(v - u_t) dx = 0, \qquad \forall\, (v - u_t) \in C, \tag{8.23}$$

where a stress tensor can obviously be identified as,

$$\sigma_t = \frac{\partial W_t}{\partial \varepsilon} = \mathbb{C} : (\varepsilon_t - \varepsilon_0) + bN(b(\epsilon_t - \epsilon_0) - \Delta \phi_t) I. \tag{8.24}$$

Similarly testing with $v = u_t$, $\beta = \alpha_t$ in Eq.(8.22) one obtains a zeroth-order balance equation associated to small variations in ϕ_t,

$$\int_\Omega \left(\frac{\partial W_t}{\partial \phi} - p_t^* \right) (\varphi - \phi_t) dx = 0, \qquad \forall\, \varphi \in \mathcal{P}, \tag{8.25}$$

Finally, using Eq.(8.23) and Eq.(8.25) in Eq.(8.22) gives the variational form of the non-local damage criterion,

$$\int_\Omega \left\{ \left(\frac{\partial W_t}{\partial \alpha} - p_t^{*\prime} \phi_t \right) (\beta - \alpha_t) + \frac{\partial W_t}{\partial (\nabla \alpha)} \cdot \nabla (\beta - \alpha_t) \right\} dx \geq 0, \qquad \forall\, \beta \in \mathcal{D}_t \tag{8.26}$$

Employing classical localization arguments of calculus of variations one can obtain from Eq.(8.23), Eq.(8.25) and Eq.(8.26) the following local (strong) forms respectively with corresponding boundary conditions,

$$\nabla \cdot \sigma_t = 0 \quad \text{in } \Omega, \quad \sigma_t \cdot \hat{n} = 0 \quad \text{on } \partial\Omega \backslash \partial\Omega_D, \tag{8.27}$$

$$-bN(\epsilon_t - \epsilon_0) + p_0^* + N\Delta\phi_t + U(\alpha_t; S_t) = p_t^* \quad \text{in } \Omega, \tag{8.28}$$

$$-\pi_t{}'\phi_t + w'(\alpha_t) - w_1\ell^2\Delta\alpha_t \geq 0 \quad \text{in } \Omega, \quad \frac{\partial\alpha_t}{\partial\hat{n}} \geq 0 \quad \text{on } \partial\Omega, \tag{8.29}$$

where $\hat{n}$ denotes the outwards unit normal vector associated to part of the boundary wherever invoked. Note the absence of surface and volume forces in the equilibrium equation according to earlier assumption.

Eq.(8.28) is the local form of the zeroth-order balance law associated to variations in porosity. Rearranging it one can identify the relation which in classical poromechanics, Eq.(3.32), is characterized as the constitutive relation for porosity,

$$\phi_t = b(\epsilon_t - \epsilon_0) + \frac{1}{N}[(p_t^* - p_0^*) - U(\alpha_t; S_t)] + \phi_0. \tag{8.30}$$

Remark: The above formulation results in an equivalent equilibrium equation to be resolved in tandem with the zeroth-order balance law for variations in porosity, compared to the formulation in Chp.(7). This can be seen by substituting Eq.(8.30) into the equilibrium equation, Eq.(8.27), giving,

$$\nabla \cdot \left(\mathbb{C} : (\varepsilon - \varepsilon_0) - b[(p_t^* - p_0^*) - U(\alpha_t; S_t)]I\right) = 0 \quad \text{in } \Omega, \tag{8.31}$$

which is similar in structure compared to Eq.(7.28). In the above the classical stress tensor for unsaturated poroelasticity can be identified as,

$$\sigma_t = \mathbb{C} : (\varepsilon_t - \varepsilon_0) - b[(p_t^* - p_0^*) - U(\alpha_t; S_t)]I. \tag{8.32}$$

This equivalence between the formulations is exploited further for the purpose of numerical approximation.

Since we have assumed the evolution is smooth in time, taking a time derivative of the *Energy balance* leads to,

$$\begin{aligned} 0 =& \frac{d}{dt}\mathcal{E}_t(u_t, \phi_t, \alpha_t) + \int_\Omega \phi_t \frac{\partial \pi_t}{\partial S_t}\dot{S}_t \, dx \\ =& \int_\Omega \left\{ \frac{\partial W_t}{\partial \varepsilon} : \varepsilon(\dot{u}_t) + \left(\frac{\partial W_t}{\partial \phi} - p_t^*\right)\dot{\phi}_t + \left(\frac{\partial W_t}{\partial \alpha} - p_t^*{}'\phi_t\right)\dot{\alpha}_t + \frac{\partial W_t}{\partial(\nabla\alpha)} \cdot \nabla\dot{\alpha}_t \right\} dx. \end{aligned} \tag{8.33}$$

Integrating by parts the gradient terms and further using the local form of the equilibrium equations Eq.(8.27) and the zeroth-order balance law Eq.(8.28) gives,

$$0 = \int_\Omega \left\{ \frac{\partial W_t}{\partial \alpha} - p_t^*{}'\phi_t - \left(\nabla \cdot \frac{\partial W_t}{\partial(\nabla\alpha)}\right) \right\} \dot{\alpha}_t dx + \int_{\partial\Omega} \left(\frac{\partial W_t}{\partial(\nabla\alpha)} \cdot \hat{n}\right) \dot{\alpha}_t dx. \tag{8.34}$$

Owing to the irreversibility of damage everywhere in Ω and the local inequalities Eq.(8.29), the two integrals on the right-hand side of the above

equation are non-negative. So, both of them should vanish. Further using classical localization arguments we obtain the KKT conditions applicable everywhere in Ω and on the boundary $\partial\Omega$ respectively,

$$\begin{aligned} \left(-\pi_t{}'\phi_t + w'(\alpha_t) - w_1\ell^2\Delta\alpha_t\right)\dot{\alpha}_t = 0 \quad &\text{in } \Omega. \\ \frac{\partial\alpha_t}{\partial\hat{n}}\dot{\alpha}_t = 0 \quad &\text{on } \partial\Omega. \end{aligned} \tag{8.35}$$

These conditions can be read in tandem with the *Irreversibility of damage*. The first condition states that everywhere in Ω, damage increases only if the local form of the damage criterion Eq.(8.29) is an equality and if it is a strict inequality then damage does not increase. The second condition states that everywhere on the boundary, $\partial\Omega$, if damage increases then the spatial derivative normal to the boundary vanishes.

8.2 NUMERICAL APPROXIMATION & ALGORITHM

In Chp.(7) an alternating algorithm inspired from the alternate minimization (Bourdin et al., 2000) used extensively for the standard gradient damage modeling is described, Alg.(1). As noted in the previous chapter, the alternate minimization algorithm is based on the observation that while the minimization problem of the regularized energy functional is non-convex, when minimized separately for u and α, the individual minimization problems are convex. The same can be said to be true in the current context for minimizations w.r.t u, ϕ and α.

If one assumes the absence of damage modeling, numerical approximation of the poromechanical problem can be done using the finite element method and resolving in tandem the equilibrium equation, Eq.(8.23) and the zeroth-order balance law for variations in porosity, Eq.(8.28), in their variational forms subject to prescribed boundary conditions. As per earlier remark, here we exploit the equivalence between the aforementioned formulation and the classical equilibrium equation of unsaturated poroelasticity, Eq.(8.31). Specifically we resolve the latter for the poromechanical part of the problem. For the transient hydraulic problem on the other hand we resolve the mixed-head form of the governing equation for pore-water pressure, Eq.(8.10), with Eq.(8.11). In the presence of damage, which is the current context, the damage problem is resolved by the minimization of the total energy under the unilateral constraint of irreversibility of damage.

Given the solution triplet $(u_{n-1}, p_{n-1}, \alpha_{n-1})$ of the solid and fluid problems at time-step $(n-1)$, Alg.(2) describes the alternating algorithm to obtain the solution at time-step n. Spatial discretization is done employing the Taylor-Hood elements for approximating the pair (u, p) and linear Lagrange finite elements for α. The time derivative within Eq.(8.10) for the hydraulic problem is discretized using the implicit Euler scheme of first-order. The coupled problem for solid displacement and fluid pressure, (u_n^i, p_n^i), at each alternate iteration i is solved employing Newton iterations and a sparse LU decomposition routine, available in the FEniCS suite (Alnaes et al., 2015), to solve the linearized systems. The minimization problem for damage within each alternate iteration is posed as,

$$\alpha_n^i = \underset{\alpha}{\operatorname{argmin}}\ \mathcal{E}_n(u_n^i, \phi_n^i, \alpha) \mid \alpha_{n-1} \leq \alpha \leq 1 \text{ in } \Omega, \tag{8.36}$$

where the unilateral constraint $\alpha_{n-1} \leq \alpha \leq 1$ is the time-discrete version of the irreversibility of damage. Numerically we solve this minimization problem using a bound-constrained optimization solver routine available as part of the TAO library (Balay et al., 2021). The convergence criterion of the alternating algorithm, at each iteration i, is the comparison against a tolerance, the ℓ^2-norm of the difference between the damage solutions of successive iterations, $\|(\alpha_n^i - \alpha_n^{i-1})\|$.

Algorithm 2: Alternating algorithm for capillary damage model

Input: $(u_{n-1}, p_{n-1}, \alpha_{n-1})$

➢ *initialization:* $(u_n^0, p_n^0, \alpha_n^0) \leftarrow (u_{n-1}, p_{n-1}, \alpha_{n-1})$;

➢ $i = 0$;

while *alternating algorithm not converged* **do**

- Solve $(u_n^i, p_n^i) := \{\text{Equlibrium, Eq.(8.31) \& pressure evolution, Eq.(8.10)}\} \mid \alpha_n = \alpha_n^{i-1}$;
- Compute $S_n^i(p_n^i, \alpha_n^{i-1}) := \{\text{Inverse retention relation, Eq.(8.11)}\}$;
- Compute $\phi_n^i(u_n^i, p_n^i, \alpha_n^{i-1}) := \{\text{Constitutive relation, Eq.(8.30)}\}$;
- Solve $\alpha_n^i := \underset{\alpha}{\operatorname{argmin}}\ \mathcal{E}_n(u_n^i, \phi_n^i, \alpha) \mid \alpha_{n-1} \leq \alpha \leq 1$ in Ω;
- $i \leftarrow i + 1$;

end

➢ *update:* $(u_n, p_n, \alpha_n) \leftarrow (u_n^i, p_n^i, \alpha_n^i)$;

Output: (u_n, p_n, α_n)

8.3 TWO-DIMENSIONAL DESICCATION PROBLEM

The above modeling approach is now applied to study the desiccation of soils, inspired by various desiccation experiments that can be found in the literature, Peron et al. (2009); Shin and Santamarina (2010, 2011a); Stirling (2014). For numerical purposes the flux on the drying face/s is estimated (Stirling, 2014) using the discharge rate that is calculated from experimental measurements of mass loss of water. In line with what was done in Sec.(7.3), we consider here as well a plane-strain assumption.

The boundary value problem formed by the coupled system of equations Eqs.(8.10, 8.31) and the bound-constrained minimization w.r.t α, Eq.(8.36), are resolved with appropriately defined boundary condition and initial conditions as laid out further in Sec.(8.3.1) and following the algorithm described in Alg.(2). Material properties of the porous medium and parameters of the model chosen for the purpose of simulations are listed in Table.(8.1), which are in the range typical of fine silica sands saturated with air-water mixture.

During the experiments in the aforementioned literature, two stages were observed in the drying process. The first stage involving large irreversible deformations with the degree of saturation close to 1 and the second stage involving noticeable decrease in the saturation degree and with smaller deformations. Fracture initiation usually has been associated to the sample close to full saturation and the air-water interface coinciding with the apparent soil surface. In the current modeling context damage initiation is associated to the threshold, w_1, appearing within the local dissipation contribution, Eq.(8.8), to the bulk energy density and this, as mentioned earlier, is understood as not directly related to a fracture toughness of the material but to the creation of a new fluid-fluid interface within the porous medium. Nevertheless, w_1 is a parameter that depends on the material and boundary conditions. For instance, Holtzman et al. (2012) have shown experimentally that the fracturing is the preferred mode of invasion of air into water saturated granular media when the confining stress is lower. So, this threshold can only be characterized through experimental observation of fracture initiation, viewed as a localization of the damage variable within the model. For the purpose of current investigation various values of w_1 are tested that either initiate damage or not and in the former case the possibility of localization is studied.

Table 8.1: Material properties, model parameters used through Chp.(8), unless mentioned otherwise.

property/ parameter	Fine Sand
ϕ [−]	0.3
E [Pa]	1.3E06
ν [−]	0.4
b [−]	0.9
N [Pa]	1.81E07
$\varkappa$ [m^2]	1.0E-12
η_w [Pa.s]	8.9E-04
π_0 [Pa]	2840.91
m [−]	0.685
S_r^{res} [−]	0.0
w_1 [$N.m^{-3}$]	1000
ℓ [m]	0.005

8.3.1 Problem setup

The problem setup is similar to what was described in Sec.(7.3.1) with some modifications adapted to the current context only which are stated below. The reference initial configuration Ω as shown in the Fig.(7.1) with the boundary $\partial\Omega$ now represents a porous solid instead of the porous skeleton as done earlier. At time $t = 0$ it is assumed that the porous solid is completely intact, stress free and fully saturated giving,

$$\alpha_0(x) = 0, \quad u_0(x) = 0, \quad \varepsilon_0(x) = 0, \quad S_0(x) = 1, \quad p_0(x) = 0. \tag{8.37}$$

The mechanical boundary conditions are exactly the same as stated in Eq.(7.46) and damage is free to evolve at all the boundaries whenever the damage criterion is met according to Eq.(7.47).

For the hydraulic problem, the lateral and bottom faces are set to be impermeable. The loading is done by a constant imposed outward flux, $-q_f e_2$, on the top face thus inducing a drying effect. While the drying flux measured using the discharge rates in Stirling (2014) is found to be a function of time, we choose to make a simplifying assumption of constant flux. These boundary conditions $\forall t \geq 0$ read,

$$\begin{aligned} \nabla p_t \cdot (-e_1)\big|_{(x_1=0)} = 0, \quad \nabla p_t \cdot e_1\big|_{(x_1=L)} = 0, \\ \left(-\frac{\varkappa}{\eta_w}\hat{k}_w(p_t)\nabla p_t\right) \cdot (-e_2)\big|_{(x_2=0)} = q_f, \quad \nabla p_t \cdot e_2\big|_{(x_2=H)} = 0. \end{aligned} \tag{8.38}$$

8.3.2 One-dimensional base solutions

It can be seen from the problem setup that the geometry, material properties and initial conditions are invariant along x_1-direction. The loading and boundary conditions on the top and bottom faces are as well invariant along x_1-direction. The boundary conditions on the lateral faces demand vanishing gradients of the solution along the x_1-direction. So, even though the problem does not render itself for obtaining an easy exact solution due to its non-linearity, one can a priori anticipate the existence of a particular class of solutions that are homogeneous in the x_1-direction and are dependent only on x_2. Such solutions are termed here as base solutions. In fact to obtain the base solutions one just needs to solve the problem in one-dimension along the x_2-direction with appropriate boundary conditions, instead of the full two-dimensional problem posed earlier. This is the purpose of this section. Rigorous mathematical proof of existence and uniqueness of such base solutions for all times is out of the scope of the current work. Instead we exhibit numerically these solutions for $t > 0$.

The domain of the one-dimensional problem is defined $\widetilde{\Omega} = (0, H)$ along the x_2-coordinate, with boundary $\partial\widetilde{\Omega} = \{(x_2 = 0) \cup (x_2 = H)\}$. The initial and boundary conditions from Sec.(8.3.1) are adapted to this domain. While studying the influence of depth H could be interesting, we choose a depth such that $H \gg \ell$.

In view of the damage criterion, Eq.(8.29), with the definition of average pore-pressure, $p_t^*(S_t, \alpha_t) = p_t(S_t, \alpha_t)\, S_t$, the solution states can be classified into two: undamaged ($\alpha_t = 0\ \forall x_2 \in \widetilde{\Omega}$) and damaged ($\exists x_2 \in \widetilde{\Omega} \mid \alpha_t > 0$). Since the initial state at $t = 0$ is assumed to be that of a uniformly intact solid, damage would initiate if the following local damage criterion is an equality.

$$\phi_t U'(\alpha_t; S_t) - p_t'\, S_t \phi_t + w'(\alpha_t) \geq 0 \quad \text{in } \widetilde{\Omega}, \tag{8.39}$$

where Eq.(8.1) gives $-p_t' = p_c'(S_t, \alpha_t) = a'(\alpha_t)\, \widetilde{p}_c(S_t)$ and Eq.(8.4) gives $U'(\alpha_t; S_t) = a'(\alpha_t)\, \widetilde{U}(S_t)$. In Eq.(8.39) the terms that drive the damage

evolution are first and second. Now for $\alpha_t = 0$, $a'(\alpha_t) = -2$ and for $0 < S_t < 1$, $\widetilde{U}(S_t) > 0$ and $\widetilde{p}_c(S_t) > 0$. Since $\phi_t \in \mathcal{P}$ the first driving term is negative whose magnitude increases with decreasing S_t and conversely with increasing α_t. With a similar reasoning also the second term is negative. The third term is a positive constant, $w'(\alpha_t) = w_1$, acting as the threshold for damage initiation. Owing to the drying flux applied at $x_2 = 0$ the saturation degree is the lowest here. Thus one can anticipate that starting from a uniformly undamaged state the damage initiates at $x_2 = 0$ within a finite depth and propagates into the domain driven by desaturation. However, at initial times since a minimum amount of capillary energy needs to be stored before damage initiation according to Eq.(8.39), the saturation degree everywhere in the domain could be such that the damage criterion is a strict inequality and damage does not initiate at all. So, one can envisage a finite time $t_d > 0$ beyond which the damage criterion is an equality at the drying boundary and so damage initiates. All the solution states for $t \geq t_d$ are called the damaged states and this t_d depends on the intensity of the drying flux for a given material.

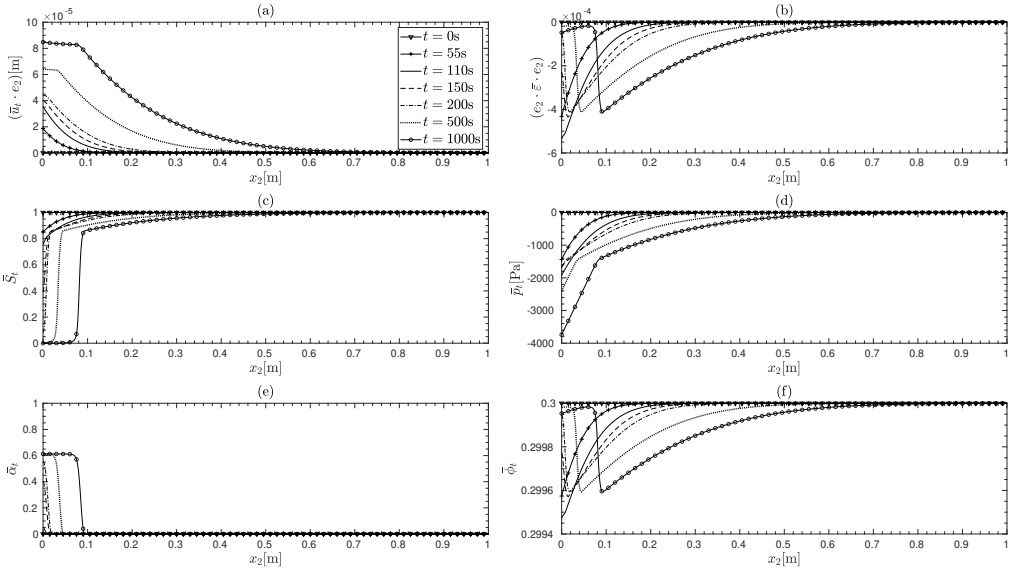

Figure 8.3: Evolution of the one-dimensional base solution and functions of the solution within the full computational domain, $\widetilde{\Omega} = (0, 1\text{m})$.

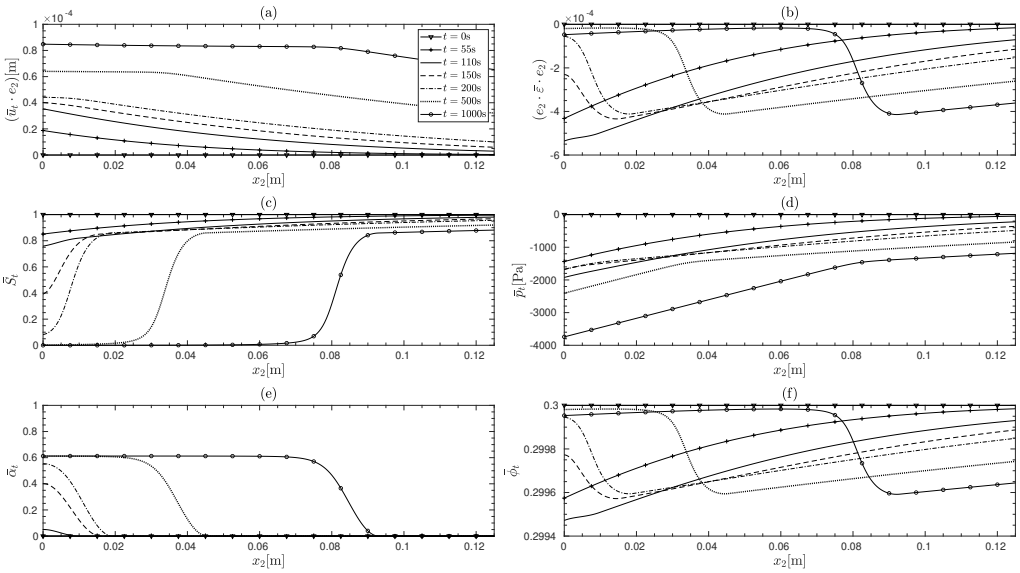

Figure 8.4: Evolution in Fig.(8.3) shown within a restricted computational domain, $\widetilde{\Omega} = (0, 0.05\text{m})$, close to the drying boundary for clarity.

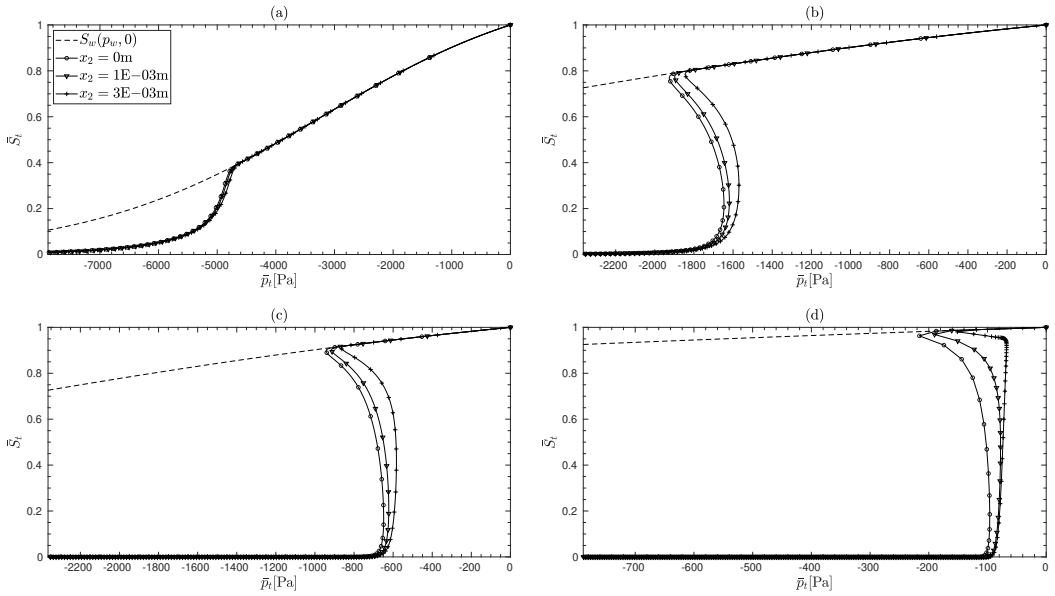

Figure 8.5: Path followed by the solution in the space (S_t, p_t) at the boundary $x_2 = 0$m and two locations within the domain close to this boundary for values of w_1 (a) 2000N.m^{-3} (b) 1000N.m^{-3}, (c) 500N.m^{-3} (d) 100N.m^{-3}. Dashed line represents the standard non-degraded retention curve.

Figs.(8.3 & 8.4) show the time evolution of the solution and functions of the solution, with $H = 1.0$m, $q_f = 10$m.s^{-1}, $w_1 = 1000$N.m^{-3}. The material properties correspond to sand and the fluid combination to air-water. It can be seen that initially damage does not evolve anywhere in the domain even though flux induced desaturation initiates at $x_2 = 0$ and progresses into the domain. During this stage of evolution the strain remains compressive and the porosity reduces from the initial value as expected within the unsaturated zone. However, once the damage criterion becomes an equality, damage initiates at $x_2 = 0$. With damage growing from 0, the saturation degree degrades close to 0 indicating invasion of air phase while the pore-water pressure only reduces slightly in magnitude.

The path followed by the solution, in the space (S_t, p_t), at $x_2 = 0$ and within the domain close to this boundary are shown in Fig.(8.5(a)). It is clear that the path followed during the initial damage evolution is that of a 'softening' with respect to pore-water pressure. Also interesting to observe is that even though the drying flux at the boundary continues to drive the

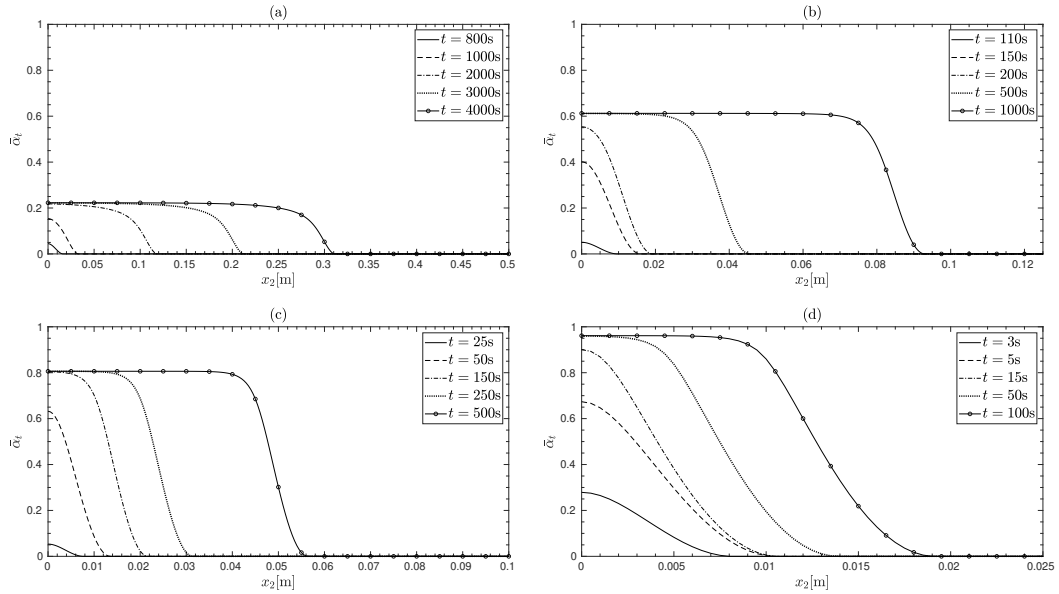

Figure 8.6: Evolution of damage for values of w_1 (a) 2000N.m^{-3} (b) 1000N.m^{-3}, (c) 500N.m^{-3} (d) 100N.m^{-3}.

desaturation process, the damage stagnates at a maximum value at larger times and this is replicated also within the domain, thus creating a zone of uniform damage. This is due to the simultaneous reduction in magnitude of the first driving term in Eq.(8.39) with increasing damage so that after a certain value of damage, the criterion does not become an equality anymore even though desaturation progresses.

Fig.(8.6) shows the time evolution of damage for different thresholds w_1. In all cases the damage initiates at $x_2 = 0$ as anticipated and then propagates into the domain supported by a finite depth, d_t, that increases with time. Lower thresholds are characterized by earlier initiation of damage and a damage value closer to 1 at the drying boundary.

8.3.3 Bifurcation from and instability of the fundamental branch

The one-dimensional base solutions resolved in Sec.(8.3.2) are the x_1-homogeneous solutions or the so-called fundamental states of the corresponding two-dimensional problem. These solutions are denoted by $(\bar{u}_t, \bar{\phi}_t, \bar{\alpha}_t)$ at time t and, for consistency, the solution of the hydraulic problem by $(\bar{S}_t, \bar{p}_t)$. The branch of the evolution along which all the states remain x_1-homogeneous is called the fundamental branch. Following the works of Benallal and Marigo (2006); Pham et al. (2011b); Sicsic et al. (2014) for standard gradient damage models, we investigate the possibility of bifurcation from the fundamental branch of evolution. A bifurcation in this sense is understood as the availability of admissible solution state/s other than the fundamental one. Whether or not the solution shifts from the fundamental branch depends on the loss of stability of the fundamental state itself and the characteristics of the perturbation that can cause such a shift. In the earlier mentioned works concerning standard gradient damage models, the possibility of bifurcations was associated to a loss of uniqueness criterion of the fundamental state. We follow a similar approach, by first analyzing the loss of stability of the fundamental state and then the possibility of bifurcation.

Loss of stability

By construction the fundamental state, $(\bar{u}_t, \bar{\phi}_t, \bar{\alpha}_t)$, satisfies the first-order stability, Eq.(8.22). The question is, if it satisfies the full stability condition. To verify this one needs to analyze the condition Eq.(8.18) that is obtained by the expanding the perturbed state of energy in the vicinity of the one associated to the fundamental state,

$$\begin{aligned} &h\mathcal{E}_t'(\bar{u}_t, \bar{\phi}_t, \bar{\alpha}_t)(v - \bar{u}_t, \varphi - \bar{\phi}_t, \beta - \bar{\alpha}_t) \\ &+ \frac{h^2}{2}\mathcal{E}_t''(\bar{u}_t, \bar{\phi}_t, \bar{\alpha}_t)(v - \bar{u}_t, \varphi - \bar{\phi}_t, \beta - \bar{\alpha}_t)^2 + o(h^2) \geq 0. \end{aligned} \tag{8.40}$$

By virtue of the equilibrium, Eq.(8.23), and zeroth-order balance, Eq.(8.25), the FDD in Eq.(8.40) reduces to,

$$\begin{aligned} \mathcal{E}_t'(\bar{u}_t, \bar{\phi}_t, \bar{\alpha}_t)(v - \bar{u}_t, \varphi - \bar{\phi}_t, \beta - \bar{\alpha}_t) = \int_\Omega \Big\{ &\left(-\pi_t' \bar{\phi}_t + w'(\bar{\alpha}_t)\right)(\beta - \bar{\alpha}_t) \\ &+ w_1 \ell^2 \nabla \bar{\alpha}_t \cdot \nabla(\beta - \bar{\alpha}_t) \Big\} dx, \end{aligned} \tag{8.41}$$

with the directions $(v - \bar{u}_t, \varphi - \bar{\phi}_t, \beta - \bar{\alpha}_t) \in C \times \widehat{\mathcal{P}} \times \widehat{\mathcal{D}}_t^d$, with $\widehat{\mathcal{P}}$ defined in Eq.(8.21) and

$$\widehat{\mathcal{D}}_t^d = \{\widehat{\beta} \in H^1(\Omega) : 0 \leq \widehat{\beta} < 1 \text{ in } \Omega_t^d,\ \widehat{\beta} = 0 \text{ in } \Omega_t^e\}, \tag{8.42}$$

where $\Omega_t^d = (0, L) \times (0, d_t)$ is the damaged strip if damage initiates and $\Omega_t^e = \Omega \backslash \Omega_t^d$ is the undamaged region.

➢ *Undamaged states:*

For $t < t_d$, $\bar{\alpha}_t = 0$ throughout Ω and the FDD is positive for all directions $(v - \bar{u}_t, \varphi - \bar{\phi}_t, \beta)$ if $\beta \neq 0$. For directions such that $\beta = \bar{\alpha}_t = 0$, the FDD vanishes and the SDD, Eq.(8.20), reduces to,

$$\mathcal{E}_t''(\bar{u}_t, \bar{\phi}_t, \bar{\alpha}_t)(v - \bar{u}_t, \varphi - \bar{\phi}_t, \beta - \bar{\alpha}_t)^2 = \int_\Omega \Big\{ \varepsilon(v - \bar{u}_t) : \mathbb{C} : \varepsilon(v - \bar{u}_t) + N \left(b\epsilon(v - \bar{u}_t) - (\varphi - \bar{\phi}_t) \right)^2 \Big\} dx. \tag{8.43}$$

which is positive. Hence, full stability of the fundamental state is guaranteed for $t < t_d$.

➢ *Damaged states:*

For $t \geq t_d$, the damage criterion is an equality within the damaged strip $\Omega_t^d = (0, L) \times (0, d_t)$ and an inequality everywhere else, $\Omega_t^e = \Omega \backslash \Omega_t^d$. If we consider directions such that $\beta \neq \bar{\alpha}_t$ then the FDD is positive within Ω_t^e owing to the strict inequality of the local damage criterion. Whereas a vanishing FDD corresponds to directions such that $\beta = \bar{\alpha}_t = 0$ in Ω_t^e. In such directions stability of the fundamental state is guaranteed *if*,

$$\mathcal{E}_t''(\bar{u}_t, \bar{\phi}_t, \bar{\alpha}_t)(v - \bar{u}_t, \varphi - \bar{\phi}_t, \beta - \bar{\alpha}_t)^2 > 0, \quad \forall (v, \varphi, \beta) \in C \times \mathcal{P} \times \mathcal{D}_t^d, \tag{8.44}$$

and *only if* the above the inequality is not strict. Note that in the above the expression of SDD is given by Eq.(8.20) and not by the reduced Eq.(8.43) owing to the possibility of $\beta \neq \bar{\alpha}_t$ in Ω_t^d. $\mathcal{D}_t^d \subset \mathcal{D}_t$, is the set of admissible damage fields given by,

$$\mathcal{D}_t^d = \{ \beta \in H^1(\Omega) : \bar{\alpha}_t \leq \beta < 1 \text{ in } \Omega_t^d, \ \beta = 0 \text{ in } \Omega_t^e \}. \tag{8.45}$$

The directions $(v - \bar{u}_t, \varphi - \bar{\phi}_t, \beta - \bar{\alpha}_t)$ are further denoted as $(\widehat{v}, \widehat{\varphi}, \widehat{\beta}) \in C \times \widehat{\mathcal{P}} \times \widehat{\mathcal{D}}_t^d$, with an abuse of notation w.r.t the notation introduced in Sec.(8.1.4).

Noting, for the moment, that SDD in the damaged states is evaluated at the fundamental state, analysis of the condition in Eq.(8.44) is deferred to a later moment in view of studying the possibility of bifurcations.

Synopsis: While the undamaged states are fully stable, the damaged states are conditionally stable and this condition amounts to verifying the positive definiteness of the quadratic form $\mathcal{E}_t''(\bar{u}_t, \bar{\phi}_t, \bar{\alpha}_t)(\bullet)^2$ when applied on directions belonging to $C \times \widehat{\mathcal{P}} \times \widehat{\mathcal{D}}_t^d$. Specifically,

$$\forall (\widehat{v}, \widehat{\varphi}, \widehat{\beta}) \in C \times \widehat{\mathcal{P}} \times \widehat{\mathcal{D}}_t^d \begin{cases} \mathcal{E}_t''(\bar{u}_t, \bar{\phi}_t, \bar{\alpha}_t)(\widehat{v}, \widehat{\varphi}, \widehat{\beta})^2 > 0 \implies \textit{stability} \\ \mathcal{E}_t''(\bar{u}_t, \bar{\phi}_t, \bar{\alpha}_t)(\widehat{v}, \widehat{\varphi}, \widehat{\beta})^2 < 0 \implies \textit{instability}. \end{cases} \tag{8.46}$$

Possibility of bifurcations

As mentioned earlier, the notion of bifurcation from the fundamental branch is intertwined with the availability of admissible solution state/s other than the fundamental one. This amounts to studying the evolution problem at time $t + \eta$, with $\eta > 0$ small enough, knowing that the solution has followed the fundamental branch up until t, i.e., knowing the solution at t is $(\bar{u}_t, \bar{\phi}_t, \bar{\alpha}_t)$. Before proceeding further we assume that such an evolution is smooth

enough that forward time derivatives of the solution components exist at time t and are defined as,

$$\dot{u} = \lim_{\eta\to 0} \frac{u_{t+\eta} - \bar{u}_t}{\eta}, \quad \dot{\phi} = \lim_{\eta\to 0} \frac{\phi_{t+\eta} - \bar{\phi}_t}{\eta}, \quad \dot{\alpha} = \lim_{\eta\to 0} \frac{\alpha_{t+\eta} - \bar{\alpha}_t}{\eta}. \tag{8.47}$$

Further a smooth growth of the damage zone is assumed within the time interval $(t, t+\eta)$. More detail of such a hypothesis can be found in Sicsic et al. (2014). Now, if the solution continues to stay on the fundamental branch then it implies that $(\dot{u}, \dot{\phi}, \dot{\alpha})$ are as well x_1-homogeneous giving, $(\dot{u}, \dot{\phi}, \dot{\alpha}) = (\dot{\bar{u}}, \dot{\bar{\phi}}, \dot{\bar{\alpha}})$. However, if bifurcation is to happen then there should be some other solution rate $(\dot{u}, \dot{\phi}, \dot{\alpha})$. To check this possibility we derive from the evolution problem at $t+\eta$, a rate problem that any solution rate needs to satisfy.

Imposing $(u_{t+\eta}, \phi_{t+\eta}, \alpha_{t+\eta})$ to satisfy the three evolution principles in Sec.(8.1.3) we get:

(a) *Irreversibility of damage:* Damage must be non-decreasing, i.e., $\dot{\alpha} \geq 0$. Consequently $(\dot{u}, \dot{\phi}, \dot{\alpha}) \in C \times \dot{\mathcal{P}} \times \dot{\mathcal{D}}$, with,

$$\dot{\mathcal{P}} = \{\varphi \in H^1(\Omega)\}, \quad \dot{\mathcal{D}} = \{\beta \in H^1(\Omega) : \beta \geq 0 \text{ in } \Omega\}. \tag{8.48}$$

(b) *Stability:* Directionally stability implies first-order stability which at $(u_{t+\eta}, \phi_{t+\eta}, \alpha_{t+\eta})$ reads,

$$\mathcal{E}'_{t+\eta}(u_{t+\eta}, \phi_{t+\eta}, \alpha_{t+\eta})(\widehat{v}, \widehat{\varphi}, \widehat{\beta}) \geq 0 \quad \forall\, (\widehat{v}, \widehat{\varphi}, \widehat{\beta}) \in C \times \widehat{\mathcal{P}} \times \mathcal{D}. \tag{8.49}$$

As analyzed earlier for loss of stability of the fundamental state at time t, for directions $(\widehat{v}, \widehat{\varphi}, \widehat{\beta})$ such that $\mathcal{E}'_t(\bar{u}_t, \bar{\phi}_t, \bar{\alpha}_t)(\widehat{v}, \widehat{\varphi}, \widehat{\beta}) > 0$, by continuity, Eq.(8.49) and consequently full stability of the state $(u_{t+\eta}, \phi_{t+\eta}, \alpha_{t+\eta})$ hold true.

Whereas for directions such that $\mathcal{E}'_t(\bar{u}_t, \bar{\phi}_t, \bar{\alpha}_t)(\widehat{v}, \widehat{\varphi}, \widehat{\beta}) = 0$ this is not evident. In fact such directions correspond to $\widehat{\beta} = 0$ in Ω^e_t, i.e., $\widehat{\beta} \in \widehat{\mathcal{D}}^d_t$. Dividing Eq.(8.49) by η and passing to the limit when η tends to 0 gives the following condition on any $(\dot{u}, \dot{\phi}, \dot{\alpha}) \in C \times \dot{\mathcal{P}} \times \dot{\mathcal{D}}^d_t$,

$$\begin{aligned}\mathcal{E}''_t(\bar{u}_t, \bar{\phi}_t, \bar{\alpha}_t)\langle(\dot{u}, \dot{\phi}, \dot{\alpha}), (\widehat{v}, \widehat{\varphi}, \widehat{\beta})\rangle + \dot{\mathcal{E}}'_t(\bar{u}_t, \bar{\phi}_t, \bar{\alpha}_t)(\widehat{v}, \widehat{\varphi}, \widehat{\beta}) \geq 0 \\ \forall\, (\widehat{v}, \widehat{\varphi}, \widehat{\beta}) \in C \times \widehat{\mathcal{P}} \times \widehat{\mathcal{D}}^d_t,\end{aligned} \tag{8.50}$$

with[2],

$$\dot{\mathcal{D}}^d_t = \{\beta \in H^1(\Omega) : \beta \geq 0 \text{ in } \Omega^d_t,\ \beta = 0 \text{ in } \Omega^e_t\}. \tag{8.51}$$

(c) *Energy Balance:* The energy balance at time $t+\eta$ reads,

$$\mathcal{E}_{t+\eta}(u_{t+\eta}, \phi_{t+\eta}, \alpha_{t+\eta}) = \mathcal{E}_t(\bar{u}_t, \bar{\phi}_t, \bar{\alpha}_t) - \int_t^{t+h} \int_\Omega \left(\frac{\partial \pi_s}{\partial S_s}\phi_s\right) \dot{S}_s \, dx \, ds. \tag{8.52}$$

[2]Note the restriction of $\dot{\alpha}$ to $\dot{\mathcal{D}}^d_t$ as opposed to $\dot{\mathcal{D}}$ done a few steps earlier when imposing *irreversibility of damage*. This is a consequence of the restriction imposed on the directions to be considered for $\mathcal{E}'_t(\bar{u}_t, \bar{\phi}_t, \bar{\alpha}_t)(\widehat{v}, \widehat{\varphi}, \widehat{\beta}) = 0$ to hold true.

A first expansion of $\mathcal{E}_{t+\eta}(u_{t+\eta}, \phi_{t+\eta}, \alpha_{t+\eta})$ on the left-hand side of the above equation up to second-order leads to,

$$\begin{aligned}
&\mathcal{E}_{t+\eta}(\bar{u}_t, \bar{\phi}_t, \bar{\alpha}_t) + \mathcal{E}'_{t+\eta}(\bar{u}_t, \bar{\phi}_t, \bar{\alpha}_t)(u_{t+\eta} - \bar{u}_t, \phi_{t+\eta} - \bar{\phi}_t, \alpha_{t+\eta} - \bar{\alpha}_t) \\
&+ \frac{1}{2}\mathcal{E}''_{t+\eta}(\bar{u}_t, \bar{\phi}_t, \bar{\alpha}_t)(u_{t+\eta} - \bar{u}_t, \phi_{t+\eta} - \bar{\phi}_t, \alpha_{t+\eta} - \bar{\alpha}_t)^2 \\
&+ o(\|(u_{t+\eta} - \bar{u}_t, \phi_{t+\eta} - \bar{\phi}_t, \alpha_{t+\eta} - \bar{\alpha}_t)\|^2) \\
&= \mathcal{E}_t(\bar{u}_t, \bar{\phi}_t, \bar{\alpha}_t) - \int_t^{t+h}\int_\Omega \left(\frac{\partial \pi_s}{\partial S_s}\phi_s\right)\dot{S}_s \, dx \, ds,
\end{aligned} \tag{8.53}$$

where $\|\cdot\|$ denotes the norm of $C \times \widehat{\mathcal{P}} \times \mathcal{D}$. A second expansion in time up to second-order of the operators at $t + \eta$ leads to,

$$\begin{aligned}
&\mathcal{E}'_t(\bar{u}_t, \bar{\phi}_t, \bar{\alpha}_t)(u_{t+\eta} - \bar{u}_t, \phi_{t+\eta} - \bar{\phi}_t, \alpha_{t+\eta} - \bar{\alpha}_t) + \eta^2\dot{\mathcal{E}}'_t(\bar{u}_t, \bar{\phi}_t, \bar{\alpha}_t)(\dot{u}, \dot{\phi}, \dot{\alpha}) \\
&+ \frac{\eta^2}{2}\mathcal{E}''_t(\bar{u}_t, \bar{\phi}_t, \bar{\alpha}_t)(\dot{u}, \dot{\phi}, \dot{\alpha})^2 + \eta\dot{\mathcal{E}}_t(\bar{u}_t, \bar{\phi}_t, \bar{\alpha}_t) + \frac{\eta^2}{2}\ddot{\mathcal{E}}_t(\bar{u}_t, \bar{\phi}_t, \bar{\alpha}_t) + o(\eta^2) \\
&= -\eta\int_\Omega \left(\frac{\partial \pi_t}{\partial S_t}\bar{\phi}_t\right)\dot{S}_t \, dx - \frac{\eta^2}{2}\frac{d}{dt}\left(\int_\Omega \left(\frac{\partial \pi_t}{\partial S_t}\bar{\phi}_t\right)\dot{S}_t \, dx\right).
\end{aligned} \tag{8.54}$$

The following definitions are obtained by differentiating w.r.t time the energy balance written at time t,

$$\begin{aligned}
\dot{\mathcal{E}}_t(\bar{u}_t, \bar{\phi}_t, \bar{\alpha}_t) &= -\int_\Omega \left(\frac{\partial \pi_t}{\partial S_t}\bar{\phi}_t\right)\dot{S}_t \, dx, \\
\ddot{\mathcal{E}}_t(\bar{u}_t, \bar{\phi}_t, \bar{\alpha}_t) &= -\frac{d}{dt}\left(\int_\Omega \left(\frac{\partial \pi_t}{\partial S_t}\bar{\phi}_t\right)\dot{S}_t \, dx\right).
\end{aligned} \tag{8.55}$$

The term $\mathcal{E}'_t(\bar{u}_t, \bar{\phi}_t, \bar{\alpha}_t)(u_{t+\eta} - \bar{u}_t, \phi_{t+\eta} - \bar{\phi}_t, \alpha_{t+\eta} - \bar{\alpha}_t)$ is $o(\eta^2)$ due to the assumption of smooth growth of the damage zone and $\dot{\alpha} \in \dot{\mathcal{D}}^d_t$, see Sicsic et al. (2014) for a detailed deduction. So, one obtains by diving Eq.(8.54) by η^2 and passing to the limit when η tends to 0,

$$\dot{\mathcal{E}}'_t(\bar{u}_t, \bar{\phi}_t, \bar{\alpha}_t)(\dot{u}, \dot{\phi}, \dot{\alpha}) + \mathcal{E}''_t(\bar{u}_t, \bar{\phi}_t, \bar{\alpha}_t)(\dot{u}, \dot{\phi}, \dot{\alpha})^2 = 0. \tag{8.56}$$

➢ *The rate problem:*

Subtracting Eq.(8.56) from Eq.(8.50) gives the following inequality that the rate at any time $t > 0$, $(\dot{u}, \dot{\phi}, \dot{\alpha}) \in C \times \dot{\mathcal{P}} \times \dot{\mathcal{D}}^d_t$, needs to satisfy,

$$\begin{aligned}
&\mathcal{E}''_t(\bar{u}_t, \bar{\phi}_t, \bar{\alpha}_t)\langle(\dot{u}, \dot{\phi}, \dot{\alpha}), (\widehat{v} - \dot{u}, \widehat{\varphi} - \dot{\phi}, \widehat{\beta} - \dot{\alpha})\rangle \\
&+ \dot{\mathcal{E}}'_t(\bar{u}_t, \bar{\phi}_t, \bar{\alpha}_t)(\widehat{v} - \dot{u}, \widehat{\varphi} - \dot{\phi}, \widehat{\beta} - \dot{\alpha}) \geq 0 \quad \forall\, (\widehat{v}, \widehat{\varphi}, \widehat{\beta}) \in C \times \widehat{\mathcal{P}} \times \widehat{\mathcal{D}}^d_t.
\end{aligned} \tag{8.57}$$

To verify if any rate other than the x_1-homogeneous rate, $(\dot{\bar{u}}, \dot{\bar{\phi}}, \dot{\bar{\alpha}})$, satisfies the rate problem we proceed as follows. First choosing $(\widehat{v}, \widehat{\varphi}, \widehat{\beta}) = (\dot{\bar{u}}, \dot{\bar{\phi}}, \dot{\bar{\alpha}})$ in Eq.(8.57) we get,

$$\begin{aligned}
&\mathcal{E}''_t(\bar{u}_t, \bar{\phi}_t, \bar{\alpha}_t)\langle(\dot{u}, \dot{\phi}, \dot{\alpha}), (\dot{\bar{u}} - \dot{u}, \dot{\bar{\phi}} - \dot{\phi}, \dot{\bar{\alpha}} - \dot{\alpha})\rangle \\
&\qquad + \dot{\mathcal{E}}'_t(\bar{u}_t, \bar{\phi}_t, \bar{\alpha}_t)(\dot{\bar{u}} - \dot{u}, \dot{\bar{\phi}} - \dot{\phi}, \dot{\bar{\alpha}} - \dot{\alpha}) \geq 0.
\end{aligned} \tag{8.58}$$

Whereas by choosing $(\widehat{v}, \widehat{\varphi}, \widehat{\beta}) = (\dot{u}, \dot{\phi}, \dot{\alpha})$ in Eq.(8.57) that is already written with $(\dot{\bar{u}}, \dot{\bar{\phi}}, \dot{\bar{\alpha}})$ as the solution we get,

$$\begin{aligned}\mathcal{E}_t''(\bar{u}_t, \bar{\phi}_t, \bar{\alpha}_t)\langle(\dot{\bar{u}}, \dot{\bar{\phi}}, \dot{\bar{\alpha}}), (\dot{u} - \dot{\bar{u}}, \dot{\phi} - \dot{\bar{\phi}}, \dot{\alpha} - \dot{\bar{\alpha}})\rangle \\ + \dot{\mathcal{E}}_t'(\bar{u}_t, \bar{\phi}_t, \bar{\alpha}_t)(\dot{u} - \dot{\bar{u}}, \dot{\phi} - \dot{\bar{\phi}}, \dot{\alpha} - \dot{\bar{\alpha}}) \geq 0.\end{aligned} \tag{8.59}$$

Adding Eq.(8.58) and Eq.(8.59) we get the inequality,

$$\mathcal{E}_t''(\bar{u}_t, \bar{\phi}_t, \bar{\alpha}_t)(\dot{u} - \dot{\bar{u}}, \dot{\phi} - \dot{\bar{\phi}}, \dot{\alpha} - \dot{\bar{\alpha}})^2 \leq 0, \tag{8.60}$$

This condition holds true *only if* $(\dot{u}, \dot{\phi}, \dot{\alpha}) = (\dot{\bar{u}}, \dot{\bar{\phi}}, \dot{\bar{\alpha}})$, when $\mathcal{E}_t''(\bar{u}_t, \bar{\phi}_t, \bar{\alpha}_t)$ is positive definite thus indicating a uniqueness criterion for the solution of the rate problem. Note that both $(\dot{u}, \dot{\phi}, \dot{\alpha})$ and $(\dot{\bar{u}}, \dot{\bar{\phi}}, \dot{\bar{\alpha}})$ come from the same space. Whereas, $(\dot{u} - \dot{\bar{u}}, \dot{\phi} - \dot{\bar{\phi}}, \dot{\alpha} - \dot{\bar{\alpha}}) \in C \times \dot{\mathcal{P}} \times \dot{\mathcal{D}}_t$ where $\dot{\mathcal{D}}_t$ is the linear space associated to $\dot{\mathcal{D}}_t^d$ at time t defined as,

$$\dot{\mathcal{D}}_t = \{\beta \in H^1(\Omega) : \beta = 0 \text{ in } \Omega_t^e\}. \tag{8.61}$$

Synopsis: The uniqueness of the x_1-homogeneous rate solution of the rate problem and consequently the impossibility of bifurcation from the fundamental branch are ensured by the positive definiteness of the quadratic form $\mathcal{E}_t''(\bar{u}_t, \bar{\phi}_t, \bar{\alpha}_t)(\bullet)^2$ when applied on directions belonging to $C \times \dot{\mathcal{P}} \times \dot{\mathcal{D}}_t$. Specifically,

$$\forall (\widehat{v}, \widehat{\varphi}, \widehat{\beta}) \in C \times \dot{\mathcal{P}} \times \dot{\mathcal{D}}_t \begin{cases} \mathcal{E}_t''(\bar{u}_t, \bar{\phi}_t, \bar{\alpha}_t)(\widehat{v}, \widehat{\varphi}, \widehat{\beta})^2 > 0 \implies \textit{no bifurcation} \\ \mathcal{E}_t''(\bar{u}_t, \bar{\phi}_t, \bar{\alpha}_t)(\widehat{v}, \widehat{\varphi}, \widehat{\beta})^2 \leq 0 \implies \textit{bifurcation possible.} \end{cases} \tag{8.62}$$

> *Remark:* One can notice from the above results that both the loss of stability of the fundamental state and the possibility of bifurcation from it, amount to studying the positive definiteness of the same quadratic form, $\mathcal{E}_t''(\bar{u}_t, \bar{\phi}_t, \bar{\alpha}_t)(\bullet)^2$, when applied on directions belonging to different spaces: $C \times \widehat{\mathcal{P}} \times \widehat{\mathcal{D}}_t^d$ and $C \times \dot{\mathcal{P}} \times \dot{\mathcal{D}}_t$ respectively. If t_b and t_s are two positive times at which respectively, bifurcation from and instability of the fundamental state first occur, then one can prove as a consequence of $\widehat{\mathcal{P}} \subset \dot{\mathcal{P}}$ and $\widehat{\mathcal{D}}_t^d \subset \dot{\mathcal{D}}_t$ that $t_b \leq t_s$. This proof is considered to be out of scope of the current work. However, one can find such a proof in Sicsic et al. (2014) employing the minimization of 'Rayleigh' ratios for both cases in a thermal shock problem which has a similar structure.

8.3.4 Characterization of bifurcations

Now we are in a position to study the possibility of bifurcations by assuming general forms of the directions on which the quadratic form is to be applied. To this end, let $(\widehat{v}, \widehat{\varphi}, \widehat{\beta}) \in C \times \dot{\mathcal{P}} \times \dot{\mathcal{D}}_t$ be a general direction. Its components can be decomposed into their respective Fourier modes with characteristic wave numbers $k \in \mathbb{N}$ as follows,

$$\begin{aligned}\widehat{v}(x) &= \sum_k v^k(x), \quad v^k(x) = v_1^k(x_2) \sin\left(\frac{k\pi x_1}{L}\right) e_1 + v_2^k(x_2) \cos\left(\frac{k\pi x_1}{L}\right) e_2, \\ \widehat{\varphi}(x) &= \sum_k \varphi^k(x), \quad \varphi^k(x) = \varphi_1^k(x_2) \cos\left(\frac{k\pi x_1}{L}\right), \\ \widehat{\beta}(x) &= \sum_k \beta^k(x), \quad \beta^k(x) = \beta_1^k(x_2) \cos\left(\frac{k\pi x_1}{L}\right).\end{aligned} \tag{8.63}$$

While choosing the above decomposition, the boundary conditions that apply to the admissible perturbations to the fundamental state are a priori adapted to $(\widehat{v}, \widehat{\varphi}, \widehat{\beta})$. Specifically, since the KKT conditions, Eq.(8.35), demand that on any boundary where damage grows the spatial derivative normal to it vanishes. This applies to the lateral boundaries of the damaged strip and to the drying boundary, respectively $\{(x_1 = 0) \cup (x_2 \in (0, d_t))\}$ and $\{(x_1 = L) \cup (x_2 \in (0, d_t))\}$. Whereas in Ω_t^e since damage is uniformly zero, its spatial derivative as well vanishes at its boundaries, $\{(x_1 = 0) \cup (x_2 \in (d_t, H))\}$ and $\{(x_1 = L) \cup (x_2 \in (d_t, H))\}$. Consequently for the damage rate one gets, $\partial\widehat{\beta}/\partial x_1 = 0$ on $x_1 = 0$ and $x_1 = L$. Similarly using the boundary conditions on displacement imply that on $x_1 = 0$ and $x_1 = L$, $\widehat{v}_1 = 0$ uniformly, implying $\partial\widehat{v}_1/\partial x_2 = 0$ and since the shear stress at this boundary vanishes we get $\partial\widehat{v}_2/\partial x_1 = 0$. In addition to the above, the x_1 independence of the fundamental state justifies the forms assumed for $\widehat{v}$ an $\widehat{\beta}$ in Eq.(8.63). Consequently the following definitions for their gradients hold for each k,

$$\begin{aligned}\varepsilon(v^k) = v_1^k \frac{k\pi}{L} \cos\left(\frac{k\pi x_1}{L}\right) e_1 \otimes e_1 + \frac{dv_2^k}{dx_2} \cos\left(\frac{k\pi x_1}{L}\right) e_2 \otimes e_2 \\ + \frac{1}{2} \sin\left(\frac{k\pi x_1}{L}\right) \left(\frac{dv_1^k}{dx_2} - v_2^k \frac{k\pi}{L}\right) (e_1 \otimes e_2 + e_2 \otimes e_1), \\ \nabla\beta^k = -\beta_1^k \frac{k\pi}{L} \sin\left(\frac{k\pi x_1}{L}\right) e_1 + \frac{d\beta_1^k}{dx_2} \cos\left(\frac{k\pi x_1}{L}\right) e_2.\end{aligned} \tag{8.64}$$

Owing to the classical constitutive relation for porosity, Eq.(8.30), obtained by rearranging the zeroth-order balance law for variations in porosity, the above definition of $\varepsilon(v^k)$ and the boundary conditions of the hydraulic problem for p_t, Eq.(8.38), one can justify the form assumed for $\widehat{\varphi}$ in Eq.(8.63).

Exploiting the orthogonality among different Fourier modes allows to uncouple them and evaluate the functional $\mathcal{E}_t''(u_t, \phi_t, \alpha_t)(\widehat{v}, \widehat{\varphi}, \widehat{\beta})^2$ in Eq.(8.20) at $(\bar{u}_t, \bar{\phi}_t, \bar{\alpha}_t)$, in directions for each k separately. Following this and integrating once along x_1 gives,

$$\begin{aligned}&\mathcal{E}_t''(\bar{u}_t, \bar{\phi}_t, \bar{\alpha}_t)(v^k, \varphi^k, \beta^k)^2 = \\ &\frac{L}{2} \int_{x_2=0}^{x_2=H} \left\{ \lambda \left[v_1^k \frac{k\pi}{L} + \frac{dv_2^k}{dx_2} \right]^2 + 2\mu \left[\left(v_1^k \frac{k\pi}{L} \right)^2 + \left(\frac{dv_2^k}{dx_2} \right)^2 \right] \right. \\ &+ \mu \left[\frac{dv_1^k}{dx_2} - v_2^k \frac{k\pi}{L} \right]^2 + N \left[b \left(v_1^k \frac{k\pi}{L} + \frac{dv_2^k}{dx_2} \right) - \varphi_1^k \right]^2 \\ &\left. - \bar{\phi}_t \bar{\pi}_t''(\beta_1^k)^2 - 2\bar{\pi}_t' \varphi_1^k \beta_1^k + w_1 \ell^2 \left[\left(\beta_1^k \frac{k\pi}{L} \right)^2 + \left(\frac{d\beta_1^k}{dx_2} \right)^2 \right] \right\} dx,\end{aligned} \tag{8.65}$$

where functions denoted $(\bar{\cdot})$ are to be understood as evaluated at the fundamental state. Dependency on the wave number in the above expression can be understood as a parametrization and study of the positivity of quadratic form can be recast into a comparison with 0 the smallest eigenvalue of the eigenproblem,

$$\left(\mathcal{E}_t''(\bar{u}_t, \bar{\phi}_t, \bar{\alpha}_t; k) - \mu_k I\right) (v_1^k, v_2^k, \varphi_1^k, \beta_1^k)^2 = 0, \quad \forall k \in \mathbb{N}, \tag{8.66}$$

where μ_k denotes the eigenvalues and $(v_1^k, v_2^k, \varphi_1^k, \beta_1^k)$ the eigenvectors for each k.

Accordingly the criterion for bifurcation, Eq.(8.62), at each time $t > 0$ can be translated to,

$$\begin{aligned}&\forall k \in \mathbb{N}\\ &\forall (v_1^k, v_2^k, \varphi_1^k, \beta_1^k) \in \\ &H^1(\widetilde{\Omega}) \times H_0^1(\widetilde{\Omega}) \times H^1(\widetilde{\Omega}) \times H_t^1(\widetilde{\Omega})\end{aligned} \quad \begin{cases} \inf\{\mathfrak{R}(\mu_k)\} > 0 \implies \textit{no bifurcation} \\ \inf\{\mathfrak{R}(\mu_k)\} \leq 0 \implies \textit{bifurcation possible.} \end{cases} \tag{8.67}$$

With $\widetilde{\Omega}$ as defined in Sec.(8.3.2), $H_0^1(\widetilde{\Omega})$ are the space of H^1 functions in $\widetilde{\Omega}$ that vanish at $x_2 = H$ and $H_t^1(\widetilde{\Omega})$ are those vanishing in the undamaged region $x_2 \in (d_t, H)$.

Indicative study of bifurcations

While the true possibility of bifurcations could be understood by the criterion Eq.(8.67), we can investigate the behavior of the coefficients of the quadratic form $\mathcal{E}_t''(\bar{u}_t, \bar{\phi}_t, \bar{\alpha}_t)(\widehat{v}, \widehat{\varphi}, \widehat{\beta})^2$ which gives a qualitative indication. This is the purpose of the current section. By virtue of Eq.(8.20) we can classify the various terms within the functional as follows,

$$\mathcal{E}_t''(\bar{u}_t, \bar{\phi}_t, \bar{\alpha}_t)(\widehat{v}, \widehat{\varphi}, \widehat{\beta})^2 = \mathcal{A}_t(\bar{u}_t, \bar{\phi}_t, \bar{\alpha}_t)(\widehat{v}, \widehat{\varphi}, \widehat{\beta})^2 + \mathcal{B}_t(\bar{u}_t, \bar{\phi}_t, \bar{\alpha}_t)(\widehat{v}, \widehat{\varphi}, \widehat{\beta})^2, \tag{8.68}$$

with,

$$\begin{aligned}\mathcal{A}_t(\bar{u}_t, \bar{\phi}_t, \bar{\alpha}_t)(\widehat{v}, \widehat{\varphi}, \widehat{\beta})^2 &= \int_\Omega \Big\{ \varepsilon(\widehat{v}) : \mathbb{C} : \varepsilon(\widehat{v}) + N\,(b\epsilon(\widehat{v}) - \widehat{\varphi})^2 - \bar{\phi}_t \bar{\pi}_t'' \widehat{\beta}^2 \\ &\qquad + w_1 \ell^2 \nabla\widehat{\beta} \cdot \nabla\widehat{\beta} \Big\} dx, \\ \mathcal{B}_t(\bar{u}_t, \bar{\phi}_t, \bar{\alpha}_t)(\widehat{v}, \widehat{\varphi}, \widehat{\beta})^2 &= -\int_\Omega 2\bar{\pi}_t' \widehat{\varphi}\widehat{\beta}\, dx.\end{aligned} \tag{8.69}$$

We can conclude that the first term, $\mathcal{A}_t(\bar{u}_t, \bar{\phi}_t, \bar{\alpha}_t)(\widehat{v}, \widehat{\varphi}, \widehat{\beta})^2$, is positive definite because N, w_1 are positive constants, the stiffness tensor, $\mathbb{C}$, is positive definite, $\bar{\phi}_t \in \mathcal{P}$ and $\bar{\pi}_t'' = 2(-\widetilde{p}_c(\bar{S}_t)\bar{S}_t - U(\bar{S}_t)) < 0$. Thus this term acts to prevent any bifurcations from occurring.

The term $\mathcal{B}_t(\bar{u}_t, \bar{\phi}_t, \bar{\alpha}_t)(\widehat{v}, \widehat{\varphi}, \widehat{\beta})^2$ on the other hand contributes to the possibility of bifurcations. Even if the sign of the cross term in $(\widehat{\varphi}\widehat{\beta})$ could only be determined by solving the eigenproblem, its coefficient however is positive since $\bar{\pi}_t' = -2(1 - \bar{\alpha}_t)(-\widetilde{p}_c(\bar{S}_t)\bar{S}_t - \widetilde{U}(\bar{S}_t)) > 0$. For the sake of being conservative this cross term is considered negative in the following analysis.

In view of the above analysis, one can study the strength of $\mathcal{B}_t$ by studying the strength of its coefficient as a function of time in order to understand the behavior of bifurcations, if they occur. It can be observed that this coefficient is function of the fundamental states that were resolved in Sec.(8.3.2). Fig.(8.7) shows the evolution of $\bar{\pi}_t'$, with respect to the saturation degree for different values of the threshold w_1. As the saturation degree reduces with time during the drying process it can be seen that this function deviates from its undamaged path as soon as damage is initiated and its magnitude tends to reduces as damage propagates into the domain. This indicates that the term $\mathcal{B}_t$ reduces with time and one can infer that the tendency to bifurcate from the fundamental branch reduces as well. For higher values of w_1 however the magnitude of $\bar{\pi}_t'$ starts to pickup after the initial reduction. However, the rate of this increase was found to be extremely slow due to the saturation degree being close to vanishing and the path followed is on a very steep degraded retention curve as seen in

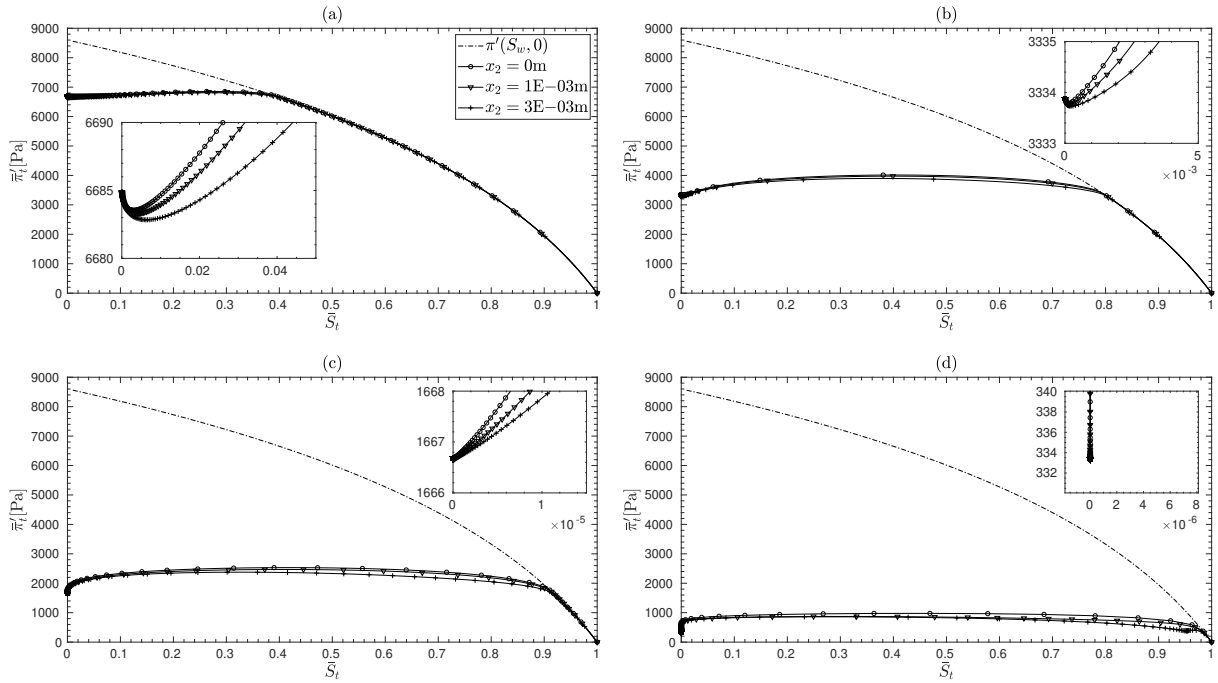

Figure 8.7: Evolution of the function $\bar{\pi}'_t$ with $\bar{S}_t$ at the boundary $x_2 = 0$m and two locations within the domain close to this boundary. The different values of w_1 used are (a) 2000N.m^{-3}, (b) 1000N.m^{-3}, (c) 500N.m^{-3}, (d) 100N.m^{-3}. In each plot the possible evolution if damage remains vanishing, $\pi'(S_w, 0)$, is also plotted for reference.

Fig.(8.5(a)). One can make similar inferences for the loss of stability as well since, as remarked earlier, it also amounts to the study of a quadratic form involving the same operator, $\mathcal{E}''_t(\bar{u}_t, \bar{\phi}_t, \bar{\alpha}_t)$ according to Eq.(8.46).

8.4 SYNOPSIS

In this chapter a novel approach to modeling of capillary force driven fracturing phenomenon has been proposed, inspired by the experimental results mainly obtained by Shin and Santamarina (2010, 2011a) and based in the gradient damage modeling following Marigo et al. (2016). The evolution problem for damage is posed starting from a total energy of the porous solid and following a variational approach assuming a minimization principle to hold true at each time. First-order stability conditions and necessary conditions are derived that form the governing equations that can be resolved numerically. Criterion for loss of stability of the base solutions and possibility of bifurcation from the fundamental branch are derived respectively from the second-order stability conditions and a rate problem. An indicative study reveals that, at the current state the model does not exhibit a clear bifurcation and similarly loss of stability of the damage base solution, which should induce damage localization, notwithstanding the behavior of $\bar{\pi}'_t$ which seems to indicate this possibility for relatively large values of w_1.

While the solution of an eigenproblem could reveal more details, we claim that the lack of clear bifurcation is due to the simplified approach adopted in this paper. Specifically, we did not account in a comprehensive manner for the degradation of the resistance to fluid flow within the damaged zone and eventually along localized fracture planes. This could in principle be achieved via a suitable coupling between the intrinsic permeability and the damage parameter, for instance as proposed in Miehe et al. (2015).

9 CONCLUSION & PERSPECTIVES

Conclusion The current thesis dealt with two types of instabilities: hydraulic and mechanical, that are intrinsic to partially saturated porous media such as geomaterials. It starts with a recount of the phenomenology of these two types of instabilities. Then a concise description of two modeling approaches to partial saturation is done: a classical approach and a phase field based approach. Following this, the thesis diverged into two parts each focusing on the one type of instability.

In Part II a one-dimensional analysis of the phase field approach, assuming a rigid porous skeleton, revealed that moving fronts of invading fluid phase can occur under suitable initial and boundary conditions. This is observed both in imbibition and drainage, thanks to the use of a non-convex flux function. These moving fronts are further resolved as traveling waves setting the stage for a linear stability analysis. The LSA and two-dimensional simulations shed light on the hydraulic instabilities that can manifest themselves as fluid fingering phenomena.

In Part III focused on mechanical instabilities in fine-grained geomaterials that result in formation of fractures typically with a complex pattern. An extension of widely used gradient damage modeling of fracture to the context of partial saturation is done under the framework of a variational approach. This modeling approach is tested in the case of a desiccating soil mass revealing its ability to describe fracture pattern that is periodic as observed in representative experiments. While such a modeling perspective is the prevailing one, an investigation of a novel approach is done. This approach is inspired by experimental observations which have revealed that opening mode fractures of desaturating fine-grained soils is due to the invading fluid film rearranging the grains and not due to build-up of tensile stresses.

Perspectives This work leaves in its wake various possibilities, both modeling and experimental. The most natural one being the study of coupling between hydraulic and mechanical instabilities. The initiation of fractures induced by advancing drainage fingers is of particular interest in the context of CO_2 sequestration.

Concerning the phase field partial saturation model, the rich structure of fluid invasion involving coalescence and pinching needs cleverly designed experiments to validate. Also, the validation of results concerning the drainage front could be realized using quasi one-dimensional experiments that are scarce in existing literature. Coming to the capillarity induced damage model, while an indicative study of the bifurcation from fundamental branch is done, this modeling approach merits a full numerical resolution with material properties of various possible fine-grained soils.

Advanced numerical schemes are definitely warranted both for the phase field partial saturation model and the capillary gradient damage model, in view of accurate predictions.

BIBLIOGRAPHY

Alnaes, M. S., J. Blechta, J. Hake, A. Johansson, B. Kehlet, A. Logg, C. Richardson, J. Ring, M. E. Rognes, and G. N. Wells (2015). The fenics project version 1.5. Archive of Numerical Software 3.

Amor, H., J.-J. Marigo, and C. Maurini (2009). Regularized formulation of the variational brittle fracture with unilateral contact: Numerical experiments. *Journal of the Mechanics and Physics of Solids*, 57(8):1209–1229.

ANR-STOWENG (2018). underground storage of renewable energies in low permeability geomaterials. Available at https://anr.fr/Project-ANR-18-CE05-0033.

Auradou, H., K. J. Måløy, J. Schmittbuhl, A. Hansen, and D. Bideau (1999). Competition between correlated buoyancy and uncorrelated capillary effects during drainage. *Phys. Rev. E*, 60:7224–7234.

Balay, S., S. Abhyankar, M. F. Adams, S. Benson, J. Brown, P. Brune, K. Buschelman, E. Constantinescu, L. Dalcin, A. Dener, V. Eijkhout, W. D. Gropp, V. Hapla, T. Isaac, P. Jolivet, D. Karpeev, D. Kaushik, M. G. Knepley, F. Kong, S. Kruger, D. A. May, L. C. McInnes, R. T. Mills, L. Mitchell, T. Munson, J. E. Roman, K. Rupp, P. Sanan, J. Sarich, B. F. Smith, S. Zampini, H. Zhang, H. Zhang, and J. Zhang (2021). PETSc/TAO users manual. Technical Report ANL-21/39 - Revision 3.16, Argonne National Laboratory.

Bauters, T., D. DiCarlo, T. Steenhuis, and J.-Y. Parlange (2000). Soil water content dependent wetting front characteristics in sands. *Journal of Hydrology*, 231-232:244–254.

Bear, J. (1972). *Dynamics of Fluids in Porous Media*. Elsevier.

Benallal, A. and J.-J. Marigo (2006). Bifurcation and stability issues in gradient theories with softening. *Modelling and Simulation in Materials Science and Engineering*, 15(1):S283–S295.

Bertozzi, A., A. Mnch, and M. Shearer (1999). Undercompressive shocks in thin film flows. *Physica D: Nonlinear Phenomena*, 134(4):431–464.

Bertozzi, A. L. and M. Shearer (2000). Existence of undercompressive traveling waves in thin film equations. *SIAM Journal on Mathematical Analysis*, 32(1):194–213.

Biot, M. A. (1941). General theory of three-dimensional consolidation. *Journal of Applied Physics*, 12:155–164.

Biot, M. A. (1972). Theory of finite deformations of pourous solids. *Indiana Univ. Math. J.*, 21:597–620.

Biot, M. A. and D. G. Willis (1957). The elastic coefficients of the theory of consolidation. *Journal of Applied Mechanics*, 24:594–601.

Birovljev, A., L. Furuberg, J. Feder, T. Jssang, K. J. Mly, and A. Aharony (1991). Gravity invasion percolation in two dimensions: Experiment and simulation. *Phys. Rev. Lett.*, 67:584–587.

Bishop, A. W. (1959). The principle of effective stress. *Teknisk Ukeblad*, 39:859–863.

Bourdin, B., G. Francfort, and J.-J. Marigo (2000). Numerical experiments in revisited brittle fracture. *Journal of the Mechanics and Physics of Solids*, 48(4):797–826.

Bourdin, B., J.-J. Marigo, C. Maurini, and P. Sicsic (2014). Morphogenesis and propagation of complex cracks induced by thermal shocks. *Phys. Rev. Lett.*, 112:014301.

Boyer, F. and C. Lapuerta (2006). Study of a three component cahn-hilliard flow model. *ESAIM: M2AN*, 40(4):653–687.

Boyer, F., C. Lapuerta, S. Minjeaud, and B. Piar (2009). A local adaptive refinement method with multigrid preconditionning illustrated by multiphase flows simulations. *ESAIM: Proc.*, 27:15–53.

Brezzi, F. and M. Fortin (1991). *Mixed and Hybrid Finite Element Methods*. New York: Springer-Verlag.

Brooks, R. and A. Corey (1964). Hydraulic properties of porous media. *Hydrology Papers, Colorado State University*, 3.

Cahn, J. W. and J. E. Hilliard (1958). Free energy of a nonuniform system. i. interfacial free energy. *The Journal of Chemical Physics*, 28(2):258–267.

Cahn, J. W. and J. E. Hilliard (1959). Free energy of a nonuniform system. iii. nucleation in a twofiQucomponent incompressible fluid. *The Journal of Chemical Physics*, 31(3):688–699.

Cajuhi, T., L. Sanavia, and L. De Lorenzis (2018). Phase-field modeling of fracture in variably saturated porous media. *Computational Mechanics*, 61(3):299–318.

Chen, J.-D. and D. Wilkinson (1985). Pore-scale viscous fingering in porous media. *Phys. Rev. Lett.*, 55:1892–1895.

Chen, Y.-F., S. Fang, D.-S. Wu, and R. Hu (2017). Visualizing and quantifying the crossover from capillary fingering to viscous fingering in a rough fracture. *Water Resources Research*, 53(9):7756–7772.

Chiaramonte, L., M. D. Zoback, J. Friedmann, and V. Stamp (2008). Seal integrity and feasibility of co2 sequestration in the teapot dome eor pilot: geomechanical site characterization. *Environmental Geology*, 54:1667–1675.

Choo, J. and W. Sun (2018). Coupled phase-field and plasticity modeling of geological materials: From brittle fracture to ductile flow. *Computer Methods in Applied Mechanics and Engineering*, 330:1–32.

Chuoke, R., P. van Meurs, and C. van der Poel (1959). The instability of slow, immiscible, viscous liquid-liquid displacements in permeable media. *Transactions of the AIME*, 216(01):188–194.

Clothier, B. E., S. R. Green, and M. Deurer (2008). Preferential flow and transport in soil: progress and prognosis. *European Journal of Soil Science*, 59(1):2–13.

Cordero, J. A., P. C. Prat, and A. Ledesma (2021). Experimental analysis of desiccation cracks on a clayey silt from a large-scale test in natural conditions. *Engineering Geology*, 292:106256.

Coussy, O. (2004). *Poromechanics*. John Wiley & Sons, Ltd.

Coussy, O. (2010). *Mechanics and Physics of Porous Solids*. John Wiley & Sons, Ltd.

Cueto-Felgueroso, L. and R. Juanes (2009a). A phase field model of unsaturated flow. *Water Resources Research*, 45(10).

Cueto-Felgueroso, L. and R. Juanes (2009b). Stability analysis of a phase-field model of gravity-driven unsaturated flow through porous media. *Phys. Rev. E*, 79:036301.

Dell'Isola, F. and P. Seppecher (1997). Edge contact forces and quasi-balanced power. *Meccanica*, 32:33–52.

Desrues, J. and E. Andò (2015). Strain localisation in granular media. *Comptes Rendus Physique*, 16(1):26–36. Granular physics / Physique des milieux granulaires.

Desrues, J. and G. Viggiani (2004). Strain localization in sand: an overview of the experimental results obtained in grenoble using stereophotogrammetry. *International Journal for Numerical and Analytical Methods in Geomechanics*, 28(4):279–321.

DiCarlo, D. A. (2004). Experimental measurements of saturation overshoot on infiltration. *Water Resources Research*, 40(4).

DiCarlo, D. A. (2013). Stability of gravity-driven multiphase flow in porous media: 40 years of advancements. *Water Resources Research*, 49(8):4531–4544.

DiCarlo, D. A., R. Juanes, T. LaForce, and T. P. Witelski (2008). Nonmonotonic traveling wave solutions of infiltration into porous media. *Water Resources Research*, 44(2).

DiCarlo, D. A., L. D. Seale, K. Ham, and C. S. Willson (2010). Tomographic measurements of pore filling at infiltration fronts. *Advances in Water Resources*, 33(4):485–492.

Dukler, Y., H. Ji, C. Falcon, and A. L. Bertozzi (2020). Theory for undercompressive shocks in tears of wine. *Phys. Rev. Fluids*, 5:034002.

Eggers, J. and E. Villermaux (2008). Physics of liquid jets. *Reports on Progress in Physics*, 71(3):036601.

Egorov, A. G., R. Z. Dautov, J. L. Nieber, and A. Y. Sheshukov (2003). Stability analysis of gravity-driven infiltrating flow. *Water Resources Research*, 39(9).

El, G. A., M. A. Hoefer, and M. Shearer (2016). Expansion shock waves in regularized shallow-water theory. *Proceedings of the Royal Society A: Mathematical, Physical and Engineering Sciences*, 472(2189):20160141.

Eliassi, M. and R. J. Glass (2001). On the continuum-scale modeling of gravity-driven fingers in unsaturated porous media: The inadequacy of the richards equation with standard monotonic constitutive relations and hysteretic equations of state. *Water Resources Research*, 37(8):2019–2035.

Eliassi, M. and R. J. Glass (2002). On the porous-continuum modeling of gravity-driven fingers in unsaturated materials: Extension of standard theory with a hold-back-pile-up effect. *Water Resources Research*, 38(11):16–1–16–11.

Eliassi, M. and R. J. Glass (2003). On the porous continuum-scale modeling of gravity-driven fingers in unsaturated materials: Numerical solution of a hypodiffusive governing equation that incorporates a hold-back-pile-up effect. *Water Resources Research*, 39(6).

Espinoza, D. N. and J. C. Santamarina (2017). Co2 breakthrough-caprock sealing efficiency and integrity for carbon geological storage. *International Journal of Greenhouse Gas Control*, 66:218–229.

Falkowski, P., R. J. Scholes, E. Boyle, J. Canadell, D. Canfield, J. Elser, N. Gruber, K. Hibbard, P. Hgberg, S. Linder, F. T. Mackenzie, B. Moore III, T. Pedersen, Y. Rosenthal, S. Seitzinger, V. Smetacek, and W. Steffen (2000). The global carbon cycle: A test of our knowledge of earth as a system. *Science*, 290(5490):291–296.

Farthing, M. W. and F. L. Ogden (2017). Numerical solution of richards' equation: A review of advances and challenges. *Soil Science Society of America Journal*, 81(6):1257–1269.

Galdino, S. (2011). A family of regula falsi root-finding methods.

Gilfillan, S. M., M. Wilkinson, R. S. Haszeldine, Z. K. Shipton, S. T. Nelson, and R. J. Poreda (2011). He and ne as tracers of natural co2 migration up a fault from a deep reservoir. *International Journal of Greenhouse Gas Control*, 5(6):1507–1516.

Glass, R., T. Steenhuis, and J.-Y. Parlange (1988). Wetting front instability as a rapid and far-reaching hydrologic process in the vadose zone. *Journal of Contaminant Hydrology*, 3(2):207–226. Rapid and Far-Reaching Hydrologic Processes in the Vadose Zone.

Glass, R. J., T. S. Steenhuis, and J.-Y. Parlange (1989a). Mechanism for finger persistence in homogeneous, unsaturated, porous media: Theory and verification. *Soil Science*, 148:60–70.

Glass, R. J., T. S. Steenhuis, and J.-Y. Parlange (1989b). Wetting front instability: 2. experimental determination of relationships between system parameters and two-dimensional unstable flow field behavior in initially dry porous media. *Water Resources Research*, 25(6):1195–1207.

Gorman, A. R., W. S. Holbrook, M. J. Hornbach, K. L. Hackwith, D. Lizarralde, and I. Pecher (2002). Migration of methane gas through the hydrate stability zone in a low-flux hydrate province. *Geology*, 30(4):327–330.

Gray, W. G. and S. M. Hassanizadeh (1991a). Paradoxes and realities in unsaturated flow theory. *Water Resources Research*, 27(8):1847–1854.

Gray, W. G. and S. M. Hassanizadeh (1991b). Unsaturated flow theory including interfacial phenomena. *Water Resources Research*, 27(8):1855–1863.

Guo, F. and S. A. Aryana (2019). An experimental investigation of flow regimes in imbibition and drainage using a microfluidic platform. *Energies*, 12(7).

Hassanizadeh, S. M. and W. G. Gray (1990). Mechanics and thermodynamics of multiphase flow in porous media including interphase boundaries. *Advances in Water Resources*, 13(4):169–186.

Hassanizadeh, S. M. and W. G. Gray (1993). Toward an improved description of the physics of two-phase flow. *Advances in Water Resources*, 16(1):53–67. Research Perspectives in Hydrology.

Hayes, B. and M. Shearer (1999). Undercompressive shocks and riemann problems for scalar conservation laws with non-convex fluxes. *Proceedings of the Royal Society of Edinburgh: Section A Mathematics*, 129(4):733–754.

Heider, Y. and W. Sun (2020). A phase field framework for capillary-induced fracture in unsaturated porous media: Drying-induced vs. hydraulic cracking. *Computer Methods in Applied Mechanics and Engineering*, 359:112647.

Hilfer, R. and R. Steinle (2014). Saturation overshoot and hysteresis for twophase flow in porous media. *Eur. Phys. J. Spec. Top*, 223(1):2323–2338.

Holtzman, R., M. L. Szulczewski, and R. Juanes (2012). Capillary fracturing in granular media. *Phys. Rev. Lett.*, 108:264504.

Homsy, G. M. (1987). Viscous fingering in porous media. *Annual Review of Fluid Mechanics*, 19(1):271–311.

Hu, T., J. Guilleminot, and J. E. Dolbow (2020). A phase-field model of fracture with frictionless contact and random fracture properties: Application to thin-film fracture and soil desiccation. *Computer Methods in Applied Mechanics and Engineering*, 368:113106.

Jacqmin, D. (2000). Contact-line dynamics of a diffuse fluid interface. *Journal of Fluid Mechanics*, 402:57–88.

Jain, A. K. and R. Juanes (2009). Preferential mode of gas invasion in sediments: Grain-scale mechanistic model of coupled multiphase fluid flow and sediment mechanics. *Journal of Geophysical Research: Solid Earth*, 114(B8).

Jarvis, N. J. (2007). A review of non-equilibrium water flow and solute transport in soil macropores: principles, controlling factors and consequences for water quality. *European Journal of Soil Science*, 58(3):523–546.

Kim, J. (2012). Phase-field models for multi-component fluid flows. *Communications in Computational Physics*, 12(3):613–661.

Lakshmikantha, M., P. C. Prat, and A. Ledesma (2012). Experimental evidence of size effect in soil cracking. *Canadian Geotechnical Journal*, 49(3):264–284.

LeFloch, P. G. (2002). *Hyperbolic Systems of Conservation Laws*. Birkhäuser, Basel.

Lenormand, R. (1985). Capillary and viscous fingering in an etched network. In *Physics of Finely Divided Matter*, N. Boccara and M. Daoud, eds., Pp. 289–294, Berlin, Heidelberg. Springer Berlin Heidelberg.

Lenormand, R. (1990). Liquids in porous media. *Journal of Physics: Condensed Matter*, 2(S):SA79–SA88.

Lenormand, R., E. Touboul, and C. Zarcone (1988). Numerical models and experiments on immiscible displacements in porous media. *Journal of Fluid Mechanics*, 189:165–187.

Leverett, M. (1941). Capillary Behavior in Porous Solids. *Transactions of the AIME*, 142(01):152–169.

Liu, X. and P. B. Flemings (2006). Passing gas through the hydrate stability zone at southern hydrate ridge, offshore oregon. *Earth and Planetary Science Letters*, 241(1):211–226.

Loria, P. and M. B. Bright (2021). Lessons captured from 50 years of ccs projects. *The Electricity Journal*, 34(7):106998. Special Issue: Carbon Capture and Storage Today: Applications, Needs, Perceptions and Barriers.

Løvoll, G., Y. Méheust, K. J. Måløy, E. Aker, and J. Schmittbuhl (2005). Competition of gravity, capillary and viscous forces during drainage in a two-dimensional porous medium, a pore scale study. *Energy*, 30(6):861–872. Second International Onsager Conference.

Lowengrub, J. and L. Truskinovsky (1998). Quasi-incompressible cahn-hilliard fluids and topological transitions. *Proceedings of the Royal Society of London. Series A: Mathematical, Physical and Engineering Sciences*, 454(1978):2617–2654.

Luckner, L., M. T. Van Genuchten, and D. R. Nielsen (1989). A consistent set of parametric models for the two-phase flow of immiscible fluids in the subsurface. *Water Resources Research*, 25(10):2187–2193.

Macminn, C. W., M. L. Szulczewski, and R. Juanes (2010). Co2 migration in saline aquifers. part 1. capillary trapping under slope and groundwater flow. *Journal of Fluid Mechanics*, 662:329–351.

Marigo, J.-J., C. Maurini, and K. Pham (2016). An overview of the modelling of fracture by gradient damage models. *Meccanica*, 51:3107–3128.

Martin, D. F., P. Colella, M. Anghel, and F. L. Alexander (2005). Adaptive mesh refinement for multiscale nonequilibrium physics. *Computing in Science & Engineering*, 7(03):24–31.

Matos, C. R., J. F. Carneiro, and P. P. Silva (2019). Overview of large-scale underground energy storage technologies for integration of renewable energies and criteria for reservoir identification. *Journal of Energy Storage*, 21:241–258.

Méheust, Y., G. Løvoll, K. J. Måløy, and J. Schmittbuhl (2002). Interface scaling in a two-dimensional porous medium under combined viscous, gravity, and capillary effects. *Phys. Rev. E*, 66:051603.

Miehe, C. and S. Mauthe (2016). Phase field modeling of fracture in multi-physics problems. part iii. crack driving forces in hydro-poro-elasticity and hydraulic fracturing of fluid-saturated porous media. *Computer Methods in Applied Mechanics and Engineering*, 304:619–655.

Miehe, C., S. Mauthe, and S. Teichtmeister (2015). Minimization principles for the coupled problem of darcy-biot-type fluid transport in porous media linked to phase field modeling of fracture. *Journal of the Mechanics and Physics of Solids*, 82:186–217.

Miller, C. T., G. Christakos, P. T. Imhoff, J. F. McBride, J. A. Pedit, and J. A. Trangenstein (1998). Multiphase flow and transport modeling in heterogeneous porous media: challenges and approaches. *Advances in Water Resources*, 21(2):77–120.

Miller, C. T., C. N. Dawson, M. W. Farthing, T. Y. Hou, J. Huang, C. E. Kees, C. Kelley, and H. P. Langtangen (2013). Numerical simulation of water resources problems: Models, methods, and trends. *Advances in Water Resources*, 51:405–437. 35th Year Anniversary Issue.

Morrow, N. R. (1970). Physics and thermodynamics of capillary action in porous media. *Industrial & Engineering Chemistry*, 62(6):32–56.

Münch, A. (2000). Shock transitions in marangoni gravity-driven thin-film flow. *Nonlinearity*, 13(3):731–746.

Nahlawi, H. and J. K. Kodikara (2006). Laboratory experiments on desiccation cracking of thin soil layers. *Geotechnical & Geological Engineering*, 24(6):1641–1664.

Nieber, J., T. Bauters, T. Steenhuis, and J.-Y. Parlange (2000). Numerical simulation of experimental gravity-driven unstable flow in water repellent sand. *Journal of Hydrology*, 231-232:295–307.

Nieber, J. L., R. Z. Dautov, A. G. Egorov, and A. Y. Sheshukov (2005). Dynamic capillary pressure mechanism for instability in gravity-driven flows; review and extension to very dry conditions. *Transport in Porous Media*, 58(1):147–172.

Parlange, J.-Y. and D. E. Hill (1976). Theoretical analysis of wetting front instability in soils. *Soil Science*, 122:236–239.

Pasten, C. and J. Carlos Santamarina (2011). Energy geo-storage - analysis and geomechanical implications. *KSCE Journal of Civil Engineering*, 15:655.

Paull, C. K., P. G. Brewer, W. Ussler, E. T. Peltzer, G. Rehder, and D. Clague (2002). An experiment demonstrating that marine slumping is a mechanism to transfer methane from seafloor gas-hydrate deposits into the upper ocean and atmosphere. *Geo-Marine Letters*, 22:198–203.

Peron, H., T. Hueckel, L. Laloui, and L. B. Hu (2009). Fundamentals of desiccation cracking of fine-grained soils: experimental characterisation and mechanisms identification. *Canadian Geotechnical Journal*, 46(10):1177–1201.

Peters, E. J. and D. L. Flock (1981). The onset of instability during two-phase immiscible displacement in porous media. *Society of Petroleum Engineers Journal*, 21(02):249–258.

Pham, K., H. Amor, J.-J. Marigo, and C. Maurini (2011a). Gradient damage models and their use to approximate brittle fracture. *International Journal of Damage Mechanics*, 20(4):618–652.

Pham, K. and J.-J. Marigo (2010a). Approche variationnelle de l'endommagement : I. les concepts fondamentaux. *Comptes Rendus Mcanique*, 338(4):191–198.

Pham, K. and J.-J. Marigo (2010b). Approche variationnelle de l'endommagement : Ii. les modles gradient. *Comptes Rendus Mcanique*, 338(4):199–206.

Pham, K. and J.-J. Marigo (2013). From the onset of damage to rupture: construction of responses with damage localization for a general class of gradient damage models. *Continuum Mechanics and Thermodynamics*, 25:147–171.

Pham, K., J.-J. Marigo, and C. Maurini (2011b). The issues of the uniqueness and the stability of the homogeneous response in uniaxial tests with gradient damage models. *Journal of the Mechanics and Physics of Solids*, 59(6):1163–1190.

Ren, H., X. Zhuang, N.-T. Trung, and T. Rabczuk (2021). Nonlocal operator method for the cahn-hilliard phase field model. *Communications in Nonlinear Science and Numerical Simulation*, 96:105687.

Richards, L. A. (1931). Capillary conduction of liquids through porous mediums. *Physics*, 1(5):318–333.

Richardson, L. F. (1922). Weather prediction by numerical process. by lewis f. richardson. cambridge (university press), 1922. 4. pp. xii + 236. 30s.net. *Quarterly Journal of the Royal Meteorological Society*, 48(203):282–284.

Saffman, P. G. and G. I. Taylor (1958). The penetration of a fluid into a porous medium or hele-shaw cell containing a more viscous liquid. *Proceedings of the Royal Society of London. Series A. Mathematical and Physical Sciences*, 245(1242):312–329.

Schneider, A., F. Hirsch, A. Raab, and T. Raab (2018). Dye tracer visualization of infiltration patterns in soils on relict charcoal hearths. *Frontiers in Environmental Science*, 6.

Sciarra, G. (2016). Phase field modeling of partially saturated deformable porous media. *Journal of the Mechanics and Physics of Solids*, 94:230–256.

Selker, J., P. Leclerq, J.-Y. Parlange, and T. Steenhuis (1992). Fingered flow in two dimensions: 1. measurement of matric potential. *Water Resources Research*, 28(9):2513–2521.

Shampine, L. F. and M. W. Reichelt (1997). The matlab ode suite. *SIAM Journal on Scientific Computing*, 18(1):1–22.

Shin, H. and J. C. Santamarina (2010). Fluid-driven fractures in uncemented sediments: Underlying particle-level processes. *Earth and Planetary Science Letters*, 299(1):180–189.

Shin, H. and J. C. Santamarina (2011a). Desiccation cracks in saturated fine-grained soils: particle-level phenomena and effective-stress analysis. *Gotechnique*, 61(11):961–972.

Shin, H. and J. C. Santamarina (2011b). Open-mode discontinuities in soils. *Gotechnique Letters*, 1(4):95–99.

Shiozawa, S. and H. Fujimaki (2004). Unexpected water content profiles under flux-limited one-dimensional downward infiltration in initially dry granular media. *Water Resources Research*, 40(7).

Sicsic, P., J.-J. Marigo, and C. Maurini (2014). Initiation of a periodic array of cracks in the thermal shock problem: A gradient damage modeling. *Journal of the Mechanics and Physics of Solids*, 63:256–284.

Sloan, E. D. (2003). Fundamental principles and applications of natural gas hydrates. *Nature*, 426:353–359.

Song, J. and D. Zhang (2013). Comprehensive review of caprock-sealing mechanisms for geologic carbon sequestration. *Environmental Science & Technology*, 47(1):9–22. PMID: 23020638.

Stewart, G. W. (2002). A krylov–schur algorithm for large eigenproblems. *SIAM Journal on Matrix Analysis and Applications*, 23(3):601–614.

Stirling, R. A. (2014). *Multiphase Modelling of Desiccation Cracking in Compacted Soil*. PhD thesis, Newcastle University.

Stokes, J. P., D. A. Weitz, J. P. Gollub, A. Dougherty, M. O. Robbins, P. M. Chaikin, and H. M. Lindsay (1986). Interfacial stability of immiscible displacement in a porous medium. *Phys. Rev. Lett.*, 57:1718–1721.

Taylor, G. I. (1950). The instability of liquid surfaces when accelerated in a direction perpendicular to their planes. i. *Proceedings of the Royal Society of London. Series A. Mathematical and Physical Sciences*, 201(1065):192–196.

Terzaghi, K. (1943). Theoretical soil mechanics. In *Theoretical Soil Mechanics*.

Tocci, M. D., C. T. Kelley, and C. T. Miller (1997). Accurate and economical solution of the pressure-head form of richards' equation by the method of lines. *Advances in Water Resources*, 20:1–14.

van Genuchten, M. (1980). A closed-form equation for predicting the hydraulic conductivity of unsaturated soils. *Soil Sci. Soc. Am. J.*, 44:892–898.

Vardoulakis, I., M. Goldscheider, and G. Gudehus (1978). Formation of shear bands in sand bodies as a bifurcation problem. *International Journal for Numerical and Analytical Methods in Geomechanics*, 2(2):99–128.

Wiprut, D. and M. D. Zoback (2000). Fault reactivation and fluid flow along a previously dormant normal fault in the northern North Sea. *Geology*, 28(7):595–598.

Witelski, T. P. (1996). The structure of internal layers for unstable nonlinear diffusion equations. *Studies in Applied Mathematics*, 97(3):277–300.

Xiong, Y. (2014). Flow of water in porous media with saturation overshoot: A review. *Journal of Hydrology*, 510:353–362.

Yamabe, H., T. Tsuji, Y. Liang, and T. Matsuoka (2015). Lattice boltzmann simulations of supercritical co2-water drainage displacement in porous media: Co2 saturation and displacement mechanism. *Environmental Science & Technology*, 49(1):537–543. PMID: 25427299.

Yao, T.-m. and J. M. H. Hendrickx (1996). Stability of wetting fronts in dry homogeneous soils under low infiltration rates. *Soil Science Society of America Journal*, 60(1):20–28.

Zacharoudiou, I., E. S. Boek, and J. Crawshaw (2018). The impact of drainage displacement patterns and haines jumps on co2 storage efficiency. *Scientific Reports*, 8(1):2045–2322.

Zufkhlsdorff, L. and V. Spie (2004). Three-dimensional seismic characterization of a venting site reveals compelling indications of natural hydraulic fracturing. *Geology*, 32(2):101–104.

PART IV
APPENDICES

APPENDIX A

A1 - CONVERGENCE PROPERTIES OF THE ONE-DIMENSIONAL SOLUTIONS

In order to validate the robustness of the numerical scheme adopted to solve the one-dimensional problem of Secs.(4.4.1 & 4.4.2) a mesh convergence analysis has been conducted for two test cases relative to the imbibition and the drainage problem. As expected reducing the element size implies a decrease of the 2-norm of the difference between solutions, for the saturation degree and the generalized chemical potential, computed with successive mesh refinements, see Fig.(9.1). Data relative to the test cases are reported in the caption of the figure.

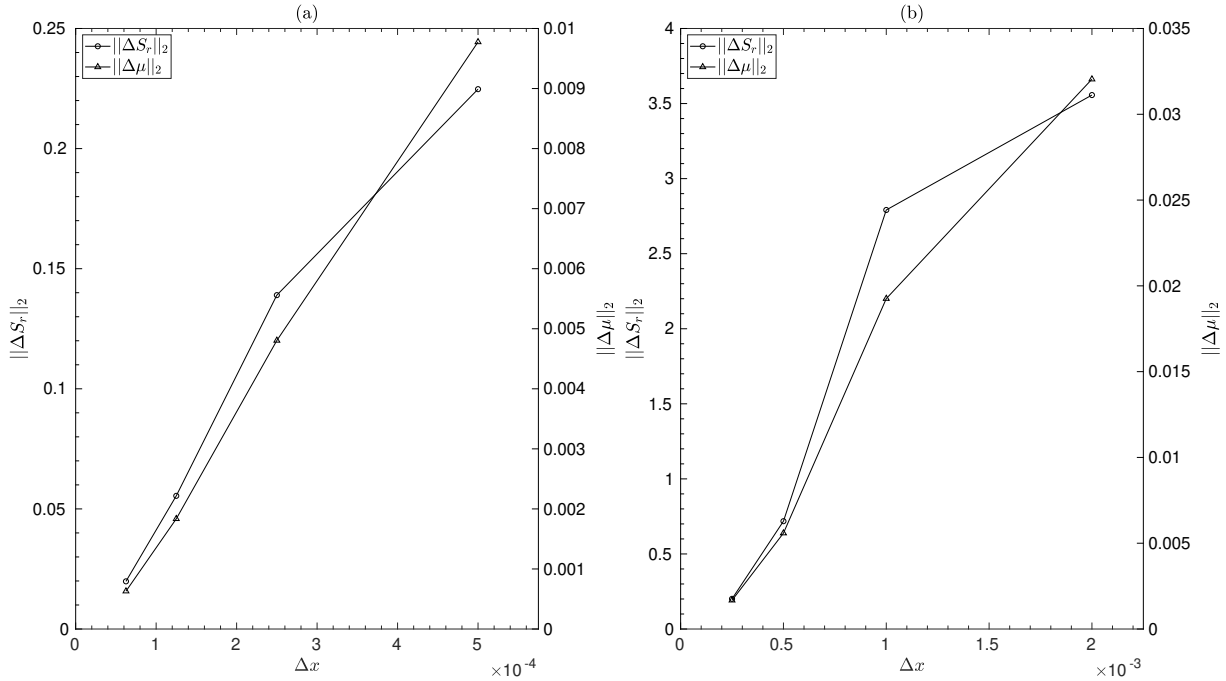

Figure 9.1: Mesh convergence for one-dimensional simulations in Sec.(3.1) with $\lambda = \rho_w g$, $\Delta x/\Delta t = 50$. $||\Delta(\cdot)||_2$ represents the 2-norm of the difference between solutions computed with successive mesh refinements. (a) Imbibition simulations with $S_r^0 = 0.20$, $S_- = 0.80$, Δx = 6.25E-05 1.25E-04 2.5E-04, 5E-04, 1E-03. (b) Drainage simulations with $S_r^0 = 0.99$, $S_r^d = 0.20$, Δx = 2.5E-04, 5E-04, 1E-03, 2E-03, 4E-03.

A2 - LINEARIZATION IN THE VICINITY OF $(s_e, 0, 0)$

Starting from the system of equations Eq.(4.27) rewritten as,

$$\mathcal{S}_\xi(\xi) = \mathcal{F}(\mathcal{S}(\xi)), \tag{9.1}$$

where $\mathcal{S}(\xi) = [s, v, w]^T$ and $\mathcal{F}(\mathcal{S}(\xi)) = [f(v), g(w), h(s, v)]^T$ is the associated short-hand notation for the right hand side of Eq.(4.27). The system can then be expanded about an equilibrium $\mathcal{S}_e(\xi) = [s_e, 0, 0]^T$ as,

$$\mathcal{S}_\xi(\xi) = \mathcal{F}(\mathcal{S}_e(\xi)) + D\mathcal{F}(\mathcal{S}_e(\xi))\epsilon + D^2\mathcal{F}(\mathcal{S}_e(\xi))\frac{\epsilon^2}{2!} + \dots, \tag{9.2}$$

where $D\mathcal{F}(\mathcal{S}_e(\xi))$ and $D^2\mathcal{F}(\mathcal{S}_e(\xi))$ represent the Jacobian and Hessian respectively, of $\mathcal{F}(\mathcal{S}(\xi))$ evaluated at the equilibrium. Subsequently $\epsilon = [s_\epsilon, v_\epsilon, w_\epsilon]^T$ being a small perturbation in the vicinity of $\mathcal{S}_e(\xi)$ allows us to ignore $O(\epsilon^2)$ and higher order terms, leaving us the linear system of equations governing ϵ as,

$$\epsilon_\xi = D\mathcal{F}(\mathcal{S}_e(\xi))\epsilon = \begin{bmatrix} 0 & 1 & 0 \\ 0 & 0 & 1 \\ h_s(s_e, 0) & h_v(s_e, 0) & 0 \end{bmatrix} \begin{bmatrix} s_\epsilon \\ v_\epsilon \\ w_\epsilon \end{bmatrix}, \tag{9.3}$$

where,

$$h_s(s_e, 0) = \frac{C_a\left(\phi c - K'(s_e)\right)}{\delta_R \phi D_{NL} K(s_e)}; \quad h_v(s_e, 0) = \frac{\mu_e'(s_e)}{\phi D_{NL}}. \tag{9.4}$$

The characteristic polynomial, $p(\beta)$, whose roots are the eigen values associated with the system Eq.(9.3) is thus given by,

$$p(\beta) = \det[D\mathcal{F}(\mathcal{S}_e(\xi)) - \beta\mathbb{I}] = \beta^3 - h_v(s_e, 0)\beta - h_s(s_e, 0). \tag{9.5}$$

APPENDIX B: NOTATIONS

- $\bullet$ generic quantity

Algebra

- $\bullet \otimes \bullet$ tensor product between two vectors
- $\bullet \cdot \bullet$ inner product between two tensors involving a single contraction
- $\bullet : \bullet$ inner product between two tensors involving a double contraction
- $\bullet \vdots \bullet$ inner product between two tensors involving a triple contraction
- $\bullet \times \bullet$ Cartesian product of two function spaces

Operators

$\nabla \bullet$	gradient
$\nabla \cdot \bullet$	divergence
$\Delta \bullet$	Laplacian
$\bullet^T$	transpose
$\bullet_D$	deviatoric part of a tensor
$\bullet^+$ or $\bullet_+$	positive part of a tensor or an operator or a functional (as defined when invoked)
$\bullet^-$ or $\bullet_-$	negative part of a tensor or an operator or a functional (as defined when invoked)
$\det \bullet$	determinant of a square matrix or a second-order tensor
$\mathrm{tr} \bullet$	trace of a square matrix or a second-order tensor
$\max(\bullet, \bullet)$	maximum among two arguments
$\min(\bullet, \bullet)$	minimum among two arguments
$\lvert \bullet \rvert$	absolute value
$\lVert \bullet \rVert$	norm as defined when invoked

Colophon

This document is composed
using LaTeX macros and compiled
using pdfTeX engine. The typeface used is
Linux Libertine. The layout is inspired and adapted
from the tufte-book, classic-thesis and two-thirds classes.

CENTRALE NANTES

Titre : Étude des instabilités hydro-mécaniques dans les géomatériaux

Mot clés : saturation partielle ; géomatériaux ; modélisation de champ de phase ; fluide non-uniforme ; gradient d'endommagement ;

Résumé : Les instabilités hydro-mécaniques dans les géomatériaux font référence à une variété de phénomènes non-linéaires qui peuvent être déclenchés par les hétérogénéités intrinsèques de ces matériaux. Les instabilités hydrauliques dans des conditions partiellement saturées peuvent se manifester comme invasion hétérogène d'un fluide 'par digitation'. Les instabilités mécaniques, d'autre part, peuvent se présenter sous la forme de localisations de déformations et/ou de fissures. Ces instabilités potentiellement couplées constituent un obstacle majeur pour une myriade d'applications impliquant les géomatériaux comme la séquestration du dioxyde de carbone (CO_2), l'infiltration des eaux pluviales et aussi pour des prédictions fiables telles que le flux de contaminants dans les eaux souterraines. Les modèles classiques existants ne résolvent pas ce comportement en raison de leur manque d'éléments capable de modéliser la formation d'une microstructure dans leur formulation et sont donc stables contre toute perturbation. Cette thèse vise à proposer et étudier des techniques de modélisation permettant de décrire ces instabilités de manière simple et naturelle. L'approche en loi de comportement adoptée est celle des milieux continus à micro-structure, en particulier celle des milieux continus équipés d'une loi de comportement dépendant du gradient de variables de type champ de phase.

La première partie du travail porte sur la description d'un front fluide-fluide qui a été modélisé comme une interface diffuse. Cela a été fait en interprétant la présence de deux fluides dans l'espace poreux comme un seul fluide non-uniforme et le degré de saturation de l'un des fluides comme un champ de phase. Alors qu'on s'attend à ce que la relation bijective classique entre la pression capillaire et le degré de saturation décrive les propriétés de rétention du réseau poreux en raison de sa texture, une relation enrichie est obtenue en prescrivant un potentiel chimique dans l'esprit de la modélisation de type Cahn-Hilliard de fluides multiphasiques. Cette relation enrichie, associée à une contribution énergétique non-locale, fournit les ingrédients nécessaires pour décrire les écoulement par digitation et les phénomènes non-locaux tels que le pincement et la coalescence des fluides dus aux variations des forces capillaires. En utilisant des techniques de développement asymptotique, il a été démontré analytiquement, dans le cadre d'un modèle unidimensionnel, que le choix des contributions énergétiques utilisées permet de reproduire des profils de saturation non-monotones de type 'overshoot' lors d'une infiltration à vitesse constante dans un milieu relativement sec. Cela s'est avéré correspondre qualitativement à l'observation expérimentale. De plus, l'introduction d'une légère non-convexité dans la fonction de perméabilité relative a a permis , numériquement, de modéliser des fronts de drainage, en plus de l'imbibition, sans employer de complexités supplémentaires dans le modèle. Une soigneuse analyse de stabilité linéaire (ASL) des solutions homogènes contre des perturbations arbitraires a été effectuée. La croissance dans le temps de l'amplitude des perturbations transversales imposées est comprise comme le phénomène de digitation. Les prédictions de l'ASL ont étés suivies par des simulations 2D mettant en lumière la capacité du modèle proposé de décrire le phénomène de digitation et la ségrégation des fluides.

Dans la deuxième partie, le déclenchement d'une fissure au sein d'un milieu poreux asséchant a été étudié. Dans l'esprit de la modélisation à gradient d'endommagement, un modèle de milieu poreux endommagé a d'abord été testé pour sa capacité à reproduire la formation de fissures périodiques telle qu'observée dans des expériences de laboratoire. A partir de ce cadre de la modélisation une généralisation de cette approche a été proposée en interprétant la présence d'une fissure dans un milieu poreux en train de sécher comme une perte de ses propriétés capillaires, permettant ainsi le passage d'un fluide non mouillant sous une pression capillaire évanescente. Ce paradigme est particulièrement intéressant dans la modélisation des sols à grains fins sans cohésion et non-consolidés, où la résistance à traction est négligeable et donc la fissuration induite en raison du développement des contraintes de traction n'est pas le phénomène dominant. Partant des principes qui caractérisent l'approche variationnelle utilisés pour construire le modèle, il a été montré que une dessiccation suffisamment forte peut amorcer l'endommagement de manière homogène sur la face en train de sécher tout en progressant dans le domaine dans le temps. L'apparition éventuelle de bifurcations de cette solution de base a été analysée, toujours dans le cadre de l'ASL.

Ce travail ouvre la voie à plusieurs pistes de recherche, la plus naturelle étant l'étude du couplage entre les instabilités présentées ci-dessus. En dehors de cela, des simulations bidimensionnelles de l'écoulement par digitation ont montré que le modèle prédit des caractéristiques supplémentaires d'écoulement instable, telles que le pincement et la coalescence de la phase de mouillage, qui doivent être étudiées à l'aide d'un campagne expérimentale soigneusement conçue. L'initiation de l'endommagement induit par l'évolution des doigts de drainage présente également un intérêt particulier dans le cadre des applications mentionnées précédemment. Enfin, des techniques numériques avancées peuvent être recherchées pour la résolution des problèmes ci-dessus dans le but de fournir des solutions précises plus efficacement.

Title: Study of hydro-mechanical instabilities in geomaterials

Keywords: partial saturation; geomaterials; phase field modeling; non-uniform fluid; gradient damage;

Abstract: Hydraulic and mechanical instabilities in geomaterials refer to a variety of non-linear phenomena that can be triggered by heterogeneities inherent to such materials. Hydraulic instabilities in partially saturated conditions can manifest themselves as heterogeneous fluid invasion causing 'fingering' phenomenon. Mechanical instabilities on the other hand can present themselves as strain localizations and/or fractures. These instabilities and their associated coupling pose a major obstacle for a myriad of applications involving geomaterials like Carbon dioxide (CO_2) sequestration, rain water infiltration and also for reliable predictions such as for contaminant flow in ground waters. Existing classical models do not resolve this behavior due to their lack of pattern-forming ingredients in their formulation and thus being stable against perturbations. The essence of current thesis work is to propose and investigate modeling techniques that allow to describe these instabilities in a simple and natural manner. The constitutive approach adopted in this thesis is that of micro-structured continua, in particular that of enhanced continua with a constitutive law depending on the gradient of so-called phase field variables.

The first part of the work deals with description of a fluid-fluid front that has been modeled as a diffused interface. This has been done by interpreting the presence of two fluids within the pore space as a single non-uniform fluid and the degree of saturation of one of the fluids as the corresponding phase field. While classical one-to-one relation between capillary pressure and saturation degree is expected to describe the retention properties of the porous network due to its texture, an enhanced relation is obtained by prescribing a chemical potential in the spirit of Cahn-Hilliard type modeling of multi-phase fluids. This enhanced relation together with a non-local energy contribution provides the ingredients required to describe fluid-fingering and non-local phenomena such as pinching and coalescence of fluids due to variations in capillary forces. Using asymptotic matching techniques it has been shown analytically, in a one-dimensional setting, that the particular choice of energy contributions employed in the above framework allows to replicate 'overshoot' type non-monotonic saturation profiles during constant-rate infiltration into relatively dry medium. This has been found to match qualitatively with experimental observation. Further, a slight non-convexity introduced into the flux function has been shown numerically to allow the modeling of drainage fronts, besides imbibition, without employing any additional complexities into the model. A careful linear stability analysis (LSA) of the homogeneous solutions against arbitrary perturbations has been done. The growth in time of the amplitude of imposed transverse perturbations is understood as the fingering phenomenon. The predictions of the LSA have been followed-up by two-dimensional simulations portraying the ability of the proposed model to describe fluid fingering and segregation.

In the second part the triggering of a fracture within a drying porous medium has been studied. A prevailing modeling perspective, in the spirit of gradient damage modeling, has been first tested for its ability to replicate periodic fracture formation as observed in representative experiments. Further an investigation is done, starting from the gradient damage modeling framework, but interpreting the presence of a fracture within a drying porous material as a loss of its capillary properties, thus allowing the passage of non-wetting fluid under vanishing capillary pressure. This paradigm is of particular interest in modeling cohesion-less and unconsolidated fine-grained soils, where the resistance against tensile loading is negligible and thus fracturing induced due to development of tensile stresses is not the prevailing phenomenon. Starting from the principles of variational approach used to construct the model, it has been shown that for sufficiently strong desiccation, damage initiates homogeneously on the drying face while progressing into the body with time. The possible occurrence of bifurcations of this base solution has been analyzed, again in the framework of LSA.

This works sets the stage for various possibilities, the most natural one being the study of coupling between the above mentioned instabilities. Apart from that, two-dimensional simulations of fluid-fingering have shown that the model predicts additional features of unstable flow, such as pinching and coalescence of the wetting phase, which need to be investigated using carefully designed experiments. Initiation of damage induced due to evolving drainage finger is also of particular interest in the context of earlier mentioned applications. Lastly, advanced numerical techniques can be sought after for resolution of the above problems with an intent to provide accurate solutions more efficiently.